Fall 12-20-2019

Engineering Hyaluronic Acid for Biomedical Applications

Deep S. Bhattacharya
University of Nebraska Medical Center

ENGINEERING HYALURONIC ACID FOR BIOMEDICAL APPLICATIONS

by

Deep S Bhattacharya

A DISSERTATION

Presented to the faculty of

the Graduate College in the University of Nebraska

in Partial Fulfilment of the Requirements

for the Degree of Doctor of Philosophy

Department of Pharmaceutical Sciences

Under the Supervision of Professor Aaron M. Mohs

University of Nebraska Medical Center

Omaha, Nebraska

November 2019

Supervisory Committee:

Amarnath Natarajan, Ph.D.; David Oupicky, Ph.D.; Jered Garrison Ph.D.

TABLE OF CONTENTS

CHAPTER II. IMPACT OF STRUCTURALLY MODIFYING HYALURONIC ACID ON CD44 INTERACTION

CHAPTER III. MODULATING TARGETING PROPERTIES OF HYALURONIC ACID FOR DELIVERY OF IMAGING AGENTS TO TUMOR MICROENVIRONMENT

ACKNOWLEDGMENT

Firstly, I would like to express my sincere gratitude to my advisor Dr. Aaron M Mohs for the continuous support of my Ph.D. curriculum and related research, for his patience, motivation, scientific freedom, and knowledge. His guidance and perseverance helped me grow during the time of research and graduate career. I could not have imagined having a better advisor for my Ph.D. graduate career. I would also like to sincerely thank Dr. Mohs for letting me intern at GlaxoSmithKline as a Co-op to explore plethora of opportunities in the pharmaceutical industry. This experience indeed turned out to be a very beneficial for my professional and personal goals in life.

Besides my advisor, I would like to thank my Ph.D. advisory committee: Dr. Oupicky, Dr. Natarajan, and Dr. Garrison for their insightful comments and encouragement, but also for the engaging discussions during committee meetings and my comprehensive examination which taught me to widen my research from various perspectives and think outside the box for solutions.

As correctly said by Karl Popper that "*Whenever a theory appears to you as the only possible one, take this as a sign that you have neither understood the theory nor the problem which it was intended to solve*", I clearly understood this through ups and downs in the past 5 years of my Ph.D. career. I am glad that this roller coaster journey as a Ph.D. student is ending but I have learnt a lot in this short time which I will cherish all my life.

This acknowledgment will be incomplete without mentioning the friends I have made in the past 5 years. Shrey, Tanmay, Aneesha, Aishwarya, Suyash, and all my friends at UNMC who have become like family to me. They helped me get through graduate school smoothly, enjoyed weekends, and eventful unplanned trips. I could not have asked more, and I thank god for all.

I would like to thank Dr. Joshua Souchek, Dr. Denis Svechkarev, and Dr. Tanner Hill who have mentored me throughout my Ph.D. career. I am also fortunate to have cheerful lab members: Bowen, Maddie, Paul, Nick, Lucas, Xiang, and summer rotation students who made it a wonderful environment to work and grow professionally.

I would especially like to thank Katina Winters and Renee Kaszynski who helped me on-board smoothly and always unhesitatingly helped me with any requests in the PGSP program. I would also like to thank all the UNMC research core facilities (NMR, Flow cytometry, Confocal microscopy, and TEM) for the help in my projects and funding support from NIH and UNMC Program of Excellence Graduate Fellowship.

Last but not least, I would not be able to get to this position in life if I did not have support from my wonderful god-like parents. My mother Manideepa Bhattacharya and my father Sandip Bhattacharya helped me in all ways possible to foster my dreams in pursuing a Ph.D. thousands of miles away from them. I am indeed thankful to god to have such amazing parents as pillars in my life.

-Deep S Bhattacharya, 2019

ENGINEERING HYALURONIC ACID FOR BIOMEDICAL APPLICATIONS

Deep S Bhattacharya, Ph.D.

University of Nebraska, 2019

Supervisor: Aaron M. Mohs, Ph.D.

This work presents research using the naturally available non-sulfated carbohydrate glycosaminoglycan hyaluronic acid (HA) for the synthesis of different chemical derivatives of HA for evaluation of binding kinetics with CD44 and P-selectin proteins for applications in fluorescence image-guided surgery. Chemical derivatives of HA such as deacetylated HA (deHA), sulfated HA (sHA), and deacetylated and sulfated HA (s-deHA) were synthesized by modulating sulfating and deacetylating reagents to alter binding specificities to CD44. Modified HA derivatives and CD44 biophysical interactions were assessed by fluorescence polarization. In silico techniques were also used to determine binding using molecular docking and MM-PBSA approaches. Both modifications represent the first step to effectively re-target HA-based materials. Re-targeting HA was successfully conducted by tuning the sulfate distribution on HA to P-selectin. Sulfate modifications render HA with dual-targeting potential to both CD44 and P-selectin. Three derivatives of HA were synthesized by controlling the sulfation agent to give selectively sulfated HA (ssHA), moderately sulfated HA (msHA), and completely sulfated HA (csHA). The strongest binding was observed for the csHA with recombinant P-selectin when compared with fucoidan. Amphiphilic conjugates

were prepared for the three derivatives of HA by conjugating a hydrophobic ligand (1-pyrenebutanamide- PBA) followed by chemical conjugation of Cyanine7.5 dye to give near-infrared fluorescent nanoparticles. Modified HA nanoparticles were assessed for uptake in P-selectin and CD44 positive cells along with knockout cell lines. Preference for P-selectin mediated uptake was observed *in vitro* binding assays. *In vivo* performance for image-guided surgery applications indicated higher uptake of sulfated HA nanoparticles compared to non-sulfated HA nanoparticles in S2-013 tumors grown subcutaneously in nude mice. HA as a non-toxic, biocompatible material is an ideal precursor for generating newer imaging probes for biomedical applications. HA as a non-fluorescent precursor was conjugated with non-fluorescent biocompatible amino acids to form a novel fluorescent organic nanoparticle (FONPs) using one-pot green chemistry conditions. The FONPs exhibited high water solubility due to the existence of hydrophilic functional groups on its surface, acceptable stability profiles, superior biocompatibility, and high quantum yield photo-luminescent properties. Also, the FONPs demonstrated drug carrier properties with enhanced drug loading and delivery of the anticancer drug doxorubicin (DOX) in cancer cells and 3D tumor spheroid model. Results demonstrate the efficacy of a novel fluorescent HA-based with potential future applications in image-guided drug delivery.

LIST OF FIGURES

LIST OF TABLES

Chapter 3

LIST OF ABBREVIATIONS

MMP9: Matrix Metalloproteinase 9

HA: Hyaluronic acid

CD147: Emmprin

TSG-6: Tumor necrosis factor-stimulated gene 6

LYVE-1: Lymphatic vessel endothelial hyaluronan receptor 1

HABD: Hyaluronic acid binding domain

PD: Partially disordered

DSSP: Dialog system for structured programming

HAS: Hyaluronan synthase

ECM: Extracellular matrix

RHAMM: Receptor for hyaluronan mediated motility

TLR: Toll-like receptors

HARE: Hyaluronan receptor for endocytosis

EDC: 1-ethyl-3-(3-dimethyl aminopropyl) carbodiimide

GTA: glutaraldehyde

DVS: divinyl sulfone

PEGDE: poly(ethylene glycol) diglycidyl ether

TBA: tetrabutylammonium

VEGF: Vascular endothelial growth factor

NMR: Nuclear Magnetic Resonance

IR: Infrared

FGF: Fibroblast growth factor

GDNF: Glial cell-derived neutrophic factor

TGF-β: Transforming growth factor

CD26P: P-selectin

CD62E: E-selectin

CD62L: L-selectin

PSGL-1: P-selectin glycoprotein ligand-1

sLeX: Sialyl lewis^{x}

RES: Reticular endothelial system

FONP: Fluorescent organic nanoparticle

CEE: Cross-linked enhanced emission

AIE: Aggregation induced emission

deHA: Deacetylated hyaluronic acid

sHA: Sulfated hyaluronic acid

s-deHA: Sulfated and deacetylated HA

FP: Fluorescence Polarization

CRISPR/Cas9: clustered regularly interspaced short palindromic repeats and CRISPR-associated protein 9

EPR: Enhanced permeation retention

SPR: Surface Plasma resonance

ssHA: Selectively sulfated hyaluronic acid

msHA: Moderately sulfated hyaluronic acid

csHA: Completely sulfated hyaluronic acid

NCPD: non-conjugated polymer dots

CHAPTER I

INTRODUCTION

1.1 CD44 Introduction

CD44, a cell surface glycoprotein also referred to as P-glycoprotein[1] part of a larger group of hyaluronan-binding proteins, termed hyaladherins[2] is highly expressed in many cancers which regulate metastasis. A single gene encodes CD44 on a chromosome locus 11p13[3] with a molecular weight of 75-150 kDa[4]. The standard CD44 is post-translated from the transcription of exons 1-5 and 16-20[5] that are spliced together by protein-development machinery in the cell giving rise to primary domains of CD44 as extracellular or ectodomain, transmembrane, and cytoplasmic domains (**Figure 1**)[6].

The primary binding domain of CD44 which is homologous to B loop of cartilage binding link proteins[7] coined a link module is responsible for binding/interacting with external microenvironment and hyaluronic acid[8]. The transmembrane domain of the protein is involved in interacting with co-factors, adaptor proteins, and ions[9]. The intracellular domain has a short-and long-tail spliced configuration which functions with multiple downstream and nuclear factors responsible for localization and mediation of cellular responses such as growth-promoting tumor receptor tyrosine kinases[10,11,12]. CD44 is also involved in other cellular functions such as proliferation, cellular migration, differentiation, angiogenesis, protease docking, cell survival, chemokines and growth factors, and adhesive properties[13,14,15,16].

Dynamic regulation of actin cytoskeleton with different CD44 conformations is involved in migration of and interactions of matrix metalloproteinase 9 (MMP9) with various cancer cells[17,18]. Abundant literature reports highlight the clinicopathological importance of cancer cells by undergoing epithelial to mesenchymal transition acquiring stem-cell-like properties promote increased CD44 expression for proliferation, adhesion, migration, and invasion[19,20,21].

1.2 CD44 composition

CD44, a single non-kinase transmembrane glycoprotein was first cloned in 1989[22], gene derived from a single copy of located on the short arm of human chromosome 11 and chromosome 2 in mice species, roughly extending 50 kb in genomic DNA[13]. The protein varies in molecular size due to differences in glycosylation patterns (O-and N-glycosylation) in the extracellular domains[23,24]. CD44 proteins contain roughly ten variants varying between gene 5 and gene 16 with insertions of different lengths governing the splicing and transcription of final protein[25]. The ligand-binding domain in the extracellular space and the protein has a half-life of 8 h[26]. Theoretically, 900 CD44-isoforms can be generated by alternative gene-splicing among exons, but all of them are not expressed by the cell.

The standard form of CD44 is the most abundantly found variant of CD44, which contains six potential phosphorylation sites in the intracellular variable fragment. All the other variants are glycosylated mostly at the asparagine or serine sites located dispersed in the extra-cellular domain[27].

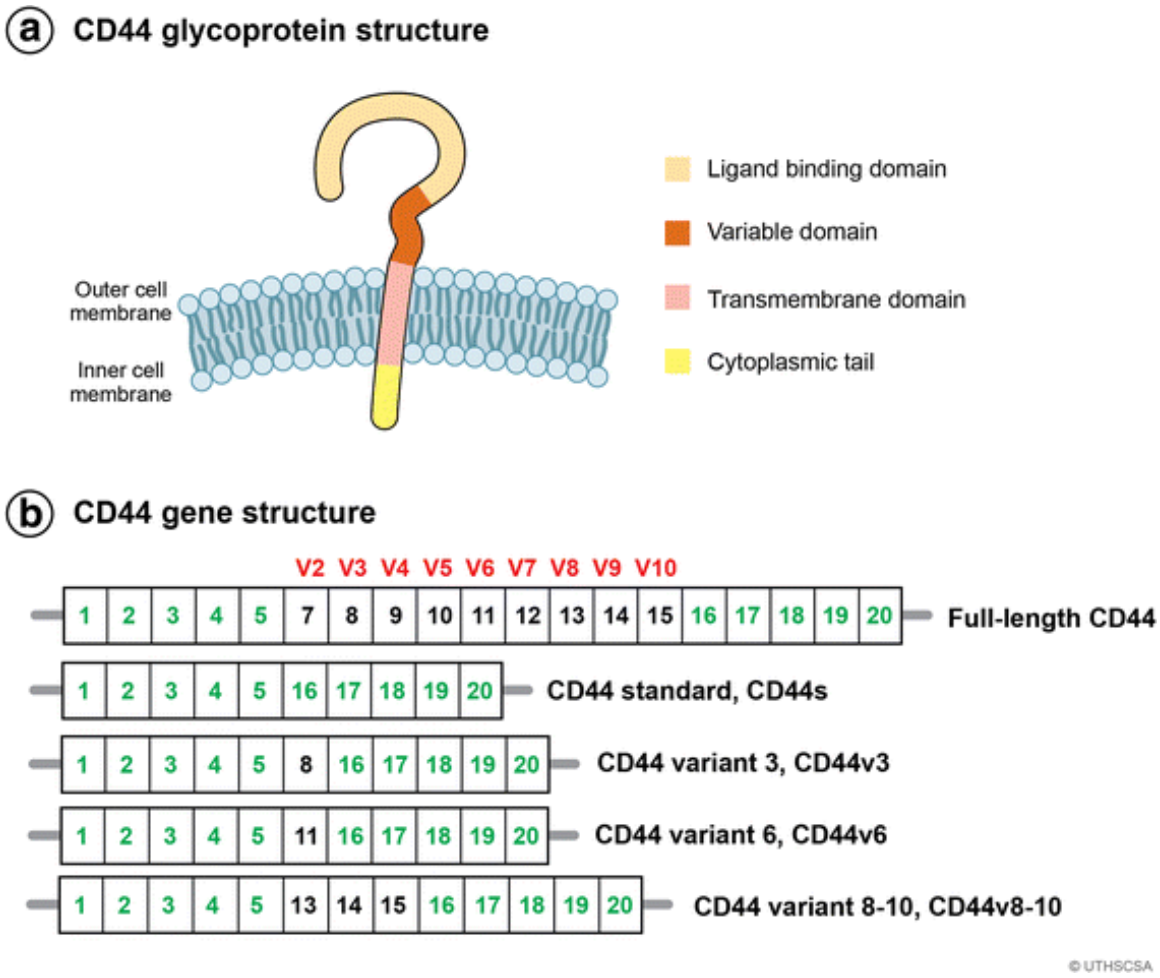

Figure 1: (a) Four domains of CD44 glycoprotein are presented with corresponding colors: ligand binding domain, variable domain, transmembrane domain, and cytoplasmic tail. (b) CD44 is encoded by 20 exons in mice but 19 exons in humans. Exon 6 coding for CD44 variant 1 (CD44v1) is lacking in humans. Green color exons are always expressed as a standard form of CD44 (CD44s), and up to nine exon variants can be inserted by alternative splicing. Full-length CD44, CD44s, CD44v3, CD44v6, and CD44v8-10 are shown schematically

1.3. Functional significance of CD44 and molecular targets in cancer and non-cancerous cells

The role of CD44 and its isoforms expression plays a vital in the pathogenesis of cancer. Distribution of both is widely found in healthy adult and fetal states of evolution[28]. The CD44 standard protein was initially isolated from tissues of the central nervous system, lung, and epidermis, which were part of the hematopoietic cellular system[29]. In healthy tissues, keratinocytes, macrophages, epithelial cells, CD44 play a vital role in regulation of hyaluronic acid (HA) metabolism and turnover, lymphocyte activation, the release of cytokines, wound healing, and proliferation. CD44 in cancerous states play a significant role in metastasis at distant sites for growth[30]. CD44 is also defined as cancer-initiating cell marker due to its cross-talk with multiple cell types. Cell-to-cell or cell-to-matrix interactions involving CD44 might protect tumor cells recognition from the immune system, facilitating colonization. Levels of CD44 and its variants can be used in assessments of resected tumor biopsies for prognosis and neoplastic properties of diseases.

CD44 along with its variants can undergo dynamic switching depending on tumor phenotype, e.g., pancreatic cancer cells were mainly dependent on upregulation of standard CD44 and variant 6[31]; prostate cancer cells that are benign express higher CD44 variant 5; breast cancer cells have abnormal expression profiles of both CD44 and multiple isoforms[28]. Among the many CD44 functions, it plays a significant role in transforming cell lines that are non-metastatic by altering the adaptive plasticity to more fiercely positive metastatic

behavior[32]. CD44 and its variants are also related to the poor prognosis in colorectal cancer. Clinicopathological characteristics and prognosis of gastrointestinal patients are linked to higher expression of CD44 variant 6 and variant 9 along with standard CD44 expression[31]. Varying molecular biology techniques have evaluated CD44 expression in normal and cancerous cells, and the association of a gradual increase in CD44 expression from less malignant to more advanced stages is another indication of importance in the cancer progression/malignant process[33]. CD44 and its isoforms are also highly expressed in thyroid carcinoma, hepatocellular carcinoma, renal cell carcinoma, endometrial cancer, and ovarian cancer carcinoma.

CD44 is known to interact with various signaling pathways such as protein kinases playing a crucial role in drug resistance and tumor invasiveness properties[34]; cytoskeletal alterations in Ezrin-Radixin-Moesin pathway by altering phosphorylation patterns in other pathways[35]; modulation of transcriptional factors and pathways such as hippo signaling[36], β-catenin pathway[37], TGF-β[38], Emmprin (CD147)[39], and STAT3[40].

Hyaluronidases also termed as “spreading factor” that degrades high molecular weight HA to lower molecular weight in the extracellular matrix[41]. The enzyme also has clinical relevance as degradation of HA by hyaluronidases is known to facilitate tumor invasiveness by the support of CD44-HA interactions, mediating cell migration, and spreading[42]. Extensive degradation of HA in the extracellular matrix might for pockets, reducing the viscosity of HA, giving room for tumor cells to invade and spread. A previous study reported elevated levels

of hyaluronidases with increasing degree of colon carcinoma[43]. However, many factors, such as tumor type variance, hyaluronidase enzyme isotype, the molecular weight of HA in the matrix, might influence the degradation kinetics and role in cancer spreading.

1.4. CD44 structure, ligands, and biophysical mechanism of hyaluronic acid binding

CD44, a type I transmembrane protein, interacts with HA as its primary ligand via link module[44]. Structurally, the canonical form of human CD44 consists of 723 residues, divided into four distinct domains. The important extracellular HA binding domain is conserved, which contains an α/β-fold consisting of approximately 158-residues in length[45]. The link module, comprising of N-terminal and C-terminal flanking regions with six β-strands and two α-helices similar to C-type lectin domain, form the globular HA-binding unit stabilized by three disulfide bridges[46]. The binding regions also interact with similar HA-binding proteins, such as TSG-6[47] and LYVE-1[48]. Majority of the binding domain to HA is also retained in the soluble portion of the protein allowing successful protein expression and purification.

Currently, there is only one crystal structure of CD44 bound to HA been used extensively for two decades[46]. The CD44 protein shows substantial selectivity for recognition of HA over other carbohydrate glycosaminoglycans due to its highly specific interactions. HA has shown to bind to the shallow binding groove of the active site with multiple specific hydrogen bonds and van-der-wall interactions

along with smaller pockets of hydrophobic patches to accommodate the methyl group of N-acetyl glucosamine[49]. Other interactions include oxygen atoms of the carboxylate group forming hydrogen bonds; the N-acetyl group forms hydrophobic and multiple water-mediated hydrogen bonds. Lacking critical CH-π interactions in the complex is characteristic of the protein-carbohydrate complex. The minimum number of units that can bind to CD44 has been reported to be an octamer-variant of HA. This specificity arises due to the characteristics peculiar to glucuronic acid and N-acetyl glucosamine repeat units in HA[50].

The crystallographic complex of HA-CD44 has been shown to exist in two conformation states (called “A” and “B”). CD44 HABD exchanges its conformation between ordered (O) and partially disordered (PD) states in either the absence or presence of the HA ligand, respectively. This change in conformation causes “B” conformation to correspond to more intimate contact between HA and CD44 compared to conformation “A”. This interconversion between two distinct conformations has the exchange rate of hundreds of milliseconds[51]. Thirteen critical residues in the Link binding-module (Arg45, Tyr46, Cys81, Arg82, Tyr83, Ile92, Asn98, Ile100, Cys101, Ala102, Ala103, His105, and Tyr109) make contacts with HA, and there is a notably large contribution from aliphatic side chains to HA binding (including Ile92, Ile100, Ala102, and Ala103, which are all located in the β4-β5 loop). The remainder of the binding groove is lined by aromatic and basic residues (Arg45, Tyr46, Arg82, and Tyr83) brought together from the β1-α1 and α2-β3 loops, together with Tyr109 from the β5 strand. HA-binding surface on CD44 on the link domain also found (R29, K38, R41) and

another in the C-terminal extension (R150, R154, K158, R162)—to be crucial for the binding. N-glycosylation post-translational modifications also have a crucial role in HA binding, as negatively charged sialic acid can impede interactions of -COOH of HA with basic residues in the active site[52]. Such interactions can be exploited to modulate interactions of HA with CD44.

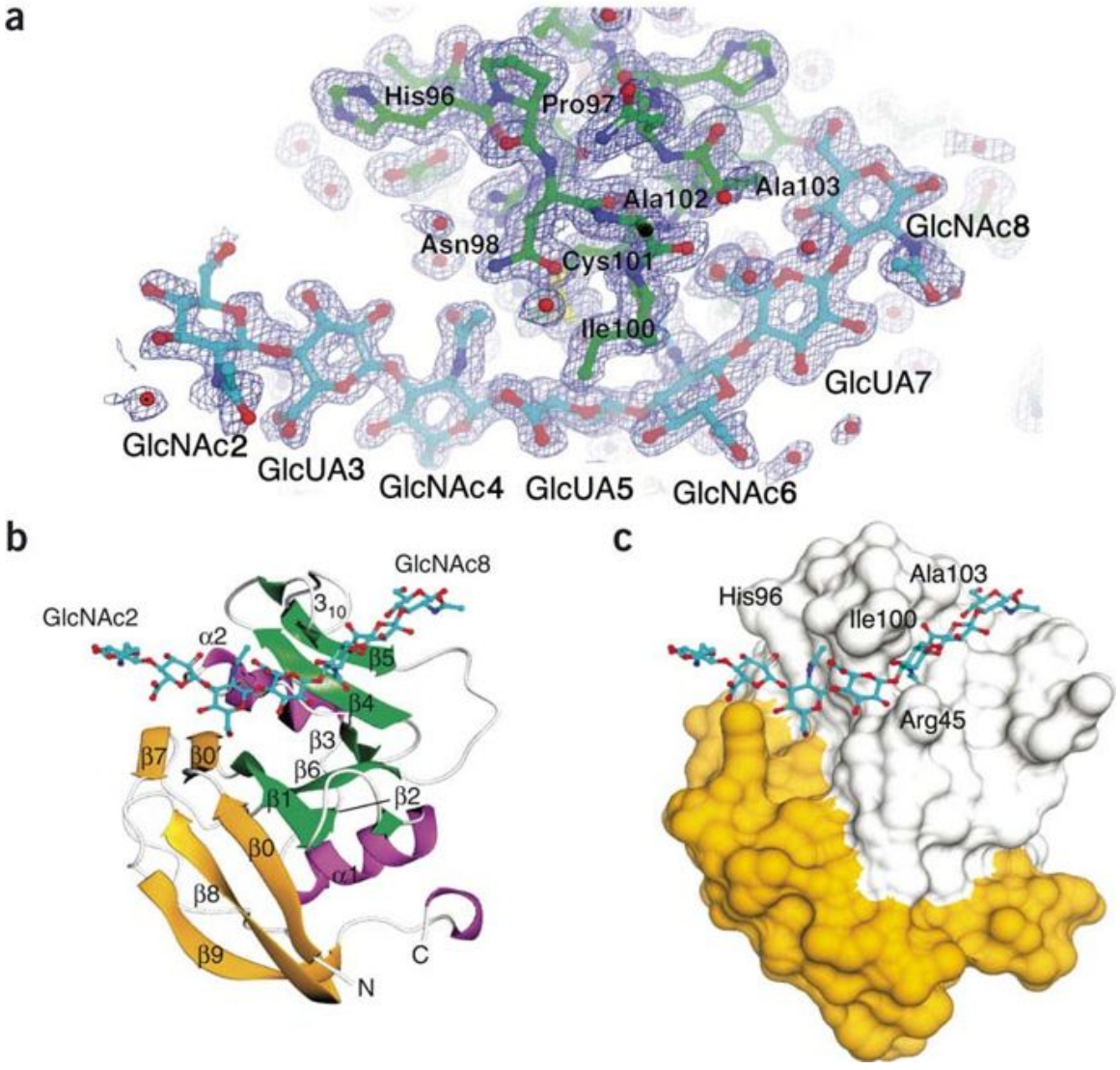

Figure 2: (a) Final 1.25 -Å-resolution electron density for the binding site of CD44 with hyaluronic acid polymer generated by SIGMAA. (b) A ribbon diagram of mouse Cd44 (type B complex), with secondary structure identified using the

DSSP algorithm33. Pink, α-helices; white, loops; green and gold, β-sheets I and II, respectively; cyan, bound HA. (c) Surface representation of the HA-binding site in the type B crystal complex. The shallow HA-binding groove is shown as molecular surface. Gold, supplementary lobe formed from N- and C-terminal Link extensions; cyan, HA. Selected residues marking the boundaries of the groove are labeled. The type A crystal form shows similar features but lacks the lower platform for the HA interaction provided by reorientation of Arg45.

1.5. Hyaluronic acid structure, cell surface receptors, and its chemical modifications thereof

HA is a linear polysaccharide composed of alternating units of D-glucuronic acid and N-acetyl-D-glucosamine with β-(1→4) glycoside linkage between the two units and with no known post-synthetic modifications. HA amongst all other glycosaminoglycan is the only non-sulfated variant in the extracellular matrix and synovial fluid, making it uniquely popular for applications in the field of biomaterials[53]. The unique β-bond configuration renders the carbohydrate a very energetically-stable structure, with its functional groups in favorable equatorial positions. HA exists as negatively charged molecule in an aqueous solution in which readily forms salts generally termed as hyaluronan or hyaluronate[54]. In solution, HA forms a double-fold helical duplex with an interplay of hydrophobic CH groups and inter-molecular H-bonds, enabling the formation of the mesh network. HA solutions display a non-Newtonian, shear-thinning, and viscoelastic behavior[55] (**Figure 3**).

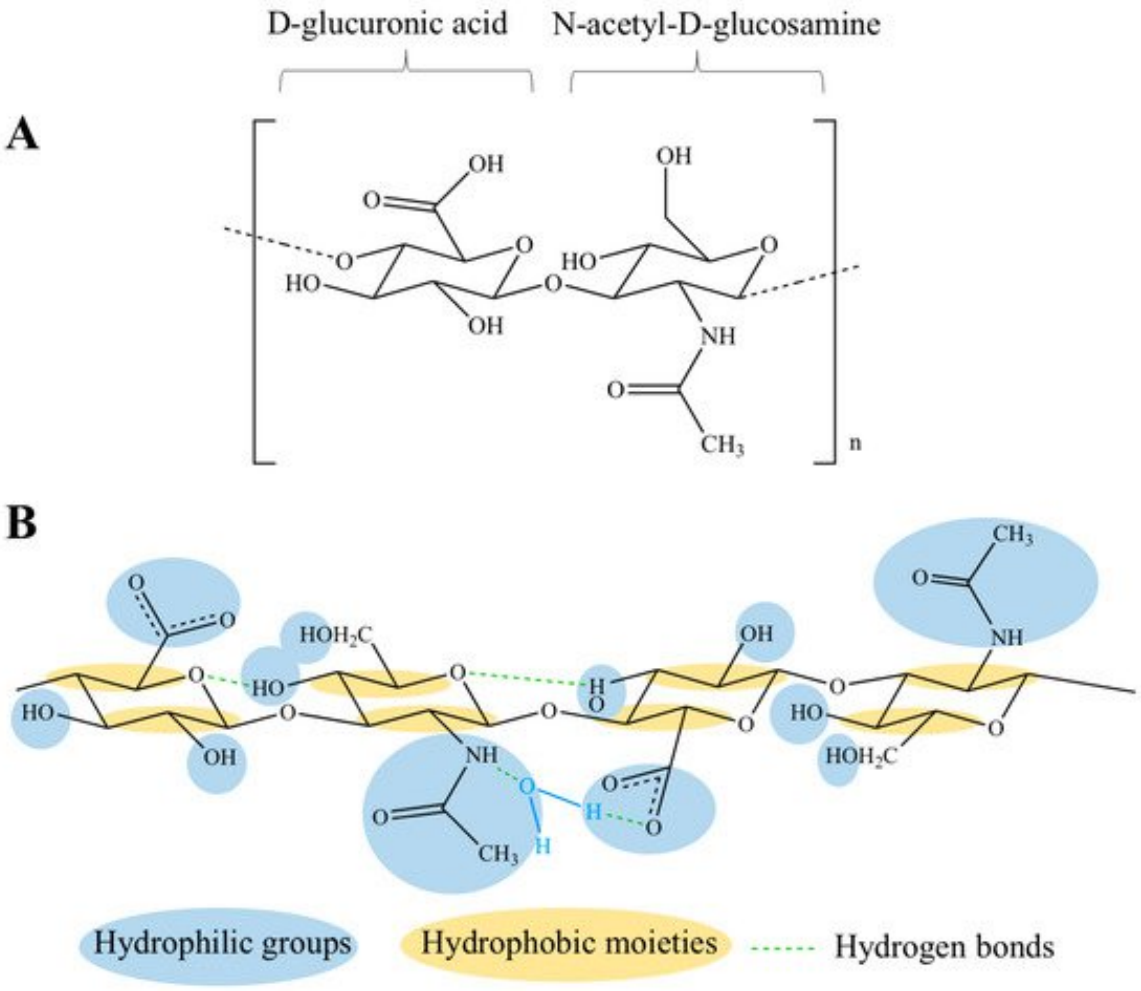

Figure 3: Chemical structures of HA disaccharide unit (A) and HA tetrasaccharide unit where the hydrophilic functional groups and the hydrophobic moieties are respectively evidenced in blue and yellow, while the hydrogen bonds are represented by green dashed lines (B).

HA is uniquely synthesized by hyaluronan synthase (HAS1, 2, 3) at the inner face of the plasma membrane rather than in the Golgi apparatus without any covalent bond to a protein core, unlike any typical glycosaminoglycans such as heparin sulfate, chondroitin sulfate, dermatan sulfate, keratin sulfate etc[56]. The average content of HA in a 70-kg adult is about 15 g forming the pericellular coating and extracellular matrix (ECM) in connective tissues[57]. Hyaluronan degrades to glucuronic acid and N-acetylglucosamine in lysosomes (pH 3-4) and is metabolized by hepatocytes to CO_2, H_2O and urea.

The balance between the synthesis and degradation of HA plays an essential regulatory function in determining the molecular weight of HA generated. HA, according to the vast array of literature reports, performs two underlying biological mechanisms: passive structural molecule and as a signaling moiety, both dependent on the size of HA generated in the body[58]. High molecular weight HA plays an important role in inflammation, tissue injury and repair, wound healing, and immunosuppression. It is also reported to bind fibrinogen and controls the recruitment of inflammatory cells[59]. Diversely, low molecular weight HA can also stimulate the production of proinflammatory cytokines, induce tumor progression, promote ECM remodeling, and pro-angiogenic[60]. Despite the research performed previous decades, there is still little known about all HA's biological role and the interplay of different molecular weights which will be beneficial for facilitating the development of novel-HA therapies.

HA interacts with other cellular receptors other than CD44 in mediating signal transduction, the formation of a pericellular coating, and receptor-mediated

internalization mechanism. HA is reported to interact with RHAMM (CD168)[61], HARE[62], LYVE-1[63], and TLR's[59]. RHAMM or receptor for HA-mediated cell motility is involved in tissue repair, modulating signaling pathways, and controlling internalization of macrophages and fibroblasts. Hyaluronan receptor for endocytosis (HARE) is mainly involved in clearance of glycosaminoglycans and is primarily found in liver, lymph nodes, spleen, and the endothelial lining of eye and kidney. Lymphatic vessel endothelial hyaluronan receptor (LYVE-1) controls HA-turnover rates, regulation of lymphangiogenesis, and tissue hydration properties (Summary in **figure 4**).

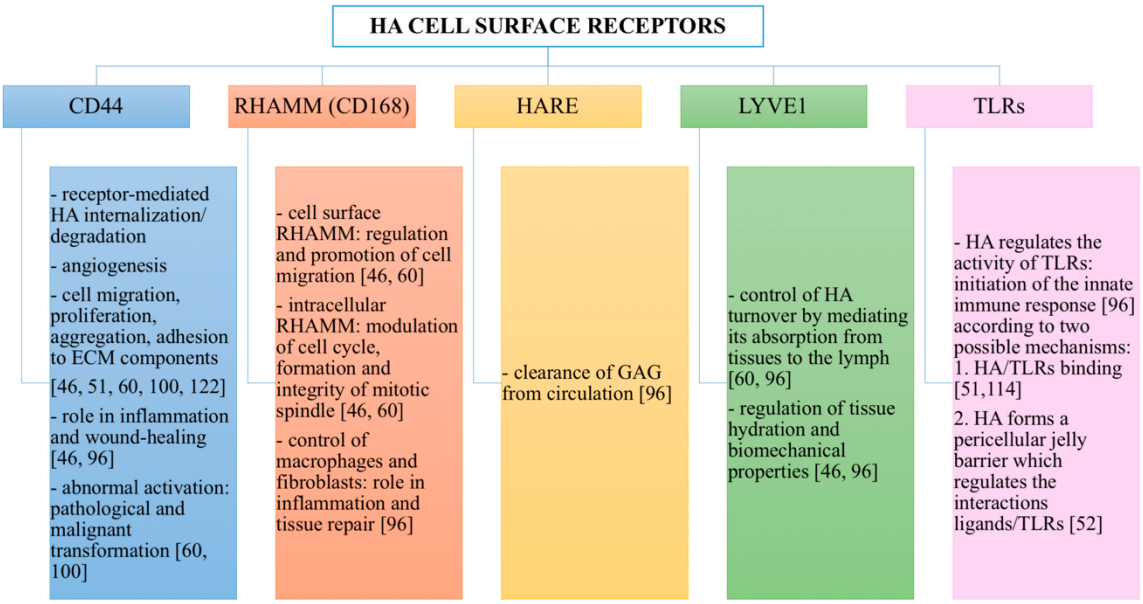

Figure 4: Summary of HA cell surface receptors and of the actions that they control when linked by HA.

HA presents multiple modifiable chemical groups for chemical modifications to prolong the half-life and improving properties for preparing new biomaterials for various medical, cosmetic, pharmaceutical and food applications[64,65]. Primary sites for modifications include the abundant hydrophilic hydroxyl groups, carboxyl groups, and N-acetyl groups on the carbohydrate structure[66]. Two major modification strategies include the conjugation and cross-linking of HA. Conjugation includes the addition of a new molecule to polymer HA for modification of amphiphilicity, improve drug delivery properties, develop pro-drugs, include additional targeting moieties of intended therapeutic outcomes. Whereas, cross-linking strategies mainly considered for improving rheological, mechanical, slowing degradation rates, controlled release of pharmaceutical compounds[67], and photophysical properties. Trends in the field of bioconjugate chemistry also include mixing both conjugation and cross-linking strategies for developing new scaffolds or biomaterials.

Selected cross-linking agents listed used are hydrazide, 1-ethyl-3-(3-dimethyl aminopropyl) carbodiimide (EDC), genipin, glutaraldehyde (GTA), divinyl sulfone (DVS), poly(ethylene glycol) diglycidyl ether (PEGDE) and poly(ethylene glycol) divinyl sulfone (PEGDVS)[68], leading to the formation of HA-based hydrogels for applications in 3D-cell culture, tumor tissue remodeling, cartilage regeneration, and drug screening assays[69,70]. Cross-linking HA directly affects degradation kinetics which seems to impact *in vivo* properties of HA for biomedical purposes[71].

HA for chemically conjugation purpose can be facilitated in aqueous phase due to its hydrophilic nature and high solubility in water. Click chemistry syntheses for simple chemo-selective modifications, Diers-Alder cycloaddition, azide-alkyne cycloadditions, thiol-ene reaction, oxidation, and photo-crosslinked controlled oxidation alternatives have been used to modify HA effectively[72,73,74,75]. Strategies to modify carboxylic groups includes esterification using alkyl halides, tosylate activation, or use of diazomethane as an activator of carboxyl groups[76]. Amidation on carboxylic acid groups includes the use of carbodiimide (i.e., N-(3-dimethyl aminopropyl)-N′-ethyl carbodiimide hydrochloride) (EDC). Co-activators such are N-hydroxy succinimide (NHS) or 1-hydroxy benzotriazole in water, 1,1′-carbonyldiimidazole or 2-chloro-1-methyl pyridinium iodide in DMSO and DMF organic solvents for effective amidation of HA[77]. Promising methods in increasing yields could include use of triazine-mediated amidation, using 2-chloro-dimethoxy-1,3,5-triazine or (4-(4,6-dimethoxy-1,3,5-triazin-2-yl)-4-methylmorpholinium (DMTMM)[78].

Modifications on hydroxyl groups of HA is carried by formation of epoxides and bisepoxides by using reagents such as butanediol-diglycidyl ether (BDDE), epichlorohydrin, and 1,2,7,8-diepoxyoctane in mildly alkaline conditions[79]. Esterification of hydroxyl groups of HA can be obtained by reacting octenyl succinic anhydride, methacrylic anhydride, or acyl-chloride carboxylates[80,81,82]. Ether derivatives can be prepared by using divinyl sulfone or ethylene sulfide reagents. Other non-typical approaches to increase the solubility of HA in organic solvents include formation of the tetrabutylammonium (TBA) salts for varied multi-

step synthetic approaches[66]. Recently, sulfation of hydroxyl groups have gained substance in past few years due to its unique properties such as slower degradation rates, promotion of chondrogenesis of human mesenchymal cells[83], binding to different protein stromal cell-derived factor 1-α, SDF-1α for drug delivery properties[84], and binding to Vascular endothelial growth factor 165 (VEGF)[85] isoforms for angiogenesis-related disease.

1.6. Role of sulfated polysaccharides in targeting different receptors in cancer and infectious diseases

Polysaccharides are an ideal natural source of supplements. As macromolecular, polysaccharides are derived from the polymerization of multiple monomeric or monosaccharide containing units linked through O/N-glyosidic bonds in either linear or branched conformations[86]. Many polysaccharides have broad or weak bioactivities due to its structure or physicochemical properties, conformational states or molecular weight. Regio-selective or full-scale chemical modifications approaches can be applied to tune chemical, physical, and biological attributes to alter binding and structural properties. Modifications could alter molecular weight, substituent groups, and positions, structure impacting bioactivity[87]. Recent reports on various modification approaches on polysaccharides include sulfation[88], phosphorylation[89], methylation[90], carboxymethylation[91], acetylation[92], deacetylation[66], etherification[93], alkylation[94]. From which, sulfation of glycosaminoglycan presents an attractive hotspot in the field of polysaccharide research due to the outstanding applications in pharmaceutical research.

Sulfated polysaccharides refer to sugar-chains containing polyanionic sulfate groups on different hydroxyl groups, carboxyl, or amino-terminal groups either introduced artificially or naturally present supporting a vast array of biological activities. Composition of sulfated polysaccharides is of keen interest due to its interesting physicochemical, biomechanical, and biological properties. Naturally available sulfated polysaccharide broadly includes chondroitin sulfate, iota-carrageenan's, fucoidan, heparin, keratan, spirulina, and galactans[95]. The presence of sulfate group on a polysaccharide sugar backbone renders binding electrostatically to positively charged biomolecules over a wide pH range (4-12). Unlike carboxylate polysaccharides, sulfated polysaccharide does not alter pH and remain stable. It has also been reported using complex computational modeling algorithms that sulfated polysaccharide possess an open extended stiffer conformation in solution to minimize the negative charge[96].

Given the interest in sulfated polysaccharides, several methods for preparing sulfated polysaccharides have been developed to understand structure-property-activity relationships. Methods include the use of chlorosulfonic acid, sulfuric acid, sulphamic acid-pyridine, and sulfur-trioxide-pyridine complex[87]. The most common and reliable method today employs the use of sulfur-trioxide pyridine complex in a polysaccharide sulfated synthetic scheme. Newer methodologies include utilization of microwave reactions, DMAP as catalysts to decrease reaction time, and chemoenzymatic selective reactions[96]. Regioselectivity of sulfation patterns in polysaccharides seem to be influenced mainly due to steric effects, polarity of O-H bonds in equatorial and axial positions, and acidity of

hydroxyl group present for substitution. Characterization methods such as NMR and IR spectroscopy and elemental analysis are widely popular methods for determining site and degree of sulfation on polysaccharides.

Subtle variations in sulfation patterns can confer a polysaccharide precise and physiologically relevant interactions with various binding partner proteins such as cytokines, growth factors, cell-surface proteins, morphogens, plaque proteins, nuclear proteins, lipid-binding proteins, viral envelope proteins, enzymes, and extracellular proteins.

Perhaps, the most extensively studied example of a protein-sulfated polysaccharide interact is the binding of anti-thrombin with heparin and heparin sulfate due to its pharmacological anti-coagulant relevance[97]. Structural information from crystal structure at 2.6-Å resolution revealed the docking site of heparin pentasaccharide. The active site in proximity was lined with multiple arginine and lysine residues in a helical conformation effectively binding to heparin. Heparin is also reported to bind to growth factors such as FGF1, FGF2, and VEFG. Heparin (Fondaparinux- synthetic analog) is also the only first clinically approved sulfated polysaccharide since 1935. Limitations of heparin include shorter half-life, uncontrolled bleeding, an unwanted large number of binding interactions leading to side-effects.

Other examples include binding of glial cell-derived neurotrophic factor (GDNF) to sulfated polysaccharides for differentiation of dopaminergic neurons[98], lectin galectin-3 with chondroitin sulfate, dermatan sulfate with heparin cofactor

II[99], and human transforming growth factor-β1 (TGF-β1) with chondroitin sulfate[100].

Similar to heparin, Fucoidan is known to bind to fibroblast growth factor-1 and 2 (FGF-1,2) and similar heparin-binding proteins[101]. Selectins as a sub-class of heparin-binding proteins have attracted much attention in the past few years as an important therapeutic target for delivery of polymers and nanoparticles[102]. Reports of fucoidan as a sulfated delivery polysaccharide have been explored for anti-tumor effects of various chemotherapeutics (MEK and protein-kinase inhibitors) [**Figure 5**].

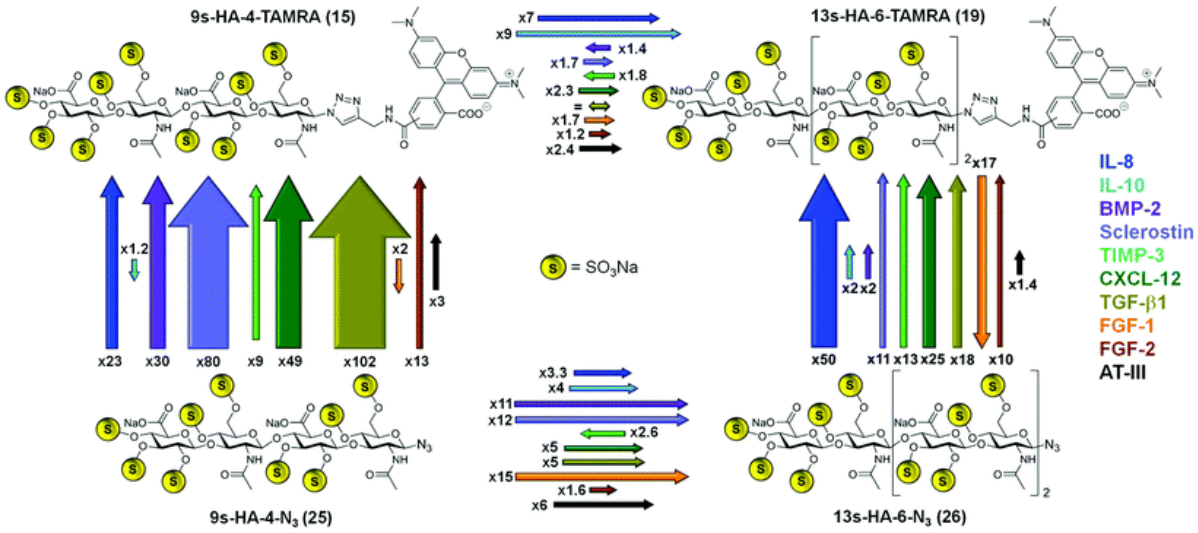

Figure 5: Summary of the recognition of four defined sulfated hyaluronanes by ten regulatory proteins obtained experimentally by fluorescence polarization. Affinity ratios of fluorophor-labeled tetra- and hexahyaluronans 15 and 19 (top) versus the azide-functionalized tetra- and hexahyaluoronans 25 and 26 (bottom) are represented schematically by arrows. Each of the ten regulatory proteins analyzed is labeled with a different color, which is also used for the arrows

representing its affinity ratios. The length and thickness of each arrow correspond to the ratio of the experimentally determined KD values for this case. A ratio of < = 10 is illustrated by the length of the arrow and a ratio >10 is represented by the thickness of the arrow. Each arrow is labeled with a number representing the determined affinity ratio for this case.

1.7. Selectins: a new class of receptors

Leukocytes are constantly patrolling the body as “security guards” for sites of infections or injury as a critical component of both adaptive and innate immune response. Upon injury or infection, four essential steps are involved in the transfer of leukocytes, (i) attachment and rolling with the help of selectins, (ii) activation, (iii) adherence via integrins, and (iv) transendothelial migration via allosteric structural rearrangements of integrins. Recruitment, trafficking, and extravasation of leukocytes are orchestrated in a dynamic and coordinated multi-step pattern by carbohydrate-binding proteins called selectins[103].

Selectins belong to a family of type-I cell surface carbohydrate-binding proteins which are calcium-dependent and are classified in three classes: P-, L-, E- selectins. All the selectins consist of five domains: an amino-terminal lectin domain with 50% homology across all selectins, epidermal growth factor domain, a variable number of complement regulatory-like repeats, and an intracellular tail. P-selectin (CD62P) is stored within Weibel-Palade bodies of endothelial cells and are secreted to the surface upon excitation with external factors such as chemokines, injury, trypsin, oxygen-free radicals[104]. P-selectin is highly

expressed on platelets and activated endothelium. E-selectin (CD62E) is present mainly on endothelial cells and facilitate slow-rolling of leukocyte with weak binding affinity. L-selectin (CD62L) found on microvilli of most leukocytes are the majority of leukocyte trafficking at sites of inflammation (**Figure 6**).

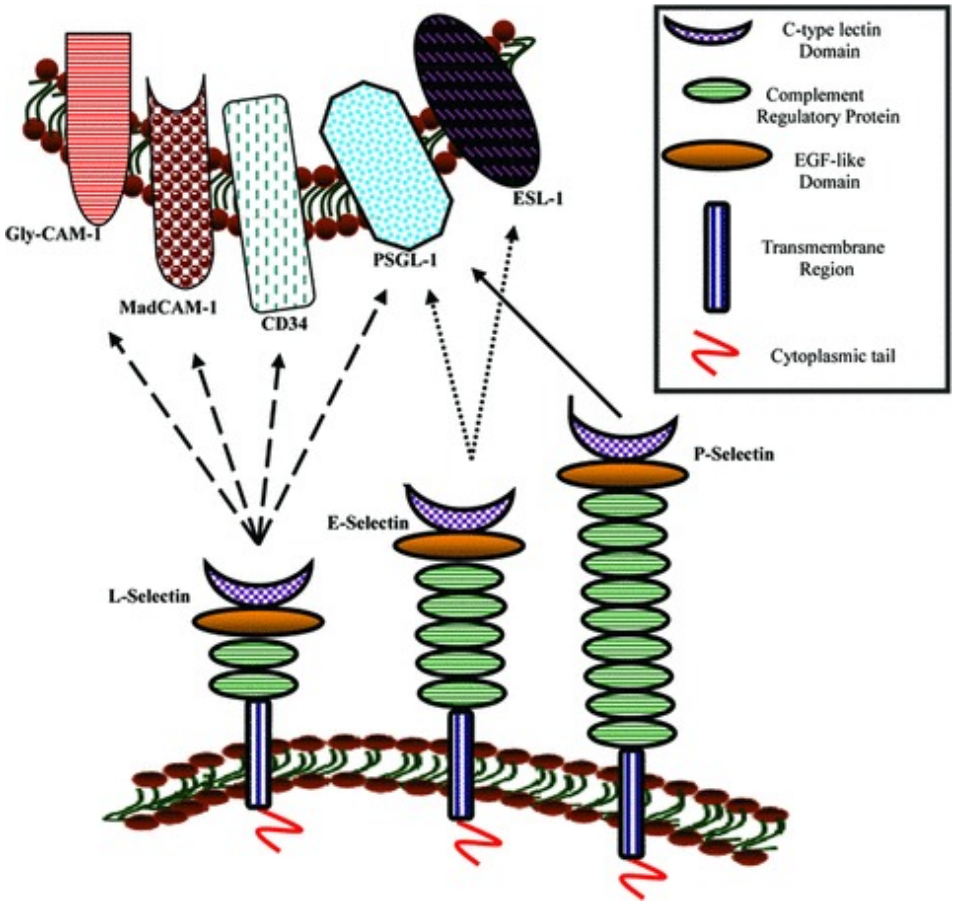

Figure 6: Selectins and their ligands. L-selectin ligands: Glycosylation-dependent CAM 1 (GlyCAM-1), Mucosal addressin CAM 1 (MadCAM-1), leucocyte leukosialin (CD34), P-Selectin-Glycoprotein Ligand 1 (PSGL-1). E-selectin ligands: E-Selectin Ligand 1 (ESL-1) and PSGL-1. P-selectin ligands:

PSGL-1. Selectins bind their carbohydrate ligands via the c-type lectin domain in calcium-mediated manner

The best characterized and physiologically studied ligand for P-selectin is P-selectin glycoprotein ligand-1 (PSGL-1) which is a mucin-like glycoprotein. The epitope for recognition for P-selectin on PSGL-1 is a tetrasaccharide sialyl Lewis^x (or CD15s)[105]. Sialyl Lewis^x [sLe^X] are carbohydrates as O- or N-linked glycans generally found highly expressed on tumor cells but also is important for homing malignant cells to bone marrow. sLe^X binds to both E- and P-selectin with very low-affinity of 0.5-0.8 mM affinities. sLe^X is post-translationally modified by glycosylation to add multiple sulfated groups on terminal tyrosine residues near the N-terminus resulting in a negative charge of -9. The active site in the lectin domain of P-selectin is lined with multiple lysines, histidine, and arginine residues resulting in a net positive charge of +9. However, L- and E-selectin have a lesser degree of basic residues in the active site accruing/leading to a net positive charge of +4 and neutral charge.

Experimental and theoretical calculations between PSGL-1 and selectins confirmed a dominance of electrostatics, long-range electrostatics, and salt-bridge mediated interactions[106]. The highest degree of binding was observed for PSGL-1 was in the order of P-selectin< L-< E-selectin in the decreasing manner. A report investigating the effects of numerous anions on dendritic polyglycerol scaffold (carboxylate, bisphosphonates, phosphate, sulfate) confirmed that sulfate as an anion had the highest binding capacity compared to carboxylate in binding to P-selectin due to its spatial orientation and highest acidity variable dictating strong binding capacity to the basic amino acid residues in the P-selectin active site[107].

Interestingly, the crystal structure presents the fact that the carboxylate of sialic acid does not interact with the active site confirming the lowest binding of carboxylate as an anion[108]. Similar binding positively charged electrostatic surfaces also support anionic sulfated glycosaminoglycans such as heparin and fucoidan. Very few hydrophobic interactions were observed between PSGL-1 and P-selectin at Ser47 and Lys113 residues indicating little to no-effect of hydrophobic modifications affecting P-selectin binding. In human P-selectin, arginine85 and histidine114 provide crucial contacts with sulfated PSGL-1; mechanical perturbations upon P-selectin binding causes a conformational change allowing more extensive contacts with the post-translationally modified PSGL-1 leading to high-affinity form (**Figure 7**). No role of epidermal growth factor or complement regulatory-like repeats in the structure has been reported to affect PSGL-1 binding. Majority of the drug design approach has been focused on studying lectin domain interface for the rational design of small-molecules or glycomimetic as P-selectin antagonists. Four classes of selectin inhibitors have been developed and tested in preclinical models: carbohydrate-based selectin inhibitors; antibodies specific to P-or L-selectin (DREG-55, humanized version of anti-L-selectin in clinical trial for treatment of multiple trauma); truncated versions of PSGL-1 immunoglobulin for suitable pharmacokinetic parameters; and small-molecule inhibitors using in silico modeling approaches (TBC-1269, Bimosiamose as selectin inhibitor for pediatric asthma).

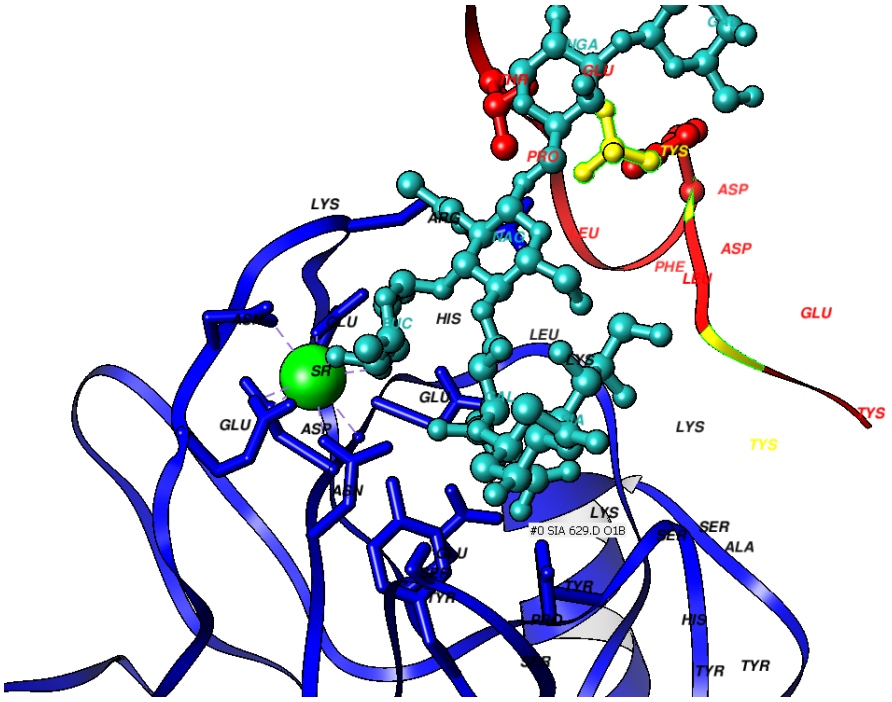

Figure 7: Closer insight into P-selectin active complexed with PSGL-1 highlighting crucial basic amino acids.

In the past decade, selectins have been implicated in the progression of cancer[109]. Tumor cells take advantage of the leukocyte regulation process for its benefits for extravasation merits particular attention to metastasize to distant locations. A critical report published in science translational medicine showed that P-selectin is overexpressed not only at the tumor vascular endothelium but also on many types of tumors, such as lung, ovarian, lymphoma, and breast cancers, emphasizing its possible role as a targeting molecule at the tumor cellular level[110]. Cancer tumor cells take advantage by increasing its P-selectin expression forming immune complexes with leukocytes expressing PSGL-1, evading recognition by macrophages allowing easy access to spread to distant organs.

Various targeting strategies to direct delivery systems to P-selectins have been explored; researchers demonstrated in vitro cellular drug targeting by low-molecular-weight fucoidan nanoparticles resulting in increased cell death over the untargeted, nanoparticle control[110]. Fucoidan nanoparticle design exploits selectin expression on tumor cells for delivery of chemotherapeutic drugs in addition to the EPR effect for increased drug delivery. Several other examples, researchers have targeted highly aggressive P-selectin positive glioblastoma cells by using dendritic polyglycerol sulfate for delivery of paclitaxel and anti-angiogenic protein thrombospondin-1 for synergistic therapeutic outcomes[111]; another group utilized spatiotemporal targeting approach using a dual-ligand display nanoparticle system for targeting integrin and P-selectin positive MDA-MB-231 and 4T1 breast for detection of early metastasis[112]. This indicates the

potential of sulfated polysaccharides as nanoparticles which can be developed to excite discoveries, research, innovation, and translation.

1.8. Nanoparticles in Biomedical Research and Applications

Research in recent years in the field of nanomaterials have received considerable attention and seen significant advancements in areas of diagnostics and the therapeutic realm (**Figure 8**). Nanoparticles (NPs) with differences in molecular or atomic compositions are generally considered in size range of 1-1000 nm[113]. NPs are defined as solid colloidal mass particles with an increased surface-to-volume ratio over larger particles providing interest in the field of targeted drug/imaging agent delivery, tissue engineering, and diagnostic purposes. Combination of both applications in diagnostic and therapeutic categories can be commonly termed as “theranostic”[114]. The exact function and behavior of these nanosystems will depend on stability, size, shape, scaffold design, targeting ligands, toxicity profiles, biodistribution, and pharmacokinetic profiles, for optimized therapeutic outcome. Desirable features of a NPs system will include; high drug/imaging agent loading for more modalities; targeted delivery to diseased tissue; long circulation time to limit frequent dosing; non-toxic, highly biocompatible, and biodegradable; controlled interactions with blood components to prevent degradation; and predictable in vivo profiles[115].

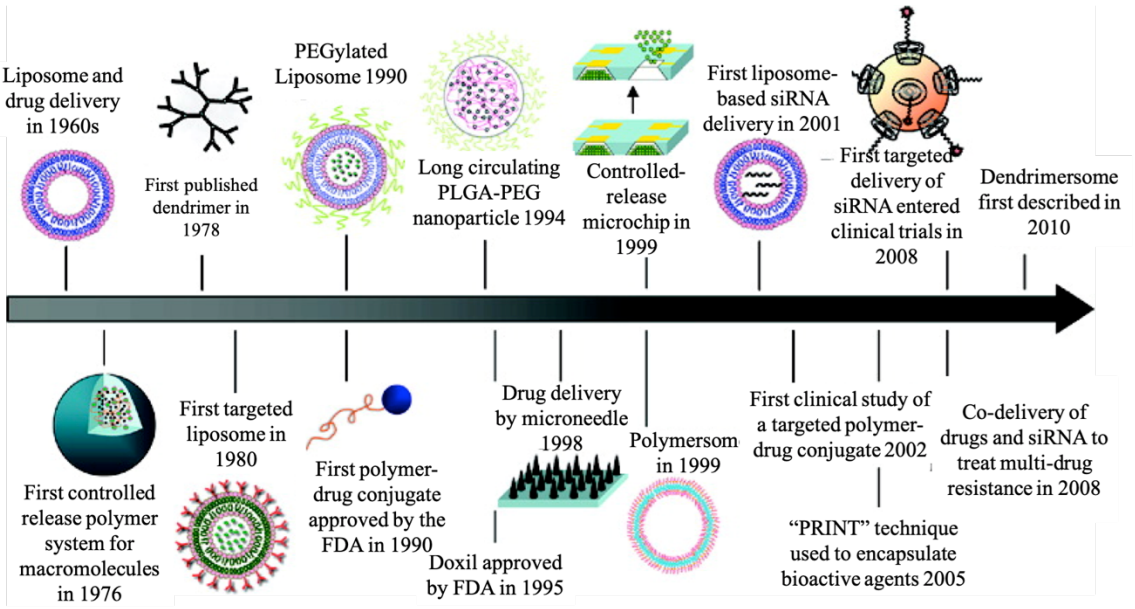

Figure 8: Timeline of nanotechnology-based drug delivery. Here, we highlight some nanoscale delivery systems that serve as important milestones throughout the history of drug delivery.

Taking into account every design parameter of a NPs, size is the most widely investigated variable that can influence chemical and physical properties affecting the fate of NPs. Effective interaction of NPs with cellular membranes are a critical factor in dictating uptake and circulation[116]. The particle size of less than 5 nm is more likely to stay in the circulation longer, undergo high renal clearance; large NPs in the size range of 150nm+ have a higher tendency to interact more with the reticular endothelial system (hepatocytes, spleen) decreasing the payload reaching the tumor. A careful optimal balance between tumor uptake and RES clearance is required to be investigated for different NPs. Smaller NPs seem to be favorable for accumulating in poorly permeable tumors, whereas all size ranges seem to accumulate in highly permeable classes of tumors. The paradigm of the EPR effect has been in many discussions in the field of nanoparticles as one of the main determinants for passive tumor accumulation. Researchers determined that the NPs targeting capacity to navigate to interstitial tumor spaces increased with decrease in size[117].

However, most likely, EPR depends on anatomy and permeability characteristics of the tumor site as “leaky” property of tumor vessels[118]. Selective antibodies with high specificities can be conjugated to NPs to seek biomarkers along with EPR mechanism can accumulate inside tumors leading to better localization. Nevertheless, conjugating a biologic entity might increase the overall hydrodynamic size, compromise in terms of targeting ability and size needs to be considered while designing NPs. However, tumor accumulation of NPs is always

represented as a fraction of injected dose of NPs, which is usually ranging from 1-10% as the majority end up in MES/RED or cleared by liver and spleen[119].

The shape of the NPs system has a significant impact on cellular internalization, circulation time, and residence time[120]. Elongated rod shaped-like NPs have shown to have a higher adhering property compared to spherical particles due to its higher surface facilitating multivalent interactions with proteins on the cellular membrane. Spherical nanoparticle have a lower aspect ratio compared to rod-like NPs have shown to be less efficiently taken up by Hela and Caco-2 cells[121]. NPs having sharp edges similar to the exoskeleton of a virus have higher penetration into the endosome and mainly localized in the cytoplasm[122]. The elliptical shape has shown to be least favored compared to the spherical and rod-like architecture of NPs for gold NPs. The shape of the NPs has also shown to influence the corona formation influencing blood circulation and pharmacokinetic properties[123].

Tailoring the nanoparticle surface charge influences different physical, chemical, and biological characteristics; highly positively charged particles more likely are cleared quicker and higher incidence of systemic toxicities compared to negatively charged particles. The charge also is expected to influence RES uptake, positively charge implicated to have lower uptake by RES. Neutral-charged particles exhibit low sequestration in liver and spleen and high tumor penetration[124]. A higher charge density is expected to have more interactions with charged molecules in the circulation limiting overall tumor penetration, thus neutral species exhibit slightly higher tumor penetration. Cationic carriers are

internalized via caveolae-dependent via electrostatic interactions and escape the endosomes through a mechanism called “proton sponge effect”[125].

Self-assembled polymeric NPs have been extensively investigated as drug carriers to solubilize insoluble drugs/imaging agents to tumors. HA has been previously used for NPs formulations due to its hydrophilic nature and presence of abundant conjugatable groups to form discrete hybrid-tunable NPs (**Figure 9**)[126]. HA was conjugated to various hydrophobic block-co-polymers to form amphiphilic systems for delivery of gemcitabine chemotherapeutics[127]. The cross-linking strategy was utilized by conjugating 2-(pyridyl dithio)-ethyl of methacrylate chain to HA to form block-co-polymers[128]. To improve selective accumulation in the tumor, these particles were further coated with poly (ethylene glycol) to improve circulation time and decrease liver uptake[129]. Photodynamic therapy applications were explored for HA-based systems by loading doxorubicin and IR780 dye onto Poly(maleic anhydride-alt-1-octadecene) (PMAO) was grafted-HA NPs, under near-infrared (NIR) excitation, the photo-dynamic effect from IR780 was observed along with synergistic cytotoxicity from Dox release to breast cancer cells[130].

HA-based micelles have also been studied for the treatment of ocular diseases by conjugating hydrophobic alkyl group (hexadodecyl, C16) to loaded hydrophobic corticosteroids (triamcinolone acetonide and dexamethasone). The high entrapment efficiency of paclitaxel (93.2%) was observed by increasing hydrophobicity of HA-based deoxycholic acid NPs, implying tunability of amphiphilic nature of HA-based nanosystems[131].

Other application of HA includes the coating of positively charged carriers to facilitate CD44-mediated targeting for increased anti-tumor efficacy. A research group used positively charged pyridinium group moiety with indocyanine dye to form micelles with HA. Higher tumor accumulation in SCC-7 model compared to pyridinium complex indicated HA as an essential polymer for superior targeting and anti-tumor efficacy[132].

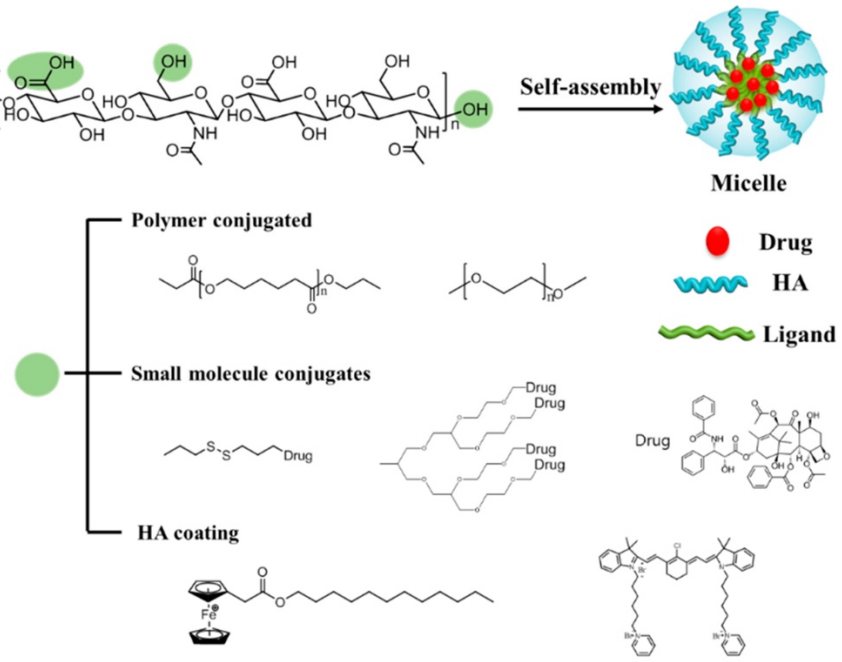

Figure 9: Schematic representation of hyaluronic acid (HA) polymeric micelles. Three possible sites for modification are shown as green circles. In aqueous solution, amphiphilic HA-ligands can self-assemble into micelles by encapsulating drugs or conjugating with drugs. Polymers can be grafted to the HA backbone. Block-co-polymers and small molecules, such as drugs and dendrimers, can be conjugated with HA. Positively charged molecules or polymers can form micelles with HA via electrostatic interactions.

HA has also shown promise in the field of cancer imaging, especially in the fluorescence-based image surgery (FIGS). In a research study, Indocyanine green (ICG) was physically entrapped in hydrophobically-modified [using either aminopropyl-1-pyrenebutanamide (PBA), aminopropyl-5β-cholanamide (5βCA), or octadecylamine (ODA) as small hydrophobic molecules], dye loading, optical properties, and its application in FIGS was evaluated to detect positive MDA-MB-231 tumor margins, and local malignant tissues in a xenograft model[133]. Similar studies from the same group evaluated the use of cyanine7.5 amine (Cy7.5) in HA-based nanoformulations to identify promising formulations. NanoICG with PBA as the hydrophobic ligand and NanoCy7.5 from 100 kDa HA and 30 wt.% conjugated PBA were identified as lead formulations with outstanding tumor contrast, and tumor margin detection in immune-competent BALB/c mice bearing orthotopic 4T1 breast cancer tumors[134].

Another group[135] demonstrated the use of manganese dioxide (MnO_2) NPs complexed with HA mixing sodium permanganate. HA served as a reducing agent, surface-coating, and displayed improved colloidal stability, water dispersibility, and low toxicity. HA-MnO_2 effectively detected rat intracranial glioma with MRI up to 3 days. Highly toxic Gadolinium was doped in HA derived NPs (HA-GdIO) as MRI contrast agents. HA-GdIO NPs provided a promising role in targeting CD44-overexpressed atherosclerotic plaques with high magnetic susceptibility and good biocompatibility[136].

1.9. Nanoparticles as conjugated and non-conjugated systems in biomedical applications

Development of fluorescent NPs for both therapeutic and diagnostic value has emerged from the advantages of EPR effect, drug delivery, and effective bioconjugation purposes. Fluorescent NPs or polymer dots are broadly classified into two groups: conjugated NPs and non-conjugated NPs (**Figure 10**). Conjugated fluorescent NPs (CF NPs) are a class of promising probes due to their extensive π-conjugated backbones and delocalized electronic structure[137]. CF NPs are derived from π-conjugated small organic dyes which are water-insoluble as monomeric units forming nanoscale polymeric aggregates. In principle, such particles can be combined with inorganic particles to form stable vesicles or micelles as highly-fluorescent dynamic NPs[138].

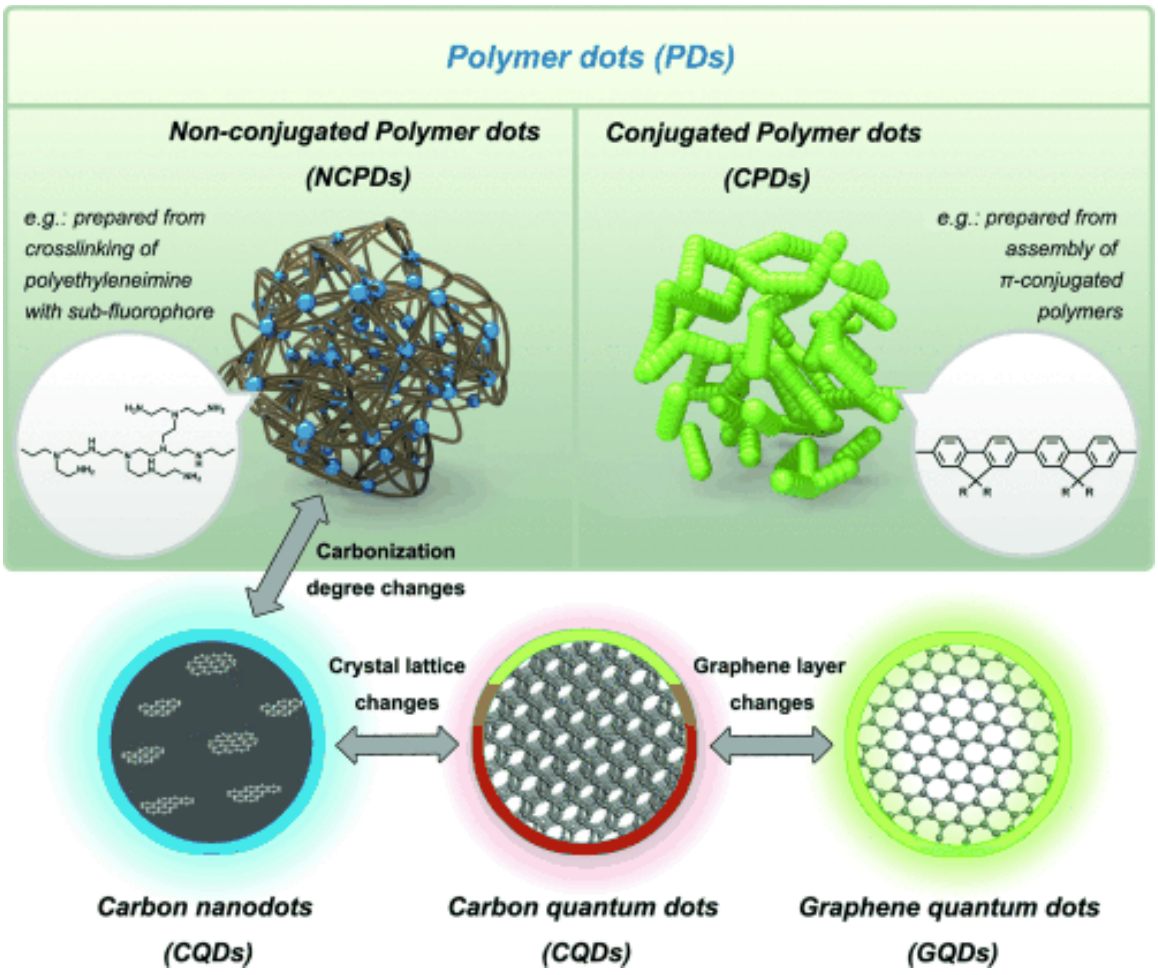

Figure 10: Representation of polymer dots as Conjugated fluorescent NPs (CF NPs) and Non-conjugated fluorescent NPs.

Typical CF NPs have been traditionally synthesized via-classical step-wise growth through Suzuki[139], Heck[140], Sonogashira[141], and Knoevenagel polymerization[142] using individual starting precursors like acetylene, p-phenylene, thiophene, polypyrrole, p-phenylene vinylene, phenylene ethynylene, and fluorene structures[143]. Disadvantages of these name-reactions are lack of control of molecular weight distribution, regioregularity, and strict stoichiometry requirements[144]. Applications of the CF NPs are used in electrochemical coating of charged surfaces for photovoltaics and field-effect transistors. Final products of CF NPs can be classified into three classes: hydrophobic π-conjugated polymers, ionic π-conjugated polymers, and solid-state fluorescence emitting polymers[145]. CF NPs as ionic versions have charged side chains such as charged ammonium and negatively charged carboxyl, phosphate, and sulfonate moieties to provide CF NPs with good water solubility and dispersibility. Ionic groups can also form binding sites that can interact with oppositely charged biomolecules or metallic NPs. Solid-state emitting fluorescent polymers (SSEF) have shown to possess unique photophysical properties that differ from those of typical fluorescent organic dyes. In the isolated solution state, fluorescence is unusually quenched as a result of the formation of nonplanar geometries with torsional freedom, whereas their emission is greatly enhanced by solidification as a result of restricted torsional motion and minimized quenching interaction[146]. Thus, they can maintain bright fluorescence in concentrated or aggregated states without conventional aggregation-induced fluorescence quenching. Such molecules are also termed as Aggregation-induced emission dyes (AIE). Examples of SSEF-

molecules include siloles, cyanostilbene, tetraphenylethene, and distyrylanthracene-based derivatives[147,148,149,150].

The most frequently used method to prepare CF NPs is the solvent exchange technique. In this procedure, a water-miscible solvent is sequentially added to water with sonication; this causes the polymeric solution to precipitate in small particles. These particles are then purified by evaporation of organic residues. This technique is also referred to as nanoprecipitation[151]. Other less employed techniques include self-assembly method and emulsion-polymerization[152,153].

Upon the formation of CF NPs, strategies have been used to implement the application for biological systems; researchers prepared low bandgap NIR fluorescent CF NPs by developing a push–pull conjugated polymer based on a strong fluorinated thieno [3,4-b]thiophene acceptor via the mini-emulsion technique[154]. The NPs were further functionalized with PEGylated (PEG = polyethylene glycol) surfactant which is beneficial for bioimaging because of a lower autofluorescence and reduced photon scattering in biological tissues, resulting in a higher spatial resolution and deeper tissue penetration. However, a low quantum yield was obtained due to the low-energy bandgap in the NIR region. Water-solubilizing techniques such as attachment of polar side chains, use of unreacted carboxyl groups, and stabilization with phospholipids. Surface-functionalization also offers bioconjugation of CF NPs to target specific biomarkers on cancer cells for theranostic purposes[155].

For practical uses, more environmentally friendly engineering of CF NPs needs to be utilized to avoid potential long-term toxic effects[156], immunogenicity, and metabolism of CF NPs derived from sophisticated synthetic strategies.

Fluorescent polymer dots as non-conjugated polymeric systems (NCPS) have gained much attention in recent years due to its easy preparation and non-toxic properties. NCPSs do not typically possess a fluorophore which makes it an exciting kind of fluorescent organic material. Instead, NCPS contain weak sub-fluorophoric groups such as heteroatom-containing double bonds (C-O, C-N, N-O) and single bonds (amino-based groups, C-O), upon suitable immobilization demonstrate increased fluorescent properties[157].

NCPSs are typically prepared by three major types: covalently cross-linked, supramolecular interactions, and rigidity aggregated. The former two are based on non-covalent interactions and physical aggregation. The enhancement of fluorescent properties for NCPS type systems is generally referred to as cross-linked enhanced effect (CEE). It should be noted that CEE is different from AIE, which is mainly observed in small organic molecules.

Yang and co-workers first demonstrated the Fluorescence mechanism for NCPSs using hydrothermal treatment to generate covalent linked NCPSs[158]. During these processes, the amino groups and saccharide molecules can undergo dehydration to form the aggregated structures. These aggregated structures contain abundant C=N Schiff bonds show high fluorescence with cross-linking. Using branched polyethylene amine as a model non-conjugated

polymer and small molecule carbon tetrachloride was used to cross-link the NP. PEI upon cross-linking possessed potential sub-fluorophore units (secondary and tertiary amines) on suitable immobilization due to cross-linking lead to a decrease in vibration and rotation.

Furthermore, this decrease in vibration leads to increased blue fluorescence generation due to a decrease in energy-dependent radiative and non-radiative transitions. A more red-shifted emission could be obtained if the band-gap between the two states could be decreased is still under investigation. These NCPSs possess λ_{ex}-dependent fluorescence behavior due to the presence of multiple excited states (presence of plentiful sub-fluorophore groups in the polymeric NP mesh). The CEE fluorescence effect is also further enhanced in a “ship-in-a-bottle” approach where a small organic molecule forming sub-fluorophore units be entrapped in a porous-NP matrix leading to an overall decrease in vibrations and relaxations.

NCPSs possess interesting optical properties regarding absorption and fluorescence. The absorption of the NCPSs typically shows strong absorption in the UV region (230–320 nm), with a tail extending to the visible range. The maximum peak in the UV region may be ascribed to an n–π* transition of C=N and C=O bonds or other sub-fluorophore groups. Furthermore, the connected chemical groups and differences in hybridization derivatives may contribute to the absorption in the UV/Vis range[159]. NCPSs possess exceptional physiological solubility in water (>20 mg/ml) as they are mainly derived from building blocks which are hydrophilic molecules such as starch, glucose, and saccharides.

NCPSs is also reported to possess good biocompatibility and low toxicity. Zhu and co-workers demonstrated[160], no *in vitro* cytotoxicity (cell viability higher than 95%) of different NCPSs with differentiated rat adrenal pheochromocytoma (PC12) cells by methyl thiazolyl diphenyltetrazolium bromide (MTT) assay. The toxicity of the NCPDs was also tested in HeLa and 293T cells, and the result showed that the cell viabilities of both cell types declined by less than 2 % upon addition of the NCPDs at up to 80 mg mL^{-1}.

Currently, significant progress has been made in the field of functional non-conjugated PDs. The current functionality of the NCPSs is still relatively monotonous and straightforward; therefore, the design, development, and scale-up of multiple functional NCPSs have become an urgent and indispensable need. Furthermore, a large number of biodegradable, biocompatible, or bioresorbable synthetic polymers can be exploited, such as polyols, polyether's, polyesters, polylactides, and polyphosphates. The majority of functional NCPDs have only been used for *in vitro* biomedical applications, and thus there is still a long way to go before they are applied to clinical diagnosis and therapy.

2.0. Conclusions

The body of research into polymeric materials for biomedical application indicates that there is a current and future place for this technology in medicine. Drug and contrast agent delivery using NPs has already found a place in clinical medicine for pre-clinical and clinical investigations. Among the many possible uses, drug and fluorescent contrast agent delivery to solid tumors is of high

importance. It has already been seen that NP formulations can improve the total quantity of drug delivered to tumors, and perhaps equally important, they can also reduce associated toxicities and thereby lessen the already high burden placed on patients dealing with chemotherapy. Current surgical practices do not adequately identify the extent of solid tumors, local metastases, and sentinel lymph nodes, resulting in disease recurrence. It is therefore crucial that new technologies are developed and moved into the clinic that assists surgeons in the identification of these tissues.

In the following chapters, we will examine research into polymeric natural glycosaminoglycan HA, and the application of these systems in studying interactions with CD44 and P-selectin proteins for applications in image-guided surgery. We first outline the different approaches using selective regioselective to study interactions with CD44. Furthermore, narrowing down to one of the synthetic approaches, we studied interactions with P-selectin. The modified HA polymers were then formulated to form NPs which were used to deliver imaging agents to tumor microenvironment using dual-targeting strategy for implementation in image-guided surgery. Moreover, we have also demonstrated interesting use of HA along with different amino acids to form fluorescent organic nanoparticles (FONPs) for applications in bioimaging and drug delivery.

2.1. References:

1. Senbanjo, L. T. & Chellaiah, M. A. CD44: A multifunctional cell surface adhesion receptor is a regulator of progression and metastasis of cancer cells. *Frontiers in Cell and Developmental Biology* (2017). doi:10.3389/fcell.2017.00018
2. Gallatin, W. M., Weissman, I. L. & Butcher, E. C. A cell-surface

molecule involved in organ-specific homing of lymphocytes. *Nature* (1983). doi:10.1038/304030a0
3. Iczkowski, K. A. Cell adhesion molecule CD44: Its functional roles in prostate cancer. *Am. J. Transl. Res.* (2011).
4. Basakran, N. S. CD44 as a potential diagnostic tumor marker. *Saudi Medical Journal* (2015). doi:10.15537/smj.2015.3.9622
5. Rail, C. J. N. & Rustgi, A. K. CD44 Isoform Expression in Primary and Metastatic Pancreatic Adenocarcinoma. *Cancer Res.* (1995).
6. Rudzki, Z. CD44 and the adhesion of neoplastic cells. *Journal of Clinical Pathology - Molecular Pathology* (1997). doi:10.1136/mp.50.2.57
7. Goetinck, P. F., Stirpe, N. S., Tsonis, P. A. & Carlone, D. The tandemly repeated sequences of cartilage link protein contain the sites for interaction with hyaluronic acid. *J. Cell Biol.* (1987). doi:10.1083/jcb.105.5.2403
8. Yu, Q., Banerjee, S. D. & Toole, B. P. The role of hyaluronan-binding protein in assembly of pericellular matrices. *Dev. Dyn.* (1992). doi:10.1002/aja.1001930206
9. Williams, K., Motiani, K., Giridhar, P. V. & Kasper, S. CD44 integrates signaling in normal stem cell, cancer stem cell and (pre)metastatic niches. *Experimental Biology and Medicine* (2013). doi:10.1177/1535370213480714
10. Okamoto, I. *et al.* Proteolytic release of CD44 intracellular domain and its role in the CD44 signaling pathway. *J. Cell Biol.* (2001). doi:10.1083/jcb.200108159
11. Orian-Rousseau, V., Chen, L., Sleeman, J. P., Herrlich, P. & Ponta, H. CD44 is required for two consecutive steps in HGF/c-Met signaling. *Genes Dev.* (2002). doi:10.1101/gad.242602
12. Orian-Rousseau, V. *et al.* Hepatocyte growth factor-induced Ras activation requires ERM proteins linked to both CD44v6 and F-actin. *Mol. Biol. Cell* (2007). doi:10.1091/mbc.E06-08-0674
13. Naor, D., Nedvetzki, S., Golan, I., Melnik, L. & Faitelson, Y. CD44 in cancer. *Critical Reviews in Clinical Laboratory Sciences* (2002). doi:10.1080/10408360290795574
14. Lokeshwar, B. L., Lokeshwar, V. B. & Block, N. L. Expression of CD44 in prostate cancer cells: Association with cell proliferation and invasive potential. *Anticancer Res.* (1995).
15. Bourguignon, L. Y. W. *et al.* CD44v3,8-10 is involved in cytoskeleton-mediated tumor cell migration and matrix metalloproteinase (MMP-9) association in metastatic breast cancer cells. *J. Cell. Physiol.* (1998). doi:10.1002/(SICI)1097-4652(199807)176:1<206::AID-JCP22>3.0.CO;2-3
16. Wang, S. J. & Bourguignon, L. Y. W. Hyaluronan and the interaction between CD44 and epidermal growth factor receptor in oncogenic signaling and chemotherapy resistance in head and neck cancer. *Arch. Otolaryngol. - Head Neck Surg.* (2006). doi:10.1001/archotol.132.7.771

17. Desai, B., Rogers, M. J. & Chellaiah, M. A. Mechanisms of osteopontin and CD44 as metastatic principles in prostate cancer cells. *Mol. Cancer* (2007). doi:10.1186/1476-4598-6-18
18. Gupta, A. *et al.* Promising noninvasive cellular phenotype in prostate cancer cells knockdown of matrix metalloproteinase 9. *Sci. World J.* (2013). doi:10.1155/2013/493689
19. Zhao, S. *et al.* CD44 expression level and isoform contributes to pancreatic cancer cell plasticity, invasiveness, and response to therapy. *Clin. Cancer Res.* (2016). doi:10.1158/1078-0432.CCR-15-3115
20. Mani, S. A. *et al.* The Epithelial-Mesenchymal Transition Generates Cells with Properties of Stem Cells. *Cell* (2008). doi:10.1016/j.cell.2008.03.027
21. Li, L. *et al.* Antibody against CD44s inhibits pancreatic tumor initiation and postradiation recurrence in mice. *Gastroenterology* (2014). doi:10.1053/j.gastro.2013.12.035
22. Stamenkovic, I., Amiot, M., Pesando, J. M. & Seed, B. A lymphocyte molecule implicated in lymph node homing is a member of the cartilage link protein family. *Cell* (1989). doi:10.1016/0092-8674(89)90638-7
23. Bennett, K. L. *et al.* Cd44 isoforms containing exon V3 are responsible for the presentation of heparin-binding growth factor. *J. Cell Biol.* (1995). doi:10.1083/jcb.128.4.687
24. Greenfield, B. *et al.* Characterization of the heparan sulfate and chondroitin sulfate assembly sites in CD44. *J. Biol. Chem.* (1999). doi:10.1074/jbc.274.4.2511
25. Idzerda, R. L. *et al.* Isolation and DNA sequence of a cDNA clone encoding a lymphocyte adhesion receptor for high endothelium. *Proc. Natl. Acad. Sci. U. S. A.* (1989). doi:10.1073/pnas.86.12.4659
26. Harada, H. & Takahashi, M. CD44-dependent intracellular and extracellular catabolism of hyaluronic acid by hyaluronidase-1 and -2. *J. Biol. Chem.* (2007). doi:10.1074/jbc.M608358200
27. Brown, T. A., Bouchard, T., St. John, T., Wayner, E. & Carter, W. G. Human keratinocytes express a new CD44 core protein (CD44E) as a heparan-sulfate intrinsic membrane proteoglycan with additional exons. *J. Cell Biol.* (1991). doi:10.1083/jcb.113.1.207
28. Brown, R. L. *et al.* CD44 splice isoform switching in human and mouse epithelium is essential for epithelial-mesenchymal transition and breast cancer progression. *J. Clin. Invest.* (2011). doi:10.1172/JCI44540
29. Sneath, R. J. S. & Mangham, D. C. The normal structure and function of CD44 and its role in neoplasia. *Journal of Clinical Pathology - Molecular Pathology* (1998). doi:10.1136/mp.51.4.191
30. Yu, Q. & Stamenkovic, I. Localization of matrix metalloproteinase 9 to the cell surface provides a mechanism for CD44-mediated tumor invasion. *Genes Dev.* **13**, 35–48 (1999).
31. Wielenga, V. J. M. *et al.* Expression of CD44 Variant Proteins in Human Colorectal Cancer Is Related to Tumor Progression. *Cancer Res.*

(1993).
32. Heider, K. H. *et al.* A human homologue of the rat metastasis-associated variant of CD44 is expressed in colorectal carcinomas and adenomatous polyps. *J. Cell Biol.* (1993). doi:10.1083/jcb.120.1.227
33. Stetler-Stevenson, W. G., Aznavoorian, S. & Liotta, L. A. Tumor cell interactions with the extracellular matrix during invasion and metastasis. *Annual Review of Cell Biology* (1993). doi:10.1146/annurev.cb.09.110193.002545
34. Orian-Rousseau, V. CD44, a therapeutic target for metastasising tumours. *Eur. J. Cancer* (2010). doi:10.1016/j.ejca.2010.02.024
35. Nam, K. S., Oh, S., Lee, K. min, Yoo, S. ah & Shin, I. CD44 regulates cell proliferation, migration, and invasion via modulation of c-Src transcription in human breast cancer cells. *Cell. Signal.* (2015). doi:10.1016/j.cellsig.2015.05.002
36. Xu, Y., Stamenkovic, I. & Yu, Q. CD44 attenuates activation of the Hippo signaling pathway and is a prime therapeutic target for glioblastoma. *Cancer Res.* (2010). doi:10.1158/0008-5472.CAN-09-2505
37. Schmitt, M., Metzger, M., Gradl, D., Davidson, G. & Orian-Rousseau, V. CD44 functions in Wnt signaling by regulating LRP6 localization and activation. *Cell Death Differ.* (2015). doi:10.1038/cdd.2014.156
38. Janda, E. *et al.* Ras and TGFβ cooperatively regulate epithelial cell plasticity and metastasis: Dissection of Ras signaling pathways. *J. Cell Biol.* (2002). doi:10.1083/jcb.200109037
39. Biswas, C. *et al.* The Human Tumor Cell-derived Collagenase Stimulatory Factor (Renamed EMMPRIN) Is a Member of the Immunoglobulin Superfamily. *Cancer Res.* (1995).
40. So, J. Y. *et al.* Targeting CD44-STAT3 Signaling by Gemini Vitamin D Analog Leads to Inhibition of Invasion in Basal-Like Breast Cancer. *PLoS One* (2013). doi:10.1371/journal.pone.0054020
41. Buhren, B. A. *et al.* Hyaluronidase: From clinical applications to molecular and cellular mechanisms. *Eur. J. Med. Res.* (2016). doi:10.1186/s40001-016-0201-5
42. McAtee, C. O., Barycki, J. J. & Simpson, M. A. Emerging roles for hyaluronidase in cancer metastasis and therapy. in *Advances in Cancer Research* (2014). doi:10.1016/B978-0-12-800092-2.00001-0
43. Liu, D. *et al.* Expression of hyaluronidase by tumor cells induces angiogenesis in vivo. *Proc. Natl. Acad. Sci. U. S. A.* (1996). doi:10.1073/pnas.93.15.7832
44. Ponta, H., Sherman, L. & Herrlich, P. a. CD44: from adhesion molecules to signalling regulators. *Nat. Rev. Mol. Cell Biol.* **4**, 33–45 (2003).
45. Teriete, P. *et al.* Structure of the regulatory hyaluronan binding domain in the inflammatory leukocyte homing receptor CD44. *Mol. Cell* **13**, 483–496 (2004).
46. Banerji, S. *et al.* Structures of the Cd44-hyaluronan complex

provide insight into a fundamental carbohydrate-protein interaction. *Nat. Struct. Mol. Biol.* **14**, 234–9 (2007).
47. Kahmann, J. D. *et al.* Localization and characterization of the hyaluronan-binding site on the Link module from human TSG-6. *Structure* (2000). doi:10.1016/S0969-2126(00)00163-5
48. Banerji, S. *et al.* LYVE-1, a new homologue of the CD44 glycoprotein, is a lymph-specific receptor for hyaluronan. *J. Cell Biol.* (1999). doi:10.1083/jcb.144.4.789
49. Plazinski, W. *et al.* Interactions between CD44 protein and hyaluronan: insights from the computational study. *Mol. BioSyst.* **8**, 543–547 (2012).
50. Vuorio, J., Vattulainen, I. & Martinez-Seara, H. Atomistic fingerprint of hyaluronan–CD44 binding. *PLoS Comput. Biol.* (2017). doi:10.1371/journal.pcbi.1005663
51. Ogino, S. *et al.* Two-state conformations in the hyaluronan-binding domain regulate CD44 adhesiveness under flow condition. *Structure* **18**, 649–656 (2010).
52. Lesley, J., English, N., Perschl, A., Gregoroff, J. & Hyman, R. Variant cell lines selected for alterations in the function of the hyaluronan receptor CD44 show differences in glycosylation. *J. Exp. Med.* (1995). doi:10.1084/jem.182.2.431
53. Fallacara, A., Baldini, E., Manfredini, S. & Vertuani, S. Hyaluronic acid in the third millennium. *Polymers* (2018). doi:10.3390/polym10070701
54. Toole, B. P. Hyaluronan in morphogenesis. *Semin. Cell Dev. Biol.* (2001). doi:10.1006/scdb.2000.0244
55. Scott, J. E., Cummings, C., Brass, A. & Chen, Y. Secondary and tertiary structures of hyaluronan in aqueous solution, investigated by rotary shadowing-electron microscopy and computer simulation. Hyaluronan is a very efficient network-forming polymer. *Biochem. J.* (1991). doi:10.1042/bj2740699
56. Fraser, J. R. E., Laurent, T. C. & Laurent, U. B. G. Hyaluronan: Its nature, distribution, functions and turnover. in *Journal of Internal Medicine* (1997). doi:10.1046/j.1365-2796.1997.00170.x
57. Volpi, N., Schiller, J., Stern, R. & Soltes, L. Role, Metabolism, Chemical Modifications and Applications of Hyaluronan. *Curr. Med. Chem.* (2009). doi:10.2174/092986709788186138
58. Cyphert, J. M., Trempus, C. S. & Garantziotis, S. Size Matters: Molecular Weight Specificity of Hyaluronan Effects in Cell Biology. *International Journal of Cell Biology* **2015**, (2015).
59. Jiang, D., Liang, J. & Noble, P. W. Hyaluronan as an immune regulator in human diseases. *Physiological Reviews* (2011). doi:10.1152/physrev.00052.2009
60. Wu, M. *et al.* A novel role of low molecular weight hyaluronan in breast cancer metastasis. *FASEB J.* (2015). doi:10.1096/fj.14-259978
61. Vigetti, D. *et al.* Hyaluronan: Biosynthesis and signaling. *Biochimica et Biophysica Acta - General Subjects* (2014).

doi:10.1016/j.bbagen.2014.02.001
62. Harris, E. N. & Weigel, P. H. The ligand-binding profile of HARE: Hyaluronan and chondroitin sulfates A, C, and D bind to overlapping sites distinct from the sites for heparin, acetylated low-density lipoprotein, dermatan sulfate, and CS-E. *Glycobiology* (2008). doi:10.1093/glycob/cwn045
63. Prevo, R., Banerji, S., Ferguson, D. J. P., Clasper, S. & Jackson, D. G. Mouse LYVE-1 Is an Endocytic Receptor for Hyaluronan in Lymphatic Endothelium. *J. Biol. Chem.* (2001). doi:10.1074/jbc.M011004200
64. Tripodo, G. *et al.* Hyaluronic acid and its derivatives in drug delivery and imaging: Recent advances and challenges. *European Journal of Pharmaceutics and Biopharmaceutics* (2015). doi:10.1016/j.ejpb.2015.03.032
65. Schanté, C. E., Zuber, G., Herlin, C. & Vandamme, T. F. Chemical modifications of hyaluronic acid for the synthesis of derivatives for a broad range of biomedical applications. *Carbohydrate Polymers* (2011). doi:10.1016/j.carbpol.2011.03.019
66. Bhattacharya, D. S. *et al.* Impact of structurally modifying hyaluronic acid on CD44 interaction. *J. Mater. Chem. B* (2017). doi:10.1039/c7tb01895a
67. Collins, M. N. & Birkinshaw, C. Physical properties of crosslinked hyaluronic acid hydrogels. *J. Mater. Sci. Mater. Med.* (2008). doi:10.1007/s10856-008-3476-4
68. Gallo, N. *et al.* Hyaluronic acid for advanced therapies: Promises and challenges. *European Polymer Journal* (2019). doi:10.1016/j.eurpolymj.2019.05.007
69. Burdick, J. A. & Prestwich, G. D. Hyaluronic acid hydrogels for biomedical applications. *Adv. Mater.* (2011). doi:10.1002/adma.201003963
70. Mayol, L. *et al.* Effect of hyaluronic acid on the thermogelation and biocompatibility of its blends with methyl cellulose. *Carbohydr. Polym.* (2014). doi:10.1016/j.carbpol.2014.06.020
71. Keizers, P. H. J. *et al.* A high crosslinking grade of hyaluronic acid found in a dermal filler causing adverse effects. *J. Pharm. Biomed. Anal.* (2018). doi:10.1016/j.jpba.2018.06.066
72. Felgueiras, H. P. *et al.* Octadecyl Chains Immobilized onto Hyaluronic Acid Coatings by Thiol-ene “Click Chemistry” Increase the Surface Antimicrobial Properties and Prevent Platelet Adhesion and Activation to Polyurethane. *ACS Appl. Mater. Interfaces* (2017). doi:10.1021/acsami.6b16415
73. Smith, L. J. *et al.* Diels-Alder Click-Cross-Linked Hydrogels with Increased Reactivity Enable 3D Cell Encapsulation. *Biomacromolecules* (2018). doi:10.1021/acs.biomac.7b01715
74. Fu, S., Dong, H., Deng, X., Zhuo, R. & Zhong, Z. Injectable hyaluronic acid/poly(ethylene glycol) hydrogels crosslinked via strain-promoted azide-alkyne cycloaddition click reaction. *Carbohydr. Polym.* (2017). doi:10.1016/j.carbpol.2017.04.028

75. Bencherif, S. A. *et al.* Influence of the degree of methacrylation on hyaluronic acid hydrogels properties. *Biomaterials* (2008). doi:10.1016/j.biomaterials.2007.11.047
76. Levett, P. A. *et al. Photocrosslinkable hydrogels for cartilage tissue engineering*. *Journal of Tissue Engineering and Regenerative Medicine* (2012).
77. Bellini, D. & Topai, A. Amides of hyaluronic acid and the derivatives thereof and a process for their preparation. *Patent* (1998).
78. D'Este, M., Eglin, D. & Alini, M. A systematic analysis of DMTMM vs EDC/NHS for ligation of amines to Hyaluronan in water. *Carbohydr. Polym.* (2014). doi:10.1016/j.carbpol.2014.02.070
79. Schramm, C. *et al.* The cross-linked biopolymer hyaluronic acid as an artificial vitreous substitute. *Investig. Ophthalmol. Vis. Sci.* (2012). doi:10.1167/iovs.11-7322
80. Nobuhiko, Y., Teruo, O. & Yasuhisa, S. Inflammation responsive degradation of crosslinked hyaluronic acid gels. *J. Control. Release* (1992). doi:10.1016/0168-3659(92)90195-W
81. GUTMAN, A. L., BRENNER, D. & BOLTANSKI, A. ChemInform Abstract: Convenient Practical Resolution of Racemic Alkyl-Aryl Alcohols via Enzymatic Acylation with Succinic Anhydride in Organic Solvents. *ChemInform* (2010). doi:10.1002/chin.199340081
82. Seidlits, S. K. *et al.* The effects of hyaluronic acid hydrogels with tunable mechanical properties on neural progenitor cell differentiation. *Biomaterials* (2010). doi:10.1016/j.biomaterials.2010.01.125
83. Feng, Q. *et al.* Sulfated hyaluronic acid hydrogels with retarded degradation and enhanced growth factor retention promote hMSC chondrogenesis and articular cartilage integrity with reduced hypertrophy. *Acta Biomater.* (2017). doi:10.1016/j.actbio.2017.02.015
84. Purcell, B. P. *et al.* Incorporation of Sulfated Hyaluronic Acid Macromers into Degradable Hydrogel Scaffolds for Sustained Molecule Delivery. *Biomater. Sci.* **2**, 693–702 (2014).
85. Lim, D.-K., Wylie, R. G., Langer, R. & Kohane, D. S. Selective binding of C-6 OH sulfated hyaluronic acid to the angiogenic isoform of VEGF165. *Biomaterials* **77**, 130–138 (2016).
86. Xu, Y. *et al.* Chemically modified polysaccharides: Synthesis, characterization, structure activity relationships of action. *International Journal of Biological Macromolecules* (2019). doi:10.1016/j.ijbiomac.2019.03.213
87. Li, S. *et al.* Molecular Modification of Polysaccharides and Resulting Bioactivities. *Compr. Rev. Food Sci. Food Saf.* (2016). doi:10.1111/1541-4337.12161
88. Liang, L. *et al.* Sulfated modification and anticoagulant activity of pumpkin (Cucurbita pepo, Lady Godiva) polysaccharide. *Int. J. Biol. Macromol.* (2018). doi:10.1016/j.ijbiomac.2017.08.035
89. Wang, X., Zhang, Z., Yao, Z., Zhao, M. & Qi, H. Sulfation, anticoagulant and antioxidant activities of polysaccharide from green algae

Enteromorpha linza. *Int. J. Biol. Macromol.* (2013). doi:10.1016/j.ijbiomac.2013.04.005
90. Shi, X. dan, Li, O. ye, Yin, J. yi & Nie, S. ping. Structure identification of α-glucans from Dictyophora echinovolvata by methylation and 1D/2D NMR spectroscopy. *Food Chem.* (2019). doi:10.1016/j.foodchem.2018.07.160
91. Tao, Y. *et al.* Carboxymethylated hyperbranched polysaccharide: Synthesis, solution properties, and fabrication of hydrogel. *Carbohydr. Polym.* (2015). doi:10.1016/j.carbpol.2015.04.012
92. Xie, J. H. *et al.* Preparation, characterization and antioxidant activities of acetylated polysaccharides from Cyclocarya paliurus leaves. *Carbohydr. Polym.* (2015). doi:10.1016/j.carbpol.2015.07.031
93. Meng, X. & Edgar, K. J. 'Click' reactions in polysaccharide modification. *Progress in Polymer Science* (2016). doi:10.1016/j.progpolymsci.2015.07.006
94. Lawandi, J., Rocheleau, S. & Moitessier, N. Regioselective acylation, alkylation, silylation and glycosylation of monosaccharides. *Tetrahedron* (2016). doi:10.1016/j.tet.2016.08.019
95. Wijesekara, I., Pangestuti, R. & Kim, S. K. Biological activities and potential health benefits of sulfated polysaccharides derived from marine algae. *Carbohydrate Polymers* (2011). doi:10.1016/j.carbpol.2010.10.062
96. Caputo, H. E., Straub, J. E. & Grinstaff, M. W. Design, synthesis, and biomedical applications of synthetic sulphated polysaccharides. *Chemical Society Reviews* (2019). doi:10.1039/c7cs00593h
97. Kaila, N. & Thomas IV, B. E. Design and synthesis of sialyl Lewisx mimics as E- and P-selectin inhibitors. *Medicinal Research Reviews* (2002). doi:10.1002/med.10018
98. Lin, L. F. H., Doherty, D. H., Lile, J. D., Bektesh, S. & Collins, F. GDNF: A glial cell line - Derived neurotrophic factor for midbrain dopaminergic neurons. *Science (80-.).* (1993). doi:10.1126/science.8493557
99. Talaga, M. L. *et al.* Multitasking Human Lectin Galectin-3 Interacts with Sulfated Glycosaminoglycans and Chondroitin Sulfate Proteoglycans. *Biochemistry* (2016). doi:10.1021/acs.biochem.6b00504
100. Hintze, V. *et al.* Sulfated hyaluronan and chondroitin sulfate derivatives interact differently with human transforming growth factor-??1 (TGF-??1). *Acta Biomater.* **8**, 2144–2152 (2012).
101. Matou, S., Helley, D., Chabut, D., Bros, A. & Fischer, A. M. Effect of fucoidan on fibroblast growth factor-2-induced angiogenesis in vitro. *Thromb. Res.* (2002). doi:10.1016/S0049-3848(02)00136-6
102. Shamay, Y. *et al.* P-selectin is a nanotherapeutic delivery target in the tumor microenvironment. *Sci. Transl. Med.* **8**, 345ra87 (2016).
103. Ley, K. The role of selectins in inflammation and disease. *Trends in Molecular Medicine* (2003). doi:10.1016/S1471-4914(03)00071-6
104. Iwamura, T. *et al.* P-selectin expression in a metastatic pancreatic tumor cell line (SUIT- 2). *Cancer Res.* (1997).

105. Natoni, A., Macauley, M. S. & O'Dwyer, M. E. Targeting selectins and their ligands in cancer. *Frontiers in Oncology* (2016). doi:10.3389/fonc.2016.00093
106. Woelke, A. L. *et al.* Understanding selectin counter-receptor binding from electrostatic energy computations and experimental binding studies. *J. Phys. Chem. B* (2013). doi:10.1021/jp4099123
107. Weinhart, M., Gröger, D., Enders, S., Dernedde, J. & Haag, R. Synthesis of dendritic polyglycerol anions and their efficiency toward L-selectin inhibition. *Biomacromolecules* (2011). doi:10.1021/bm200250f
108. Somers, W. S., Tang, J., Shaw, G. D. & Camphausen, R. T. Insights into the molecular basis of leukocyte tethering and rolling revealed by structures of P-and E-seiectin bound to SLe(X) and PSGL-1. *Cell* (2000). doi:10.1016/S0092-8674(00)00138-0
109. Kedmi, R. & Peer, D. Zooming in on selectins in cancer. *Sci. Transl. Med.* (2016). doi:10.1126/scitranslmed.aag1802
110. Shamay, Y. *et al.* P-selectin is a nanotherapeutic delivery target in the tumor microenvironment. *Sci. Transl. Med.* (2016). doi:10.1126/scitranslmed.aaf7374
111. Ferber, S. *et al.* Co-targeting the tumor endothelium and P-selectin-expressing glioblastoma cells leads to a remarkable therapeutic outcome. *Elife* **6**, 1–34 (2017).
112. Doolittle, E. *et al.* Spatiotemporal Targeting of a Dual-Ligand Nanoparticle to Cancer Metastasis. *ACS Nano* (2015). doi:10.1021/acsnano.5b01552
113. Liu, J., Zhang, R. & Xu, Z. P. Nanoparticle-Based Nanomedicines to Promote Cancer Immunotherapy: Recent Advances and Future Directions. *Small* (2019). doi:10.1002/smll.201900262
114. Hill, T. K. & Mohs, A. M. Image-guided tumor surgery: Will there be a role for fluorescent nanoparticles? *Wiley Interdisciplinary Reviews: Nanomedicine and Nanobiotechnology* (2015). doi:10.1002/wnan.1381
115. Salatin, S., Maleki Dizaj, S. & Yari Khosroushahi, A. Effect of the surface modification, size, and shape on cellular uptake of nanoparticles. *Cell Biology International* (2015). doi:10.1002/cbin.10459
116. Owens, D. E. & Peppas, N. A. Opsonization, biodistribution, and pharmacokinetics of polymeric nanoparticles. *International Journal of Pharmaceutics* (2006). doi:10.1016/j.ijpharm.2005.10.010
117. Albanese, A., Tang, P. S. & Chan, W. C. W. The Effect of Nanoparticle Size, Shape, and Surface Chemistry on Biological Systems. *Annu. Rev. Biomed. Eng.* (2012). doi:10.1146/annurev-bioeng-071811-150124
118. Maeda, H., Nakamura, H. & Fang, J. The EPR effect for macromolecular drug delivery to solid tumors: Improvement of tumor uptake, lowering of systemic toxicity, and distinct tumor imaging in vivo. *Advanced Drug Delivery Reviews* (2013). doi:10.1016/j.addr.2012.10.002
119. Tang, L., Fan, T. M., Borst, L. B. & Cheng, J. Synthesis and biological response of size-specific, monodisperse drug-silica

nanoconjugates. *ACS Nano* (2012). doi:10.1021/nn300149c
120. Dasgupta, S., Auth, T. & Gompper, G. Shape and orientation matter for the cellular uptake of nonspherical particles. *Nano Lett.* (2014). doi:10.1021/nl403949h
121. Gratton, S. E. A. *et al.* The effect of particle design on cellular internalization pathways. *Proc. Natl. Acad. Sci. U. S. A.* (2008). doi:10.1073/pnas.0801763105
122. Overchuk, M. & Zheng, G. Overcoming obstacles in the tumor microenvironment: Recent advancements in nanoparticle delivery for cancer theranostics. *Biomaterials* (2018). doi:10.1016/j.biomaterials.2017.10.024
123. Tenzer, S. *et al.* Rapid formation of plasma protein corona critically affects nanoparticle pathophysiology. *Nat. Nanotechnol.* (2013). doi:10.1038/nnano.2013.181
124. Arvizo, R. R. *et al.* Effect of nanoparticle surface charge at the plasma membrane and beyond. *Nano Lett.* (2010). doi:10.1021/nl101140t
125. Benjaminsen, R. V., Mattebjerg, M. A., Henriksen, J. R., Moghimi, S. M. & Andresen, T. L. The possible "proton sponge " effect of polyethylenimine (PEI) does not include change in lysosomal pH. *Mol. Ther.* (2013). doi:10.1038/mt.2012.185
126. Sakurai, Y. & Harashima, H. Hyaluronan-modified nanoparticles for tumor-targeting. *Expert Opin. Drug Deliv.* (2019). doi:10.1080/17425247.2019.1645115
127. Wang, J., Li, Y., Wang, L., Wang, X. & Tu, P. Comparison of hyaluronic acid-based micelles and polyethylene glycol-based micelles on reversal of multidrug resistance and enhanced anticancer efficacy in vitro and in vivo. *Drug Deliv.* (2018). doi:10.1080/10717544.2018.1428385
128. Han, H. S. *et al.* Bioreducible shell-cross-linked hyaluronic acid nanoparticles for tumor-targeted drug delivery. *Biomacromolecules* (2015). doi:10.1021/bm5017755
129. Choi, K. Y. *et al.* Smart nanocarrier based on PEGylated hyaluronic acid for cancer therapy. *ACS Nano* (2011). doi:10.1021/nn202070n
130. Thomas, A. P., Palanikumar, L., Jeena, M. T., Kim, K. & Ryu, J. H. Cancer-mitochondria-targeted photodynamic therapy with supramolecular assembly of HA and a water soluble NIR cyanine dye. *Chem. Sci.* (2017). doi:10.1039/c7sc03169f
131. Kalam, M. A. Development of chitosan nanoparticles coated with hyaluronic acid for topical ocular delivery of dexamethasone. *Int. J. Biol. Macromol.* (2016). doi:10.1016/j.ijbiomac.2016.04.070
132. Mao, H. L. *et al.* Delivery of Doxorubicin from Hyaluronic Acid-Modified Glutathione-Responsive Ferrocene Micelles for Combination Cancer Therapy. *Mol. Pharm.* (2019). doi:10.1021/acs.molpharmaceut.8b00862
133. Hill, T. K. *et al.* Indocyanine green-loaded nanoparticles for image-guided tumor surgery. *Bioconjug. Chem.* **26**, 294–303 (2015).
134. Hill, T. K. *et al.* Near infrared fluorescent nanoparticles derived from

hyaluronic acid improve tumor contrast for image-guided surgery. *Theranostics* **6**, 2314–2328 (2016).
135. Fu, C. *et al.* Targeted Magnetic Resonance Imaging and Modulation of Hypoxia with Multifunctional Hyaluronic Acid-MnO2 Nanoparticles in Glioma. *Adv. Healthc. Mater.* (2019). doi:10.1002/adhm.201900047
136. Yu, M. *et al.* Hyaluronic acid-functionalized gadolinium doped iron oxide nanoparticles for atherosclerosis-targeted MR imaging. *J. Biomed. Nanotechnol.* (2019). doi:10.1166/jbn.2019.2660
137. Seo, Y. H. *et al.* Nanoparticles of Conjugated Molecules and Polymers for Biomedical Applications. in (2015). doi:10.1007/12_2015_324
138. Tuncel, D. & Demir, H. V. Conjugated polymer nanoparticles. *Nanoscale* (2010). doi:10.1039/b9nr00374f
139. Liu, B., Wang, S., Bazan, G. C. & Mikhailovsky, A. Shape-Adaptable Water-Soluble Conjugated Polymers. *J. Am. Chem. Soc.* (2003). doi:10.1021/ja0365072
140. Chu, H. C. *et al.* Novel reversible chemosensory material based on conjugated side-chain polymer containing fluorescent pyridyl receptor pendants. *J. Phys. Chem. B* (2011). doi:10.1021/jp201586c
141. Vokatá, T. & Moon, J. H. Synthesis of phenyleneethynylene-doped poly(p -phenylenebutadiynylene)s for live cell imaging. *Macromolecules* (2013). doi:10.1021/ma3019975
142. Liao, J. & Wang, Q. Ruthenium-catalyzed knoevenagel condensation: A new route toward cyano-substituted poly(p-phenylenevinylene)s. *Macromolecules* (2004). doi:10.1021/ma049243s
143. Inzelt, G. Classification of Electrochemically Active Polymers. in (2012). doi:10.1007/978-3-642-27621-7_2
144. Huang, W. S., Humphrey, B. D. & MacDiarmid, A. G. Polyaniline, a novel conducting polymer. Morphology and chemistry of its oxidation and reduction in aqueous electrolytes. *J. Chem. Soc. Faraday Trans. 1 Phys. Chem. Condens. Phases* (1986). doi:10.1039/F19868202385
145. Demchenko, A. P. Nanoparticles and nanocomposites for fluorescence sensing and imaging. *Methods Appl. Fluoresc.* **1**, 022001 (2013).
146. Hong, Y., Lam, J. W. Y. & Tang, B. Z. Aggregation-induced emission. *Chemical Society Reviews* (2011). doi:10.1039/c1cs15113d
147. Wang, Z. *et al.* Folic acid-functionalized mesoporous silica nanospheres hybridized with AIE luminogens for targeted cancer cell imaging. *Nanoscale* (2013). doi:10.1039/c2nr33685e
148. Shi, C. *et al.* Self-assembly solid-state enhanced red emission of quinolinemalononitrile: Optical waveguides and stimuli response. *ACS Appl. Mater. Interfaces* (2013). doi:10.1021/am302466m
149. Lim, C. K., Kim, S., Kwon, I. C., Ahn, C. H. & Park, S. Y. Dye-condensed biopolymeric hybrids: Chromophoric aggregation and self-assembly toward fluorescent bionanoparticles for near infrared bioimaging. *Chem. Mater.* (2009). doi:10.1021/cm902379x

150. Shin, S., Gihm, S. H., Park, C. R., Kim, S. & Park, S. Y. Water-soluble fluorinated and PEGylated cyanostilbene derivative: An amphiphilic building block forming self-assembled organic nanorods with enhanced fluorescence emission. *Chem. Mater.* (2013). doi:10.1021/cm400988a
151. Wu, C., Peng, H., Jiang, Y. & McNeill, J. Energy transfer mediated fluorescence from blended conjugated polymer nanoparticles. *J. Phys. Chem. B* (2006). doi:10.1021/jp0618126
152. Park, S. J., Kang, S. G., Fryd, M., Saven, J. G. & Park, S. J. Highly tunable photoluminescent properties of amphiphilic conjugated block copolymers. *J. Am. Chem. Soc.* (2010). doi:10.1021/ja1004569
153. Feng, L. *et al.* Conjugated polymer nanoparticles: Preparation, properties, functionalization and biological applications. *Chem. Soc. Rev.* (2013). doi:10.1039/c3cs60036j
154. Hong, G. *et al.* Ultrafast fluorescence imaging in vivo with conjugated polymer fluorophores in the second near-infrared window. *Nat. Commun.* (2014). doi:10.1038/ncomms5206
155. Chen, C. P. *et al.* Near-infrared fluorescent semiconducting polymer dots with high brightness and pronounced effect of positioning alkyl chains on the comonomers. *ACS Appl. Mater. Interfaces* (2014). doi:10.1021/am506577r
156. Braeken, Y., Cheruku, S., Ethirajan, A. & Maes, W. Conjugated polymer nanoparticles for bioimaging. *Materials* (2017). doi:10.3390/ma10121420
157. Zhu, S., Song, Y., Shao, J., Zhao, X. & Yang, B. Non-conjugated polymer dots with crosslink-enhanced emission in the absence of fluorophore units. *Angew. Chemie - Int. Ed.* (2015). doi:10.1002/anie.201504951
158. Zhu, S. *et al.* The crosslink enhanced emission (CEE) in non-conjugated polymer dots: From the photoluminescence mechanism to the cellular uptake mechanism and internalization. *Chem. Commun.* (2014). doi:10.1039/c4cc05806b
159. Sun, B. *et al.* Fluorescent non-conjugated polymer dots for targeted cell imaging. *Nanoscale* (2016). doi:10.1039/c6nr01909a
160. Zhu, S. *et al.* A general route to make non-conjugated linear polymers luminescent. *Chem. Commun.* (2012). doi:10.1039/c2cc36080b

CHAPTER II

IMPACT OF STRUCTURALLY MODIFYING HYALURONIC ACID ON CD44 INTERACTION

Abstract: CD44 is a widely-distributed type I transmembrane glycoprotein that binds hyaluronic acid (HA) in most cell types, including primary tumor cells and cancer-initiating cells and has roles in cell migration, cell-cell, and cell-matrix adhesion. HA-derived conjugates and nanoparticles that target the CD44 receptor on cells have been reported for targeted delivery of therapeutics and imaging agents. Altering crucial interactions of HA with CD44 active sites holds significant importance in modulating targeting ability of hyaluronic acid to other cancer types that do not express the CD44 receptor or minimizing the interaction with $CD44^+$ cells that are not target cells. The approach adopted here was deacetylation of the N-acetyl group and selective sulfation on the C6-OH on the HA polymer, which form critical interactions with the CD44 active site. Major interactions identified by molecular modeling were confirmed to be hydrogen bonding of the C6-OH with Tyr109 and hydrophobic interaction of the N-acetyl group with Tyr46, 83 and Ile 92. Modified HA was synthesized and characterized, and its interactions were assessed by *in vitro* and molecular modeling approaches. *In vitro* techniques included flow cytometry and fluorescence polarization, while *in silico* approaches included docking and binding calculations by MM-PBSA approach. These studies indicated that while both deacetylation and sulfation of HA individually decrease CD44 interaction, both chemical modifications are required to minimize interaction with $CD44^+$ cells. The results

of this study represent the first step to effective retargeting of HA-derived NPs for imaging and drug delivery.

INTRODUCTION

Hyaluronic acid (HA) is a linear, non-sulfated, and negatively charged polysaccharide that is comprised of {β1→3} N-acetylglucosamine (GlcNAc) and {β1→4} glucuronic acid (GlcUA) units. HA, an integral part of the extracellular matrix (ECM),[1–3] contributes to lubrication of joints,[4] cell migration[5] during embryonic morphogenesis,[2] cell adhesion, tumor cell proliferation,[2,3,6] metastasis, angiogenesis, tissue regeneration, leukocyte trafficking, and progression of inflammation and cancer.[2,3,7–13] The native ligand for HA is the transmembrane receptor CD44.[14–16] HA binds to the N-terminus of CD44, which functions as the docking site and is lined by a mixture of primarily basic and hydrophobic amino acids.[17] The CD44 gene contains 20 exons, 10 of which can be regulated by alternative splicing leading to generation of other splice variants (variant or 'v' exons), which are translated to a polypeptide of molecular weight 80-90 kDa depending on the splice variant.[18] Biological functions, such as cell migration, adhesion, and structural integrity during anti-inflammatory processes, rely on HA-CD44 interaction.[10,11,19–21] The smallest CD44 isoform, CD44 standard (CD44s), is ubiquitously expressed, whereas the variant isoforms are expressed in a few epithelial tissues and in cancers.[10,22,23] The expression of variants of CD44 is heterogeneous among progression of various tumors. For example, CD44v10 and v3 are significantly associated with head and neck squamous cell carcinoma (HNSCC) primary tumors, and were shown to stimulate

cell growth, proliferation and over-expression of metalloproteinases (MMP), whereas high expression of CD44v4-9 is observed in other tumors.[24–33] HA is also known to bind to other receptors such as RHAMM and TSG-6. Major interactions of RHAMM involve association of CD44 for binding[34], whereas for TSG-635 the binding events are controlled by a small 45 amino acid binding domain, as compared to large 160 amino acid domain in CD44. Recognition of hyaluronic acid by CD44 regulates various downstream pathways, e.g. activating/inhibiting phosphorylation of tyrosine kinases, activation of Nanog, which leads to overexpression of MDR1/P-gp gene, phosphorylation of c-Jun n-terminal kinases (JNK), and activation of GSK3β.[36–44] The downstream events are triggered when CD44 recognizes certain key moieties in the hyaluronic acid polymer chain,[38] which include hydrophobic interactions between the N-acetyl group of HA with the phenyl ring of Tyr83, the side chain of Ile92 and the disulfide bond between Cys81 and Cys101 of CD44; water-mediated hydrogen bonding between the carboxylate group of HA with Tyr46 and Arg45 of CD44; hydrogen bonding between the C6-hydroxy group of HA with Tyr109 of CD44, which serves to lock HA to the CD44 active site; and hydrogen bonding between the vicinal diols of HA with guanidine groups of Arg45 and Arg82.[17] These interactions are summarized in **Figure 1**. Desirable features of CD44-HA binding are the absence of ionic interactions and strong prevalence of a hydrophobic core.[17] The molecular weight (MW) of HA is also known to play a crucial role in the recognition and binding to the CD44 protein in the ECM.[45]

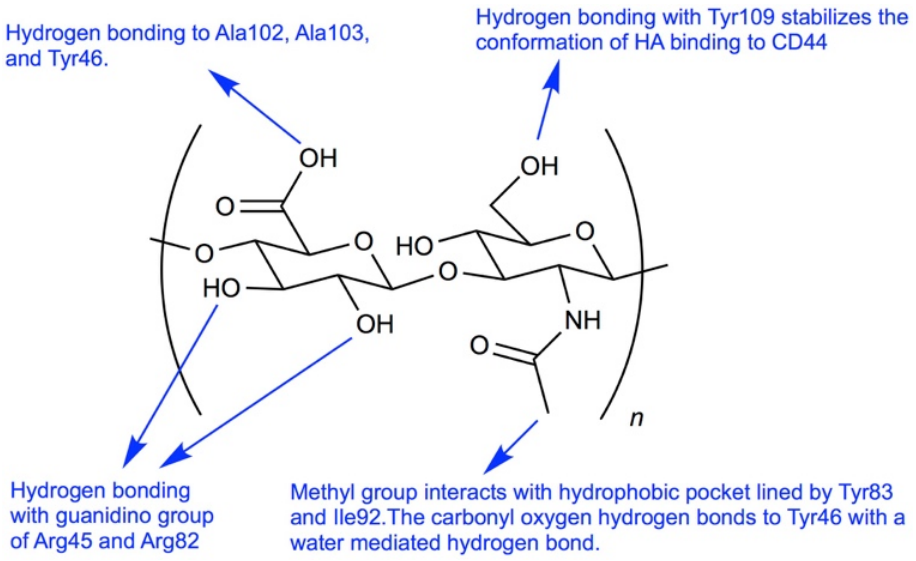

Figure 1. Interactions of {β1→3} N-acetylglucosamine (GlcNAc) and {β1→4} glucuronic acid (GlcUA) repeat unit of hyaluronic acid with crucial amino acids in the murine CD44 active site.

Recently, several groups have attempted to alter the properties of HA by chemical modification. The modified HA target other proteins and enzymes and regulate CD44-independent biological processes. One such chemical modification that has been extensively explored is the sulfation of HA. Sulfated HA showed selective binding, as measured by surface plasmon resonance (SPR), for isoform 165a of vascular endothelial growth factor ($VEGF_{165a}$)[46] and sclerostin, a secreted glycoprotein that has an integral role in bone biology.[47] Integration of *in silico* (molecular docking and dynamics simulations) and *in vitro* SPR studies showed that binding to sclerostin was dependent on the degree and pattern of HA sulfation. Others showed that increased sulfation of HA resulted in higher binding affinity to TGF-β1 compared with native HA or chondroitin sulfate.[48]

In the current study, HA was rationally modified to investigate the potential to minimize its interaction with CD44. Our group has previously observed the uptake of HA-derived nanoparticles (NPs) into CD44-expressing tumors and organs, e.g. liver and speen.[49–51] Liver cells express stabilin-2 (sub-family of CD44) and spleen cells have high expression of CD44.[52] Similar results were observed by Lin et al.[53], where HA-IR-780-based nanosystems accumulated largely in liver and spleen. HA-functionalized glycyrrhetinic acid nanoparticles accumulate in major CD44 clearance organs–liver and spleen[54]. This demands new approaches to design polymers by precisely tuning their structure to achieve maximum tumor accumulation by reducing CD44 interactions to non-target organs.

Ultimately, we postulate that NPs derived from structurally-modified HA could have decreased uptake in liver and spleen and/or could be retargeted by conjugation of other targeting ligands to specific receptors with the end goal of increasing accumulation of NPs in tumor. By chemically modifying HA, a wide spectrum of binding partners can be exploited in rationally designing a robust drug/dye delivery system for enhanced tumor recognition. The investigation reported here studies HA-CD44 binding after HA deacetylation, sulfation, and a combination thereof. We hypothesized that deacetylating the HA backbone as one modification, selectively sulfating the C6-OH as a second modification, and incorporation of both deacetylation and sulfation as a third modification, would decrease the binding of these modified derivatives of HA to CD44. Interactions

of the modified HA with CD44 were measured using flow cytometry, fluorescence polarization, and *in silico* approaches.

Materials and Methods

Sodium hyaluronate, 10 kDa, was purchased from Lifecore Biomedical (Chaska, MN). Tetrabutylammonium (TBA) hydroxide, DOWEX 50WX8-400 ion exchange resin, sulfur trioxide pyridine complex (SO3-pyridine 98%), hydrazine, hydrazine sulfate, N-(3-Dimethylaminopropyl)-N-ethylcarbodiimide hydrochloride (EDC), N-hydroxysuccinimide (NHS) and fetal bovine serum (FBS) were purchased from Sigma-Aldrich (St. Louis. MO). All water was purified with Barnstead™ Nanopure™ Diamond system (Thermo Scientific; Waltham, MN). Methanol, N,N-dimethylformamide (DMF), 96-well tissue culture plates (Falcon), 12-well tissue culture plates and dialysis tubing (MWCO = 3500) were purchased from Fisher Scientific (Pittsburgh, PA). Ethanol was purchased from the Warner-Graham Company (Cockeysville, MD). Recombinant human CD44-Fc Tag (HPLC–verified) was purchased from Acrobiosystems. Ninhydrin reagent and hydridantin dehydrate 96% and fluoresceinamine isomer I, 99% were purchased from ACROS Organics and 2-methoxyethyl acetate was obtained from TCI America. Anti-CD44 antibody was purchased from BD Pharmigen BD Biosciences. NMR was performed on a 500 MHz Bruker or 600 MHz Varian system using a 5 mm probe at room temperature. Deuterated water (D_2O, 99.9% D) was purchased from Cambridge Isotope Laboratories. FTIR measurements were performed on Nicolet IR200 FT-IR instrument using single-reflection ZnSe ATR crystal. Penicillin/streptomycin (100X solution) was purchased from

Corning. Cell lines (PC-3, MDA-MB-231, RKO and LNCaP cells) were obtained from American Type Culture Collection (Manassas, VA) and were grown in RPMI-1640 (HyClone, GE Healthcare Life Sciences) with 10% fetal bovine serum and 1% penicillin/streptomycin (P/S).

Preparation of modified HA derivatives

Modifications to HA were synthesized based on methods described in the literature[46,55] with slight modifications as described below (**Scheme 1**).

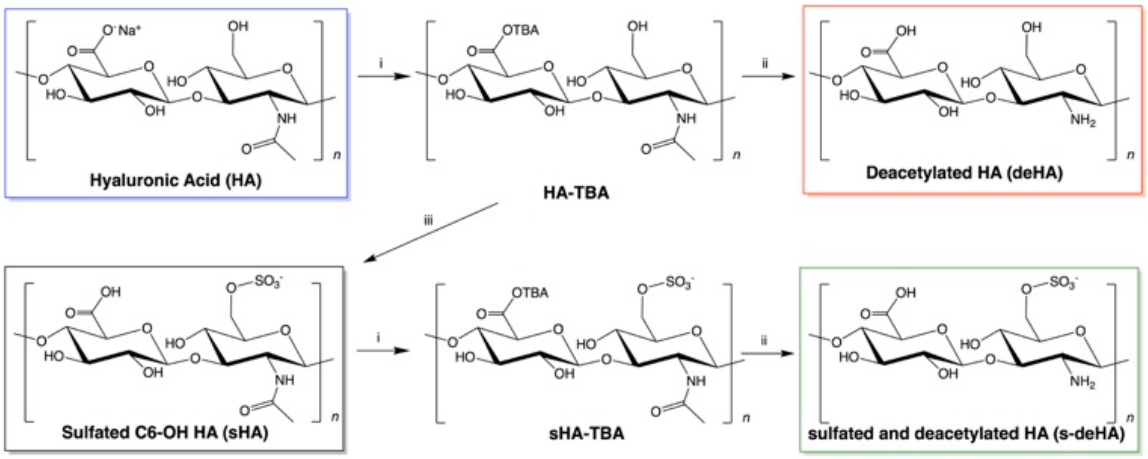

Scheme 1. Synthesis of deacetylated, sulfated, and deacetylated and sulfated HA. i: ion exchange with TBA in H_2O; ii: hydrazine, hydrazine sulfate, DMF; and iii: sulfur trioxide pyridine, DMF.

Synthesis of TBA salt of hyaluronic acid (HA-TBA). Sodium hyaluronate (10 kDa, 250 mg) was dissolved in 100 ml ultrapure water, which was mixed with 5 g of DOWEX 50WX8-400 ion- exchange resin to allow the substitution of sodium ions with TBA. This mixture was stirred for 6-8 h for the effective exchange process. The reaction mixture was then filtered through a 0.45 µm membrane

filter paper obtained from Millipore. This solution was then lyophilized to yield a white powder with a yield of 90% (HA-TBA).

Synthesis of deacetylated HA-TBA (deHA-TBA). HA-TBA (200 mg) was dissolved in a three-neck round bottom flask with 20 mL DMF under argon flow at room temperature (rt) to aid the formation of a homogenous mixture. Hydrazine (20 mL) and hydrazine sulfate (200 mg) were added to the mixture and the reaction was allowed to proceed for 8 h under an atmosphere of argon at 100°C. After the reaction was complete, the mixture was cooled to rt and the pH was adjusted to 10 using 4.0 M aqueous NaOH. The mixture was dissolved in 100 mL of 1:1 acetone:water, which was then extensively dialyzed (MWCO = 3500 Da, Spectrum Laboratories) against 1:1 methanol:water for 24 h, followed by 1:1 ethanol:water for 24 h with 4 changes and finally 8 changes of water over 72 h to remove unreacted TBA. The material obtained had a yield of 24% and was then lyophilized and stored at -20°C.

Selective sulfation of hyaluronic acid at C6 position (sHA). HA-TBA (200 mg) was dissolved in a three-neck round bottom flask with 20 mL DMF under argon for 15 min. Sulfur trioxide pyridine complex (0.325 g) was dissolved in 4 mL of DMF and added dropwise to the reaction mixture. The temperature was maintained at rt for 40 min, and then the reaction was quenched by adding 20 mL of ultrapure water. Acetone was added to the reaction mixture to precipitate the product, which was then filtered and washed with acetone and water. The product was dissolved in water and dialyzed against 1:1 ethanol:water for 24 h with 4 changes followed by 48 h of ultrapure water with 8 changes. This solution was

then lyophilized yielding an off-white solid with 82% yield that was stored at -20°C.

Synthesis of deacetylated and sulfated hyaluronic acid (s-deHA). Sulfated HA-TBA, as prepared above, was utilized for the preparation of deacetylated and sulfated hyaluronic acid. Sulfated hyaluronic acid-TBA compound (200 mg) was dissolved in 20 mL of DMF under argon for 15 min in a three-neck round bottom flask. Hydrazine (20 mL) and hydrazine sulfate (200 mg) were added to the reaction under argon. The reaction mixture was stirred for 8 h at 100°C. It was then allowed to cool to rt and its pH was adjusted to 10 using 4.0 M NaOH. The mixture was then dissolved and dialyzed as described for deHA-TBA above, lyophilized, and stored at -20°C (yield = 34%).

Deacetylation quantification. The colorimetric ninhydrin assay was used to quantify the primary amine produced by deacetylation of the N-¬acetyl-D-glucosamine monosaccharide. Standard solution (0.1 mg/mL) of glucosamine was used to build the standard curve in acetate buffer (0.5 mL; pH 5.5; 4 M). deHA (0.5 mg) and s-deHA (0.5 mg) were used for the assay. The ninhydrin reagent was prepared by mixing 1 g ninhydrin, 0.12 g hydridantin, 23 mL of 2-methoxyethyl acetate with 12.8 mL of 4 N acetate buffer. The total volume of the sample was 2 mL, and this solution was heated in a boiling water bath for 15 min. The reaction mixture was cooled subsequently to rt followed by measuring the absorbance at 570 nm. Absorption and spectra were recorded on Evolution 220 spectrophotometer (Thermo Scientific) in quartz cells with the optical path length of 10.0 mm at 25°C.

Synthesis of hyaluronic acid conjugate with fluoresceinamine (HA-FITC).

Sodium hyaluronate (90-95 mg, Mn = 10-20 kDa) was dissolved in 20 mL of ultrapure water in a 50 mL round bottom flask. Fluoresceinamine (8 mol %) was dissolved in 10 mL DMSO under constant stirring. NHS and EDC, 96-132 mmol (10x molar excess to fluoresceinamine) were dissolved into HA solution and stirred for 30 mins to allow activation of carboxylic groups on HA. The fluoresceinamine DMSO solution was then added dropwise to HA solution under constant stirring. The reaction mixture was stirred for 24 h at rt, wrapped in foil to prevent light exposure. The reaction mixture was then dialyzed against 1:1 ethanol:water for 48 h with 4 changes followed by water alone for 72 h with 8 changes. The product was lyophilized and stored at -20°C with a yield of 68%.

Flow cytometry analysis for binding assays

A cellular binding assay was performed using HA-FITC as the competing probe. MDA-MB-231, PC-3, RKO and LNCaP cells, approximately 90,000 cells/well, were seeded in a 12-well plate. The cells were pre-incubated with sHA, deHA, s-deHA and HA (200 μM) for 1 h at rt with constant shaking. HA-FITC (20 μg/mL) was added to the mixture for 1 h under constant shaking in the dark as the competing ligand to allow for displacement of the unlabeled sample. Cells incubated with unlabeled HA served as the negative control, whereas cells incubated with HA-FITC alone served as the positive control. After incubation, the cells were diluted to 300 μL with PBS in FACS tubes. A FACS LSRII-green flow cytometer (BD) was used for all flow cytometry measurements. A total of 10,000 gated events were acquired per sample and the mean fluorescence

intensity was plotted in a histogram-based graphical representation. Each data point is representative of the mean of three independent measurements on the flow cytometer. Data were analyzed with FlowJo (Tree Star) software.

Fluorescence polarization assay

Fluorescence polarization measurements were performed in a 384-well low-volume black round-bottom polystyrene NBS microplate (Corning) using a Spectromax M5 plate reader (Molecular Devices, Sunnyvale, CA, USA). Polarization values are reported as millipolarization units (mP). The fluorescent probe, HA-FITC, synthesized above and rhCD44-Fc were dissolved in 1X PBS. For direct binding assay between the fluorescent probe and the CD44 protein, 1 µL of 50 nM fluorescent probe and 10 µL of solution with increasing concentration of recombinant CD44 protein (130 nM-72 µM) in PBS were transferred to the microplate wells. The final volume of the reaction mixture was 11 µL in each well, and all measurements were performed in triplicate. The microplate was shaken for 5 min in the dark at rt before being read by the plate reader (λex = 489 nm; λem = 538 nm). Estimation of binding of modified HA derivatives was carried out using a competitive binding assay. To each well in the 384-well plate, 10 µl of 23.4 µM recombinant CD44 was added along with 1 µl of increasing concentration of unlabeled HA derivatives (64 nM - 1000 µM) and 1 µl of fluorescent probe (HA-FITC, 50 nM). The total volume of the reaction mixture was 12 µL in each well. Fluorescence measurements were made after a 15 min

incubation. The data was fitted and IC_{50} values were determined using a non-linear least square fit to a single site binding model (Graphpad v7.0).

Molecular docking of hyaluronic acid derivatives

The X-ray diffraction crystal structure of mouse CD44 hyaluronan-binding domain was obtained from Protein Data Bank (PDB ID: 4MRD).[17] There is similarity in binding of HA between the murine and human CD44 active site, which is conserved.[17,56] Molecular docking was performed to gain deeper insight into the interaction of modified hyaluronic acid derivatives compared to native hyaluronic acid. The protein structure was cleaned by removing water molecules and other inorganic ions/atoms. The HA ligand consisting of 12 units was prepared in Maestro molecular modelling software (Schrodinger). Docking studies were performed using Auto-DockTools (AutoDock Vina).[57] The grid box of dimensions 40 Å X 40 Å X 40 Å was generated with a 0.375 Å spacing to perform docking. AutoDock Tools were used to add Gasteiger charges and polar hydrogens to CD44 and modified hyaluronic acid derivatives. The structures were saved in .pdbqt file format. These systems were loaded in the graphic user panel and the grid pane, grid box, and the box dimensions were set accordingly to completely occupy the entire ligand-protein surface to perform docking using AutoDock vina software.[58] 10 runs were performed for statistical analysis on the obtained docking results. Docking was also performed using SwissDock (http://swissdock.vital-it.ch/),[59,60] provided as a free web service. The ligands were docked to the desired protein structures by using suitable docking parameters allowing the online web service to produce docking results using

CHARMM energies.[60] Similar grid size box dimensions used in AutoDock were used for SwissDock. The docked ligand file was visualized with the protein using UCSF Chimera 1.4.[61].

Statistical Analysis

Analysis of competitive binding flow cytometry, fluorescence polarization, and molecular docking were performed with one-way ANOVA with Tukey multiple comparisons test, Student's t test, and non-linear least squares fit to a single site binding model.

All statistical analysis was done in Prism 7.0 (GraphPad Software; La Jolla, CA) and Microsoft Excel.

Results and Discussion

Synthesis and characterization of modified hyaluronic acid derivatives (deHA, sHA and s-deHA)

Deacetylated, sulfated, and deacetylated sulfated HA derivatives were prepared according to **Scheme 1** using previously reported methods with slight modifications. Based on their importance for CD44-HA binding,[17] the N-acetyl and the C6-OH moieties were chosen for synthetic modifications. We synthesized deacetylated, sulfated, and deacetylated sulfated derivatives of HA of molecular weight 10 kDa by controlling the amount of hydrazine and hydrazine sulfate for deacetylation reaction and molar ratios of sulfur trioxide-pyridine complex per repeat units of HA for selective sulfation reaction. The N-acetyl group was deacetylated using the hydrazine/hydrazine sulfate mixture following the Wolff-Kishner reaction under reflux conditions under an atmosphere of argon, cleaving the acetyl group with the initial evolution of gas to produce the amino group during the reaction. The degree of deacetylation of HA changed with the reaction times from 4 to 8 h. The 8 h reaction time was close to 100% deacetylation with complete absence of N-acetyl peak in the corresponding ^{1}H NMR spectra (2-2.2 ppm) as seen in **Figure S5** with reference to ^{1}H and ^{13}C NMR spectra of HA in **Figures S6-7**. The deacetylation reaction by hydrazinolysis has been reported to cause a reduction in overall molecular weight[62] due to C-5 epimerization and β-elimination at the C-4 position leading to breakdown of the glycosidic bonds.[63] We observed a lower yield of deacetylated HA presumably due to the above

explanation. At the reaction temperature, the deacetylating agents, hydrazine and hydrazine sulfate, convert the free carboxylic group to carboxylic hydrazides. For this reason, the TBA salt was synthesized to avoid generation of side products. Ninhydrin colorimetric assay was used to quantify the degree of deacetylation of HA. The ninhydrin reaction is specific to the primary amino group generated during deacetylation reaction producing a distinct purple violet color which was quantified by absorption spectroscopy. ^{1}H-NMR was also used to assess the degree of deacetylation, where one repeat unit of native HA bears 3 methyl protons for every 2 anomeric protons leading to the theoretical integral ratio between the two of 3:2, respectively. Using this ratio equation,[64] the degree of deacetylation was calculated to be 82.6 and 88% for deHA and s-deHA obtained from Ninhydrin assay standard curve. Selective sulfation of HA was controlled by using 3:1 molar ratio of sulfur trioxide-pyridine complex to repeat units of HA. Major sulfation sites on HA are the primary hydroxyl group being the most reactive, while other (secondary) hydroxyl groups are less susceptible to the attack of the sulfating nucleophile moiety due to steric hindrance and spatial orientation of these groups on HA. ^{1}H and ^{13}C NMR analysis was performed on sHA and s-deHA to confirm the sulfation of HA (**Figure 2a-d**). The reactive center C-6 OH linked to CH_2 exhibited a downward shift to 3.55 ppm due to the increased electron withdrawing caused by the sulfate group. Absence of additional peaks between 3.9-4.4 confirmed no side products at positions C-2', C-3' and C-4', indicating selective sulfation of the C-6 OH (Figures S1-S4). The FTIR data in Figure 2 demonstrates the peaks for vibrations of C-O-S and S=O

in the range of 800 and 1290 cm^{-1}, indicating the presence of sulfate moieties in sHA and s-deHA. These results were also confirmed by elemental analysis for sulfate content (Table S1). ^{13}C NMR spectra confirmed that HA was sulfated at C6 position by the shift of the C-6 peak from 61.9 to 68 ppm with complete disappearance of the former shown in Figure S3. The surface charge for the modified polymers was assessed using zeta potential to further support the results from colorimetric assay and NMR spectroscopy. Deacetylation was responsible for introducing positive charges in the polymer, thereby shifting the zeta potential of highly negative HA to near neutral values. The s-deHA had a zeta potential of -6 mV, indicating counter balancing effects of both positive and negative charges induced due to deacetylation and sulfation (Figure 3). At the same time, sulfation lead to further negative charge.

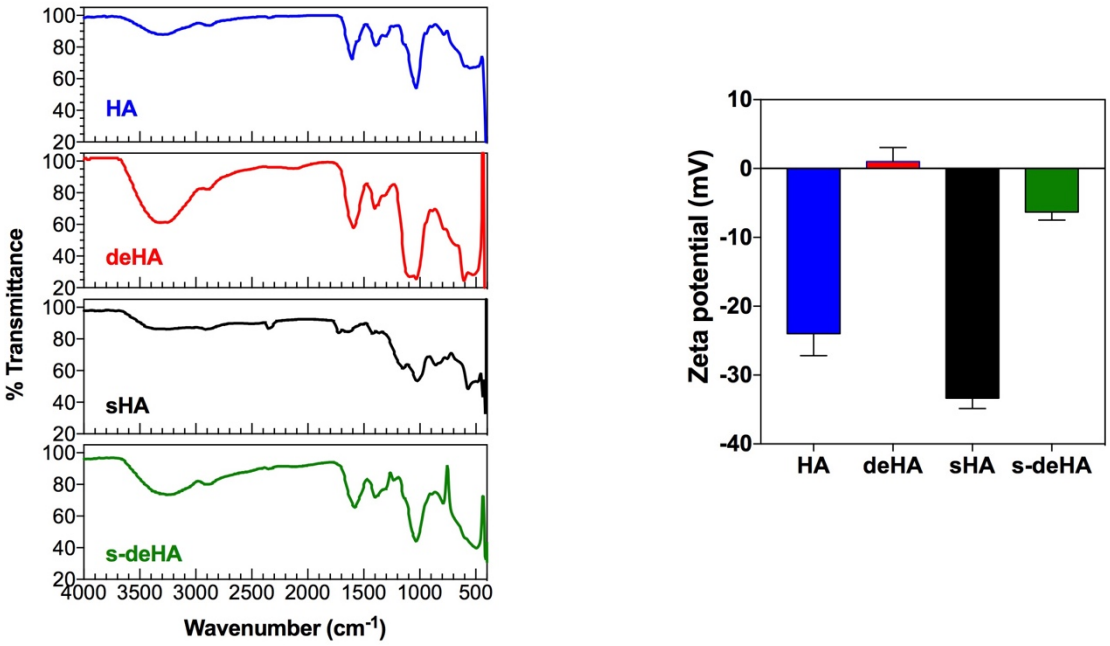

Figure 2 and 3: FTIR spectra of native and modified 10 kDa HA, Zeta potential of HA and modified HA.

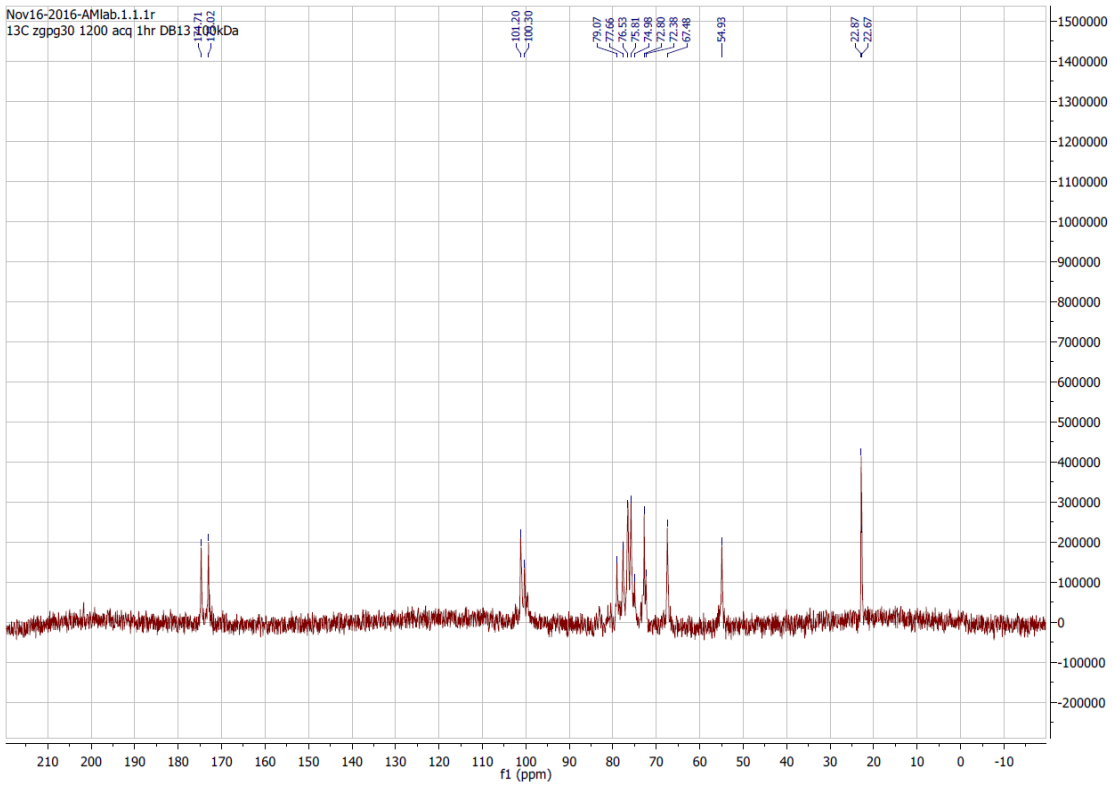

Figure 2a: ^{13}C NMR spectra of sulfated HA (sHA)

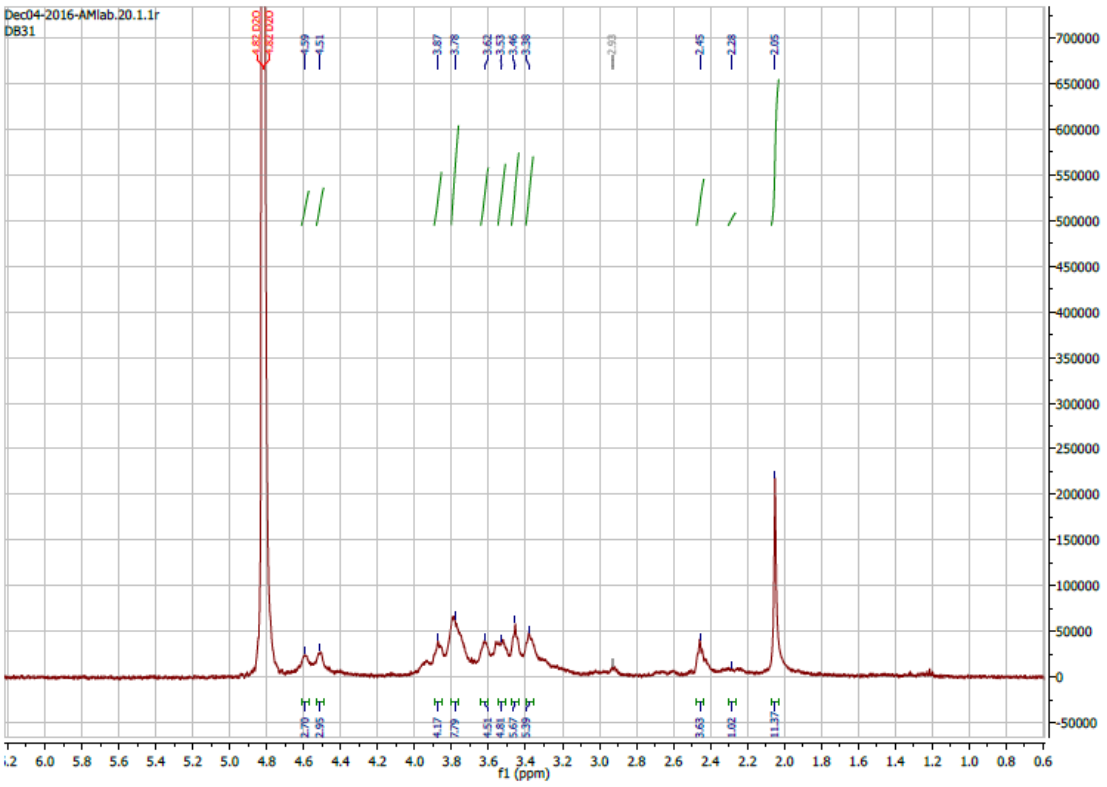

Figure 2b: ^{1}H NMR of sulfated HA

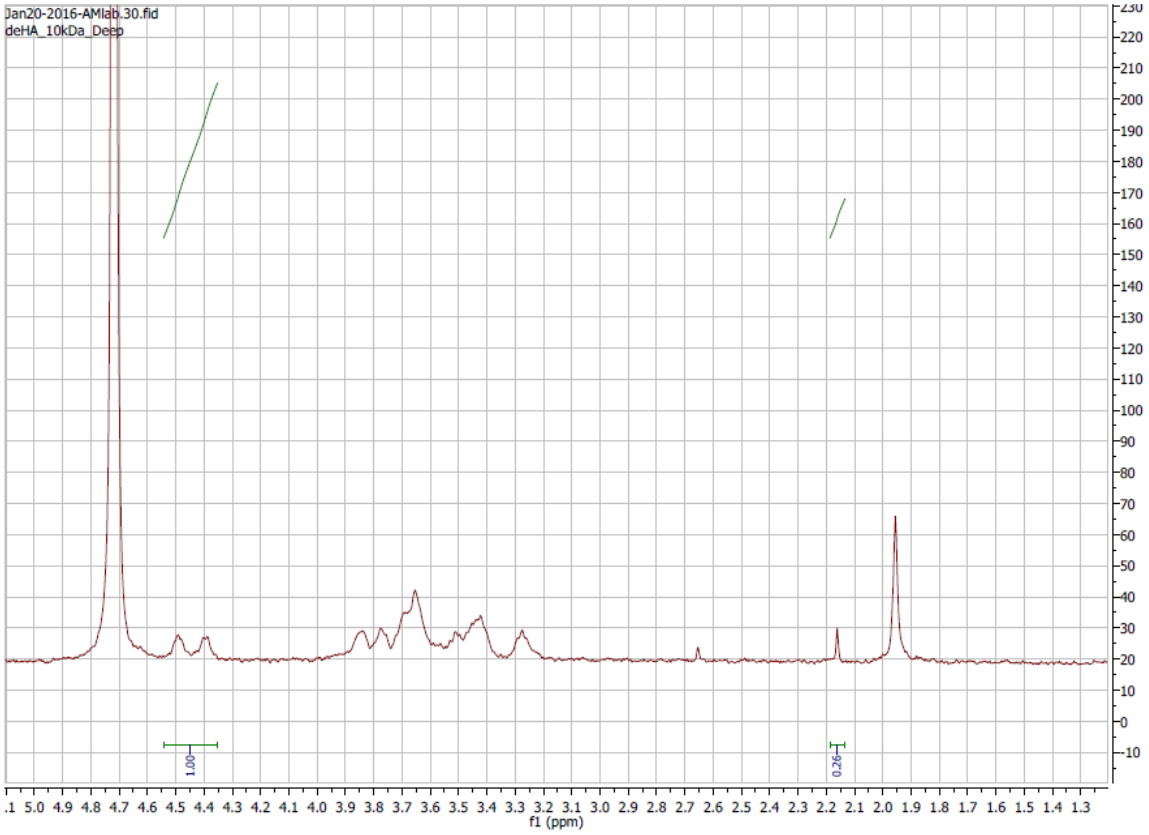

Figure 2d: ^{1}H NMR of deacetylated HA (deHA)

Flow cytometry analysis of binding of modified HA polymers to CD44

The *in vitro* binding affinity of modified hyaluronic acid polymers was studied using CD44-expressing cell lines (PC-3, MDA-MB-231 and RKO) and a CD44-negative cell line (LNCaP). PC-3 prostate, MDA-MB-231 breast, RKO colon cancer cells overexpress CD44 on their surface. The cell lines were first confirmed for CD44 expression using a PE-labelled anti-CD44 antibody. Analysis confirmed that the LNCaP prostate cancer cells did not express the CD44 receptor, while the other cell lines had pronounced CD44 expression (**Figure 4**).

To study the interactions of modified HA with $CD44^+$ and $CD44^-$ cell lines we used an assay based on the concept of competitive binding, where the modified HA polymers were initially pre-incubated with the cells for 1 h to allow their binding to the CD44 receptor on the cell surface. This was followed by incubation with HA-FITC for another 1 h to allow competition of the native ligand with the modified HA for the CD44 receptor. Cell staining was then analyzed using the FITC gate to allow acquisition of FITC fluorescence intensity over 10,000 events. In all $CD44^+$ cell lines, HA-FITC effectively displaced the modified polymers, yielding a higher fluorescence intensity compared to the cells incubated with HA. When the cells were incubated with native unlabeled HA, the displacement by the HA-FITC was not effective compared to the modified HA polymers, indicating that unlabeled HA had a higher binding affinity than modified HA. To confirm the findings, the assay was performed using the $CD44^-$ cell line, LNCaP. Here, the overall fluorescence intensity for all HA derivatives was significantly lower compared to $CD44^+$ cell lines, demonstrating little or no affinity for $CD44^-$ cells.

Results are reported as both fluorescence intensity and fluorescence intensity for the modified HA polymers for individual cell lines (Figure 5). Fluorescence index (FI) values were calculated using the following equation, where MFI is mean fluorescence intensity:

$$MFI = (MFI_{sample} - MFI_{negative\ control})/(MFI_{positive\ control} - MFI_{negative\ control})$$

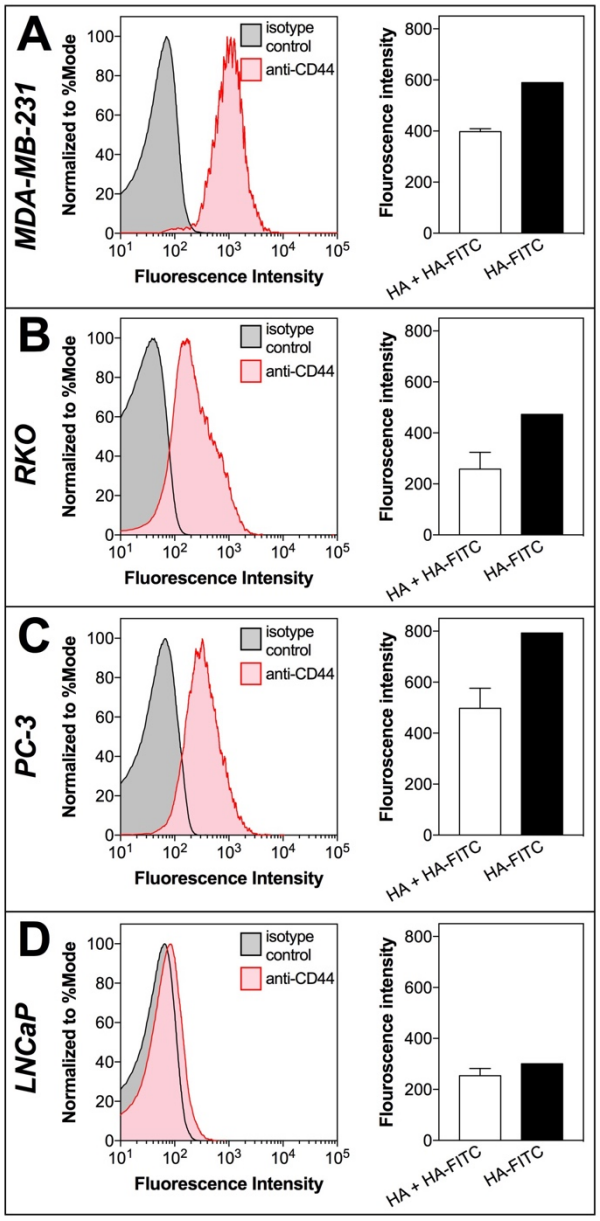

Figure 4. CD44 expression studies. Flow-cytometry histograms showing the expression of CD44 receptor (left plot) and the ability for HA to block HA-FITC binding (right plot) of $CD44^{+}$ (A) MDA-MB-231, (B) RKO, (C) PC-3 and $CD44^{-}$ (D) LNCaP cell lines. HA competitively inhibited HA-FITC binding in $CD44^{+}$ cell lines,

while CD44^{-} cell lines had lower HA-FITC signal and no difference in signal after competition with HA.

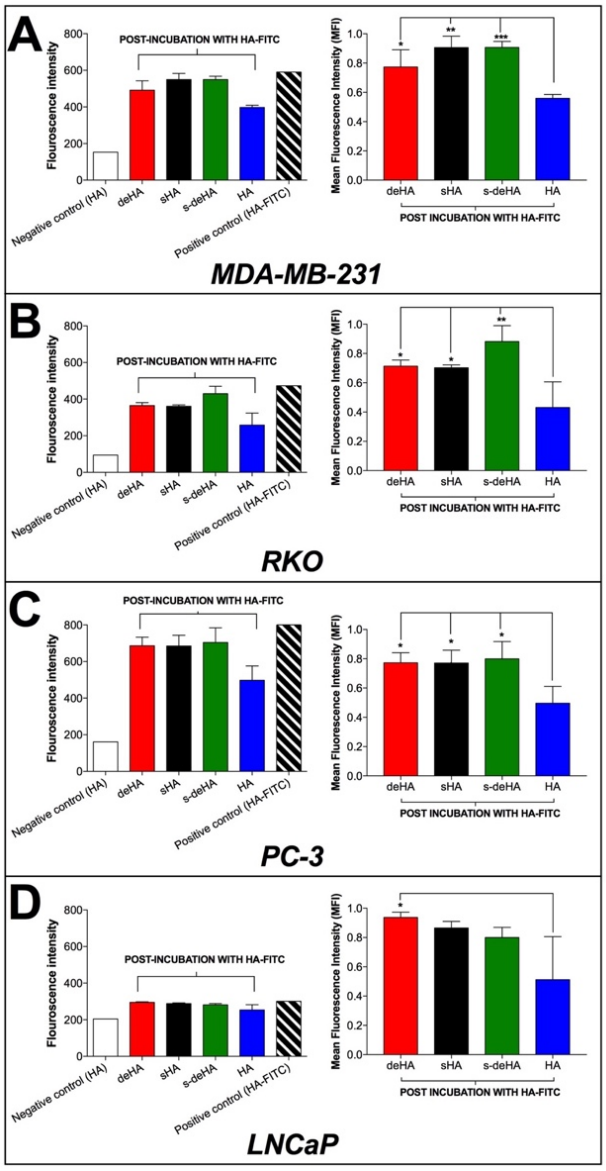

Figure 5. Competition binding assay using flow cytometry analysis. Binding of HA-FITC (20 μg/ml) for 1 hr in the presence of modified HA and native HA determined in (A) MDA-MB-231, (B) RKO, (C) PC-3, and (D) LNCaP cancer cell lines. Negative control comprised of incubation of cells with unlabeled HA while

positive control cells were incubated only with HA-FITC. The left column indicates fluorescence intensities obtained after competition binding of modified HA polymers during flow analysis, while the right column indicates the normalized fluorescence intensities based on the obtained negative and positive fluorescence intensities. Data are shown as mean ± S.D., * $p<0.05$, ** $p<0.01$, *** $p<0.001$; One-way ANOVA with Tukey multiple comparisons test.

Interaction of modified HA polymers with CD44 recombinant protein studied by fluorescence polarization

The interactions between CD44 and modified HA polymers were studied using fluorescence polarization via a competitive binding assay method. Fluorescence polarization (FP) is a powerful technique used to study biomolecular interactions. FP assays require relatively small amounts of expensive reagents as they have been miniaturized to 384 and 1536 well formats. FP values in an assay are dependent on the rotational rate which correlates with the molecular weight of the fluorescent species. A low FP value indicates the presence of unbound fluorescent probe, which rotates rapidly, resulting in depolarization of light, whereas binding of the fluorescent probe to a high molecular weight protein or bio-macromolecule rotates the complex slowly, thereby yielding higher FP values. Fluorescence polarization is usually recorded in mP (millipolarization units). The advantage of using FP is that the protein and the fluorescent probe are not immobilized on the surface, therefore allowing no interference between the probe and the binding site domain of the protein.

The binding affinity of HA for CD44 was determined by titrating HA-FITC probe (50 nM) with CD44 (130 nM - 72 μM) (Figure 6A). A dose-dependent increase in the FP values was observed in HA-CD44 binding while no such effect was observed with fluorescein as a probe, which is indicative of CD44-HA binding. Binding affinity (K_d) of HA-FITC was determined to be 21 μM using nonlinear least square fitting to a single-site binding model. This is consistent with studies reported in literature, where the binding affinity (K_d) of 24.6 μM was determined by isothermal titration calorimetry[16] and SPR.[65,66].

To evaluate the effect of HA modifications on CD44 binding, we conducted a series of competition assays. In each assay, a constant mixture of the HA-FITC and CD44 was titrated with modified HA. The IC50 values of unlabeled modified HA were determined using nonlinear least square fitting to a single-site binding model. The data shows that individual modifications (deacetylation and sulfation) indeed reduce binding to CD44 (Figure 6B). Incorporating both modifications to HA results in reduced binding to CD44 compared to single modifications; specific values could not be obtained as the slopes were very broad for double modified HA. Based on these results we suggest that the secondary amino and sulfo groups on modified HA reduce the affinity of HA for CD44.

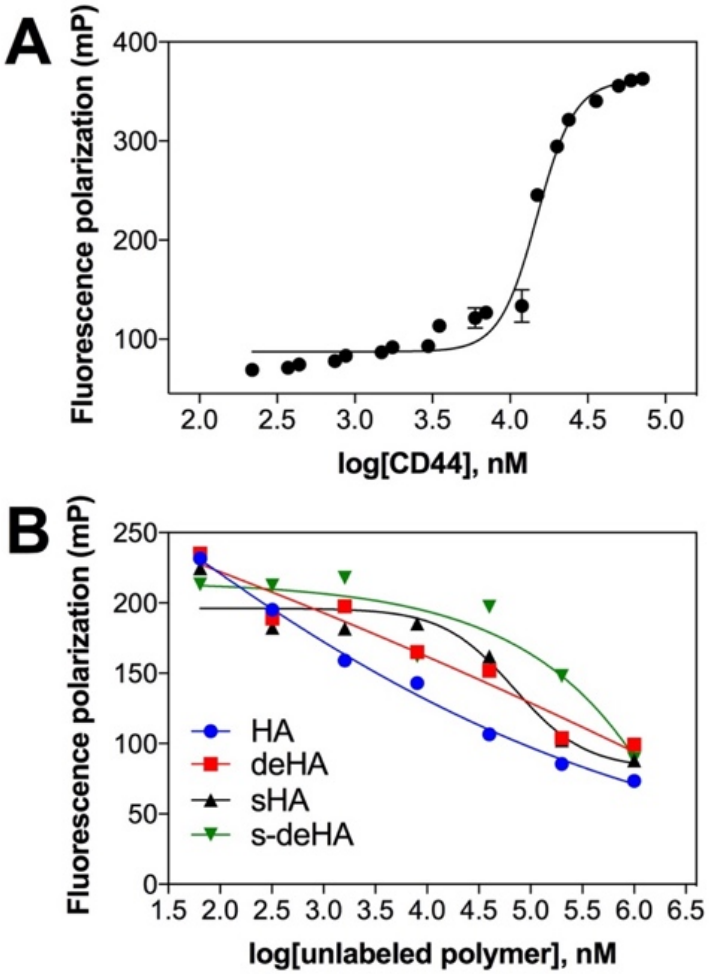

Figure 6: (A) Binding curve isotherm of HA-FITC (50 nM) to CD44-Fc protein (130 nM-72 μM). K_d value obtained for the conjugate = 21 μM. Values are expressed as mean ± s.d of n=3 (B) Effect of increasing concentration of unlabeled derivatives of HA (64nM- 1000μM) and constant CD44 concentration of 23.4 μM competing with pre-incubated HA-FITC (50 nM).

Molecular docking

Docking studies and binding energy calculations were used to predict the recognition of modified HA derivatives to CD44 receptor. Docking was carried out using modified HA derivatives and native HA with CD44 protein. Docking energies were obtained using Swissdock and Autodock docking software packages and compared to observe a trend in decrease of binding energies based on the modifications in the HA structure. The modified HA derivatives, deacetylated and sulphated HA, had lower binding energies of -8.7 kcal/mol and -7.6 kcal/mol, respectively, compared to -13.2 kcal/mol for native HA. This implies that the lower binding energies after the N-acetyl and the C6-OH group were chemically modified caused the differences in docking energies due to repulsive interactions of the amino group interactions and sulfo group. The repulsive interaction hindered locking of the HA structure on the active site of the protein, as indicated in Figure 7 and Table 1, consistent with AutoDock and SwissDock calculations. s-deHA had the lowest binding energy compared to single modifications. This implies that both modifications combined to make interaction with CD44 least favorable. Findings from FP indicate the order of affinity HA > deHA > sHA > s-deHA, whereas from molecular docking study we observe the order of HA > sHA > deHA > s-deHA. Both modifications decrease binding to CD44. It was observed that only one disaccharide unit is responsible for interaction with the active site, as illustrated in Figure 1. The described modifications on the disaccharide were observed to interfere with the major interactions which are key determining factors for HA and CD44 binding. Such

structural changes, being introduced with the same substitution ratio, should have similar effect regardless of the MW of the polymer, as only its small fragment is responsible for the interaction. This provided the rationale of exploring only one lower molecular weight (10 kDa) of hyaluronic acid. In contrast, different substitutions ratios will have different effect on the binding affinity even with the polymer backbone of the same molecular weight. However, an important consideration should be kept in mind that hyaluronic acid belongs to family of natural carbohydrates[67], where controlling the exact molecular weight and chemical substitution ratio is extremely challenging. Even with precise stoichiometric substitution ratio under control, it will be virtually impossible to control such modifications site-by-site. This will lead to the possibility for the less (or completely unmodified) fragments of the polymer to determine the interaction with CD44.

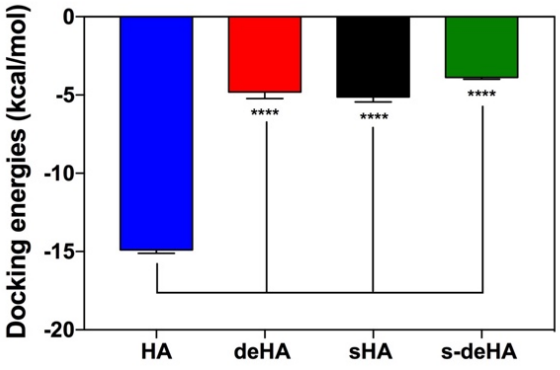

Figure 7. Docking energy calculated by Autodock software of HA and modified HA derivatives with CD44 indicate that each of the modifications had a lower binding energy compared to native HA with CD44. Graphs show mean ± SD (n=10), **** $p < 0.0001$; One-way ANOVA with Tukey multiple comparisons test.

Conclusions

The reported study was focused on evaluating the effects of chemical modifications of hyaluronic acid on its binding affinity to standard CD44 glycoprotein receptor. Chemically modified HA was previously shown to selectively bind various proteins, e.g. TIMP-3, $VEGF_{165a}$, FGF-2, sclerotin, and hBMP-4. Modifying HA structure, which alters CD44 interactions, could also potentially affect other receptors such as RHAMM and TSG-6, since these interactions are exquisitely sensitive to compromising the selectivity by altering the overall chemical structure. However, modifications such as deacetylation and sulfation of HA have not been thoroughly evaluated for their influence on CD44 binding. Here we have described a novel methodology for tuning HA properties to control its binding to CD44. Our *in vitro* and theoretical modeling studies have revealed good correlation of reduced binding with chemical modifications on HA. Future studies will evaluate higher molecular weight HA, since recognition of different molecular weight of HA and downstream activation pathways are different for the polymers of various MW.[68,45,69,70] Further, we will investigate *in vivo* the role of HA modification on overall biodistribution, tumor accumulation, and pharmacokinetic profiles by developing nanosystems based on polymers designed to increase payload of imaging agents/drugs to tumors.

References:

1) Lapcík L Jr and, L.; Lapcík, L.; De Smedt, S.; Demeester, J.; Chabrecek, P. Hyaluronan: Preparation, Structure, Properties, and Applications. Chem. Rev. 1998, 98 (8), 2663–2684.
(2) Toole, B. P. Hyaluronan: from extracellular glue to pericellular cue. Nat. Rev. Cancer 2004, 4 (7), 528–539 DOI: 10.1038/nrc1391.
(3) Toole, B. P. Hyaluronan in morphogenesis. Semin. Cell Dev. Biol. 2001, 12 (2), 79–87 DOI: 10.1006/scdb.2000.0244.
(4) Gotoh, S.; Onaya, J.; Abe, M.; Miyazaki, K.; Hamai, A.; Horie, K.; Tokuyasu, K. Effects of the molecular weight of hyaluronic acid and its action mechanisms on experimental joint pain in rats. Ann. Rheum. Dis. 1993, 52 (11), 817–822.
(5) Geiger, B.; Bershadsky, A.; Pankov, R.; Yamada, K. M. Transmembrane crosstalk between the extracellular matrix--cytoskeleton crosstalk. Nat. Rev. Mol. Cell Biol. 2001, 2 (11), 793–805 DOI: 10.1038/35099066.
(6) Camenisch, T. D.; Spicer, A. P.; Brehm-Gibson, T.; Biesterfeldt, J.; Augustine, M. Lou; Calabro, A.; Kubalak, S.; Klewer, S. E.; McDonald, J. A. Disruption of hyaluronan synthase-2 abrogates normal cardiac morphogenesis and hyaluronan-mediated transformation of epithelium to mesenchyme. J. Clin. Invest. 2000, 106 (3), 349–360 DOI: 10.1172/JCI10272.
(7) Sorokin, L. The impact of the extracellular matrix on inflammation. Nat. Rev. Immunol. 2010, 10 (10), 712–723 DOI: 10.1038/nri2852.
(8) Joyce, J. a; Pollard, J. W. Microenvironmental regulation of metastasis. Nat. Rev. Cancer 2009, 9 (4), 239–252 DOI: 10.1038/nrc2618.
(9) Lennon, F. E.; Singleton, P. a. Hyaluronan regulation of vascular integrity. Am. J. Cardiovasc. Dis. 2011, 1 (3), 200–213.
(10) Ponta, H.; Sherman, L.; Herrlich, P. a. CD44: from adhesion molecules to signalling regulators. Nat. Rev. Mol. Cell Biol. 2003, 4 (1), 33–45 DOI: 10.1038/nrm1004.
(11) Toole, B. P.; Wight, T. N.; Tammi, M. I. Hyaluronan-cell interactions in cancer and vascular disease. Journal of Biological Chemistry. 2002, pp 4593–4596.
(12) Hansson, G. K.; Libby, P. The immune response in atherosclerosis: a double-edged sword. Nat. Rev. Immunol. 2006, 6 (7), 508–519 DOI: 10.1038/nri1882.
(13) Itano, N.; Sawai, T.; Yoshida, M.; Lenas, P.; Yamada, Y.; Imagawa, M.; Shinomura, T.; Hamaguchi, M.; Yoshida, Y.; Ohnuki, Y.; et al. Three isoforms of mammalian hyaluronan synthases have distinct enzymatic properties. J. Biol. Chem. 1999, 274 (35), 25085–25092 DOI: 10.1074/jbc.274.35.25085.
(14) Gallatin, W. M.; Weissman, I. L.; Butcher, E. C. A cell-surface molecule involved in organ-specific homing of lymphocytes. Nature 1983, 304 (5921), 30–34 DOI: 10.1038/304030a0.
(15) Lesley, J.; Hyman, R.; Kincade, P. W. CD44 and its interaction with extracellular matrix. Adv. Immunol. 1993, 54 (Section V), 271–335.

(16) Peach, R. J.; Hollenbaugh, D.; Stamenkovic, I.; Aruffo, a. Identification of hyaluronic acid binding sites in the extracellular domain of CD44. J. Cell Biol. 1993, 122 (1), 257–264 DOI: 10.1083/jcb.122.1.257.
(17) Banerji, S.; Wright, A. J.; Noble, M.; Mahoney, D. J.; Campbell, I. D.; Day, A. J.; Jackson, D. G. Structures of the Cd44-hyaluronan complex provide insight into a fundamental carbohydrate-protein interaction. Nat. Struct. Mol. Biol. 2007, 14 (3), 234–239 DOI: 10.1038/nsmb1201.
(18) Nagano, O.; Okazaki, S.; Saya, H. Redox regulation in stem-like cancer cells by CD44 variant isoforms. Oncogene 2013, 32 (44), 5191–5198 DOI: 10.1038/onc.2012.638.
(19) Lesley, J.; Hascall, V. C.; Tammi, M.; Hyman, R. Hyaluronan binding by cell surface CD44. J. Biol. Chem. 2000, 275 (35), 26967–26975 DOI: 10.1074/jbc.M002527200.
(20) Misra, S.; Heldin, P.; Hascall, V. C.; Karamanos, N. K.; Skandalis, S. S.; Markwald, R. R.; Ghatak, S. Hyaluronan-CD44 interactions as potential targets for cancer therapy. FEBS J. 2011, 278 (9), 1429–1443 DOI: 10.1111/j.1742-4658.2011.08071.x.
(21) Misra, S.; Ghatak, S.; Zoltan-Jones, A.; Toole, B. P. Regulation of multidrug resistance in cancer cells by hyaluronan. J. Biol. Chem. 2003, 278 (28), 25285–25288 DOI: 10.1074/jbc.C300173200.
(22) He, Q.; Lesley, J.; Hyman, R.; Ishihara, K.; Kincade, P. W. Molecular isoforms of murine CD44 and evidence that the membrane proximal domain is not critical for hyaluronate recognition. J. Cell Biol. 1992, 119 (6), 1711–1720 DOI: (1) Lapcík L Jr and, L.; Lapcík, L.; De Smedt, S.; Demeester, J.; Chabrecek, P. Hyaluronan: Preparation, Structure, Properties, and Applications. Chem. Rev. 1998, 98 (8), 2663–2684.
(2) Toole, B. P. Hyaluronan: from extracellular glue to pericellular cue. Nat. Rev. Cancer 2004, 4 (7), 528–539 DOI: 10.1038/nrc1391.
(3) Toole, B. P. Hyaluronan in morphogenesis. Semin. Cell Dev. Biol. 2001, 12 (2), 79–87 DOI: 10.1006/scdb.2000.0244.
(4) Gotoh, S.; Onaya, J.; Abe, M.; Miyazaki, K.; Hamai, A.; Horie, K.; Tokuyasu, K. Effects of the molecular weight of hyaluronic acid and its action mechanisms on experimental joint pain in rats. Ann. Rheum. Dis. 1993, 52 (11), 817–822.
(5) Geiger, B.; Bershadsky, A.; Pankov, R.; Yamada, K. M. Transmembrane crosstalk between the extracellular matrix--cytoskeleton crosstalk. Nat. Rev. Mol. Cell Biol. 2001, 2 (11), 793–805 DOI: 10.1038/35099066.
(6) Camenisch, T. D.; Spicer, A. P.; Brehm-Gibson, T.; Biesterfeldt, J.; Augustine, M. Lou; Calabro, A.; Kubalak, S.; Klewer, S. E.; McDonald, J. A. Disruption of hyaluronan synthase-2 abrogates normal cardiac morphogenesis and hyaluronan-mediated transformation of epithelium to mesenchyme. J. Clin. Invest. 2000, 106 (3), 349–360 DOI: 10.1172/JCI10272.
(7) Sorokin, L. The impact of the extracellular matrix on inflammation. Nat. Rev. Immunol. 2010, 10 (10), 712–723 DOI: 10.1038/nri2852.
(8) Joyce, J. a; Pollard, J. W. Microenvironmental regulation of metastasis. Nat. Rev. Cancer 2009, 9 (4), 239–252 DOI: 10.1038/nrc2618.

(9) Lennon, F. E.; Singleton, P. a. Hyaluronan regulation of vascular integrity. Am. J. Cardiovasc. Dis. 2011, 1 (3), 200–213.
(10) Ponta, H.; Sherman, L.; Herrlich, P. a. CD44: from adhesion molecules to signalling regulators. Nat. Rev. Mol. Cell Biol. 2003, 4 (1), 33–45 DOI: 10.1038/nrm1004.
(11) Toole, B. P.; Wight, T. N.; Tammi, M. I. Hyaluronan-cell interactions in cancer and vascular disease. Journal of Biological Chemistry. 2002, pp 4593–4596.
(12) Hansson, G. K.; Libby, P. The immune response in atherosclerosis: a double-edged sword. Nat. Rev. Immunol. 2006, 6 (7), 508–519 DOI: 10.1038/nri1882.
(13) Itano, N.; Sawai, T.; Yoshida, M.; Lenas, P.; Yamada, Y.; Imagawa, M.; Shinomura, T.; Hamaguchi, M.; Yoshida, Y.; Ohnuki, Y.; et al. Three isoforms of mammalian hyaluronan synthases have distinct enzymatic properties. J. Biol. Chem. 1999, 274 (35), 25085–25092 DOI: 10.1074/jbc.274.35.25085.
(14) Gallatin, W. M.; Weissman, I. L.; Butcher, E. C. A cell-surface molecule involved in organ-specific homing of lymphocytes. Nature 1983, 304 (5921), 30–34 DOI: 10.1038/304030a0.
(15) Lesley, J.; Hyman, R.; Kincade, P. W. CD44 and its interaction with extracellular matrix. Adv. Immunol. 1993, 54 (Section V), 271–335.
(16) Peach, R. J.; Hollenbaugh, D.; Stamenkovic, I.; Aruffo, a. Identification of hyaluronic acid binding sites in the extracellular domain of CD44. J. Cell Biol. 1993, 122 (1), 257–264 DOI: 10.1083/jcb.122.1.257.
(17) Banerji, S.; Wright, A. J.; Noble, M.; Mahoney, D. J.; Campbell, I. D.; Day, A. J.; Jackson, D. G. Structures of the Cd44-hyaluronan complex provide insight into a fundamental carbohydrate-protein interaction. Nat. Struct. Mol. Biol. 2007, 14 (3), 234–239 DOI: 10.1038/nsmb1201.
(18) Nagano, O.; Okazaki, S.; Saya, H. Redox regulation in stem-like cancer cells by CD44 variant isoforms. Oncogene 2013, 32 (44), 5191–5198 DOI: 10.1038/onc.2012.638.
(19) Lesley, J.; Hascall, V. C.; Tammi, M.; Hyman, R. Hyaluronan binding by cell surface CD44. J. Biol. Chem. 2000, 275 (35), 26967–26975 DOI: 10.1074/jbc.M002527200.
(20) Misra, S.; Heldin, P.; Hascall, V. C.; Karamanos, N. K.; Skandalis, S. S.; Markwald, R. R.; Ghatak, S. Hyaluronan-CD44 interactions as potential targets for cancer therapy. FEBS J. 2011, 278 (9), 1429–1443 DOI: 10.1111/j.1742-4658.2011.08071.x.
(21) Misra, S.; Ghatak, S.; Zoltan-Jones, A.; Toole, B. P. Regulation of multidrug resistance in cancer cells by hyaluronan. J. Biol. Chem. 2003, 278 (28), 25285–25288 DOI: 10.1074/jbc.C300173200.
(22) He, Q.; Lesley, J.; Hyman, R.; Ishihara, K.; Kincade, P. W. Molecular isoforms of murine CD44 and evidence that the membrane proximal domain is not critical for hyaluronate recognition. J. Cell Biol. 1992, 119 (6), 1711–1720 DOI: 10.1083/jcb.119.6.1711.
(23) Sleeman, J.; Rudy, W.; Hofmann, M.; Moll, J.; Herrlich, P.; Ponta, H. Regulated clustering of variant CD44 proteins increases their hyaluronate binding

capacity. J. Cell Biol. 1996, 135 (4), 1139–1150 DOI: DOI 10.1083/jcb.135.4.1139.
(24) Wielenga, V. J.; Heider, K. H.; Offerhaus, G. J.; Adolf, G. R.; van den Berg, F. M.; Ponta, H.; Herrlich, P.; Pals, S. T. Expression of CD44 variant proteins in human colorectal cancer is related to tumor progression. Cancer Res 1993, 53 (20), 4754–4756.
(25) Marangoni, E.; Lecomte, N.; Durand, L.; de Pinieux, G.; Decaudin, D.; Chomienne, C.; Smadja-Joffe, F.; Poupon, M.-F. CD44 targeting reduces tumour growth and prevents post-chemotherapy relapse of human breast cancers xenografts. Br. J. Cancer 2009, 100 (6), 918–922 DOI: 10.1038/sj.bjc.6604953.
(26) Wang, S. J.; Wreesmann, V. B.; Bourguignon, L. Y. Association of CD44 V3-containing isoforms with tumor cell growth, migration, matrix metalloproteinase expression, and lymph node metastasis in head and neck cancer. Head Neck 2007, 29 (6), 550–558 DOI: 10.1002/hed.20544.
(27) Günthert, U.; Hofmann, M.; Rudy, W.; Reber, S.; Zöller, M.; Hauβmann, I.; Matzku, S.; Wenzel, A.; Ponta, H.; Herrlich, P. A new variant of glycoprotein CD44 confers metastatic potential to rat carcinoma cells. Cell 1991, 65 (1), 13–24 DOI: 10.1016/0092-8674(91)90403-L.
(28) Naor, D.; Vogt Sionov, R.; Zahalka, M.; Rochman, M.; Holzmann, B.; Ish-Shalom, D. Organ-Specific Requirements for Cell Adhesion Molecules During Lymphoma Cell Dissemination; Springer Berlin Heidelberg, 1998; pp 143–166.
(29) Ochiai, S.; Nakanishi, Y.; Mizuno, K.; Hashimoto, S.; Inutsuka, S.; Kawasaki, M.; Yatsunami, J.; Hara, N. [Expression of CD44 standard and CD44 variant 6 in human lung cancer]. Nihon Kyobu Shikkan Gakkai Zasshi 1997, 35 (11), 1179–1185.
(30) Kurozumi, K.; Nishida, T.; Nakao, K.; Nakahara, M.; Tsujimoto, M. Expression of CD44 variant 6 and lymphatic invasion: Importance to lymph node metastasis in gastric cancer. In World Journal of Surgery; 1998; Vol. 22, pp 853–858.
(31) Foekens, J. a; Dall, P.; Klijn, J. G.; Skroch-Angel, P.; Claassen, C. J.; Look, M. P.; Ponta, H.; Van Putten, W. L.; Herrlich, P.; Henzen-Logmans, S. C. Prognostic value of CD44 variant expression in primary breast cancer. Int. J. Cancer 1999, 84 (3), 209–215 DOI: 10.1002/(SICI)1097-0215(19990621)84:3<209::AID-IJC2>3.0.CO;2-9.
(32) Ayhan, a; Tok, E. C.; Bildirici, I.; Ayhan, a. Overexpression of CD44 variant 6 in human endometrial cancer and its prognostic significance. Gynecol. Oncol. 2001, 80 (3), 355–358 DOI: 10.1006/gyno.2000.6014.
(33) Ishida, T. Immunohistochemical expression of the CD44 variant 6 in colorectal adenocarcinoma. Surg. Today 2000, 30 (1), 28–32.
(34) Misra, S.; Hascall, V. C.; Markwald, R. R.; Ghatak, S. Interactions between hyaluronan and its receptors (CD44, RHAMM) regulate the activities of inflammation and cancer. Frontiers in Immunology. 2015.
(35) Mahoney, D. J.; Blundell, C. D.; Day, A. J. Mapping the Hyaluronan-binding Site on the Link Module from Human Tumor Necrosis Factor-stimulated Gene-6 by Site-directed Mutagenesis. J. Biol. Chem. 2001, 276 (25), 22764–22771 DOI: 10.1074/jbc.M100666200.

(36) Bourguignon, L. Y. W.; Zhu, H.; Chu, A.; Iida, N.; Zhang, L.; Hung, M. C. Interaction between the adhesion receptor, CD44, and the oncogene product, p185(HER2), promotes human ovarian tumor cell activation. J. Biol. Chem. 1997, 272 (44), 27913–27918 DOI: 10.1074/jbc.272.44.27913.
(37) Ghatak, S.; Misra, S.; Toole, B. P. Hyaluronan constitutively regulates ErbB2 phosphorylation and signaling complex formation in carcinoma cells. J. Biol. Chem. 2005, 280 (10), 8875–8883 DOI: 10.1074/jbc.M410882200.
(38) Teriete, P.; Banerji, S.; Noble, M.; Blundell, C. D.; Wright, A. J.; Pickford, A. R.; Lowe, E.; Mahoney, D. J.; Tammi, M. I.; Kahmann, J. D.; et al. Structure of the regulatory hyaluronan binding domain in the inflammatory leukocyte homing receptor CD44. Mol. Cell 2004, 13 (4), 483–496 DOI: 10.1016/S1097-2765(04)00080-2.
(39) Li, L.; Heldin, C. H.; Heldin, P. Inhibition of platelet-derived growth factor-BB-induced receptor activation and fibroblast migration by hyaluronan activation of CD44. J. Biol. Chem. 2006, 281 (36), 26512–26519 DOI: 10.1074/jbc.M605607200.
(40) Yu, Q.; Stamenkovic, I. Localization of matrix metalloproteinase 9 to the cell surface provides a mechanism for CD44-mediated tumor invasion. Genes Dev. 1999, 13 (1), 35–48 DOI: 10.1101/gad.13.1.35.
(41) Bourguignon, L. Y. W.; Peyrollier, K.; Xia, W.; Gilad, E. Hyaluronan-CD44 interaction activates stem cell marker Nanog, Stat-3-mediated MDR1 gene expression, and ankyrin-regulated multidrug efflux in breast and ovarian tumor cells. J. Biol. Chem. 2008, 283 (25), 17635–17651 DOI: 10.1074/jbc.M800109200.
(42) Ohashi, R.; Takahashi, F.; Cui, R.; Yoshioka, M.; Gu, T.; Sasaki, S.; Tominaga, S.; Nishio, K.; Tanabe, K. K.; Takahashi, K. Interaction between CD44 and hyaluronate induces chemoresistance in non-small cell lung cancer cell. Cancer Lett. 2007, 252 (2), 225–234 DOI: 10.1016/j.canlet.2006.12.025.
(43) Shigeishi, H.; Biddle, A.; Gammon, L.; Emich, H.; Rodini, C. O.; Gemenetzidis, E.; Fazil, B.; Sugiyama, M.; Kamata, N.; MaCkenzie, I. C. Maintenance of stem cell self-renewal in head and neck cancers requires actions of GSK3b influenced by CD44 and RHAMM. Stem Cells 2013, 31 (10), 2073–2083 DOI: 10.1002/stem.1418.
(44) Li, L.; Qi, L.; Liang, Z.; Song, W.; Liu, Y.; Wang, Y.; Sun, B.; Zhang, B.; Cao, W. Transforming growth factor-β1 induces EMT by the transactivation of epidermal growth factor signaling through HA/CD44 in lung and breast cancer cells. Int. J. Mol. Med. 2015 DOI: 10.3892/ijmm.2015.2222.
(45) Cyphert, J. M.; Trempus, C. S.; Garantziotis, S. Size Matters: Molecular Weight Specificity of Hyaluronan Effects in Cell Biology. International Journal of Cell Biology. 2015.
(46) Lim, D.-K.; Wylie, R. G.; Langer, R.; Kohane, D. S. Selective binding of C-6 OH sulfated hyaluronic acid to the angiogenic isoform of VEGF165. Biomaterials 2016, 77, 130–138 DOI: 10.1016/j.biomaterials.2015.10.074.
(47) Salbach-Hirsch, J.; Samsonov, S. A.; Hintze, V.; Hofbauer, C.; Picke, A.-K.; Rauner, M.; Gehrcke, J.-P.; Moeller, S.; Schnabelrauch, M.; Scharnweber, D.; et al. Structural and functional insights into sclerostin-glycosaminoglycan

interactions in bone. Biomaterials 2015, 67, 335–345 DOI: 10.1016/j.biomaterials.2015.07.021.
(48) Hintze, V.; Miron, A.; Moeller, S.; Schnabelrauch, M.; Wiesmann, H. P.; Worch, H.; Scharnweber, D. Sulfated hyaluronan and chondroitin sulfate derivatives interact differently with human transforming growth factor-??1 (TGF-??1). Acta Biomater. 2012, 8 (6), 2144–2152 DOI: 10.1016/j.actbio.2012.03.021.
(49) Hill, T. K.; Kelkar, S. S.; Wojtynek, N. E.; Souchek, J. J.; Payne, W. M.; Stumpf, K.; Marini, F. C.; Mohs, A. M. Near infrared fluorescent nanoparticles derived from hyaluronic acid improve tumor contrast for image-guided surgery. Theranostics 2016, 6 (13), 2314–2328 DOI: 10.7150/thno.16514.
(50) Kelkar, S. S.; Hill, T. K.; Marini, F. C.; Mohs, A. M. Near infrared fluorescent nanoparticles based on hyaluronic acid: Self-assembly, optical properties, and cell interaction. Acta Biomater. 2016, 36, 112–121 DOI: 10.1016/j.actbio.2016.03.024.
(51) Hill, T. K.; Abdulahad, A.; Kelkar, S. S.; Marini, F. C.; Long, T. E.; Provenzale, J. M.; Mohs, A. M. Indocyanine green-loaded nanoparticles for image-guided tumor surgery. Bioconjug. Chem. 2015, 26 (2), 294–303 DOI: 10.1021/bc5005679.
(52) Kennel, S. J.; Lankford, T. K.; Foote, L. J.; Shinpock, S. G.; Stringer, C. CD44 expression on murine tissues. J. Cell Sci. 1993, 104 (Pt 2 (1993), 373–382.
(53) Lin, T.; Yuan, A.; Zhao, X.; Lian, H.; Zhuang, J.; Chen, W.; Zhang, Q.; Liu, G.; Zhang, S.; Chen, W.; et al. Self-assembled tumor-targeting hyaluronic acid nanoparticles for photothermal ablation in orthotopic bladder cancer. Acta Biomater. 2017, 53, 427–438 DOI: 10.1016/j.actbio.2017.02.021.
(54) Wang, X.; Gu, X.; Wang, H.; Sun, Y.; Wu, H.; Mao, S. Synthesis, characterization and liver targeting evaluation of self-assembled hyaluronic acid nanoparticles functionalized with glycyrrhetinic acid. Eur. J. Pharm. Sci. 2017, 96, 255–262 DOI: 10.1016/j.ejps.2016.09.036.
(55) Becher, J.; Möller, S.; Riemer, T.; Schiller, J.; Hintze, V.; Bierbaum, S.; Scharnweber, D.; Worch, H.; Schnabelrauch, M. Sulfated Glycosaminoglycan Building Blocks for the Design of Artificial Extracellular Matrices; 2012; pp 315–328.
(56) Plazinski, W.; Knys-Dzieciuch, A.; Milas, M.; Rinaudo, M.; Pérez, S.; Imberty, A.; Cañada, F. J.; Parrilli, M.; Jiménez-Barbero, J.; Castro, C. De; et al. Interactions between CD44 protein and hyaluronan: insights from the computational study. Mol. BioSyst. 2012, 8 (2), 543–547 DOI: 10.1039/C2MB05399C.
(57) Morris, G.; Huey, R. AutoDock4 and AutoDockTools4: Automated docking with selective receptor flexibility. J. … 2009, 30 (16), 2785–2791 DOI: 10.1002/jcc.21256.AutoDock4.
(58) Trott, O.; Olson, A. J. Software news and update AutoDock Vina: Improving the speed and accuracy of docking with a new scoring function, efficient optimization, and multithreading. J. Comput. Chem. 2010, 31 (2), 455–461 DOI: 10.1002/jcc.21334.

(59) Grosdidier, A.; Zoete, V.; Michielin, O. SwissDock, a protein-small molecule docking web service based on EADock DSS. Nucleic Acids Res. 2011, 39 (SUPPL. 2) DOI: 10.1093/nar/gkr366.
(60) Grosdidier, A.; Zoete, V.; Michielin, O. Fast docking using the CHARMM force field with EADock DSS. J. Comput. Chem. 2011, 32 (10), 2149–2159 DOI: 10.1002/jcc.21797.
(61) Pettersen, E. F.; Goddard, T. D.; Huang, C. C.; Couch, G. S.; Greenblatt, D. M.; Meng, E. C.; Ferrin, T. E. UCSF Chimera--a visualization system for exploratory research and analysis. J. Comput. Chem. 2004, 25 (13), 1605–1612 DOI: 10.1002/jcc.20084.

(62) Babasola, O.; Rees-Milton, K. J.; Bebe, S.; Wang, J.; Anastassiades, T. P. Chemically modified N-acylated hyaluronan fragments modulate proinflammatory cytokine production by stimulated human macrophages. J. Biol. Chem. 2014, 289 (36), 24779–24791 DOI: 10.1074/jbc.M113.515783.
(63) Crescenzi, V.; Francescangeli, A.; Renier, D.; Bellini, D. New cross-linked and sulfated derivatives of partially deacetylated hyaluronan: Synthesis and preliminary characterization. Biopolymers 2002, 64 (2), 86–94 DOI: 10.1002/bip.10131.
(64) Tan, S. C.; Khor, E.; Tan, T. K.; Wong, S. M. The degree of deacetylation of chitosan: advocating the first derivative UV-spectrophotometry method of determination. Talanta 1998, 45 (4), 713–719 DOI: 10.1016/S0039-9140(97)00288-9.
(65) Liu, L. K.; Finzel, B. C. Fragment-based identification of an inducible binding site on cell surface receptor CD44 for the design of protein-carbohydrate interaction inhibitors. J. Med. Chem. 2014, 57 (6), 2714–2725 DOI: 10.1021/jm5000276.
(66) Ogino, S.; Nishida, N.; Umemoto, R.; Suzuki, M.; Takeda, M.; Terasawa, H.; Kitayama, J.; Matsumoto, M.; Hayasaka, H.; Miyasaka, M.; et al. Two-state conformations in the hyaluronan-binding domain regulate CD44 adhesiveness under flow condition. Structure 2010, 18 (5), 649–656 DOI: 10.1016/j.str.2010.02.010.
(67) Kogan, G.; Šoltés, L.; Stern, R.; Gemeiner, P. Hyaluronic acid: A natural biopolymer with a broad range of biomedical and industrial applications. Biotechnology Letters. 2007, pp 17–25.
(68) Wolny, P. M.; Banerji, S.; Gounou, C.; Brisson, A. R.; Day, A. J.; Jackson, D. G.; Richter, R. P. Analysis of CD44-hyaluronan interactions in an artificial membrane system: Insights into the distinct binding properties of high and low molecular weight hyaluronan. J. Biol. Chem. 2010, 285 (39), 30170–30180 DOI: 10.1074/jbc.M110.137562.
(69) Yang, C.; Cao, M.; Liu, H.; He, Y.; Xu, J.; Du, Y.; Liu, Y.; Wang, W.; Cui, L.; Hu, J.; et al. The high and low molecular weight forms of hyaluronan have distinct effects on CD44 clustering. J. Biol. Chem. 2012, 287 (51), 43094–43107 DOI: 10.1074/jbc.M112.349209.

(70) Maharjan, A. S.; Pilling, D.; Gomer, R. H. High and low molecular weight hyaluronic acid differentially regulate human fibrocyte differentiation. PLoS One 2011, 6 (10) DOI: 10.1371/journal.pone.0026078.

CHAPTER III:

MODULATING TARGETING PROPERTIES OF HYALURONIC ACID FOR DELIVERY OF IMAGING AGENTS TO TUMOR MICROENVIRONMENT

Abstract

Many targeting strategies can be employed to direct nanoparticles to tumors for imaging and therapy. However, tumors display a dynamic, heterogeneous microenvironment that undergoes spatiotemporal changes, including the expression of targetable cell-surface biomarkers. Here, we develop a nanoparticle system to effectively target two receptors overexpressed in the microenvironment of aggressive tumors. Hyaluronic acid (HA) was regioselectively modified using multi-step synthetic approach to alter binding specificities for CD44 and P-selectin for improving targetability. The dual-targeting strategy utilizes sulfate modifications that target P-selectin, in addition to native targeting of CD44, which exploits spatiotemporal alterations in the expression patterns of these two receptors in cancer sites. Using biophysical characterization, e.g. fluorescence polarization; *in vitro* evaluation by CRISPR/Cas9 system and flow cytometry binding studies; and *in vivo* infrared imaging, we demonstrate that modified HA nanoparticles effectively target tumors, offering higher specificity over conventional HA strategies. The uptake of sulfated HA nanoparticles is higher compared to non-sulfated HANPs as assessed using fluorescence image-guided surgery and whole-animal imaging systems.

Keywords: hyaluronic acid, P-selectin, CD44, re-targeting, image-guided surgery

Introduction

Targeted delivery systems are devised to provide safe, efficacious, and focused delivery of therapeutic agents or imaging probes at intended sites[1]. Common delivery systems include multi-lamellar liposomes[2], dendrimers[3], quantum dots[4], polymer dots[5,6], carbon dots[7], antibody-drug conjugates[8], protein conjugates[9], nanoparticles, and others delivery modalities. Each of the delivery systems has its unique ability which can be exploited for delivery of drugs/imaging agents. Designing an appropriate delivery system is contingent on the diverse properties such as binding affinities, shape, size, physiochemical and photophysical characteristics, uptake, stability, corona forming proteins, biodistribution, and pharmacokinetics[10,11,12,13]. These parameters primarily govern the biological fate of delivery systems depending on the chemical charge tunability, surface charge for cell uptake, cellular internalization, and cellular protein targetability. Therefore, no delivery system is perfect for fulfilling all targeting goals, but with rational approach targeting properties of a carrier can be modulated.

The clinical potential of nanomedicine is currently being exploited in terms of targeting of various cancer types for positive therapeutic outcome[14]. Usually, nanoparticles passively target the tumor microenvironment by enhanced permeation retention (EPR) effect[15]. Targeting strategies for nanoparticles have

been improved by adoption of active targeting by conjugating peptides[16], small molecules, or antibodies[17] that target specific cell surface markers that are overexpressed on cancer cells compared to normal healthy tissues. However, the tumor microenvironment presents a heterogeneous and dynamic population of multiple targetable cell-surface proteins that are over-expressed, such as, CD44[18], P-selectin[19], amino acid transporters[20], folate binding proteins[21], EGF, HER2, integrins, CXCR4, FGF, Tetraspanins, Bombesin[22].

In this work, we investigate a novel strategy of targeting two upregulated cell surface markers (CD44 and P-selectin) by regio-selective chemical modifications on hyaluronic acid. P-selectin, which is an inflammatory cell adhesion protein, is responsible for recruiting leukocytes to inflamed/infectious sites by binding to P-selectin glycoprotein-1 (PSGL-1) allowing adhesion and extravasation[23]. Cancer cells take advantage of this machinery to evade recognition by the macrophages[24] by expressing P-selectin on the surface which is induced by the harsh tumor microenvironment (endogenous cytokines, external stimuli, exposure to thrombin, and oxygen free radicals). Previously, high P-selectin expression was reported in breast, pancreatic, liver, ovarian, and lung cancers[19]. It was used as a possible target for delivery of mitogen-activated kinase protein kinase inhibitor using fucosylated nanoparticles specific to P-selectin[19]. Mizrachi et al.[25] exploited P-selectin as a target to deliver tumor-specific PI3K inhibitors via fucoidan nanoparticles to head and neck cancer tumor model. Additional reports have discussed delivering paclitaxel via dendritic polyglycerol sulfate to P-selective positive glioblastoma cells[26].

Active targeting has been widely implemented to increase cellular internalization of delivery systems for improving therapeutic/diagnostic effects[27]. CD44 and P-selectin have demonstrated increased expression in breast, pancreatic, liver, ovarian, lung cancers. In addition, poor patient survival has been reported with tumors co-expressing both receptor families[28] demonstrating the need for dual-targeted design of nanosystems. Further development of dual targeting was addressed using a DPPC cholesterol liposomal nanoparticle specific towards P-selectin and $\alpha_v\beta_3$ integrins for detection of breast cancer metastasis[29]. This suggested that P-selectin is a target with strong potential for cancer therapy.

Previously, we reported modifications of several functional groups of hyaluronic acid by deacetylation and sulfation, which resulted in a decrease, but not abolishment of CD44 binding[30]. Based on the findings that sulfation is an essential modification on hyaluronic acid, we hypothesized that modulating sulfation patterns on hyaluronic acid might potentially influence binding to both P-selectin and CD44. This may be used for applications in near-infrared image-guided surgery to improve tumor detection and surgical resection. In this study, we harnessed the targeting potential of sulfated HA towards P-selectin and CD44 in a proof-of-concept model using a pancreatic cancer cell line.

Graphical abstract

Illustration of the targeting recognition by modulated hyaluronic acid nanoparticle targeting to both CD44 and P-selectin via dual-delivery of imaging agents for image-guided surgery.

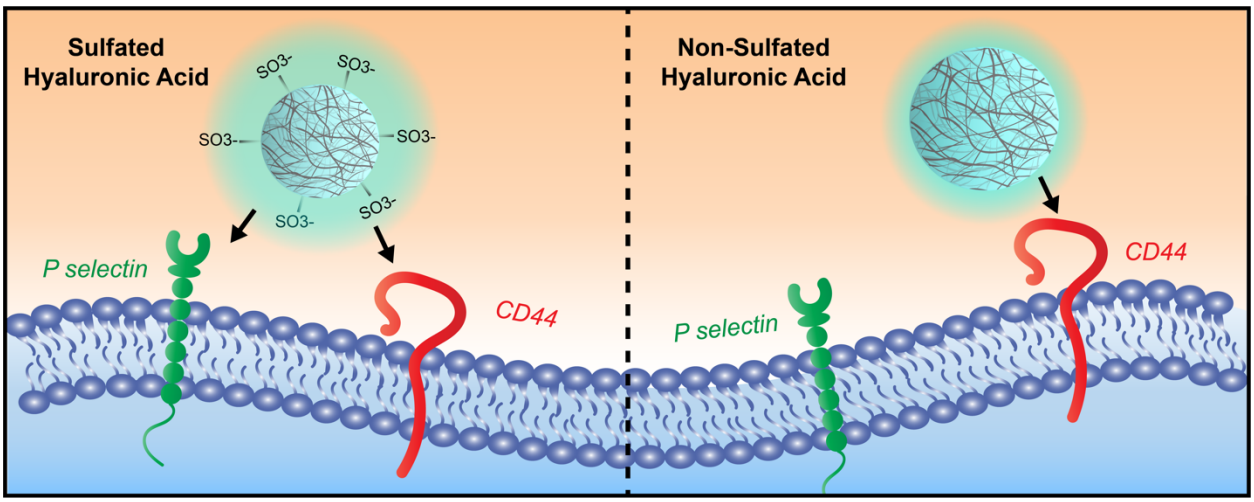

2. Material and Methods

Sodium hyaluronate, 10 and 100 kDa, was purchased from Lifecore Biomedical (Chaska, MN). All water was purified with Barnsteadt Nanopure Diamond system (Thermo Scientific, Waltham, MN). Tetrabutylammonium (TBA) hydroxide, DOWEX 50WX8-400 ion exchange resin, sulfur trioxide pyridine complex (SO_3-pyridine 98%), N-(3- dimethylaminopropyl)-N-ethylcarbodiimide hydrochloride (EDC), N-hydroxysuccinimide (NHS), fetal bovine serum (FBS), and 1-pyrenebutyric acid were purchased from Sigma-Aldrich (St. Louis. MO). Cy7.5-amine was obtained from Lumiprobe Corporation (Hallandale Beach, FL). IRDye® 800CW amine was purchased from LI-COR Biosciences (Lincoln, NE). Desalting PD10 columns, dialysis membranes (3,500 MWCO and 6,000–8,000 MWCO), Nunc™ Glass Bottom Dishes (12 mm), Nunc Lab-Tek II Chamber Slide System were purchased from GE healthcare and Fisher Scientific, respectively. Cell counting kit-8 (CCK-8) was purchased from Dojindo Molecular Technologies Inc. (Rockville, MD). Ethanol was purchased from the Warner-Graham Company (Cockeysville, MD). Recombinant human P-selectin/CD62P (Catalog# ADP3-050) and human CD62P P-selectin antibody (Catalog# AF137) was obtained from R&D systems. Lower molecular weight fucoidan powder produced from brown seaweed extract was obtained from Hi-Q Marine Biotech International Ltd. (Taiwan). Fluoresceinamine isomer I, 99% was obtained from TCI America. Anti-CD44 antibody and PE Mouse IgG2b K isotype control were purchased from BD

Pharmigen BD Biosciences. Matrigel Basement Membrane Matrix, LDEV-free (Catalog #356234) was purchased from Corning. ^{1}H-NMR was performed on a 500 MHz Bruker or 600 MHz Varian system using a 5 mm probe at room temperature. Deuterated water (D_2O, 99.9% D); deuterated DMSO and $CDCl_3$ were purchased from Cambridge Isotope Laboratories. FTIR measurements were performed on a Nicolet IR200 FT-IR instrument using single-reflection ZnSe ATR crystal. The cell line S2-013, a cloned subline of a human pancreatic tumor cell line (SUIT-2) was obtained from Dr. Pankaj Singh (UNMC). All cells were incubated at 37^{o}C in a humidified incubator maintaining 5% CO_2 in DMEM (HyClone, GE Healthcare Life Sciences) with 10% fetal bovine serum and 1% penicillin/streptomycin. 7-week-old female nude mice were purchased from Jackson Laboratories (Bar Harbor, ME). 5.0 chromic gut and 5.0 nylon surgical sutures were purchased from Johnson & Johnson (Somerville, NJ). Comprehensive diagnostic profile reagent rotor was purchased from Abaxis (Union City, CA).

2.1 *In silico* methodology

Molecular docking of sulfated derivates of HA: The X-ray diffraction crystal structure of mouse CD44 hyaluronan-binding domain (PDB ID: 4MRD) and human P-selectin protein [PDB ID: 1G1S] were obtained from Protein Data Bank. Molecular docking was performed to gain deeper insight into the interaction of modified hyaluronic acid derivatives compared to native hyaluronic acid with CD44 and P-selectin. The protein structure was cleaned by removing water molecules and other inorganic ions/atoms in CD44, whereas ions were preserved

in the P-selectin active site. The HA ligand consisting of 12 units was prepared in Maestro molecular modelling software (Schrodinger). Docking studies were performed using Auto-Dock Tools (AutoDock Vina). The grid box of dimensions 40 Å X 40 Å X 40 Å was generated with a 0.5 Å spacing to perform docking. AutoDock Tools were used to add Gasteiger charges and polar hydrogens to CD44 and modified hyaluronic acid derivatives. The structures were saved in *.pdbqt file format. Docking was also performed using SwissDock (http://swissdock.vital-it.ch/) provided as a free web service. The ligands were docked to the desired protein structures by using suitable docking parameters allowing the online web service to produce docking results using CHARMM energies. Similar grid size box dimensions used in AutoDock were used for SwissDock. The docked ligand file was visualized with the protein using UCSF Chimera 1.4.

2.2 Synthetic methods

Synthesis and purification of the different sulfate derivatives of hyaluronic acid

Synthetic procedures for preparation of different sulfated derivatives of hyaluronic acid and aminopropyl 1-pyrenebutanamide described in literature[30],[31] and have been modified and optimized and described below.

Synthesis of TBA salt of hyaluronic acid (HA-TBA): Sodium hyaluronate (10 kDa, 500 mg) was dissolved in 200 mL ultrapure water, which was mixed with 10 g of DOWEX 50WX8-400 ion-exchange resin to allow the substitution of sodium ions with TBA. This mixture was stirred for twelve hours for the effective exchange process at R.T. The reaction mixture was then filtered through a 0.45 μm membrane filter paper obtained from Millipore. This solution was then lyophilized to produce an off-white powder with a yield of 92% (HA–TBA 10 kDa).

Synthesis of sulfated derivatives of HA-TBA: HA-TBA (off-white powder, 300 mg) was dissolved in a three-neck round bottom flask with 30 mL N,N-dimethylformamide (DMF) under argon with constant stirring for 1 h. Once the polymer was dissolved, varying amount of sulfur trioxide pyridine complex (3:1 for selective sulfation to yield one sulfate group per unit of HA; 8:1 for moderate sulfation to yield 2-3 sulfate groups per unit of HA; 12:1 for complete sulfation to yield 4-5 sulfate groups per unit of HA) were added to the reaction mixture and allowed to stir for another 15 min at R.T. Once the reactants were dissolved, the reaction was maintained at 40 °C for selective sulfation for 30 min, 1.5 h for moderate sulfation, and 3 h for complete sulfation to allow successful reaction between the sulfate and the hydroxyl groups of HA. The reaction was quenched with 30 mL nanopure water and pH was maintained at 9-10 at R.T. for 30 min. Cold acetone was added to the reaction mixture to precipitate the product. The precipitate was filtered and washed thrice with water and 4 times with acetone. The product was dissolved in water and dialyzed against 1:1 EtOH:H_2O for 4 changes in 24 h followed by 8 changes of ultrapure water in 48 h. This solution

was then lyophilized yielding an off-white solid with 78% yield for selectively sulfated HA (ssHA), 62% for moderately sulfated HA (msHA), and 54% for completely sulfated HA (csHA). Sulfated HA stored at -20^{O}C for future conjugation.

Synthesis of aminopropyl 1-pyrenebutanamide [PBA]: 1-pyrenebutyric acid (300 mg) was dissolved in 10 mL methanol with 5% concentrated HCl (11 N) and refluxed for 8 h at 70 °C. The reaction produced two layers: clear light-yellow color top layer and dark oil-like bottom layer. The product in the bottom layer was dried at R.T. and stored at 4 °C, 1-pyrenebutyric acid methyl ester was confirmed in the bottom layer by ^{1}H NMR and dried under vacuum for 7 days. 1-Pyrenebutyric acid methyl ester was then dissolved into 10 mL 1,3-diaminopropane and refluxed at 120 °C for 12 h to produce a clear brown liquid. This solution was then cooled to 4 °C and PBA was precipitated by cold saturated NaCl solution, washed with cold water, and dried under vacuum for 7 days producing a 59% yield with brown powder appearance.

Synthesis of PBA conjugates of different sulfated derivatives of HA: Sulfated derivatives of HA were dissolved in 20 mL of ultrapure water and stirred for 15 mins. PBA at 10 wt. % was dissolved into 20 mL DMF at 40 °C under constant stirring to ensure complete dissolution. NHS and EDC (10× molar ratio to PBA), were then added to the sulfated HA solution to activate the carboxylic groups for conjugation. The PBA DMF yellow solution was then added dropwise to the activated HA solution under constant stirring. The reaction was allowed to stir at R.T. for 24 h. The reaction contents were then transferred to dialysis tubing

(MWCO = 3500 Da, Spectrum Laboratories) and allowed to dialyze against 1:1 EtOH:H_2O for 24 h, followed by ultrapure water for an additional 48 h with 8 changes. The individual polymer conjugates were removed from the dialysis tubing and lyophilized for storage at −20^{O}C. Yields of 78% for ssHA-PBA, 72% for ms-HA-PBA, and 62% for cs-HA-PBA (sNanoCy7.5). This procedures was adapted from a similar procedure employed to generate HA-PBA-Cy7.5 (NanoCy7.5) nanoparticles[32].

Synthesis of cyanine 7.5 amine (Cy7.5 amine) conjugates of different sulfated HA-PBA derivatives: Three sHA conjugates of PBA were dissolved in 10 mL of ultrapure water and stirred for 30 min. EDC and NHS were dissolved in above polymer conjugate solution to allow activation on carboxylic groups and stirred for another 30 min. Next, a solution of Cy7.5-amine 10 wt. % in 10 mL DMSO was prepared. This solution was added dropwise to the above activated mixture under constant stirring. The reaction was allowed to proceed with stirring for 24 h at R.T under dark conditions. The product was purified to remove excess precursors using dialysis. The reaction mixture was placed in a dialysis bag with MWCO of 3500 Da and dialyzed against water for 24 h with 4 water changes. Further, unconjugated Cy7.5 dye was removed via a PD10 desalting columns with ultrapure water as a mobile phase. The product fractions were collected and lyophilized to obtain light-green products with a yield of 57-64% for all conjugates.

Synthesis of fucoidan labeled fluoresceinamine: Fucoidan was conjugated to fluoresceinamine using the reducing end polysaccharide chemistry which is employed for conjugation of small molecules. 250 mg of low molecular weight powder of fucoidan was dissolved in 10 mL of 1,3-diaminopropane (3.5 M) and stirred for 30 min to allow the reaction mixture to be become clear. 150 mg of sodium cyanoborohydride ($NaBH_3CN$) was added to the solution slowly stirred for 24 h at $75^{O}C$. After the reaction started, 150 mg of $NaBH_3CN$ was added and stirred for another 72 h at R.T. The reaction was extensively dialyzed (MWCO:1000 Da) against EtOH:H_2O (1:1) for 48 h with 8 changes, followed by 48 h against ultrapure water with 8 changes. The dialyzed product was lyophilized to obtain a light-yellow product with a yield of 48% and stored at -20 °C. 100 mg of aminated low molecular weight fucoidan was dissolved in 10 ml of 1M carbonate buffer (pH 9.5). Fluorescein carboxylate (FITC) was mixed with 10X molar excess of EDC and NHS in carbonate buffer, stirred for 30 min to allow activation of carboxylic groups, and added to the polymer solution dropwise to the reaction was stirred under dark conditions at R.T. for 24 h. The product was dialyzed [MWCO: 1000 Da] against EtOH:H_2O (1:1) for 24 h with 8 changes, followed by 48 h against ultrapure water with 8 changes. The product was lyophilized to obtain a dark yellow product with a yield of 64% and stored at -20 °C. Additional purification by PD-10 was carried out to remove unreacted free Fluoresceinamine, lyophilized powder was dissolved in 1M aqueous NaCl, precipitated with cold ethanol, and centrifuged at 2000 rpm for 1 h.

Synthesis of IRDye800 CW amine conjugates with different sulfated HA derivatives: Different sulfated HA derivatives (10 mg) were dissolved in 10 mL ultrapure water for 30 min at R.T. Once the polymer dissolved completely, 10x molar excess of EDC and NHS was added to IRDye800 CW amine aqueous solution and stirred for 30 min to allow activation of carboxylic groups on sulfated HA. Next, 10 wt. % eq of IRDye800CW amine was dissolved in 5 mL ultrapure water and added dropwise to the activated above aqueous solution and stirred for 24 h protected from light at R.T. The product was dialyzed against water for 24 h with 4 changes, solution was lyophilized and yielded green fluffy powder (76% yield). Conjugation ratio of IRdye800 to sHA was determined using standard curve developed for IRdye800 amine in water.

Nanoparticle characterization: Particle size (hydrodynamic diameter HD) and zeta potential measurements of all sulfated derivatives of HA NPs were measured by dynamic light scattering (DLS) using ZetaSizer NanoZS90 (Malvern Instruments; Malvern UK). NPs samples were prepared by dissolving samples in ultrapure water (1mg/mL) and filtered through 0.45 μm syringe filter. Absorbance spectra of the NPs were recorded with UV-2600 spectrometer (ThermoFisher Evolution 220) in water and 1:1 (v/v) mixture of DMSO:H_2O. Fluorescence reads were obtained on a FluoroMax-4, fluorescence spectrometer equipped with a NIR extended range PMT (Horiba Jobin Yvon; Edison, NJ, USA). Conjugation ratio of Cy7.5 dye to HA was determined using standard curve developed for Cy7.5 dye in 1:1 (v/v) DMSO:H_2O. Conjugation of the hydrophobic ligand was confirmed by ^1H NMR for all the derivatives of sulfated HA-PBA. Transmission electron

microscope (TEM) images were obtained for NPs (1 mg/mL concentration), placed on formavar/silicone monoxide-coated 200 mesh copper grids using NanoVan negative stain for 30 s and imaged using the FEI Tecnai G2 Spirit TEM (FEI; Hillsboro, Oregon) at UNMC's electron microscopy core facility.

2.3. Biophysical evaluation

Fluorescence polarization assay for assessment of binding of different derivatives of sulfated HA to recombinant human P-selectin protein: Fluorescence polarization binding assay was performed in a 384-well low-volume black round-bottom polystyrene NBS microplate (Corning) by measuring the fluorescence intensities using a Spectromax M5 plate reader (Molecular Devices, Sunnyvale, CA, USA). Polarization values are reported as millipolarization units (mP). The fluorescent probe, fucoidan-FITC, synthesized above was serially diluted in 1X PBS pH 7.4, covering a range of 0.02-50 nM and dispensed in triplicates in black non-binding 384 well microplate. Blank controls contained only buffer (10 μL). Total fluorescence intensities were plotted against respective probe concentrations with GraphPad Prism v7.0 and fitted with linear regression. Binding of modified sulfated derivatives of HA to recombinant human P-selectin protein was estimated by generation of a binding curve of probe vs protein in the concentrations range of 0.02 nM-750 nM to have a wide range for accurate estimation of K_D. Direct binding assay estimation was performed by adding 1 μL of 0.5 nM fluorescent probe and 10 μl of solution with increasing concentrations of recombinant P-selectin protein. The final volume of the reaction mixture was

11 μl in each well, and all measurements were performed in triplicate. The microplate was shaken for 5 min in dark at R.T before being read by the plate reader (λ_{ex} = 489 nm; λ_{em} = 538 nm). Background correction of the fluorescence from the protein alone was obtained for the final mP value. Fluorescence polarization competition displacement assay was performed using 10 μL of 5 nM of recombinant protein with 1 μL of 0.05 nM of fluorescent probe and 1 μL of increasing concentration of unlabeled sulfated HA polymer derivatives (0.02 nM-24 μM). The total volume of the reaction mixture was 12 μL in each well. Fluorescence measurements were made after a 15 min incubation. The data was fitted and IC_{50} values were determined using a non-linear least square fit to a single site binding model (GraphPad Prism v7.0).

2.4. *In vitro* analysis

2.11. Analysis of P-selectin and CD44 expression on S2-013 cell line: Expression profiles of CD44 and P-selectin were studied using flow cytometry analysis (FACS LSRII-green flow cytometer BD). 1×10^4 S2-013 cells were plated in triplicate in 6-well plates and allowed to adhere to the bottom of the dish overnight. Cells were fixed in 150 μL of 4% paraformaldehyde solution at 37 °C for 15 mins. The fixing solution was removed by washing the cells with 1X PBS thrice. Fixed cells were then treated with anti-CD62P antibody (Catalog #ab6632 1:50) and anti-CD44 antibody (Catalog #ab157107 1:200) for 1 h at 37^{O}C. Wells were then washed thrice with 1X PBS and blocked with 5% BSA for 1 h at R.T. Cells were then incubated with 75 μL of FITC-conjugated anti-mouse secondary

antibody (Millipore AP132F) at 1:100 in blocking solution for 1 h at R.T. in dark conditions.

Effect of P-selectin and CD44 blocking on uptake of both sulfated HA nanoparticles and non-sulfated HA nanoparticles: S2-013 cells ($1X10^4$ per well) was seeded in 24-well plate in 1 mL of DMEM media overnight. Cells were washed with PBS and serum-free media was added to each well. Next, excess of anti-CD62P P-selectin antibody and anti-CD44 antibody was incubated for 1 h at 37 °C to allow blocking of P-selectin and CD44 receptors separately in the 24-well plate format. NPs solutions were made in serum-free DMEM at equimolar Cy7.5 dye concentrations of 1.5 mM, added to each well, and incubated for 1 h at 37 °C. After incubations with NPs, cells were washed thrice with 1X PBS, trypsinized, and re-suspended in 300 μL of FACS buffer (3% FBS in PBS). A FACS LSRII-green flow cytometer (BD) was used for all flow cytometry measurements. A total of 15,000 gated events were acquired per sample, and the mean fluorescence intensity was plotted in a histogram-based graphical representation. Each data point is representative of the mean of three independent measurements on the flow cytometer. Data were analyzed with FlowJo (Tree Star) software.

Investigation of the effects of PBA and dye (Cy7.5) on P-selectin binding on S2-013 cells: S2-013 cells (1×10^4 per well) were seeded in 24-well plate in 1 ml of DMEM media overnight. Cells were washed with PBS and serum-free media was added to each well. Next, excess of anti-CD62P P-selectin antibody was

added for 1 h at 37 °C to allow blocking of P-selectin receptor separately in the 24-well plate format. Polymer conjugate solutions were made in serum-free DMEM at equimolar IRdye800 dye concentrations of 1 mM, added to each well, and incubated for 1 h at 37 °C. After polymer conjugate incubations, cells were washed thrice with 1X PBS, trypsinized, and re-suspended in 300 μL of FACS buffer (3% FBS in PBS). A FACS LSRII-green using far-red laser flow cytometer (BD) was used for all flow cytometry measurements. A total of 15,000 gated events were acquired per sample and the mean fluorescence intensity was plotted in a histogram-based graphical representation. Each data point is representative of the mean of three independent measurements on the flow cytometer. Data were analyzed with FlowJo (Tree Star) software.

Development of S2-013 tumor spheroid model for studying uptake of dye vs sHA-IRDye800 conjugates: Matrigel (Matrigel #354234 from Corning, Corning, NY, USA) was thawed and added to 8-well Nunc™ Lab-Tek™ II Chamber Slide™ System (50 μL/well) to cover the bottom of each well to serve as matrix as it is rich in ECM components, such as laminin, collagen, heparin sulfate proteoglycans, entactin, and several soluble factors. Next, S2-013 cells (4×10^3) were mixed with thawed Matrigel along with media and added to Matrigel coated wells. The growth of the spheroids was monitored using Olympus CKX41 Bright Field, Infinity 1 Luminera microscope over a period of 2 weeks until the spheroids reached 500 μm in size. Next, free IRDye800 and sHA-IRDye800 polymer conjugates (3 μM concentration of IRDye800) were added to the tumor spheroids and cultured for 12 h. After washing thrice with 1X PBS and fixing in

4% paraformaldehyde, the IRDye800 fluorescence in spheroids was measured with the confocal microscope Zeiss LSM 800 with Airyscan (Jena, Germany) with 20X objective lens with a 1.4 NA using XYZ-stack with 10 µm intervals at 512*512 pixels with imaging acquisitions at 33 Hz. Images were captured and analyzed with LSM software (Jena, Germany) and processed using Carl Zeiss software. The spheroids were then treated with trypsin, the obtained single-cell suspension was washed with PBS and subjected to flow cytometry analysis for determination of uptake of IRDye800.

Development of P-selectin and CD44 knockout cell lines using CRISPR/Cas9 system: CD44 and P-selectin (SELP gene) knockout S2-013 human pancreatic cancer cell lines were generated using CRISPR/Cas9 system. pLenti-CRISPR v2 vector containing the individual guide RNAs (sgRNAs) was ordered from GeneScript USA Inc, (New Jersey). The sequences of the guide RNAs targeting CD44 and and P-selectin (SELP gene) are listed in the Supplemental Table. Stable CD44 and P-selectin (SELP gene) knockout were generated by lentivirally transducing human pancreatic cancer cell line S2-013 with pLenti-CRISPR v2 vectors containing gene specific sgRNAs. Lentivirus was generated by transfecting HEK 293T cells with psPAX2 and pMD2.G and gene specific pLenti-CRISPR v2 vector in a 3:1:4 ratio. HEK 293T cells were transfected using Lipofectamine 3000 from Invitrogen. The lentivirus was collected 24, 48, and 72 h post-transfection. The virus was passed through a 0.45 µm SCFA filter, and 10 µg/mL polybrene was added to the filtered media. The S2-013 pancreatic cancer cells were transduced with lentivirus targeting CD44

and P-selectin (SELP gene). Cells were selected for puromycin resistance using Dulbecco's modified Eagle's medium (DMEM) supplemented with 1.1 μg/mL puromycin and 10% FBS for three weeks. Once cells were selected using puromycin, the cells were cultured in DMEM supplemented with 10% FBS without puromycin.

Confocal microscopy: S2-013 cells were seeded (10^5 cells/well) on individual 12 mm Nunc™ glass bottom dishes (Invitrogen, ThermoFisher Scientific, USA) and left to adhere for 24 h. The cells were treated with sNanoCy7.5 in serum-free DMEM media and incubated at 37 °C for 1 h. After incubation, cells were washed thrice with 1X PBS, and then fixed with 4% paraformaldehyde solution for 15 min at 37 °C. Next cells were treated with 0.25% Triton-X-100 in 1X PBS to permeabilize the cell membrane, followed by blocking with 1% BSA in 1X PBS. Next, primary antibody for Rab5 endosomal marker (Rabbit polyclonal IgG, Santa Cruz Biotechnology Inc., Dallas, TX) was added in 1% BSA 1X PBS solution and incubated with the cells overnight at 4°C. Cells were incubated with the secondary antibody (FITC-conjugated anti-rabbit, Millipore AP132F) in 1% BSA added to each well at room temperature for 1 h at R.T. Cells were then washed thrice with 1X PBS, and were stained with HCS NuclearMask™ Deep Red Stain (ThermoFisher Scientific, Catalog# H10294) for 15 mins. Cells were washed and stored at 4 °C until CSLM imaging. Similar protocol was used for CSLM imaging of tumor spheroids and P-selectin blocking assay.

Confocal images were taken with Zeiss 800 Confocal Laser Scanning Microscope, 60X with 1 µm cell slices. DAPI, Alexa Flour 488 and Alexa Fluor 647 filters were used to detect blue, green and NIR signal from the cells.

Western blot analysis and flow cytometry analysis of CRISPR/Cas9 S2-013 CD44 and P-selectin KO cells: S2-013 cells were washed with 1X PBS and lysed using radioimmunoprecipitation assay (RIPA) lysis buffer containing protease inhibitor and EDTA. Cell debris were removed by centrifugation at 13,000 rpm for 20 mins, and the supernatant containing the proteins was collected. Protein content was quantified using the Bio-Rad Protein Assay dye (Bio-Rad Laboratories, Inc.) Equal amounts of total proteins (20 µg) were separated by SDS-PAGE and transferred to nitrocellulose membrane. The membranes were probed with primary antibodies against actin (1:650, JLA20, developed by J. J.-C. Lin was obtained from the Developmental Studies Hybridoma Bank, Iowa City, IA), CD44 (1:5000, ab157107), and P-selectin (1:100, AF137, R&D Cell Signaling technologies) in TBS with 5% nonfat milk and 0.1% Tween-20 on a rocker overnight at $4^{O}C$. Nitrocellulose membrane was washed with TBST thrice and incubated with anti-mouse IRDye 800CW secondary antibody (1:15000, LI-COR Biosciences, Lincoln NE) and anti-sheep IRDye680 secondary antibody (1:10000, Invitrogen, ThermoFisher Scientific) for 1 h in dark at R.T. The membrane was washed with TBST and visualized using the 700 nm and 800 nm channels of Odyssey® Imaging Systems for assessment and quantification of protein bands for knockout (KO) cell lines.

The S2-013 cell lines were plated in 12-well plates and incubated overnight to adhere to the bottom. Cells were fixed similar to procedures mentioned above and were analyzed using FACS LSRII-green using far-red laser flow cytometer (BD) was used for all flow cytometry measurements. Anti-CD44 antibody (1:250, ab46793) and anti-P-selectin antibody (1:50, BBA34) were used to quantitate the CD44 and P-selectin expression profiles.

Effect of P-selectin and CD44 KO S2-013 cells on uptake of sulfated HA nanoparticles and non-sulfated HA nanoparticles: S2-013 cells CD44 and P-selectin KO cells ($1X10^4$ per well) were seeded in 24-well plate in 1 mL of DMEM media overnight. Cells were washed with PBS and serum-free media was added to each well. NPs solutions were made in serum-free DMEM at equimolar Cy7.5 dye concentrations of 1.5 mM, added to each well, and incubated for 1 h at 37^{o}C. After NP incubations, cells were washed thrice with 1X PBS, trypsinized, and re-suspended in 300 μL of FACS buffer (3% FBS in PBS). A FACS LSRII-green far red laser flow cytometer (BD) was used for all flow cytometry measurements. A total of 15,000 gated events were acquired per sample, and the mean fluorescence intensity was plotted in a histogram-based graphical representation. Each data point is representative of the mean of three independent measurements on the flow cytometer. Data were analyzed with FlowJo (Tree Star) software.

2.5 *In vivo* studies

Tumor implantation and NIR imaging: All animal experiments were performed under approved protocol by the University of Nebraska Medical Center Institutional Animal Care and Use Committee (IACUC). S2-013 ($1X10^6$ cells) were suspended in 100 μL of 1:1 media:Matrigel (Matrigel #354234 from Corning, Corning, NY, USA), and injected subcutaneously on the right flank of 5-6-week-old female athymic nude mice (Strain: J:NU, Jackson Laboratory, Bar Harbor, ME, USA). Tumors were allowed to grow for 4 weeks prior to imaging experiments. Cy7.5amine (1.2 nmol/mouse), NanoCy7.5 (HA-PBA-Cy7.5 1.2 nmol Cy7.5/mouse), and sNanoCy7.5 (sHA-PBA-Cy7.5 1.2 nmol Cy7.5/mouse) in 100 μL ultrapure water was intravenously injected via tail vein in mice (n=3 mice per group) once tumors reached 150 mm^3. Mice were euthanized 24 h after the injections. Each mouse was necropsied, followed by relative organ distribution imaging using the Pearl Trilogy Small Animal Imaging system (LI-COR; Lincoln, NE) and Lab FLARE RP1 small animal imaging system (Curadel, Marlborough, MA) to detect Cy7.5 (800 nm channel) fluorescence from the contrast agents. Analysis was performed using LI-COR Image Studio 5.0 software to manually draw region of interest (ROI) around tumors and organs to calculate the signal to noise ratio (SNR); SNR = (average tissue intensity per pixel in an area of interest)/ (standard deviation of background of interest). Whole-body imaging of mice and FIGS was performed using the Curadel system as described previously[32,33,34] with exposure of 120 ms for the near infrared laser and 10 ms for the white light. NIR fluorescence spectra were collected at 1 cm approximate

distance from the tissue/tumor surface by a handheld spectrophotometer device that excites at 785 nm and collects emitted light in the NIR window. Laser powers of 8 (low), 30 (medium low), 80 (medium), 150 (medium high), and 200 (high) mW were used to collect the NIR emission from the contrast agents in individual organs.

Histological analysis and fluorescence microscopy: Tumor and organ tissues obtained from necropsy after FIGS were immediately placed in O.C.T. gel covering the tissue and frozen at -80^{O}C. Samples were then cut using cryostat (Leica Biosciences, Buffalo Grove, IL, USA) at a thickness of 5-10 μm at the UNMC Tissue Sciences Facility. Tumor/tissue sections were stained with hematoxylin and eosin (H&E)/unstained for NIR confocal scanning fluorescence microscopy. Representative tumor sections were stained for anti-CD31 proliferation marker (1:150, ab16667 Abcam), anti-hCD44 (1:500, #3570 Cell Signaling Technology, Danvers, MA, USA), anti-hPselectin (ab6632, Abcam). Unstained tumor, liver, spleen, and kidney sections were visualized under Zeiss LSM 800 Airscan (Carl Zeiss, Oberkochen, Germany) using 10X objective with 1.4 N.A. using FITC laser channel for autofluorescence and 687 nm excitation laser for NIR dye localization. Exposure time of Cy7.5 was constant throughout all the samples.

3. Results and Discussions

3.1. Synthesis, characterization, and computational analysis of sulfated derivatives of HA

Commercially available hyaluronic acid was modified according to scheme in figure 1A using previously published procedures to produce sulfated HA[31]. Understanding crucial hotspots for binding contacts between HA with CD44 and P-selectin respectively, three sulfated derivatives of HA were prepared using regio-selective chemistry for synthetic modifications[35].

The crystal structure of HA (copolymer of N-acetylglucosamine and glucuronic acid) complexed with CD44 was solved in 2007[36], showing key residue interactions between HA and CD44. Those interactions include hydrophobic contacts between the N-acetyl group and aromatic ring F83, the side chain of I92 and the disulfide bond between C81 and C101 of CD44; water-mediated hydrogen bonding between the carboxylate group and F46 and R45 of CD44; hydrogen bonding between the C6-hydroxy group of HA with F109 of CD44, which serves in anchoring the structure to the CD44 active site. Based on previously published computational results, we designed a sulfated derivative of HA which hindered key residue contacts with F109, thereby decreasing binding to CD44 protein compared to the native HA[37].

The structure of P-selectin protein co-crystallized with post-translated modified PSGL-1 was solved more than 10 years ago, indicating specifics of biding partners to P-selectin. P-selectin glycoprotein ligand-1 (PSGL-1) is post-

translationally modified by glycosylation on sialyl-lewis^X tetrasaccharide by multiple sulfated tyrosine residues (highly negatively charged) near the N-terminus. Interactions between P-selectin and PSGL-1 are mainly dominated by long-range electrostatic attraction between opposite charges of the binding partners. The active site of P-selectin lectin binding domain is lined with numerous positively charged amino acid residues such as histidine, lysine, arginine, glutamic acid, and strontium ion rendering an overall positive charge of +9 which is missing in E- and L-selectin, respectively. Importantly, a report published by Weinhart, et al[38] discussed the effect of individual polyanions synthesized on highly functionalized dendritic polyglycerol scaffold via click chemistry on P-selectin binding. The authors concluded that the binding potential increased in the order carboxylate < phosphate < phosphonate ≈ sulfonate < bisphosphonate < sulfate and tends to increase with the acidity of the anionic group present on the macromolecular structure[38]. Building on the importance of sulfate group in P-selectin targeting, we designed three derivatives of HA by introducing sulfate group substitutions. The importance of electrostatic interactions along with partial salt bridges between sulfate groups and active site of P-selectin was also well correlated experimentally (NMR, SPR) and computationally to confer selectivity[39].

Sulfates (esters) are primarily produced by nucleophilic substitution of hydroxyl groups. The substitution site and efficiency depend on various parameters such as sulfating reagent of choice, reaction medium, reaction time, and temperature[40]. Sulfation is performed in organic solvents such as

dimethylformamide (DMF), dimethyl sulfoxide (DMSO), and/or pyridine are most widely used. Due to the use of organic solvents, HA was synthetically modified to its tetrabutylammonium salt to allow rapid solubility in organic solvents. Sulfating reagents, mainly sulfur trioxide-pyridine complex for optimum substitution rate on polysaccharides, are used in excess compared to available free hydroxyl groups. Higher temperature of 50-60^{o}C and longer reaction time have shown to increase the rate of sulfation of the reaction.

In our work, the degree of sulfate substitutions (DS) was controlled by the addition of different molar ratios of sulfation reagent (sulfur trioxide pyridine complex in DMF) per repeat unit of HA. Major sulfation sites on HA are the primary hydroxyl groups being the most reactive, while other (secondary/vicinal) hydroxyl groups are less susceptible to the attack of the sulfating nucleophile moiety due to steric hindrance and spatial orientation. The latter can be controlled by altering the reaction kinetics by changing temperature and reaction time[40].

Sulfation of HA occurs at different hydroxyl groups, i.e. at C-2', C-3', C-4', or C-6' OH, depending on the concentration of the sulfating reagent, temperature, and reaction time[41]. Sulfation is most favored at the C-6 position since it is the only primary and most reactive hydroxyl in HA[31]. Selectively sulfated HA (ssHA) was produced by using 3:1 ratio, moderately sulfated HA (msHA) using 8:1, and completely sulfated HA (csHA) using 12:1 of moles of sulfating reagent to moles of HA per repeat unit. The reaction time was optimized for producing ssHA (30 mins), msHA (60 mins), and csHA (180 mins) under constant argon flow. Sulfation was followed by structural analysis by ^{1}H-NMR: downward shift of the

C-6 proton peaks on hydroxyl groups (due to the higher electron withdrawing properties of sulfate groups) was observed from 3.45 ppm to 3.55, 3.62, 3.9 ppm (yellow arrows in **Fig. 1B**). Complete sulfation at C-6 was achieved for ssHA, msHA, and csHA since no peak was observed at 3.45 ppm, and emergence of new peaks (red arrows) indicated additional hydroxyl sulfation at positions C-2', C-3', and C-4'. All secondary hydroxyls have similar reactivity, msHA and csHA both containing similar patterns of sulfation between 3.8-4.2 ppm positions. The increased relative peaks between 4 and 4.4 ppm for csHA indicate a higher degree of sulfation compared to msHA and ssHA. FTIR data is also conclusive in **Fig. 1D**, indicating peak vibrations of C–O–S and S=O (asymmetric and symmetric) in the range of 800 and 1290 cm^{-1}. This shows the presence of sulfate moieties for all the derivatives. DS values obtained for ssHA (0.8-1.2), msHA (1.8-2.2), and csHA (2.9-3) confirmed by elemental analysis data shown in **Fig. 1E**. Introducing sulfate groups also increased the negative surface charge of derivatives of HA (**Fig. 1C**), thereby shifting the zeta potential to a highly negative scale for each of the modified variants of HA. Importantly, sulfate groups are expected to carry a negative charge unaffected in pH ranges (4-8) due to its sufficiently low pKa, indicating charge integrity of the sulfate group for binding to the P-selectin protein in physiologic *in vivo* conditions.

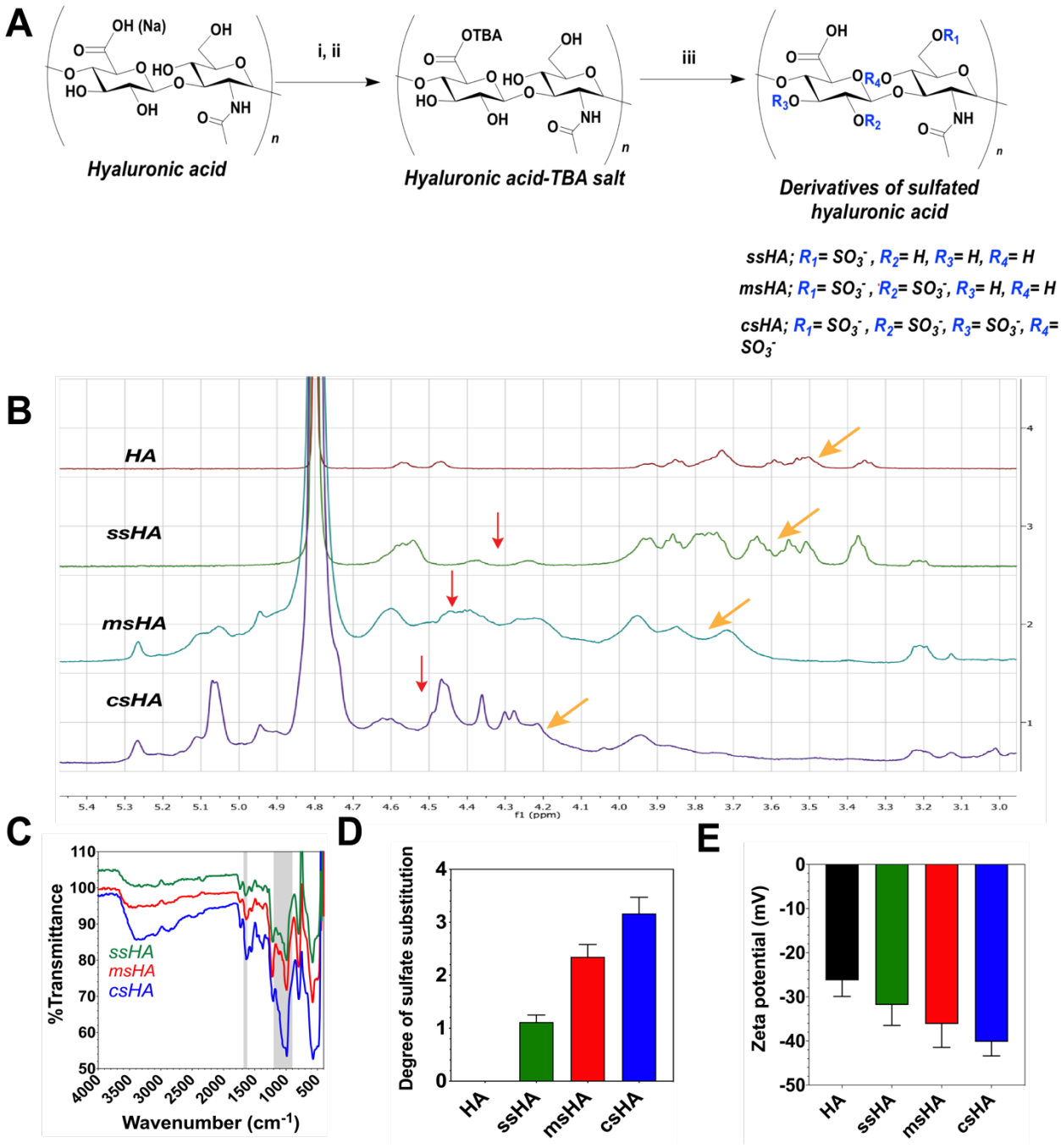

Fig 1: (A) Synthetic scheme for generation of 3 derivatives of sHA; i: ion exchange with TBA in H_2O, ii: Dowex ion exchange resin; iii: different molar ratios of sulfur trioxide pyridine complex in DMF. (B) ^1H NMR spectra (3.2-4.7 ppm) of HA and derivatives of sHA with increasing degree of substitution. The peak shift

of the methylene protons of C-6 is indicated by yellow arrows, whereas different vicinal hydroxyl groups by red arrows. (C) FTIR signatures of HA vs different variants, grey colored portion in the graph indicate S=O (asymmetric and symmetric) and C-O-S stretching and bending vibrations. (D) Sulfur elemental analysis for quantification of sulfate content in each of the variants. (E) The zeta potential (mV) of all derivatives.

Computational docking analysis of each of the derivatives of HA were assessed using SwissDock[42] and AutoDock[43] software packages. Increasing docking energies (indicating stronger binding) with increasing sulfate substitutions on HA to P-selectin protein implying favorable increase in sulfate groups with increasing binding to active site of P-selectin. We observed increasing binding trend HA < ssHA < msHA < csHA (**Fig. 2**). Also, decreasing binding interactions with CD44 were observed with increasing sulfate substitutions on HA. Structural modifications on HA were observed to be key determining factors that influence binding to P-selectin and CD44 proteins. However, an important consideration should be kept in mind that HA belongs to family of natural carbohydrates, where controlling the exact molecular weight and chemical substitution ratio is extremely challenging. Even with precise stoichiometric substitution ratio under control, it will be virtually impossible to control such site-by-site modifications. This will lead to the possibility for the less (or completely unmodified) fragments of the polymer to determine the interaction with binding partners.

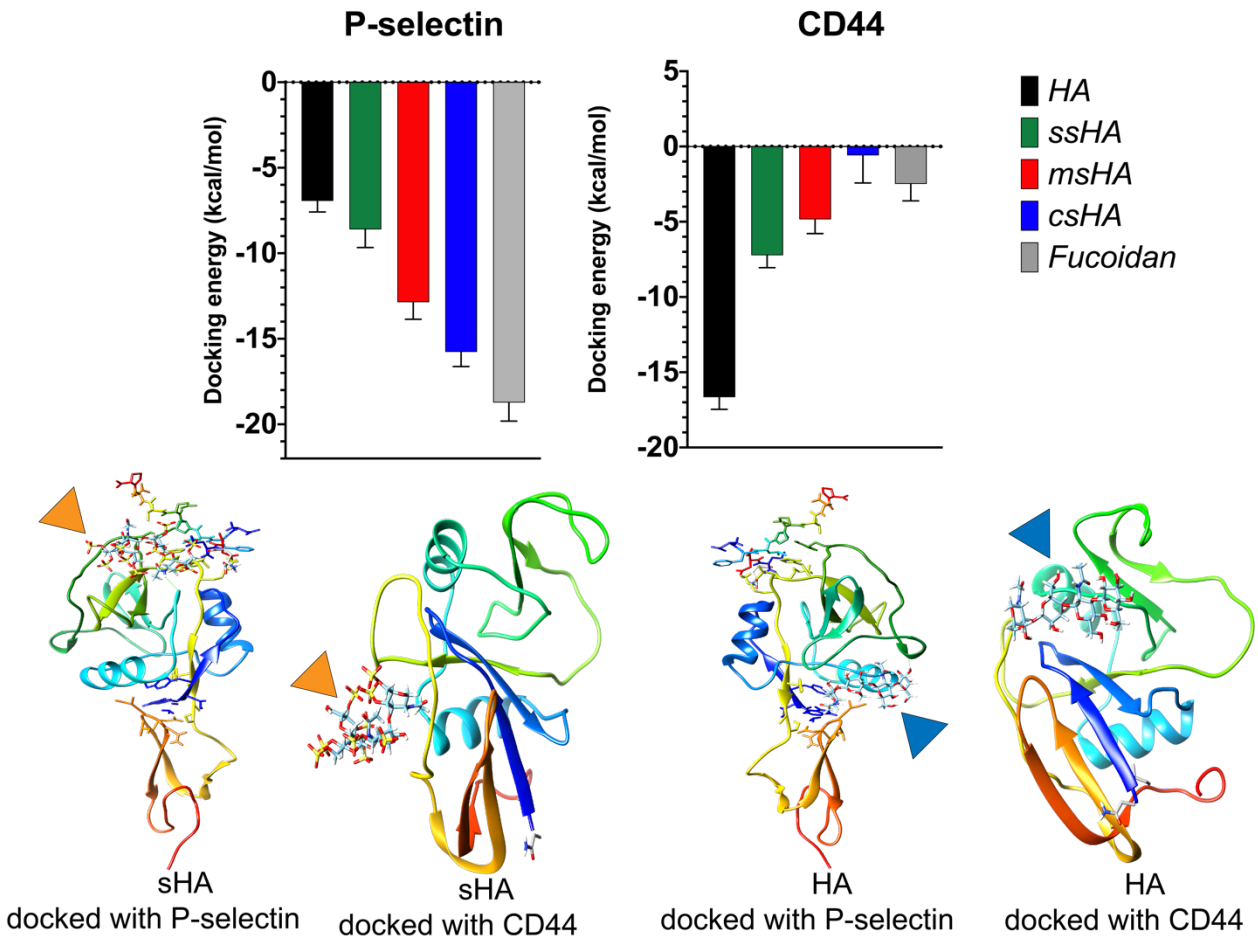

Fig 2: Computational docking energies for sulfated derivatives of HA against P-selectin and CD44. Images below are images obtained from the docking program, arrows indicate the binding pose of sulfated HA (orange) and HA (blue) in the protein structure.

3.2. Synthesis and characterization of nanoparticles derived from sulfated HA derivatives

Hydrophobic ligand, 1-pyrenebutanamide (PBA) was synthesized by formation of methyl ester followed by nucleophilic addition of 1,3 diaminopropane under reflux to produce PBA (**Fig 3A**)[44] with an amino group as a handle for conjugation to carboxylic acids of sHA. sHA was functionalized with PBA to form self-assembling amphiphilic conjugates, the extent of conjugation was characterized by ^{1}H NMR by observing the aromatic region in the range of 7-8.0 ppm (**Figure S3-5**).

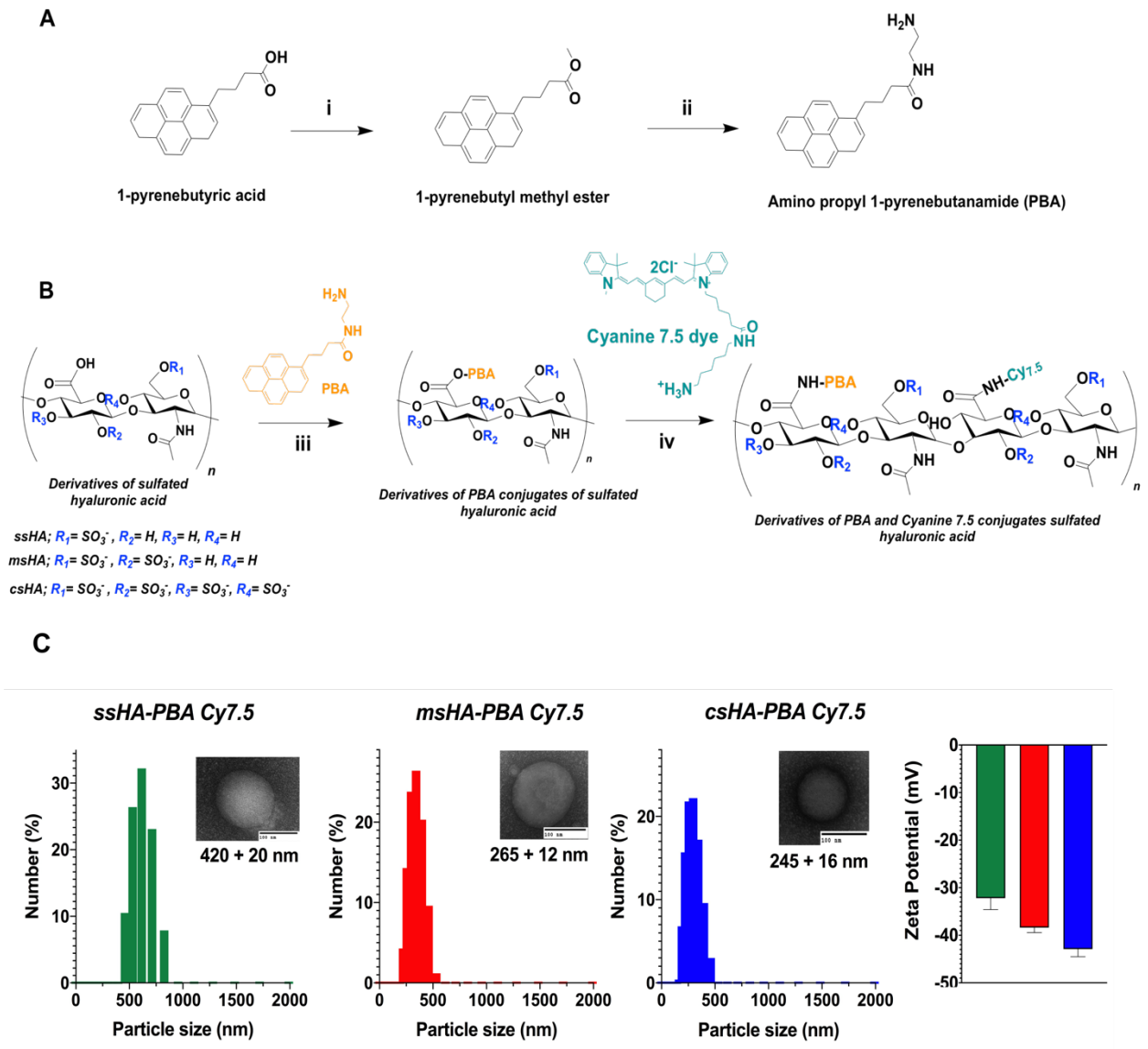

Fig. 3: (A) Synthetic scheme for preparation of hydrophobic amino-propyl 1-pyrenebutaminde from 1-pyrenebutyric acid. i: Conc. HCl with methanol at 65 C for 6 h; ii: excess of diaminopropane at 130 C for 6 h (B) Synthetic scheme for preparation of self-assembled nanoparticles by conjugating Cy7.5 amine NIR dye. iii: Addition of PBA-DMF solution to EDC NHS activated sHA solution; iv: EDC NHS activation followed by Cy7.5 addition stirred for 24 h (C) DLS analysis of size distribution of three different derivatives of sulfated HA nanoparticles.

We sequentially modified the nanoparticles with Cyanine7.5 (Cy7.5) using EDC/NHS conjugation chemistry (**Fig. 3B**)[32], and the extent of chemical conjugation of Cy7.5 was quantified by UV-vis absorption in water. We observed the self-assembly induced fluorophore quenching due to the hydrophobic ligand in the nanoparticles, similar to previous reports on NanoCy7.5[32]. Size distribution of modified HA nanoparticles was determined by DLS and TEM (**Fig. 3C**). We observed a decrease in size of the nanoparticles with increasing sulfate substitution ratio, which could be a result of electrostatic repulsion provided by charges around nanoparticles that prevent aggregation/precipitation as shown in **Fig. 3C**. Particle size determined by TEM was obviously smaller compared to the DLS data, as sample preparation demands dehydration to obtain TEM images. Optical properties were similar to reports published previously[32]. Disassembly of NPs in the DMSO solution leads to strong fluorescence as compared to their quenched state in aqueous media. This is an indication of fluorescence being quenched due to fluorophores closely packed in a nanoparticle upon its self-assembly.

3.3. Interaction of different sulfated HA derivatives with P-selectin

We designed the FP assay by selecting a suitable ligand which binds to P-selectin with high affinity. Fluorescence polarization (FP) is represented in mP which is calculated by measuring the intensities of emitted fluorescent light from a parallel and perpendicular direction w.r.t to excitation plane[45]. Biomolecules conjugated or complexed with fluorophores will retain much of the polarizability

of incident light, and any minute change in polarization can be measured by the changing ratios of intensities of parallel and perpendicular light, giving a measurement of ligand binding affinities.

For this, we constructed a low molecular weight fucoidan[46] conjugated FITC ligand by reductive amination with diaminopropane, followed by a reduction with sodium cyanoborohydride. An accurate measure of binding affinity can be obtained when the molecular weight difference between the ligand (polymers/carbohydrates) and the large biomolecules is at least 10 times in magnitude. Carboxyfluorescein was conjugated using EDC/NHS to activate the carboxylic acid, allowing formation of amide bonds with aminated fucoidan. Ideally, the attachment of a fluorophore to a ligand should not affect the binding mode or alter specificity to the receptor. In a reaction mixture, both a fluorescent ligand and a protein, the observed polarization is always the function of fraction of the ligand-protein complex.

We performed a probe titration in the assay buffer to determine the relationship between total fluorescence intensity and probe concentrations. For 0.5 nM of fluorescent probe concentration was selected to have a high fluorescence intensity at λex = 489 nm to avoid stoichiometric titration above K_D with receptor. Next, serial dilutions of P-selectin recombinant protein (0.02 nM-750 nM) were prepared and incubated with the fluorescent ligand, and FP values were measured. A dose-dependent increase in FP was observed, indicating no substantial effect of FITC on binding of sulfated derivatives to P-selectin. We determined the binding affinity of fucoidan-FITC to be 1 nM using nonlinear least

square fitting to a single-site binding model which is consistent with previous reports from surface plasma resonance data in literature to be 1.2 nM[46].

To determine the interactions of different sulfated derivatives of HA, a FP displacement/competition assay was set up by optimizing concentrations of 0.5 nM fluorescent ligand and 5 nM of P-selectin, where saturated binding is ensured. Displacement of fucoidan-FITC from P-selectin was examined by increasing concentrations of unlabeled derivatives from [0.02 nM - 24 μM], unlabeled fucoidan was used as a reference standard (**Fig. 4B-i**). Applying nonlinear least square fitting to a single-site fitting model, inhibition curves for each of the derivatives was found. The data shows that the increasing sulfate content leads to tighter/stronger binding to P-selectin indicating the importance of sulfate groups for P-selectin binding. Similar observations were reported where multiple sulfated analogs of HA was tested against IL-8, IL-10, BMP-2, sclerostin, TIMP-3, CXCL-12, TGF-b, FGF-1, FGF-2, and AT-III, increasing order of sulfation bound strongly where non-sulfated HA showed no binding to any of the tested proteins[47]. HA is shown to have the least binding which is also in accordance with literature[38]. In another report, various semi-synthetic glucan sulfates were shown to have superior P-selectin inhibitory activity[48].

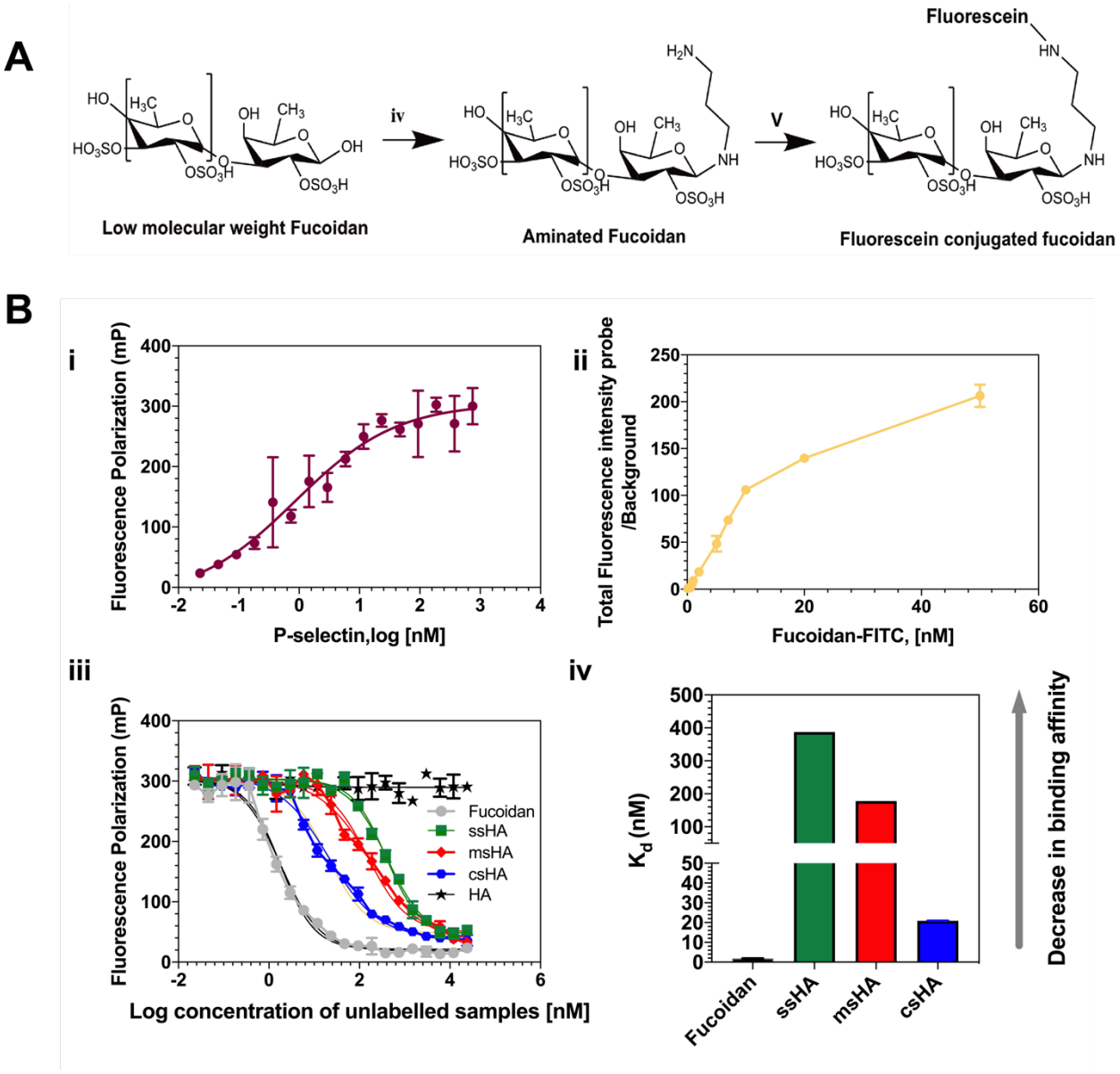

Figure 4: (A) Synthetic scheme for preparation of fluorescein labelled low molecular weight fucoidan using reducing end chemistry. (B) [i] K_D determination of the interaction between fluorescein labelled low molecular weight fucoidan and recombinant human P-selectin protein. [ii] Setup of FP binding assay for the quantification of reader protein-to- fluorescent probe by measuring linearity of the total fluorescence intensity of ligand compared to background. [iii] Dose-response inhibition curve for unlabeled HA and sHA derivatives for determination of K_D

against P-selectin. [iv] Bar graph representation of K_D values from competitive binding assessment in [iii].

3.4. Binding of sulfated HA nanoparticles from *in vitro* analysis

P-selectin expression was evaluated in S2-013 which are patient-derived pancreatic adenocarcinoma cells. They show a positive shift in FACS signal relative to control analysis implying single population, which was also confirmed[24]. CD44 was also evaluated and was positively expressed in S2-013 cells. Furthermore, breast cancer cell line MDA-MB-231, colon cancer cell line RKO, prostate cancer cell line PC-3 were also observed to overexpress P-selectin by FACS (**Fig. 5a**). All cell lines tested indicated a positive shift in fluorescence signal indicating a single population expressing P-selectin. This suggests the rationale to further pursue the application of sulfated HA as relevant drug delivery strategy to target P-selectin which is abundantly expressed in multiple cancer types.

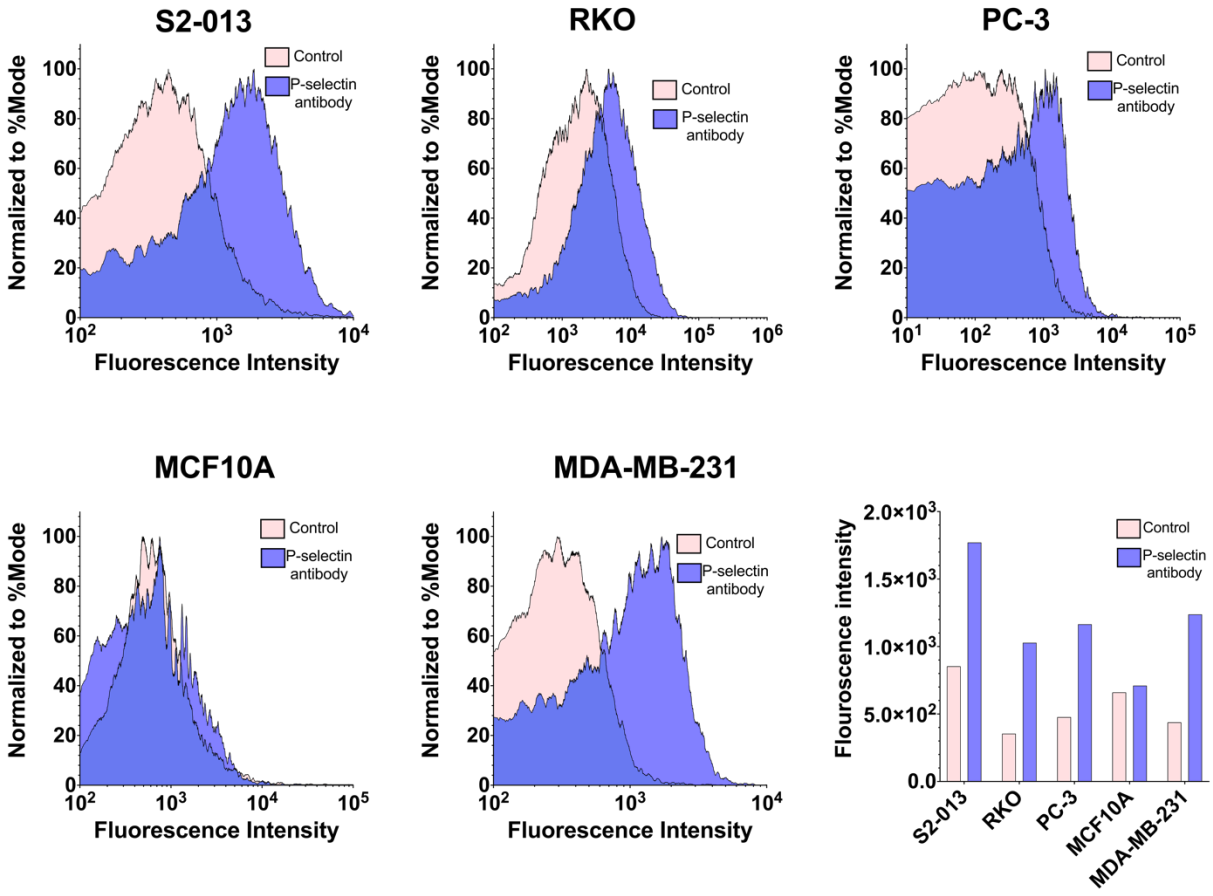

Fig. 5a: Flow cytometric analysis for P-selectin expression in S2-013 (Pancreatic cell line), RKO (Colon cancer cell line), PC-3 (Prostate cancer cell line), MCF10A (Non-malignant breast cell line), and MDA-MB-231 (Breast cancer cell line).

Evaluation of P-selectin and CD44-dependent internalization in S2-013 cells was carried out by pre-treatment with P-selectin and CD44 specific antibodies to block all available receptors. Blocking with P-selectin inhibited the uptake 4-fold, whereas CD44 blockage lead to only marginal decrease in uptake indicating preference of P-selectin mediated uptake of sNanoCy7.5 over CD44 in comprehensive FACS analysis (**Fig. 5 A-B**).

Similarly, traditional HA-based nanoparticles (NanoCy7.5) manifested a reversal in uptake with minimal effect of P-selectin and several fold decrease in CD44 mediated uptake (**Fig. 5D**). To further investigate the effect of hydrophobic ligand and imaging dye Cy7.5 on binding to P-selectin, a control conjugate of sulfated HA was designed with IRDye800. Similar results were obtained, implying that the effect of only sulfate substituent affects P-selectin targeting (**Fig. 5E**). Energy dependent internalization process was prevalent at 37 ^{o}C compared to 4 ^{o}C (**Fig. 5F**). We observed a 40-60% decrease in uptake of cells positive for Cy7.5 fluorescence at 4 ^{o}C compared to 37 ^{o}C. To investigate the intracellular trafficking of sulfated derivatives, cells were stained with endosomal marker for Rab5. As demonstrated previously by flow cytometry, conjugates were readily detected at the cytoplasm following 1 h incubation (**Fig. 5G-H**). Co-localization analysis supported these results. Additionally, confocal laser scanning microscopy analysis was performed under excess P-selectin antibody conditions to evaluate the uptake of sNanoCy7.5 at 37^{o}C. Expectedly, blocking decreased the overall uptake of the nanoparticles, demonstrating mainly P-selectin driven targeting to cancer cells.

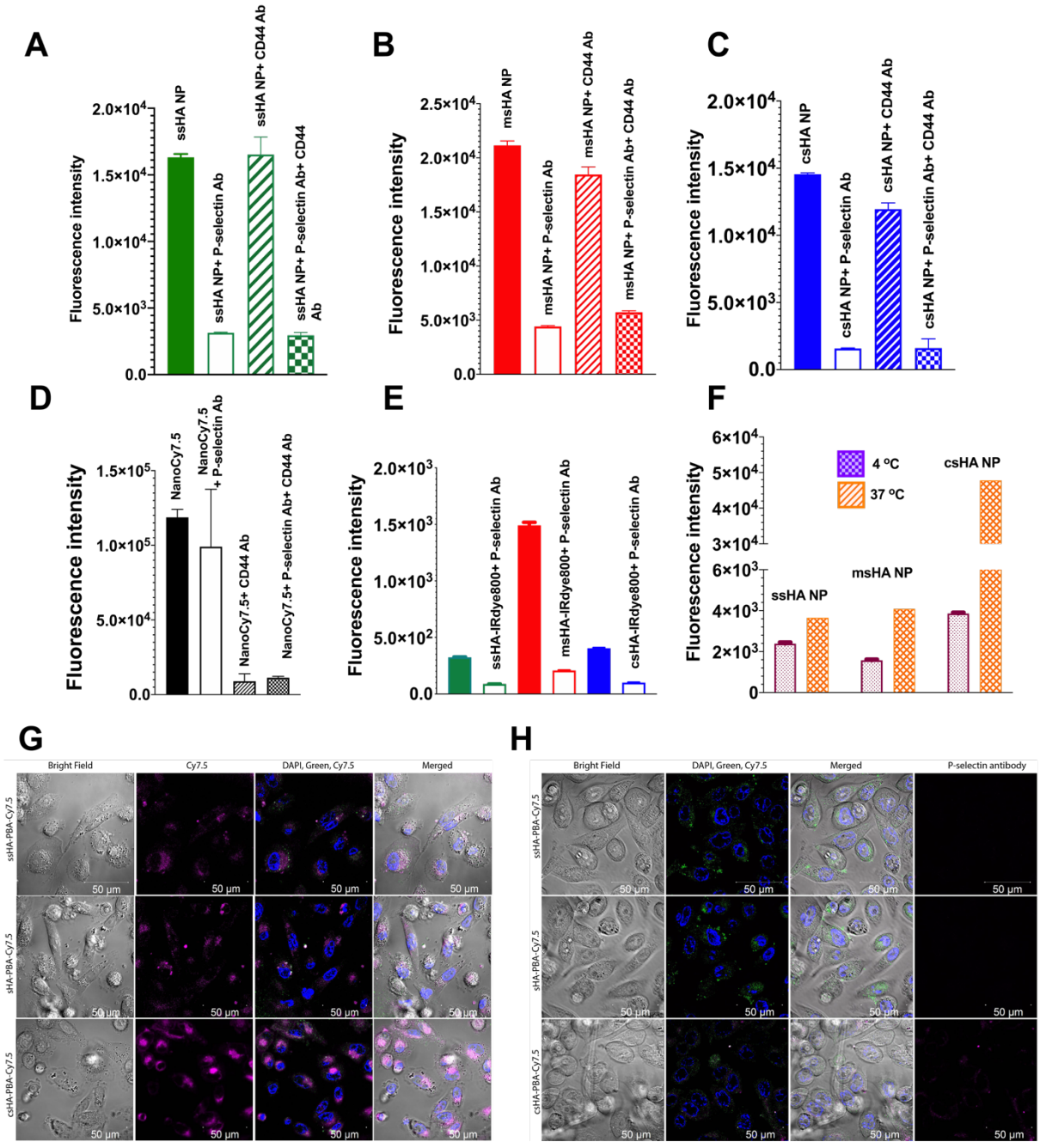

Figure 5: (A-D) Evaluation of the uptake of NanoCy.5 and NanoCy7.5 in presence of anti-hCD44 and anti-hP-selectin antibody in S2-013 cells. (E) Evaluation of uptake of ssHA, msHA, csHA-IRDye800 conjugates in presence of anti-hP-selectin antibody in S2-013 cells. (F) Temperature dependent effect on the uptake of three derivatives of HA NPs system at $4^{O}C$ vs $37^{O}C$ by FACS. (G-

H) CSLM images acquired on S2-013 cells with DAPI (blue; nucleus), NIR (Cy7.5), Green (endosomal marker Rab5 protein) staining to visualize uptake in presence and absence of anti-hP-antibody. The scale bar represents 50 μm on all images.

In order to confirm the uptake of sNanoCy7.5 via P-selectin, P-selectin and CD44 knockout (KO) cells were generated by CRISP/Cas9 system (**Table 1**). msHA based nanoparticles were selected from the three derivatives for the study due to DS of roughly 2, which ensured retaining their specificities for both P-selectin and CD44. Such characteristics are beneficial for spatiotemporal cancer cell targeting. CRISPR/Cas9 system was used to knockout the expression of the individual proteins in S2-013 cells to evaluate binding of sulfated and non-sulfated HA nanoparticles (sNanoCy7.5 and NanoCy7.5). Guide RNA sequences in (**Table 1**) were selected in CRISPR/Cas9 to generate P-selectin and CD44 KO cells. Western blot and FACS analysis confirmed the elimination of individual protein expression (**Fig. 6 A-B**). Knocking out P-selectin further validated its importance in the uptake of sNanoCy.5 vs NanoCy7.5, indicating that HA plays no significant role in P-selectin targeting. However, sNanoCy7.5 also showed a slight decrease in uptake in CD44 KO cells, indicating that the sNanoCy7.5 NPs do exhibit some degree of CD44 mediated targeting (**Fig. 6**). This confirms that sNanoCy7.5 shows both P-selectin and CD44 mediated uptake in S2-013 cells.

Imaging applications were also explored in 3D S2-013 tumoroid model to observe higher uptake of polymer-IRDye800 conjugate compared to free dye, indicating improved delivery of imaging agent (**Fig. 5b**). The results are in accordance to previous reports on targeted sulfated systems displaying P-selectin mediated uptake. Modulating properties from traditional CD44 targeting HA to affinity towards P-selectin can now be achieved by precise synthetic modifications on the polysaccharide backbone.

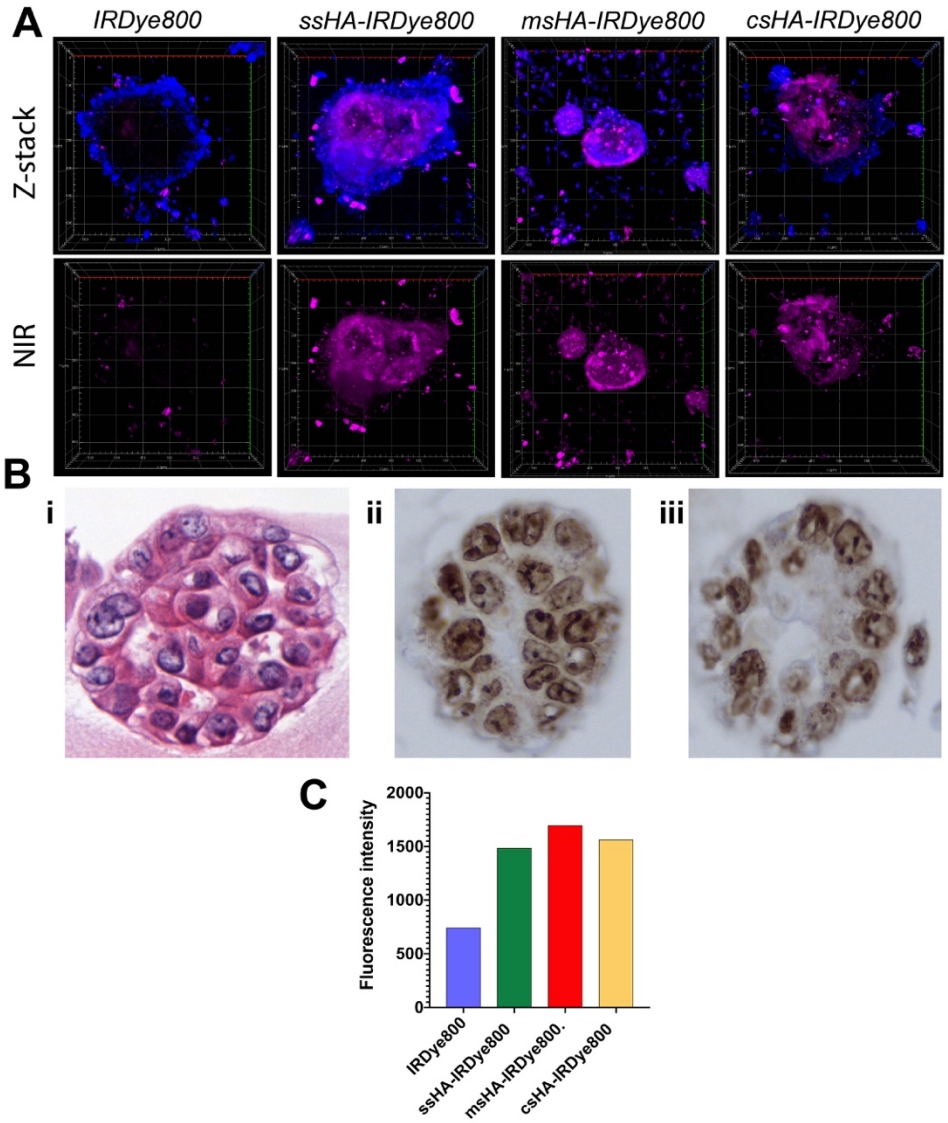

Fig 5b: (A) Z-stack model analysis of 3D-tumoroid model of S2-013 for uptake of IRDye800 by visualization of signal in NIR window using confocal laser scanning microscopy. (B) (i) H&E staining of 3D-tumoroid of S2-013, (ii) Evaluation of CD44 positive staining in tumoroids, (iii) Evaluation of P-selectin positive staining in

tumoroids. (C) FACS analysis on lysed tumoroid for quantification of NIR signal from each of the conjugate syst

Name	sgRNA sequence	Length
CD44 sgRNA 1	TCGCTACAGCATCTCTCGGA	20
CD44 sgRNA 3	AATATAACCTGCCGCTTTGC	20
SELP sgRNA 2	CAGTTCATGAGCACGTGTTG	20
SELP sgRNA 3	TGTAGTTCCCGATGGTCTCG	20

Table 1: CD44 and SELP guide RNA sequences used for CRISPR/Cas9 KO studies

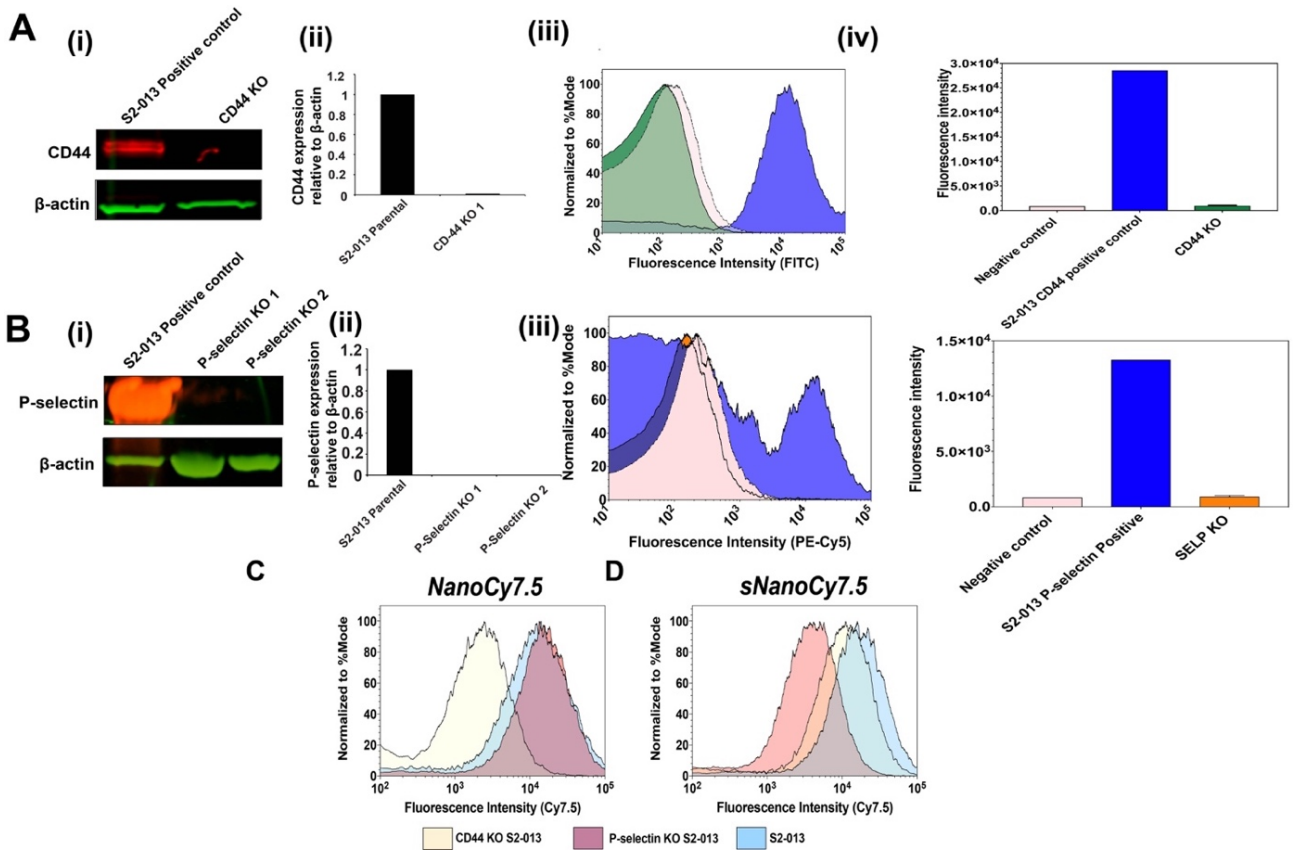

Figure 6: (A-B) (i) Protein expression by western blot analysis on KO cells derived from CRISPR/Cas9 system. (ii) Signal quantification from NIR fluorescent western analysis for the KO S2-013 cells. (iii) Confirmation of KO cells by FACS analysis using anti-hCD44 and anti-hP-selectin antibodies for cell surface protein expression on S2-013 KO cells. (iv) Quantification of FACS signal. (C) Uptake analysis of NanoCy7.5 and sNanoCy7.5 on P-selectin and CD44 KO cells by FACS.

3.5. Relative biodistribution and image-guided surgery

An *in vivo* tumor model study was performed to determine if sulfation altered tumor update and the overall relative biodistribution of the injected NPs. For this proof of principle study, the S2-013 cell line, which positively expresses both CD44 and P-selectin, was selected since pancreatic cancer is one of the deadliest ones with a median overall survival of 15 months and 13.5% survival rate in 5 years[49]. Above from *in silico* to *in vitro* data, we demonstrated that by controlling the sulfation patterns on HA, preferential interactions with receptor specific proteins in the tumor microenvironment can be tuned by understanding biophysical and biochemical interactions. Binding properties can be fine-tuned by altering chemical groups, size, and shape of NPs which will impact the biodistribution and tumor infiltration[50]. Recently, P-selectin targeting has gained immense importance in cancer-targeted therapeutics. Shamay et al.[19] showed that P-selectin specific fucoidan-based drug delivery system loaded with chemotherapeutics (mitogen activated protein kinase kinase inhibitors) had superior antitumor efficacy. Ferber et al.[26] used sulfated dendritic polyglycerol as nanocarrier for paclitaxel to target P-selectin in glioblastoma cells to treat glioblastoma with increased therapeutic efficacy. Another multi-stimuli fucoidan/protamine nanoparticle[51] reported by Lu et al. showed improved inhibitory effect of doxorubicin loaded fucoidan/protamine nanoparticle targeting P-selectin delivery against highly metastatic breast cancer MDA-MB-231 and MDA-MB-468 cells. Surprisingly in the report published by Shamay et al.[19] revealed high expression of P-selectin in multiple tumors by analyzing RNASeq

data from The Cancer Genome Atlas (TCGA) database. The TCGA database reported amplification in melanoma, liver, bladder, ovarian, lung adenocarcinoma, and breast cancers. Also, similar analysis from TCGA shown in report published by Ferber et al.[26] showed that high expression of P-selectin positively correlates with poor patient survival. In almost all the published reports, normal healthy tissues show relatively absence or lower expression of P-selectin. This corroborates the importance of P-selectin targeting and the importance of application of fluorescence image-guided surgery to accurately resect only the cancerous tissue to avoid relapse.

In this work, the relative biodistribution of near infrared (NIR) nano-formulations of HA, sulfated HA (sHA), and Cy7.5 dye alone was compared in S2-013 xenograft tumors grown subcutaneously in nude mice using LI-COR Trilogy imaging system. After 24 h post injections of the contrast agents, organs were harvested from mice following necropsy to evaluated biodistribution properties using the LI-COR imaging system represented in **Fig 7B**. Relative biodistribution was calculated as signal to noise ratio (SNR) quantified from NIR fluorescent intensities of each organs corrected for its area[32]. The overall NIR fluorescent signal emitted from S2-013 tumors was higher for sNanoCy7.5 compared to NanoCy7.5 and dye alone, and SNR of NanoCy7.5 was higher compared to Cy7.5, which is in accordance to previously published reports[32]. Higher SNR for organs was observed in liver, spleen, and kidney, demonstrating RES system uptake as an important limitation of HA-based targeted delivery. Interestingly, sNanoCy7.5 had a 2-fold higher SNR compared to NanoCy7.5 in

the tumor, suggesting that targeting P-selectin may be a potential added benefit along with CD44 targeting. Lower liver SNR, higher spleen SNR, and marginally different kidney SNR of sNanoCy7.5 compared to NanoCy7.5 indicates influence of different formulation parameters directly impacting the biodistribution profiles (**Figure S9**). It should be noted that both nanoformulations included a chemical conjugated imaging dye instead of a physically entrapped moiety, directly implying that the targeting ability via P-selectin and CD44 are the major driving factors for tumor accumulation. Image contrast and change of biodistribution was compared to surrounding high background tissues such as liver, spleen, kidney, pancreas, and surrounding muscle in the tumor location. Tumor-to-muscle ratio was significantly higher for sNanoCy7.5 compared to NanoCy7.5 and Cy7.5. Higher tumor to muscle ratio was observed for NanoCy7.5 compared to Cy7.5 in breast and prostate cancer model[33], this effect could be due to the heterogeneity of cancer model and disease type. sNanoCy7.5 also displayed higher tumor-to-liver SNR ratios compared to other groups, no significant differences were found between tumor-to-kidney, tumor-to-spleen, tumor-to-pancreas ratios (**Figure S9**). The NanoCy7.5 and sNanoCy7.5 formulations were compared with Cy7.5 dye alone for applications in image-guided surgery. In previously published literature, intraoperative imaging was successfully performed using NIR fluorescence detected by the image-guided surgery system in orthotopic 4T1 and PC3 using 1.2 nmol/mouse for Cy7.5[32,33]. Keeping the dye concentrations constant for both NanoCy7.5 and sNanoCy7.5 (1.2 nmol/mouse), the tumors were readily detected with 8 mW “low” excitation power, given the high quantum yield of Cy7.5

compared to other dyes such as indocyanine green. Whole-animal fluorescence imaging provided by LI-COR (**Figure 7**) and Lab FLARE RP1 Curadel demonstrated that both NanoCy7.5 and sNanoCy7.5 could detect tumors in the NIR window (laser excitation on 785 nm), whereas surrounding skeletal muscle showed no NIR signal (**Figure 7**). Whole body imaging after 24 h demonstrated brighter signal from tumor injected with sNanoCy7.5 compared to NanoCy7.5. Semi-quantitative analysis of spectroscopic signatures of NIR fluorescence from spectroscopic pen showed that sNanoCy7.5 resulted in 2-fold stronger signal, however not significant, based on AUC of the intensity vs wavelength curve, compared to NanoCy7.5 (**Figure 7a**). Taken together, the results could potentially imply that a higher payload of imaging agent was being delivered due to plausible spatiotemporal targeting of both CD44 and P-selectin. However, it is to be taken into consideration that importance of both P-selectin and CD44 expression on tumor cells for targeting would depend on accessibility, permeability, and morphology of the tumor microenvironment. Nevertheless, precise understanding of the targeted system in the tumor warrants further investigations.

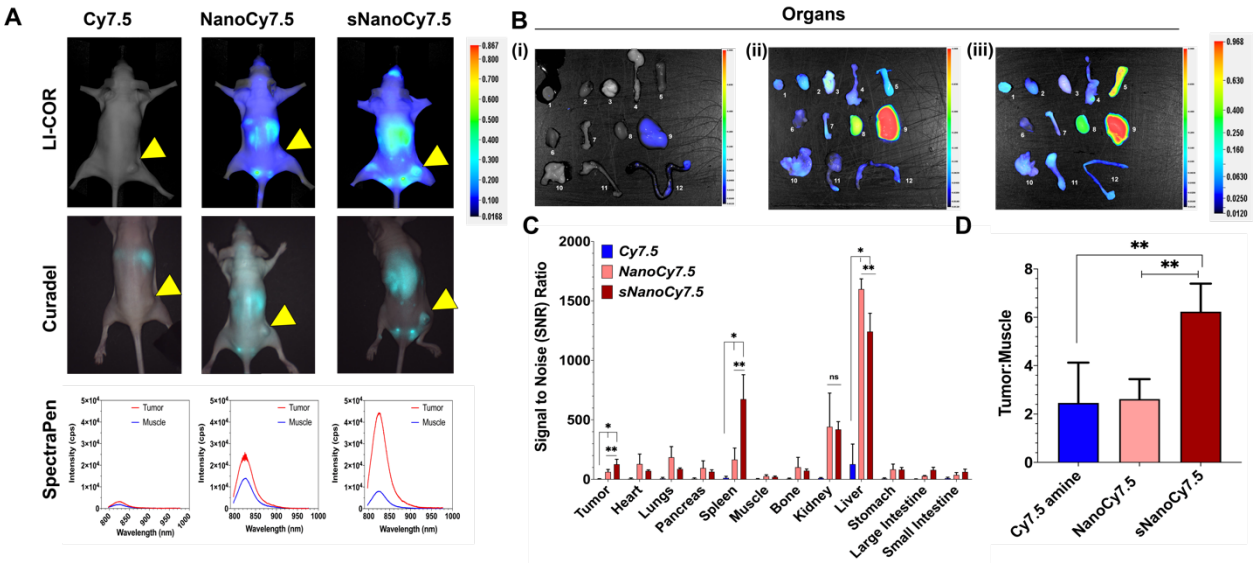

Figure 7: Biodistribution of contrast agents (Cy7.5, NanoCy7.5, and sNanoCy7.5). (A) Representative whole animal NIR imaging using LI-COR and Curadel system after 24 h post intravenous injection of the contrast agent. Spectroscopic signals from excised tumor and muscle (ie quadriceps femoris muscle) of a representative mouse from each of the groups shown at the bottom. (yellow arrow indicates the tumor) (B) Representative NIR fluorescence images from excised *ex vivo* harvested 24 h after intravenous administration of indicated contrast agent (1.2 nmol of Cy7.5/mouse for Cy7.5-amine, NanoCy7.5, and sNanoCy7.5). All images were collected at 800 nm channel overlaid onto the brightfield photograph from the Pearl Trilogy imaging system. Organ labels: 1: tumor(s), 2: heart, 3: Lung, 4: pancreas, 5: spleen; 6: muscle (i.e. quadriceps femoris muscle), 7: Bone, 8: Kidney. 9: liver, 10: Stomach, 11: Small intestine, 12: Large intestine, (C) Quantitative summary of fluorescence intensity of organs where bars represent the average pixel signal-to-noise ratio (SNR; mean ± s.d) of N = 3 mice, *$p < 0.05$, **$p < 0.01$, unpaired multiple t-test. (D) Tumor-to-muscle

ratios comparison across the groups, *$p < 0.05$, **$p < 0.01$, unpaired multiple t-test.

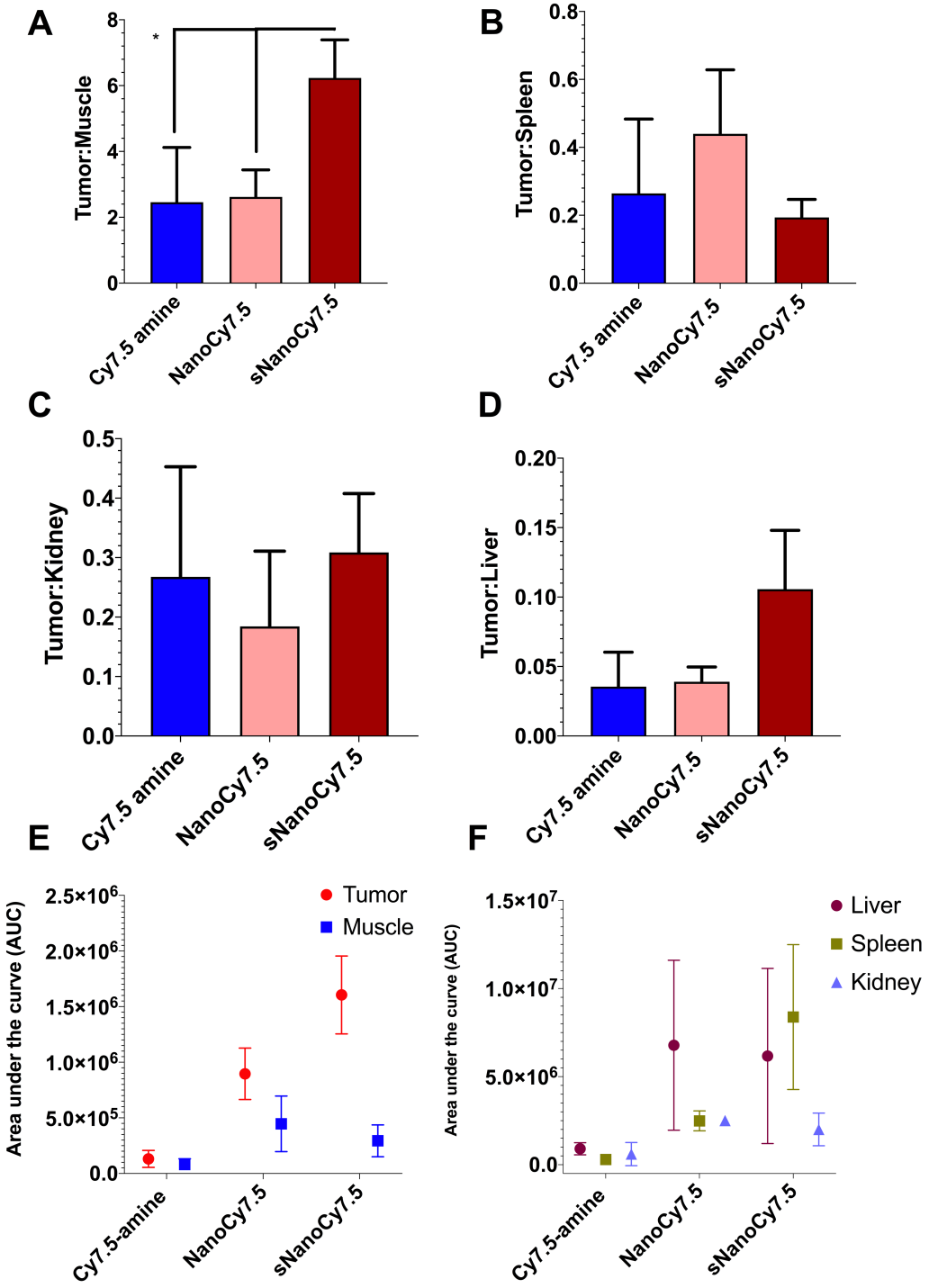

Fig 7a: Tumor-to-organ ratios in S2-013 tumor bearing nude mice. (A) Tumor-to-muscle, (B) tumor-to-spleen, (C) tumor-to-kidney, and (D) tumor-to-liver SNR ratios obtained from the ex vivo imaging in Fig. 2. *$p < 0.05$, **$p < 0.01$, ***$p < 0.001$, ****$p < 0.0001$ one-way ANOVA with Tukey's multiple comparisons test. (E-F)

Summary of spectroscopic signals of excised tumor and muscle based on AUC of the intensity vs. wavelength curves. Values are expressed as mean ± SD (n = 3 for all other groups). *$p < 0.05$, **$p < 0.01$; as determined by two-way ANOVA with Tukey's method for multiple comparisons. #$p < 0.05$; as determined by unpaired t-test.

The distribution and targeting capability of sulfated and non-sulfated system was studied by histological analysis of frozen tumor sections was performed by confocal imaging for distribution and localization of NIR dye. Sections were counter-stained for P-selectin, CD44, and CD31 expression to corroborate the targeting capabilities of sulfated and non-sulfated HA nanoparticles. Twenty-four later, substantial amount of contrast agent was still located in tumors, as exhibited by a strong fluorescence signal. To understand where sNanoCy7.5 and NanoCy7.5 locates within the tumor, we stained S2-013 tumor sections for P-selectin, CD44, and CD31. P-selectin and CD44 were highly expressed in S2-013 tumors as depicted in **Fig. 8, Fig. 8a**. Higher NIR fluorescence was observed from tumors injected with sNanoCy7.5, which correlates with highly colocalization of P-selectin and CD44 expression. At the same time, NanoCy7.5 uptake in the tumor only correlates with high CD44 expression and not P-selectin expression. CD31 staining showed that S2-013 tumors are moderately vascularized (**Fig. 8, Fig. 8a**). This indicates that sNanoCy7.5 tumor uptake in cancer cells was highly dependent on both CD44 and P-selectin expression profile whereas NanoCy7.5 was only dependent of CD44 expression. Thus, uptake of sNanoCy7.5 was greatly enhanced compared to NanoCy7.5, illustrating the importance of modulating targeting properties of HA. This suggests that the dual-targeted sulfated HA system works on both P-selectin and CD44 expressing cancer cells.

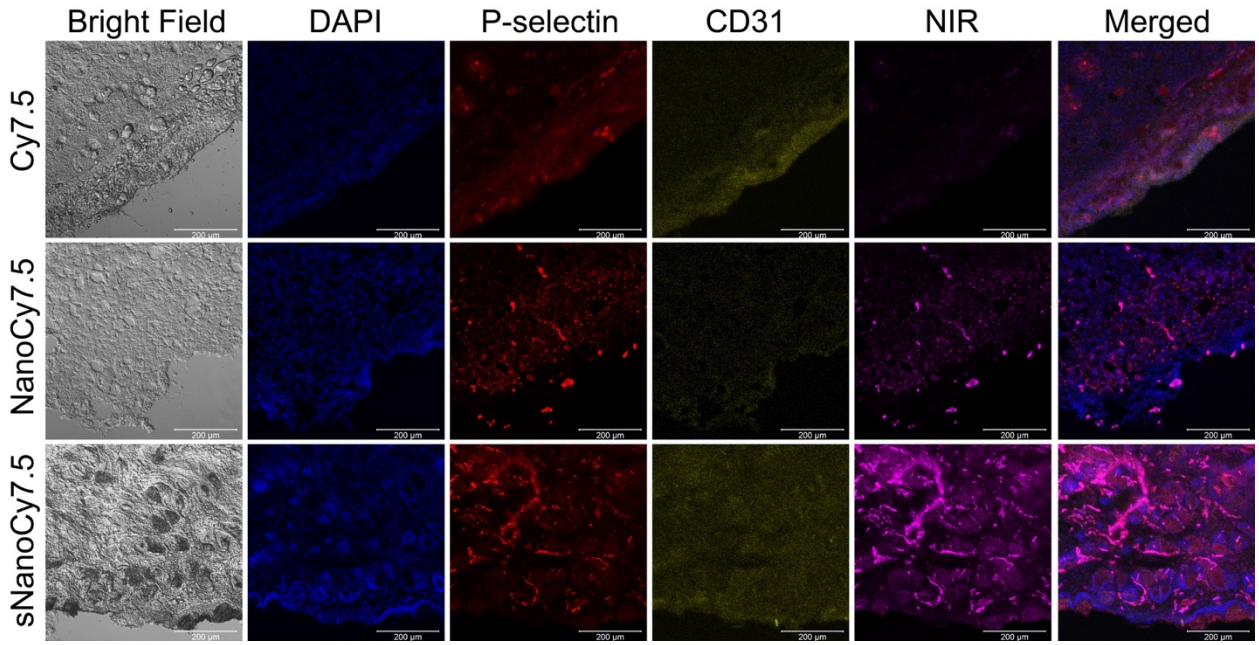

Figure 8: NIR distribution in tumors analyzed by confocal laser scanning microscopy after harvesting, fixing, and sectioning. Representative tumor sections were stained with DAPI (nuclear stain), anti-hP-selectin antibody (a cell surface protein, P-selectin), and anti-CD31 (endothelial marker).

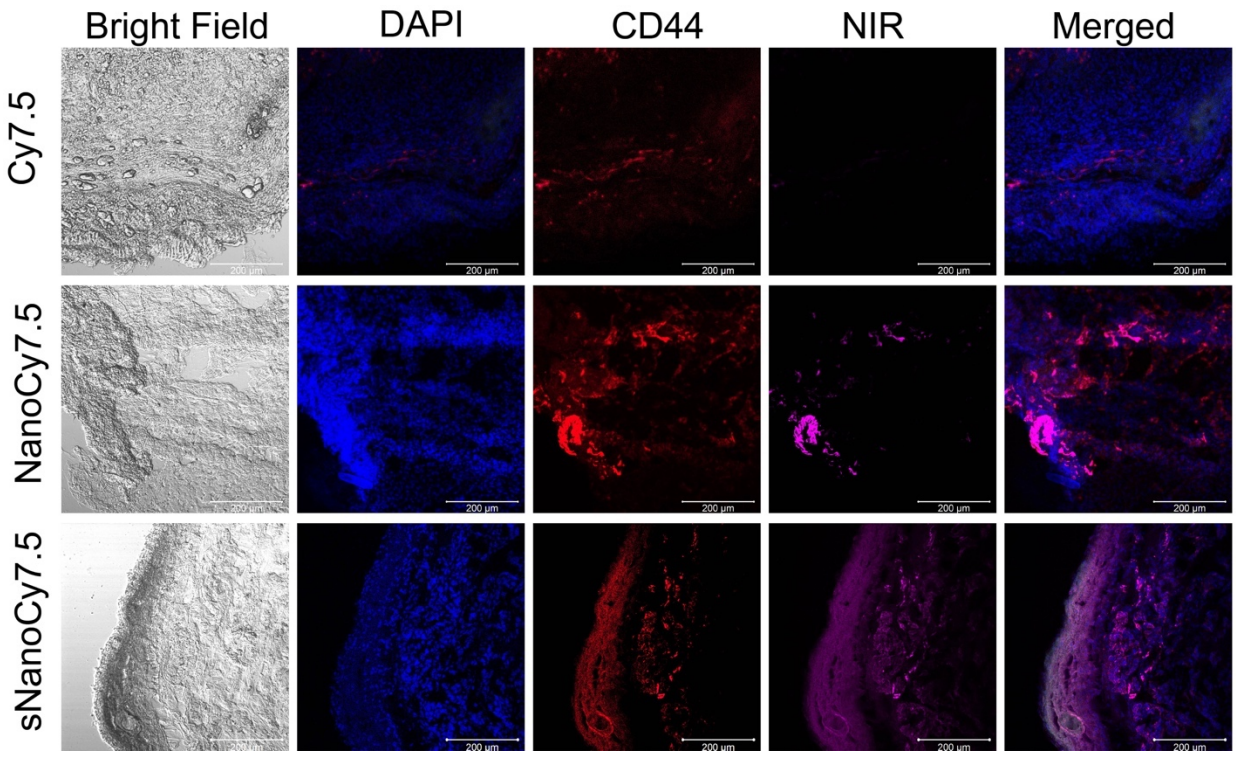

Figure 8a: NIR distribution in tumors analyzed by confocal laser scanning microscopy after harvesting, fixing, and sectioning. Representative tumor sections were stained with DAPI (nuclear stain), anti-hCD44 antibody (a cell surface protein, CD44).

Conclusions

We demonstrated the potential of HA sulfation to influence its binding affinity to P-selectin, which also applies to nanoparticles derived from sulfated HA. Assessment of CD44 and P-selectin targeting modulation by sulfated HA was studied by *in silico* docking computational algorithms, binding measurements by FP, *in vitro* binding assessments by flow cytometry, and validation by CRISPR/Cas9 KO system, and *in vivo* evaluation by fluorescence image-guided surgery. This approach can be applied to study a wide range of tumor types expressing both CD44 and P-selectin, considering the dynamic microenvironment of most cancers. Targeting expression of specific biomarkers/pharmacophores can be utilized by implementing a “dual-edge technique” over single-targeted for better therapeutic outcomes for chemotherapeutics and delivery of imaging agents. In summary, the data herein suggests that sulfated HA is a promising candidate for improved imaging through dual-targeting of P-selectin and CD44 biomarkers. Future studies for this work entails detection of metastatic lesions, using different cancer orthotopic models, deciphering changes in pharmacokinetic profiles[52], and survival analysis after tumor removal using image-guide surgery mandates the study of this classes of synthetic derivatives of HA.

References:

1. Shuvaev, V. V., Brenner, J. S. & Muzykantov, V. R. Targeted endothelial nanomedicine for common acute pathological conditions. *J. Control. Release* (2015). doi:10.1016/j.jconrel.2015.09.055
2. Alavi, M., Karimi, N. & Safaei, M. Application of various types of liposomes in drug delivery systems. *Advanced Pharmaceutical Bulletin* (2017). doi:10.15171/apb.2017.002
3. Mendes, L. P., Pan, J. & Torchilin, V. P. Dendrimers as nanocarriers for nucleic acid and drug delivery in cancer therapy. *Molecules* (2017). doi:10.3390/molecules22091401
4. Matea, C. T. *et al.* Quantum dots in imaging, drug delivery and sensor applications. *Int. J. Nanomedicine* (2017). doi:10.2147/IJN.S138624
5. Zhu, S., Song, Y., Shao, J., Zhao, X. & Yang, B. Non-conjugated polymer dots with crosslink-enhanced emission in the absence of fluorophore units. *Angew. Chemie - Int. Ed.* (2015). doi:10.1002/anie.201504951
6. Yang, L. *et al.* Doxorubicin conjugated functionalizable carbon dots for nucleus targeted delivery and enhanced therapeutic efficacy. *Nanoscale* (2016). doi:10.1039/c6nr00247a
7. Dan, N. *et al.* Antibody-drug conjugates for cancer therapy: Chemistry to clinical implications. *Pharmaceuticals* (2018). doi:10.3390/ph11020032
8. Elzoghby, A. O., Hemasa, A. L. & Freag, M. S. Hybrid protein-inorganic nanoparticles: From tumor-targeted drug delivery to cancer imaging. *Journal of Controlled Release* (2016). doi:10.1016/j.jconrel.2016.10.023
9. Zhang, J., Tang, H., Liu, Z. & Chen, B. Effects of major parameters of nanoparticles on their physical and chemical properties and recent application of nanodrug delivery system in targeted chemotherapy. *International Journal of Nanomedicine* (2017). doi:10.2147/IJN.S148359
10. Alexis, F., Pridgen, E., Molnar, L. K. & Farokhzad, O. C. Factors affecting the clearance and biodistribution of polymeric nanoparticles. in *Molecular Pharmaceutics* (2008). doi:10.1021/mp800051m
11. Anselmo, A. C. & Mitragotri, S. Impact of particle elasticity on particle-based drug delivery systems. *Advanced Drug Delivery Reviews* (2017). doi:10.1016/j.addr.2016.01.007
12. Ding, H. M. & Ma, Y. Q. Theoretical and computational investigations of nanoparticle-biomembrane interactions in cellular delivery. *Small* (2015). doi:10.1002/smll.201401943
13. Hare, J. I. *et al.* Challenges and strategies in anti-cancer nanomedicine development: An industry perspective. *Advanced Drug Delivery Reviews* (2017). doi:10.1016/j.addr.2016.04.025
14. Maeda, H., Nakamura, H. & Fang, J. The EPR effect for macromolecular drug delivery to solid tumors: Improvement of tumor uptake, lowering of systemic toxicity, and distinct tumor imaging in vivo. *Advanced Drug Delivery Reviews* (2013). doi:10.1016/j.addr.2012.10.002
15. Yang, L. *et al.* Receptor-targeted nanoparticles for in vivo imaging of breast cancer. *Clin. Cancer Res.* (2009). doi:10.1158/1078-0432.CCR-08-3289

16. Carter, T., Mulholland, P. & Chester, K. Antibody-targeted nanoparticles for cancer treatment. *Immunotherapy* (2016). doi:10.2217/imt.16.11
17. Geier, E. G. *et al.* Structure-based ligand discovery for the Large-neutral Amino Acid Transporter 1, LAT-1. *Proc. Natl. Acad. Sci.* (2013). doi:10.1073/pnas.1218165110
18. Yan, Y., Zuo, X. & Wei, D. Concise Review: Emerging Role of CD44 in Cancer Stem Cells: A Promising Biomarker and Therapeutic Target. *Stem Cells Transl. Med.* (2015). doi:10.5966/sctm.2015-0048
19. Shamay, Y. *et al.* P-selectin is a nanotherapeutic delivery target in the tumor microenvironment. *Sci. Transl. Med.* (2016). doi:10.1126/scitranslmed.aaf7374
20. Stella, B. *et al.* Design of folic acid-conjugated nanoparticles for drug targeting. *J. Pharm. Sci.* (2000). doi:10.1002/1520-6017(200011)89:11<1452::AID-JPS8>3.0.CO;2-P
21. Gorain, B. *et al.* Overexpressed Receptors and Proteins in Lung Cancer. in *Nanotechnology-Based Targeted Drug Delivery Systems for Lung Cancer* (2019). doi:10.1016/b978-0-12-815720-6.00003-4
22. Kedmi, R. & Peer, D. Zooming in on selectins in cancer. *Sci. Transl. Med.* (2016). doi:10.1126/scitranslmed.aag1802
23. Iwamura, T. *et al.* P-selectin expression in a metastatic pancreatic tumor cell line (SUIT- 2). *Cancer Res.* (1997).
24. Mizrachi, A. *et al.* Tumour-specific PI3K inhibition via nanoparticle-targeted delivery in head and neck squamous cell carcinoma. *Nat. Commun.* (2017). doi:10.1038/ncomms14292
25. Ferber, S. *et al.* Co-targeting the tumor endothelium and P-selectin-expressing glioblastoma cells leads to a remarkable therapeutic outcome. *Elife* **6**, 1–34 (2017).
26. van der Meel, R., Vehmeijer, L. J. C., Kok, R. J., Storm, G. & van Gaal, E. V. B. Ligand-targeted particulate nanomedicines undergoing clinical evaluation: Current status. *Advanced Drug Delivery Reviews* (2013). doi:10.1016/j.addr.2013.08.012
27. DiGiovanna, M. P. *et al.* Relationship of epidermal growth factor receptor expression to ErbB-2 signaling activity and prognosis in breast cancer patients. *J. Clin. Oncol.* (2005). doi:10.1200/JCO.2005.09.055
28. Doolittle, E. *et al.* Spatiotemporal Targeting of a Dual-Ligand Nanoparticle to Cancer Metastasis. *ACS Nano* (2015). doi:10.1021/acsnano.5b01552
29. Woelke, A. L. *et al.* Understanding selectin counter-receptor binding from electrostatic energy computations and experimental binding studies. *J. Phys. Chem. B* (2013). doi:10.1021/jp4099123
30. Somers, W. S., Tang, J., Shaw, G. D. & Camphausen, R. T. Insights into the molecular basis of leukocyte tethering and rolling revealed by structures of P- and E-seiectin bound to SLe(X) and PSGL-1. *Cell* (2000). doi:10.1016/S0092-8674(00)00138-0
31. Weinhart, M., Gröger, D., Enders, S., Dernedde, J. & Haag, R. Synthesis of dendritic polyglycerol anions and their efficiency toward L-selectin inhibition. *Biomacromolecules* (2011). doi:10.1021/bm200250f

32. Bhattacharya, D. S. *et al.* Impact of structurally modifying hyaluronic acid on CD44 interaction. *J. Mater. Chem. B* (2017). doi:10.1039/c7tb01895a
33. Lim, D.-K., Wylie, R. G., Langer, R. & Kohane, D. S. Selective binding of C-6 OH sulfated hyaluronic acid to the angiogenic isoform of VEGF165. *Biomaterials* **77**, 130–138 (2016).
34. Hill, T. K. *et al.* Near infrared fluorescent nanoparticles derived from hyaluronic acid improve tumor contrast for image-guided surgery. *Theranostics* **6**, 2314–2328 (2016).
35. Bhattacharya, D. S. *et al.* Impact of structurally modifying hyaluronic acid on CD44 interaction. *J. Mater. Chem. B* (2017). doi:10.1039/C7TB01895A
36. Banerji, S. *et al.* Structures of the Cd44-hyaluronan complex provide insight into a fundamental carbohydrate-protein interaction. *Nat. Struct. Mol. Biol.* **14**, 234–9 (2007).
37. Plazinski, W. *et al.* Interactions between CD44 protein and hyaluronan: insights from the computational study. *Mol. BioSyst.* **8**, 543–547 (2012).
38. Mestechkina, N. M. & Shcherbukhin, V. D. Sulfated polysaccharides and their anticoagulant activity: A review. *Appl. Biochem. Microbiol.* (2010). doi:10.1134/s000368381003004x
39. Magnani, A., Lamponi, S., Consumi, M. & Barbucci, R. Biological performance of two materials based on sulfated hyaluronic acid and polyurethane. *J. Mater. Chem.* (1999). doi:10.1039/a903581h
40. Grosdidier, A., Zoete, V. & Michielin, O. SwissDock, a protein-small molecule docking web service based on EADock DSS. *Nucleic Acids Res.* **39**, (2011).
41. Morris, G. & Huey, R. AutoDock4 and AutoDockTools4: Automated docking with selective receptor flexibility. *J. …* **30**, 2785–2791 (2009).
42. Hill, T. K. *et al.* Indocyanine green-loaded nanoparticles for image-guided tumor surgery. *Bioconjug. Chem.* **26**, 294–303 (2015).
43. Lakowicz, J. R. Fluorescence polarization. *Princ. Fluoresc. Spectrosc.* 112–151 (1983). doi:10.1007/s00216-011-5434-0
44. Rossi, A. M. & Taylor, C. W. Analysis of protein-ligand interactions by fluorescence polarization. *Nat. Protoc.* (2011). doi:10.1038/nprot.2011.305
45. Bachelet, L. *et al.* Affinity of low molecular weight fucoidan for P-selectin triggers its binding to activated human platelets. *Biochim. Biophys. Acta - Gen. Subj.* **1790**, 141–146 (2009).
46. Fritzsche, J. *et al.* The influence of various structural parameters of semisynthetic sulfated polysaccharides on the P-selectin inhibitory capacity. *Biochem. Pharmacol.* **72**, 474–485 (2006).
47. Qi, B. *et al.* Indocyanine green loaded hyaluronan-derived nanoparticles for fluorescence-enhanced surgical imaging of pancreatic cancer. *Nanomedicine Nanotechnology, Biol. Med.* **14**, 769–780 (2018).
48. Petros, R. A. & Desimone, J. M. Strategies in the design of nanoparticles for therapeutic applications. *Nature Reviews Drug Discovery* (2010). doi:10.1038/nrd2591

49. Lu, K. Y. *et al.* Development of a new type of multifunctional fucoidan-based nanoparticles for anticancer drug delivery. *Carbohydr. Polym.* (2017). doi:10.1016/j.carbpol.2017.02.065
50. Souchek, J. J. *et al.* Hyaluronic acid formulation of near infrared fluorophores optimizes surgical imaging in a prostate tumor xenograft. *Acta Biomater.* (2018). doi:10.1016/j.actbio.2018.06.016
51. Kanvinde, S. *et al.* Pharmacokinetics and efficacy of orally administered polymeric chloroquine as macromolecular drug in the treatment of inflammatory bowel disease. *Acta Biomater.* (2018). doi:10.1016/j.actbio.2018.10.027

CHAPTER IV:

ENGINEERING NOVEL FLUORESCENT NANOPARTICLES FROM NATURALLY DERIVED HYALURONIC ACID AND AMINO ACIDS FOR BIOMEDICAL APPLICATIONS

ABSTRACT

Nonconjugated fluorescent polymers have been increasingly investigated to improve the biocompatibility and theranostic application of conventional fluorescent materials. However, the accessibility of such systems remains challenging due to the scarcity of non-toxic nonconjugated nanomaterials and lack of explanation for the fluorescence mechanisms. Herein, we develop a novel fluorescent material by introducing sub-fluorophore imine groups (-C=N) by chemical conjugation/physical immobilization of naturally available hydrophobic amino acids to the hyaluronic acid (HA) polymer chain. This *in-situ* self-assembly was carried out under one-pot “green chemistry” conditions and resulted in enhancement of the fluorescence intensity of novel fluorescent organic nanoparticle (FONP) species. The FONPs exhibited high water solubility due to the existence of hydrophilic functional groups on its surface, acceptable stability profiles, superior biocompatibility, and high emission quantum yield. The FONPs emitted strong excitation-dependent fluorescence. In addition, our FONPs demonstrated drug carrier properties with enhanced drug loading and delivery of the anticancer drug doxorubicin (DOX) in contrast to the free DOX in cancer cells and 3D tumor spheroids. Results demonstrate the efficacy of a novel fluorescent

HA-based multifunctional system, with potential future applications in image-guided drug delivery.

Keywords: Non-conjugated fluorescent polymer dots, hyaluronic acid, amino acids, biocompatible, drug delivery vehicle.

Graphical abstract

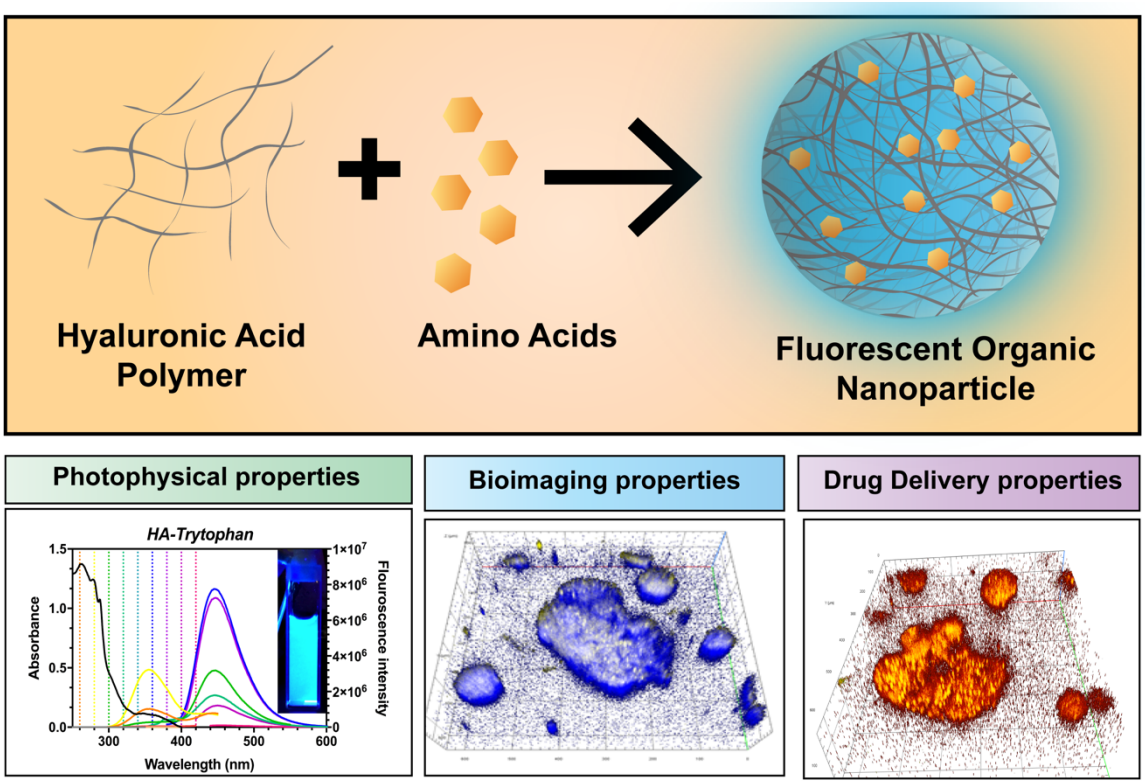

Introduction

In recent decades, there has been immense interest in the development of functional fluorescent polymeric nanomaterials for bioimaging, drug delivery, bioanalysis, and chemical sensors due to their biocompatibility, green synthetic approaches, and easy functionalization[1,2]. Previously, development of fluorescent organic nanomaterials involved sophisticated time-consuming synthetic steps, complicated purification techniques, and use of harsh non-environmentally friendly organic solvents. Other drawbacks of conventional fluorescent nanomaterials include, limited scale-up interventions and poor water solubility. These drawbacks in development bolstered research into exploring alternative strategies to generate fluorescent nanomaterials without the need for chemically conjugating a fluorescent dye. Therefore, the genesis of a non-conjugated polymer dots (NCPD) was initiated by many researchers in past years by polymerization, cross-linking, hydrothermal, and physical approaches. These methods resulted in the generation of highly water soluble materials with bright fluorescence and improved biocompatibility[3].

NCPDs do not typically possess a conjugated fluorescent dye[4] but instead contain numerous multiple sub-fluorophore chemical groups (-C=N, -N=O). These groups upon suitable immobilization in the polymeric network, show increased fluorescent properties. The heteroatom-containing double bonds are traditionally not regarded as fluorophores, which make it uniquely appealing. A non-fluorescent precursor material can be used to form a novel fluorescent

material by precisely tuning the chemical reaction for applications in chemical and biological fields. The mechanism for the generation of fluorescence in a non-conjugated system is referred to as crosslinked-enhanced emission (CEE)[3], which is different from aggregation-induced emission (AIE)[5,6]. CEE functions when a small amine-rich organic molecule upon hydrothermal reaction conditions crosslinks into a large polymeric matrix leading to enhanced fluorescence due to decreased vibrations and rotations of sub-fluorophores[7].

Recently, several groups have reported the use of the hydrothermal method with natural materials, such as chitosan[8], PEI-glucose[9], PEI-sucrose[10], PEI-formaldehyde[11], PEI-carbon tetrachloride[12], PEI-PLA, PEI-starch[13], honey[14], ginger[15], phenol-hexamethylenetetramine[16,17], ethylenediamine-carbon tetrachloride, polydopamine[18], and cocoon silk[19], to prepare water-soluble fluorescent NCPDs. During the hydrothermal treatment, the amine-rich precursor and large saccharide molecule react to form fluorescent aggregated structures for use as biomaterials.

In this work, we contributed to the field of non-conjugated fluorescent polymeric nanoparticles by using naturally derived hyaluronic acid (HA) and various amino acids to synthesize self-assembling FONPs via a Schiff-based conjugation reaction (Scheme 1). Water-soluble blue FONPs were fabricated under mild conditions without the need for any harmful organic solvents. Furthermore, by utilizing spectroscopy, the fluorescence origin of HA-derived FONPs have been proposed and explored. In this study, we not only have created

a new class of biocompatible fluorescent nanomaterials with excellent fluorescent properties and good water dispersibility but also have demonstrated application in bioimaging and drug delivery platforms.

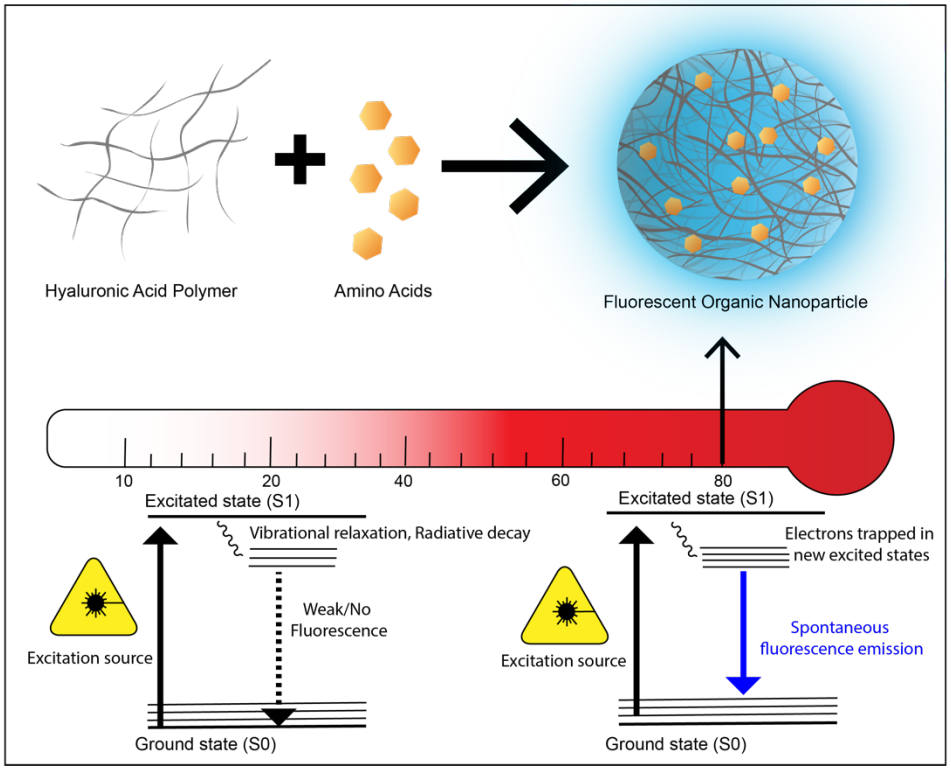

Scheme 1: Schematic representation for generation of hyaluronic acid based FONPs.

Material and Methods

Sodium hyaluronate, 10 kDa, was purchased from Lifecore Biomedical (Chaska, MN). All water was purified with Barnsteadt Ultrapuret Diamond system (Thermo Scientific; Waltham, MN). 96-well tissue culture plates (Falcon), 12-well tissue culture plates, Desalting PD10 columns and dialysis tubing (MWCO = 3500), Nunc™ Glass Bottom Dishes (12 mm), and Nunc Lab-Tek II Chamber Slide System were purchased from Fisher Scientific (Pittsburgh, PA). Doxorubicin was purchased from Ark Pharma (Catalog #AK-72874) and Indocyanine green (ICG), 5-(N-Ethyl-N-isopropyl)amiloride (Catalog #1154-25-2), Chlorpromazine hydrochloride (Catalog # 69-09-0), Methyl-β-cyclodextrin (Catalog #332615), Quinine sulfate (Catalog #1597005) and bovine serum albumin (BSA) from Sigma-Aldrich (St. Louis, MO). L-Tryptophan (Catalog # A10230), L-Tryptophan benzyl ester (Catalog #H63385), and L-Proline benzyl ester (Catalog #L15618) were purchased from Alfa Aesar. Ethanol was purchased from the Warner-Graham Company (Cockeysville, MD). Anti-CD44 antibody and PE Mouse IgG2b K Isotype Control were purchased from BD Pharmigen BD Biosciences. NMR spectra were recorded on a 500 MHz Bruker or 600 MHz Varian system using a 5 mm probe at room temperature. Deuterated water (D_2O, 99.9% D) was purchased from Cambridge Isotope Laboratories. FTIR measurements were performed on a Nicolet IR200 FT-IR instrument using single-reflection ZnSe ATR crystal. Penicillin/streptomycin (100X solution) was purchased from Corning. Cell lines (MDA-MB-231, and MCF10A cells) were obtained from American Type Culture Collection (Manassas, VA) and were grown in RPMI-1640 (HyClone, GE

Healthcare Life Sciences) with 10% fetal bovine serum and 1% penicillin/streptomycin (P/S). Murine adenocarcinoma CI66 and CI66-Doxorubicin resistant cell lines were obtained from Dr. Rakesh Singh at UNMC. All cells were incubated at 37°C in a humidified incubator with 5% CO_2. Matrigel Basement Membrane Matrix, *LDEV-free (Catalog #356234) was purchased from Corning.

Preparation and purification of the hyaluronic acid derived amino acid fluorescent nanoparticles

Hyaluronic acid amino acid fluorescent nanoparticles were synthesized by dissolving HA (25 mg) in 25 mL ultrapure water and stirred continuously for 30 mins at R.T. The next step included adding 12.5 mg of tryptophan, tryptophan benzyl ester, and proline benzyl ester in three separate reactions flasks, and stirring for another 30 mins at R.T. Once the reaction mixture was clear, the reaction mixture was placed in an oil bath maintained at 60-80 °C with constant stirring for 5 h. Subsequently, the reaction mixture was allowed to cool overnight. The cooled solution was purified against ultrapure water by dialysis. Reaction contents was placed in porous cellulose bag (molecular weight cut-off: 3500 Da) and dialyzed with a total of 8 changes over 48 h to remove all unreacted reactants. The dialyzed product was collected, lyophilized to yield a white fluffy product for all three precursor amino acids (78% yield for HA-tryptophan, 81% HA-tryptophan benzyl ester, and 73% HA-proline benzyl ester nanoparticles), and stored for further analysis at -20 °C.

Synthesis, purification, and loading efficiency of doxorubicin loaded hyaluronic acid derived amino acid fluorescent nanoparticles

20 mg of all three hyaluronic acid amino acid nanoparticles were dissolved in ultrapure water and stirred for 30 mins to allow complete dissolution. Doxorubicin was dissolved in ultrapure water (100 µg/mL), added dropwise to the aqueous solution containing the hyaluronic acid NPs to 20 wt. %, and stirred for 24 h protected from light. The reaction mixture was placed in a porous cellulose bag (molecular weight cut-off: 3500 Da) and dialyzed with a total of 8 changes over 48 h to remove all unreacted doxorubicin. After completion, the residual unconjugated doxorubicin was removed by passing the dialyzed product through a PD-10 desalting column with ultrapure water as a mobile phase. The doxorubicin loaded fraction was collected and was lyophilized to obtain light red fluffy product. (HA-tryptophan Dox = 42% yield, HA-tryptophan benzyl ester = 51%, HA-proline benzyl ester = 49%). The drug loading content were measured by UV-vis (ThermoFisher Evolution 220) by generating a calibration curve of doxorubicin concentrations (0.001-0.5 mg/mL). The loading efficiency was calculated as follows:

$$Drug\ content\ wt\% = \frac{amount\ of\ doxorubicin\ loaded}{total\ weight\ of\ doxorubicin\ loaded\ NP} * 100$$

Synthesis, purification, and loading efficiency of Indocyanine green (ICG) loaded hyaluronic acid derived amino acid fluorescent nanoparticles

20 mg of the tryptophan hyaluronic acid amino acid conjugate was dissolved in ultrapure water and stirred for 30 mins to allow complete dissolution. Indocyanine green (ICG) was dissolved in ultrapure water (0.1 mg/mL), added dropwise to the aqueous solution containing the hyaluronic acid NPs to 20 wt. %, and stirred for 24 h protected from light. The reaction mixture was placed in a porous cellulose bag (molecular weight cut-off: 3500 Da) and dialyzed with a total of 8 changes over 48 h to remove all unreacted ICG. After completion, the residual unconjugated ICG was removed by passing the dialyzed product through a PD-10 desalting column with ultrapure water as a mobile phase. The ICG loaded fraction was collected and was lyophilized to obtain light green fluffy product. (HA-Tryptophan ICG = 61% yield). The dye content was quantified by UV-vis spectroscopy (ThermoFisher Evolution 220) by generating a calibration curve of ICG concentrations (1-10 μM).

Physico-chemical characterization of hyaluronic acid derived amino acid fluorescent nanoparticles

The morphology of the fluorescent nanoparticles was visualized by transmission electron microscopy (FEI Tecnai G2 Spirit microscope; 2% aqueous methylamine vanadate, pH 8, was used for negative staining operated at 100 kV onto a carbon-coated copper grid at R.T.). The chemical structures of all amino acid nanoparticles were studied with ^{1}H and ^{13}C NMR spectroscopy (Bruker

Avance-III HD, 500, and 600 MHz respectively). FT-IR spectra were recorded on the Nicolet IR200 FT-IR instrument using single-reflection ZnSe ATR crystal. X-ray photoelectron spectra (XPS) were obtained on a Kartos Axis Ultra Imaging spectrometer, Spectra of C(1s) (275−295 eV binding energy), O(1s) (525−545 eV binding energy), and N(1s) (380−420 eV binding energy) as well as survey scans (0−1100 eV) were recorded with a tilt angle of 45°. The atomic compositions were corrected for atomic sensitivities and measured from high-resolution scans. XPS and FT-IR data were acquired for dry samples. Absorption and fluorescence spectra were recorded on a ThermoFisher Evolution 220 UV–vis spectrophotometer and Horiba Jobin Yvon FluoroMax 4 spectrofluorometer, respectively, in 10 mm quartz cells with a slit width of 5 nm. Colloidal properties were studied using a Malvern Zetasizer Nano ZS90 dynamic light scattering instrument. The quantum yield of the fluorescent nanoparticles was obtained by comparing fluorescence emission of reference dye (quinine sulfate in 0.5 M H_2SO_4, Φ= 0.54[20]).

Stability assessment of hyaluronic acid derived amino acid fluorescent nanoparticles

The fluorescence intensities of the amino acid nanoparticles were evaluated in different buffers ranging in pH from 1-14 by measuring the maximum emission intensity. Photo bleaching experiments were performed using a 365 nm UV lamp, 4 Mw cm^{-2}, and measuring the peak emission intensity over time period of 0-10 h to evaluate stability. Influence of ionic strength on the stability of the

fluorescent nanoparticles was evaluated by dissolving in salt (NaCl) concentrations ranging from 0-2 M, and fluorescence intensities were recorded at maximum emission intensity.

Cell viability assay

The cell viability of unloaded and loaded drug/dye HA-amino acid nanoparticles was evaluated using the CCK-8 assay (Dojindo). Cells [MDA-MB-231, MCF10A, CI66, and Ci66-Doxorubicin resistant] (5000 cells/well) were seeded in a 96-well plate with media (RPMI 1640, 10% FBS, 1% P/S), and allowed to adhere to the bottom of the well overnight. After 24 h, cells were incubated with different concentrations of unloaded HA-amino acid nanoparticles for 24 and 48 h, drug loaded nanoparticles for 24, 48, and 72 h, and dye loaded nanoparticles for 24 h. After incubation with various treatments, the cells were exposed to CCK-8 reagent (1:10 dilution) and incubated for 1-4 h at 37 °C. Plates were analyzed with a microplate reader (Synergy HTX Multi-mode reader BioTek) at 450 nm. The values obtained were directly proportional to the number of metabolically active cells present. Six replicate wells were used for each concentration, and the experiment was repeated three times. Relative cell survival was expressed as absorbance relative to the untreated cells.

Apoptosis assay

CI66 and CI66-Doxorubicin resistant cells (3 x 10^5 cells/well) were seeded in 12-well plates and allowed to adhere overnight. After 24 h, cells were treated for 12 h at 37 °C with unloaded and drug-loaded nanoparticles. Cells were then washed with PBS thrice, trypsinized and centrifuged at 3500 rpm for 5 mins. The cell pellet was suspended in 100 µl Annexin-V-FITC binding buffer in FACS tubes, followed by addition of Annexin-FITC (5 µl) and propidium iodide (5 µl). Samples were incubated for 30 mins at R.T. under dark conditions, as per manufacturer's recommendations in the Annexin V Apoptosis Detection Kit I (556547. BD Biosciences). Stained cells were analyzed using a BD LSRII flow cytometer at the Flow cytometry core facility, UNMC.

Confocal microscopy:

CI66 and CI66-Doxorubicin resistant cells were seeded (10^5 cells/well) on individual 12 mm Nunc™ Glass Bottom Dishes (Invitrogen, ThermoFisher Scientific, USA) and left to adhere for 24 h. The cells were treated with unloaded and drug loaded FONPs in serum-free DMEM media and incubated at 37 °C for 1 h. After incubation, cells were washed thrice with 1X PBS, and then fixed with 4% paraformaldehyde solution for 15 min at 37 °C. Next, cells were treated with 0.25% Triton-X-100 in PBS to permeabilize the cell membrane, followed by blocking with 1% BSA in 1X PBS. Next, primary antibody for Rab5 endosomal marker (Rabbit polyclonal IgG, Santa Cruz Biotechnology Inc., Dallas, TX) was added in 1% BSA 1X PBS solution and incubated with the cells overnight at 4 °C.

Cells were incubated with the secondary antibody (FITC-conjugated anti-rabbit Millipore AP132F) in 1% BSA at room temperature for 1 h. Cells were then washed thrice with 1X PBS, and were stained with HCS NuclearMask™ Deep Red Stain (ThermoFisher Scientific, Catalog# H10294) for 15 mins. Cells were washed and stored at 4°C until CSLM imaging.

Confocal images were taken with Zeiss 800 Confocal Laser Scanning Microscope, 60X with 1 μm cell slices. DAPI, Alexa Flour 488 and Alexa Fluor 647 filters were used to detect blue, green and NIR signal from the cells.

Development of CI66 and CI66-Dox resistant tumor spheroid model for studying uptake of FONPs

Matrigel (Matrigel #354234 from Corning, Corning, NY, USA) was thawed and added to 8-well Nunc™ Lab-Tek™ II Chamber Slide™ System (50 μL/well) to cover the bottom of each well to serve as matrix as it is rich in ECM components, such as laminin, collagen, heparin sulfate proteoglycans, entactin, and several soluble factors. Next, CI66 and CI66-Dox res cells (4×10^3) were mixed with thawed Matrigel along with media and added to Matrigel coated wells. The growth of the spheroids was monitored using Olympus CKX41 Bright Field, Infinity 1 Luminera microscope over a period of 2 weeks until the spheroids reached 500 μm in size. Next, unloaded and drug loaded FONPs were added to the tumor spheroids and cultured for 12 h. After washing thrice with 1X PBS and fixing in 4% paraformaldehyde, the blue and doxorubicin fluorescence in spheroids was measured with the confocal microscope Zeiss LSM 800 with

Airyscan (Jena, Germany) with 20X objective lens with a 1.4 N.A. using XYZ-stack with 10 µm intervals at 512*512 pixels with imaging acquisitions at 33 Hz. Images were captured and analyzed with LSM software (Jena, Germany). The spheroids were then treated with trypsin to obtain a single-cell suspension, washed with PBS, and subjected to flow cytometry analysis for determination of uptake of FONPs.

Evaluation of FONP endocytosis mechanism:

The effects of several membrane endocytosis mechanisms were investigated on HA based nanoparticles. CI66 cells were incubated in a 12-well plate at a density of (10^5 cells/well) and left for 24 h to adhere and cover the bottom of each well. After 24 h, cellular uptake inhibitors such as 150 mM ethyl isopropyl amiloride [EIPA] (inhibitor of micropinocytosis), 1.8 mM methyl-β-cyclodextrin (inhibitor of caveolae-independent endocytosis), 10 μg/mL chlorpromazine (inhibitor of clathrin-mediated endocytosis), and 5 mg/mL of HA (inhibitor of CD44-mediated uptake) were pre-incubated for 1 h to block respective endocytosis pathways. Next, similar concentration of FONPs to those used in confocal microscopy/cytotoxicity assessments were used to evaluate the uptake by flow cytometry. Fluorescence (ex/em 488 nm/520 nm) was detected using a FACS LSRII-green laser (BD). A total of 10000 gated events were acquired per sample, and the mean fluorescence intensity was plotted in a histogram-based graphical representation. Each data point is representative of

the mean of three independent measurements on the flow cytometer. Data were analyzed with FlowJo (Tree Star) software.

Results and Discussions

Preparation, characterization, and fluorescence origin of hyaluronic acid based fluorescent nanoparticles

We report for the first-time the generation of a novel fluorescent hyaluronic acid-amino acid nanoconjugates by hydrothermal Schiff base formation. This is referred to as a reaction between a species containing an active aldehydic group and a nucleophilic rich-amino group yielding a product containing C=N or imine bond as primary fluorescent centers interlocked in a polymeric mesh network[21]. Hyaluronic acid (HA), a non-sulfated, non-toxic glycosaminoglycan biopolymer, consists of alternating (1–3)-β linked N-acetyl-D-glucosamine and (1–4)-β linked D-glucuronic acid. It presents abundant conjugatable groups making it uniquely suited for the design of novel polymeric systems[22]. It has been reported that HA degrades with increasing temperatures from 60-120 °C[23], leading to rupture of bonds between vicinal diols forming carbonyl functional groups. These groups can be made available for conjugation with amino-rich compounds forming Schiff base- like molecules. Amino acids are the essential building blocks in proteins. Their unique zwitterionic properties from both amino ($-NH_2$) and carboxyl group (-COOH) with varying side chains[24] lead dictate different functional properties of proteins.

Due to their unique properties, amino acids can be exploited as functional groups for the formation of various nanoparticles. Hydrophobic amino acids such as tryptophan, phenylalanine, proline can be conjugated to a hydrophilic

component to modulate amphiphilic self-assembling properties, and thus to control dynamics of the nanoparticle formation.

In this context, the biocompatible amino acids can be used as ideal building blocks for the preparation of nanoparticles. In this approach, non-fluorescent HA when reacted with non-fluorescent amino acids under controlled hydrothermal conditions, results in the formation of blue fluorescent HA nanoparticles. A Schiff bond is produced in the reaction due to the Amadori rearrangement reaction[25,26]. The rearrangement reaction can also be credited to increased collision between reactants to facilitate formation of FONPs. All reactants and products formed are highly water-soluble, overcoming most of the challenges encountered during multi-step synthetic processes, making it an example for scale-up production of FONPs.

The final product that was obtained from each of the starting amino acids emitted a strong blue fluorescence under a UV lamp 365 nm excitation source. The exhibited blue fluorescence can be attributed to the generation of a new absorption band in the UV region between 280-320 nm that can be attributed to n π^* transition for C=N bonds[27]. Several Fourier transform infrared (FTIR) absorption band signatures for C-N stretching and bending vibrations between 1120-1135 cm^{-1}, broad -OH band between 3320-3340 cm^{-1}, C=N stretching vibrations at 1620-1640 cm^{-1}, and C-O stretching between 1020-1060 cm^{-1} were observed for HA-based FONPs (**Fig. 1B**). In addition, the ^{1}H-NMR spectral analysis highlighted overlapping regions between 7-8.00 ppm belonging to

hydrophobic groups of amino acids and N=CH protons (**Fig. 1C**). We also performed ^{13}C NMR to detect peaks between 170-180 ppm, confirming the formation of C=N group in the fluorescent HA nanoparticles[28] (**Fig. 1a-c**).

X-ray photoelectron spectroscopy (XPS) was used to investigate the surface state and composition of FONPs, indicating the presence of C, N, and O elements in **Fig 1E.** Analyzing high-resolution C1s spectra, peaks at 283.7 eV, 282.9 eV, and 285.9 eV were assigned to C-C, -C-O, and -C=N bond signatures respectively. These results demonstrate the successful formation of Schiff bond C=N resulting from condensation between HA and amino acids.

Formation of amphiphilic water-soluble spherical nanostructures was due to the conjugation of HA hydrophilic backbone and hydrophobic amino acids with pockets of hydrophobic C=N sub-fluorophore units. The nanoparticles were found to have a negative (ζ) zeta potential of -17 to -19 mV (**Fig. 1D**), owing to the negatively charged carboxylic groups (-COOH) of HA[29]. The FONP possess the hydrodynamic diameters between 200-400 nm by as measured by dynamic light scattering (DLS) and TEM[30] (**Fig. 1F**). Overall, the preparation of HA FONPs was simple and environmentally friendly in the absence of organic solvents, making this system particularly attractive in the field of nanomaterials as compared to other methods of preparation.

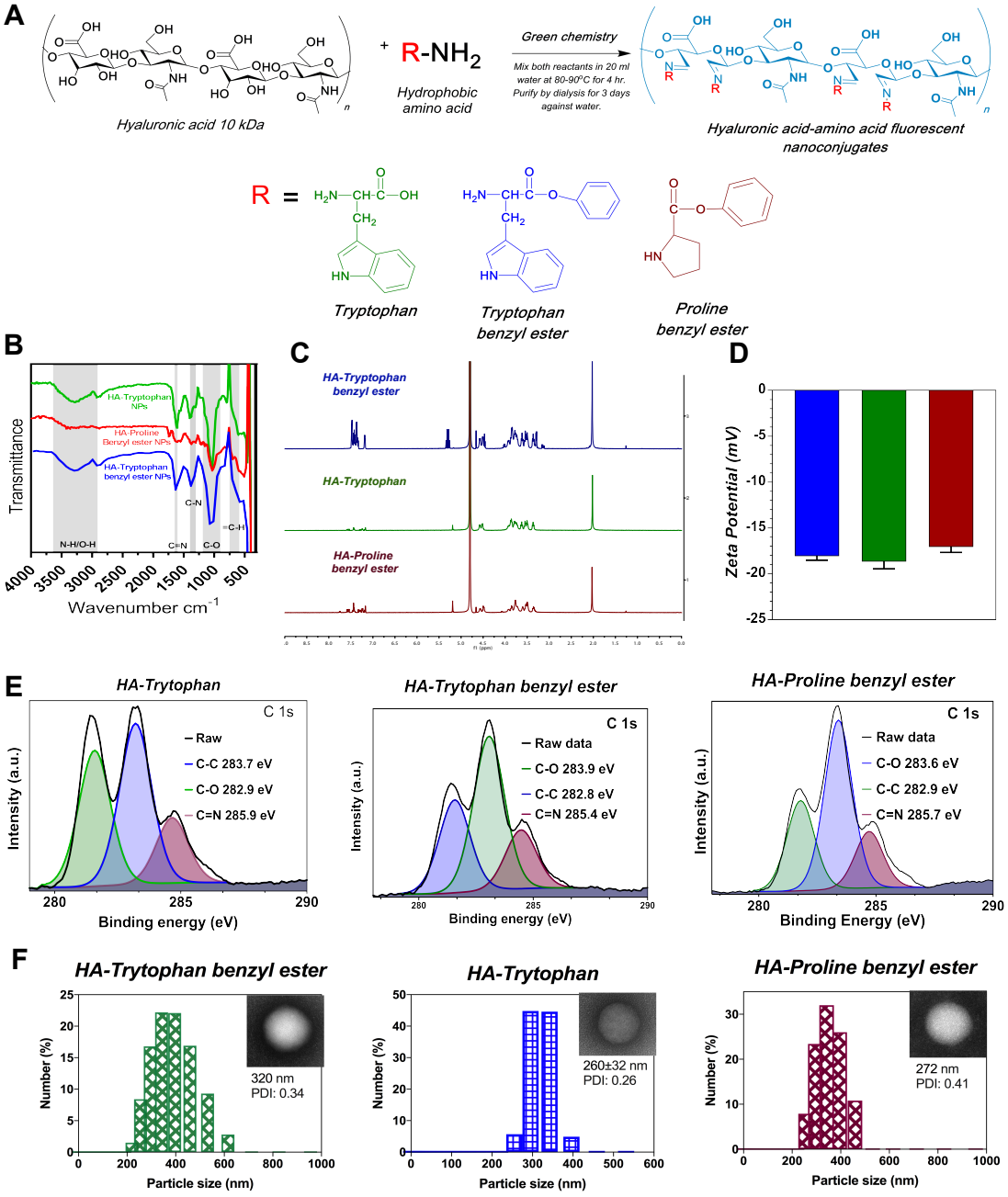

Figure 1: (A) Synthesis of fluorescent organic nanoparticles from precursor HA and amino acids. (B) FTIR spectral signatures of HA derived FONPs, grey colored portion in the graph indicate C=N, C-N, =C-H, C-O, N-H stretching and bending vibrations (C) ^{1}H-NMR spectra (7-8 ppm) indicating successful conjugation of hydrophobic ligand and C=N formation, (D) Zeta potential (mv)

analysis, (E) High resolution C1s spectra of all nanoparticles from XPS showing the C-C, C=N, and C-O bond energies, (F) Size distribution analysis of all nanoparticles with TEM insets.

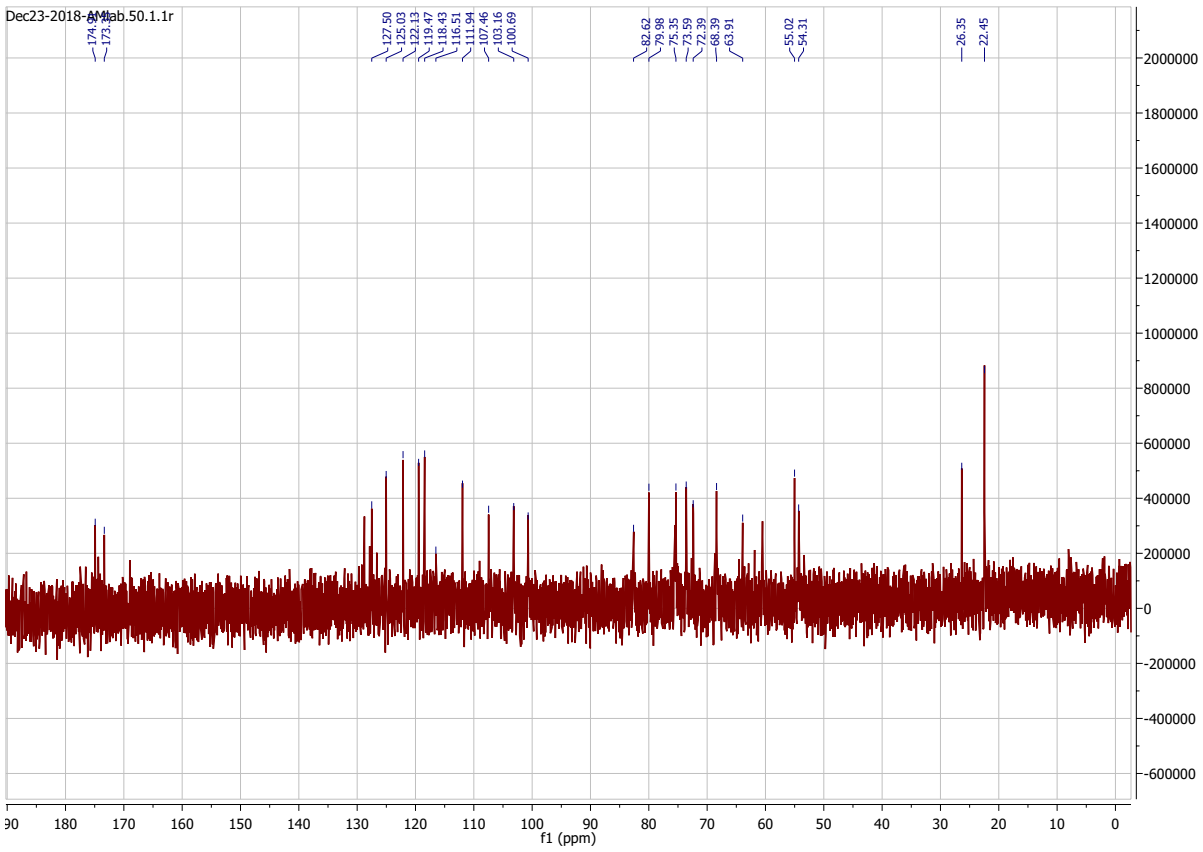

Figure 1a: ^{13}C NMR spectra of HA-tryptophan FONP.

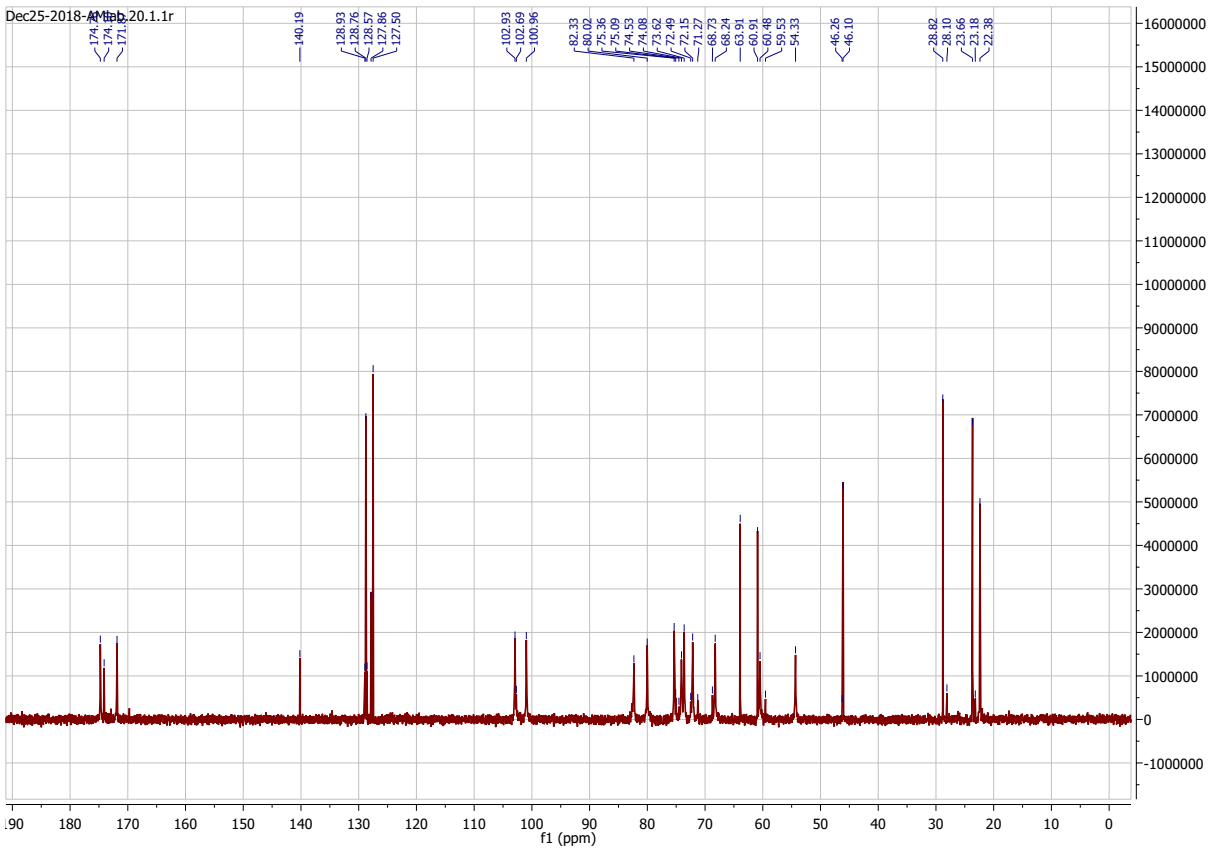

Figure 1b: ^{13}C NMR spectra of HA-tryptophan benzyl ester FONP.

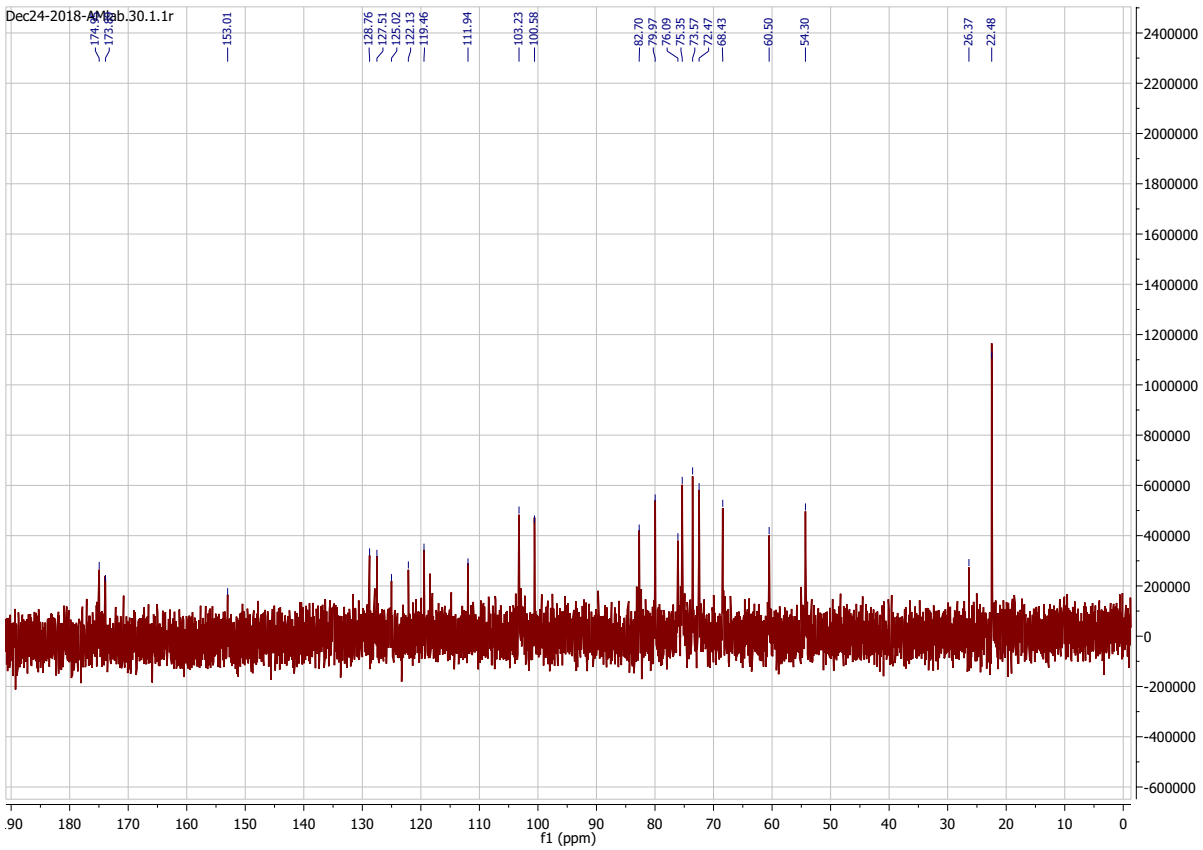

Figure 1c: ^{13}C NMR spectra of HA-proline benzyl ester FONP.

Both starting materials lack UV-sensitive chromophores or π-aromatic conjugated building blocks as the main source of fluorescence emission[31]. The exact photophysical mechanism is still under rigorous investigation; however, in published literature, it is shown that small molecular rotors such as C=N upon efficient immobilization or hindering bond rotations/vibrations significantly restricts radiative transition decay[32]. Restriction of bond rotations lead to an increase in electronic density on sub-fluorophore groups leading to fluorescence, in a process previously coined as covalent-bond enhanced emission (CEE). This leads to the formation of new excited states, thus making the resulting HA FONP fluorescent. We expect that π-π interactions between the hydrophobic groups will significantly hinder rotation of sub-fluorophore -C=N leading to further enhancement of fluorescence. Excitation wavelength, when varied from 280-420 nm (**Fig 2**), resulted in a broad emission peak with no dramatic change in the maximum wavelengths. We hypothesized this was due to the presence of numerous sub-fluorophores and diverse photoluminescent states in the core-polymeric structure. HA derived FONP also exhibited λ_{ex}-dependent photoluminescent property (**Fig. 2**)indicating the presence of multiple excited sites similar to other reports on FONPs[33].

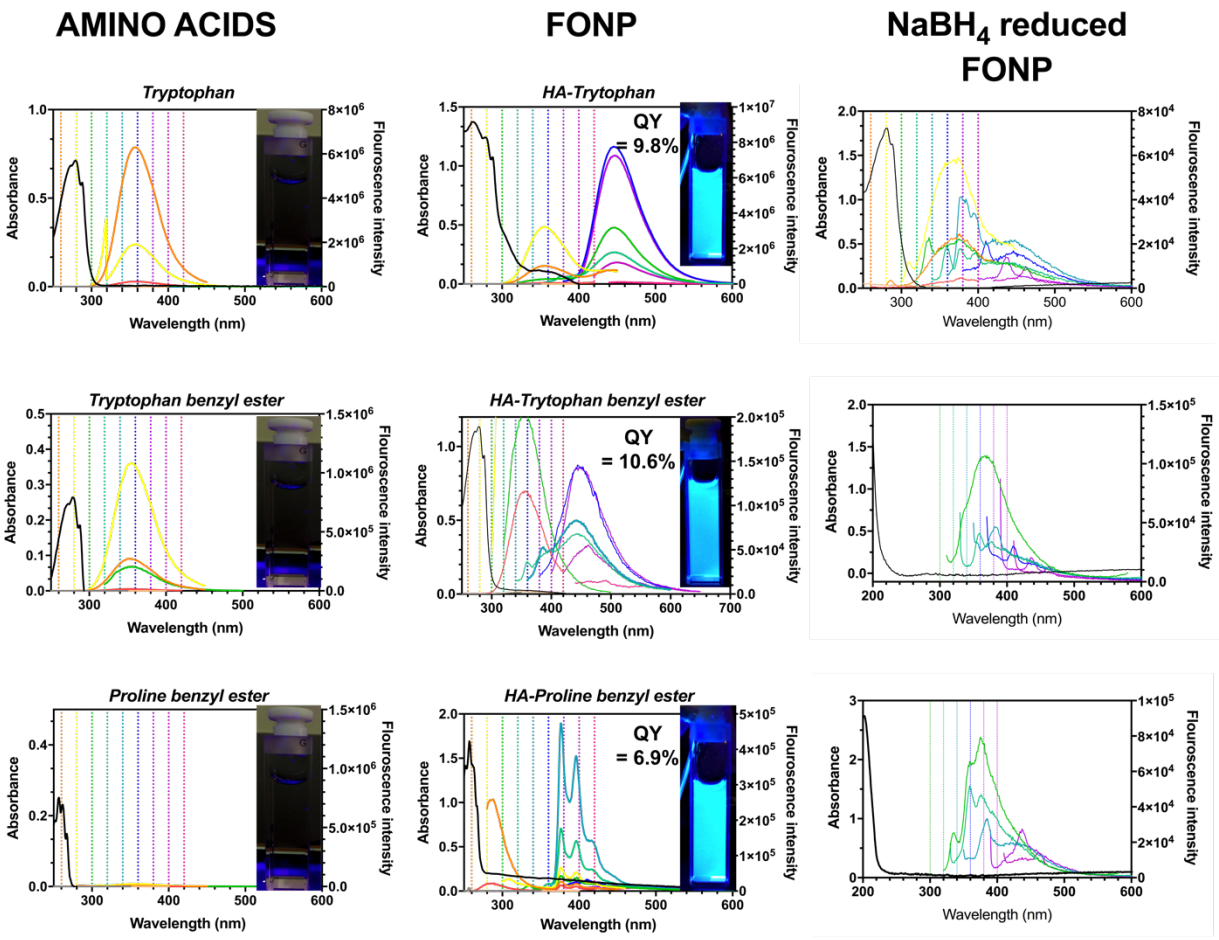

Figure 2: Photoluminescence and UV-vis absorption spectra's of FONPs in comparison with precursor amino acids and determination of fluorescence origin from $NaBH_4$ reduction method.

To verify the importance of employing a large macromolecular reactant (HA) for effective immobilization of small molecule in the polymeric network, we utilized citric acid and tryptophan to form small-molecule imine complex, and no significant fluorescence was detected. However, if carbonization reactions (150-200 °C) were employed, the formation of carbon dot was observed with size ranges between 2-6 nm. This highlights the importance of using a polymeric starting material along with small molecule precursors to effectively generate FONPs.

To further investigate the role of -C=N bond on the origin of fluorescence, Schiff bond can be reduced to its -NH-CH_2- form[34]. This reduced form possesses increased molecular rotations over single bonds, abolishing fluorescence properties due to an increase in radiative energy loss. FONP derived from Schiff-based chemistry on reduction with 0.1M $NaBH_4$ also losses its characteristic fluorescence property, demonstrating the importance of Schiff bonds as primary fluorescence-emitting moieties. Loss of UV absorbance between 280-320 nm and fluorescence emission between 380-550 nm was also observed (**Fig 2**). In a previous report, fluorescent PEI-formaldehyde polymer particles upon reduction with $NaBH_4$ displayed increased fluorescence instead of loss of fluorescence. This phenomenon was attributed to the formation of π-π* transition of -C=C bond in a double Schiff bond formation. This confirms that HA-based FONP possesses only single Schiff bond elements similar to other reports of PEI-glucose[10] and PEI-starch[13] derived FONPs.

Moreover, stability assessments were performed in buffers in pH ranging from 2-10; 0-2 M NaCl; and photostability studies were performed under irradiation for 10 h under 365 nm excitation. No drastic change in fluorescence intensity or photobleaching was observed in solutions with pH ranges 4-9, different NaCl concentrations, and upon irradiation of UV light for 10 h (**Fig. 2a**). However, at extremely low and high pH, complete disappearance of fluorescence was observed. This can be attributed to the destabilization of the chemical structure of HA or increased concentrations of H+ and OH- interrupting/preventing electronic transitions to excited states[35]. Furthermore, no apparent precipitation was observed at R.T. during long-tern storage for 10 weeks (**Fig. 2b**) These results demonstrate that the HA derived FONPs possess a good stability profile and can be expected to remain stable for at least 12 months when stored either at R.T. or at 4°C.

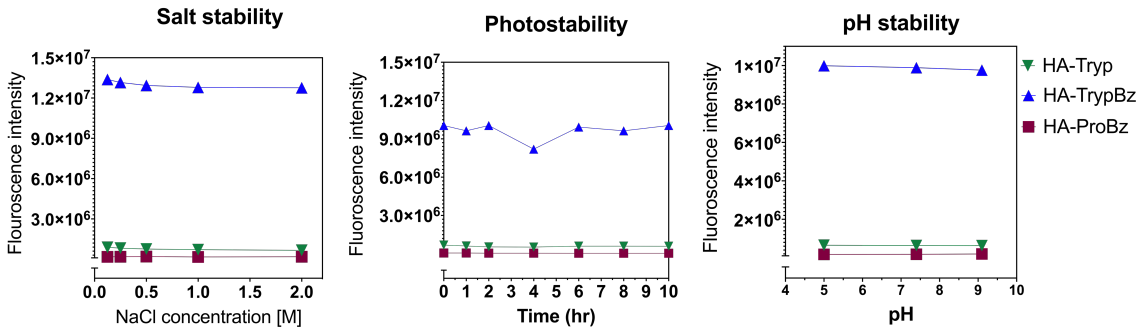

Figure 2a: Stability assessment in different salt conditions, photostability, and buffer conditions for 3 HA-derived FONPs.

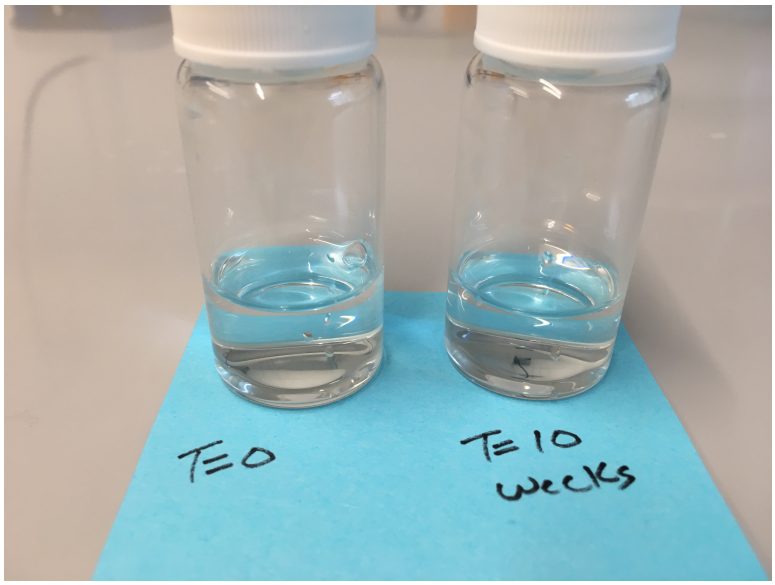

Figure 2b: Picture of HA-tryptophan FONP formulation at 0 and 10-week time interval for visual stability analysis.

Additionally, we investigated the effects of preparation time and concentrations of reactants on fluorescence. Increased concentrations of both reactants lead to increase of blue fluorescence intensity. Increase in temperature (above 100 °C) for more extended periods lead to the formation of carbon dots/formation of black sticky semi-solid mass instead of polymer dots. Therefore, a 1:0.5 ratio of HA to amino acids was chosen at 80 °C for 5 h for optimal fluorescence property and preparation of fluorescent nanoparticles.

Biocompatibility, cellular uptake mechanism, and cellular imaging application of FONP

The bioimaging field is aimed at imaging and visualizing advanced biological processes. Lower toxicity of fluorescent imaging probes is required for the use of HA-derived FONPs for applications in cellular labeling. We investigated the cytotoxicity profiles of the prepared HA-FONPs by conducting a CCK-8 assay in two breast cancer cell lines (MDA-MB-231 and CI66) and non-malignant breast cell line (MCF10A). An average of 97% of all cells remained alive across all concentrations at two-time points (24 and 48 h) for all the FONP derivatives indicating very low toxicity profiles (**Fig 3B**). Since the FONPs displayed acceptable cytotoxicity profiles with no significant differences in toxicity levels across all concentrations, design of all preliminary bioimaging studies in CI66 cell line were carried out at 4 h incubation period. FONPs were successfully internalized by cells and primarily localized in the cytoplasmic space, which was monitored through a confocal scanning laser microscope. Merged images in

Fig.3A show strong blue fluorescence in the cytoplasmic space from FONPs, green from the endosomal marker, and cyan from nuclear stain. The FONPs were observed to not have entered the nucleus of the cells.

We further investigated the endocytosis mechanism responsible for uptake of HA-derived FONPs by flow cytometry analysis. Major cellular uptake pathway inhibitors[36] used were methyl-β-cyclodextrin (inhibitor of caveolae-independent endocytosis), ethyl isopropyl amiloride (inhibitor of micropinocytosis), chlorpromazine (inhibitor of clathrin-mediated endocytosis), and HA (inhibitor for CD44-mediated uptake). CD44 and clathrin-coated pits mainly governed endocytosis of FONPs (**Fig. 3a**). Higher expression profiles of CD44 across all cell lines are expected to be the major driver for the internalization of HA-derived FONPs. Although there are multiple published reports on the use of FONPs for bioimaging applications, to the best of our knowledge, there are no reports on using HA-amino acid-based FONP materials. Above results display potential of FONPs as an imaging tool in a 2D cell culture system; however, this cannot predict the behavior of NPs system in 3D models.

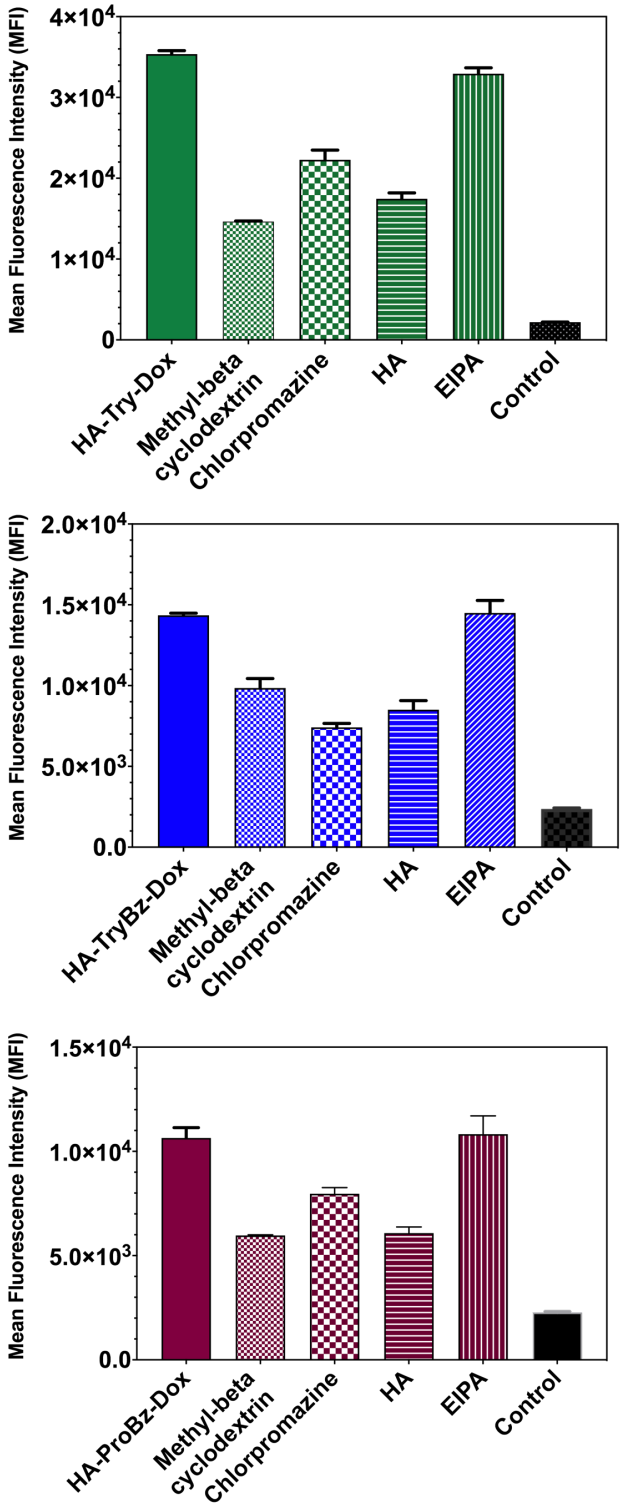

Figure 3a: Evaluation of endocytosis mechanisms for HA-FONPs using different endocytosis inhibitors.

To address this, we prepared a multicellular tumor spheroid model from CI66 cells and used it as a complementary system to evaluate the *in vitro* bioimaging performance of FONP penetration using confocal microscopy and flow cytometry. Further analysis of fluorescence intensity from FONPs confirmed penetration in the spheroids to about 4-7 layers of cells (**Fig. 3C**). Next, quantitative measurements on uptake of FONPs in the spheroids were measured by single-cell FACS analysis by trypsin digestion to produce a single-cell suspension. Consistent with above confocal observations, all the FONPs possessed high uptake in tumor spheroids (**Fig. 3C**). Drug delivery applications to cancer tumors using HA derived FONPs can be utilized for delivering a higher dose of the encapsulated chemotherapeutic drug for the increased likelihood for effective cancer cell killing. The achieved penetration depth of the FONPs is promising but can be improved by surface functionalization with varying targeting peptides, antibodies, and polysaccharides, which would significantly improve delivery to solids tumors and enhance anti-cancer effect.

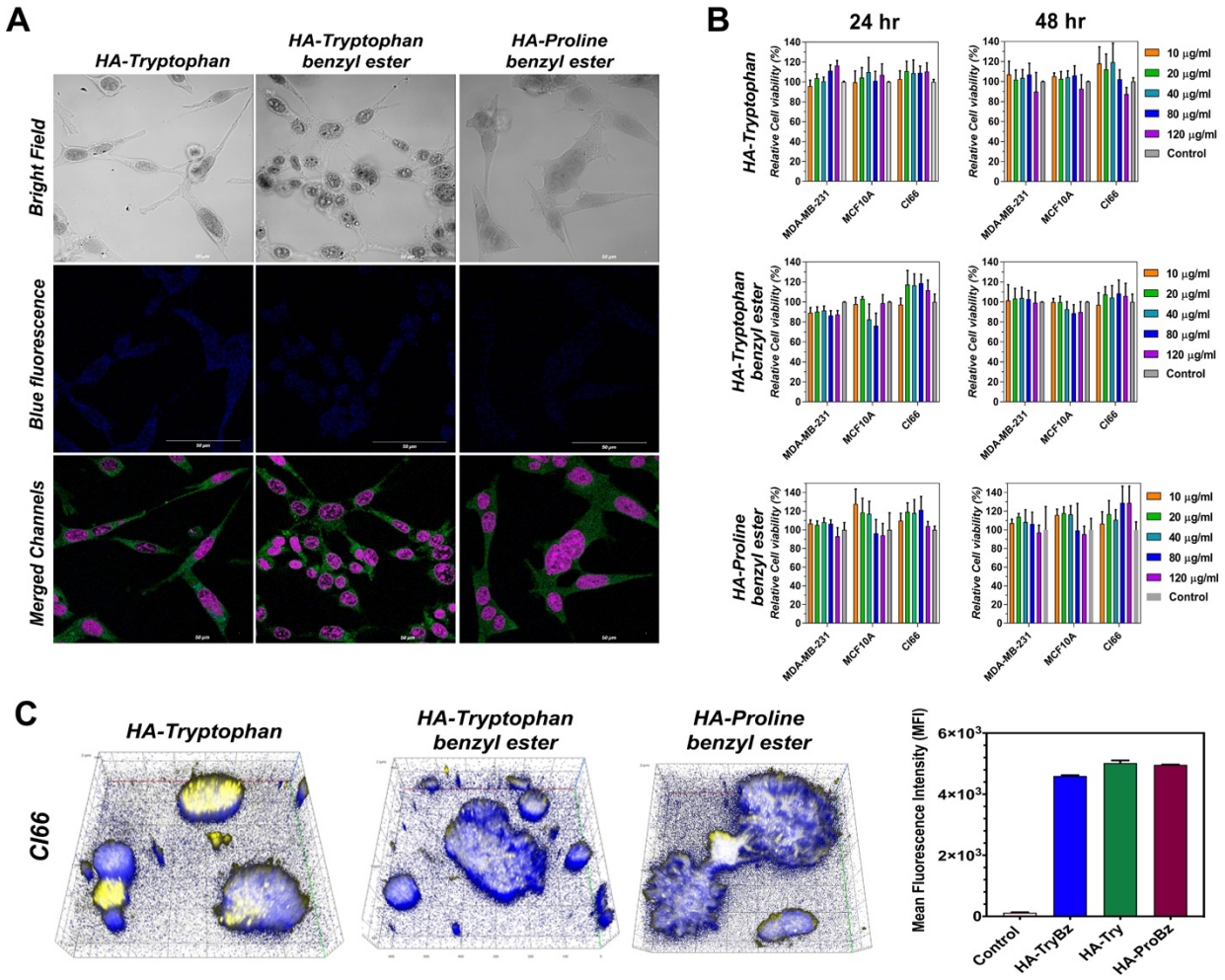

Figure 3: (A) CSLM images of CI66 cells incubated with HA-derived FONPs for 4h. Blue- FONPs, Green- Endosomal marker, Cyan-pink- Nuclear stain. (B) CCK-8 assay performed on CI66 cells incubated with library of HA-derived FONPs in MDA-MB-231, CI66, and MCF10A cell lines. (C) Penetration of FONPs in CI66-derived tumor spheroids; blue- FONPs, yellow- nuclear stain, accumulation of FONPs in CI66 cells from spheroids indicated as mean fluorescence intensity after flow cytometry analysis. Results are shown as mean ± SD.

Combined drug/imaging agent delivery properties in 3D tumor model:

We next evaluated the possibility of utilizing FONPs as a drug delivery vehicle for potential therapeutic applications in image-guided drug delivery[37]. Firstly, doxorubicin (DOX) was selected as the model drug due to its intrinsic red fluorescence and overlapping spectral region between the emission of FONP and absorption of DOX. Interestingly, DOX was chosen due to its high absorptivity in the spectral region of the absorption spectra of FONPs providing favorable spectral overlap, ideal for efficient energy transfer via the Forster energy transfer mechanism (FRET)[38]. Secondly, DOX, also known as Adriamycin is widely used in treatment regimens for the treatments of various solid cancer tumors[39]. The DOX loading content was quantified by measuring the fluorescence intensity of DOX.

According to the DOX UV-Vis absorption calibration curve (excited at 485 nm), the drug loading content in each of the FONP was calculated as 9.3 wt.% for HA-tryptophan, 9.8 wt.% for HA-tryptophan benzyl ester, and 6.7 wt.% for HA-proline benzyl ester FONPs. It is to be noted that polymeric nanomedicines have a typical drug loading capacity of around 10 wt.%[40,41]. We observed a relatively higher drug loading for the tryptophan derivatives compared to proline derivative, due to synergistic π-π interactions of benzyl groups along with electrostatic interaction (charged and hydrogen bonding) of indole ring of tryptophan, which is missing in proline benzyl precursor. DOX loaded FONP nanoparticles exhibited a spherical morphology with a size distribution of hydrodynamic diameter

relatively larger size of approximately 20-30 nm indicating successful loading of DOX. These were also confirmed by TEM images (**Fig. 4C**).

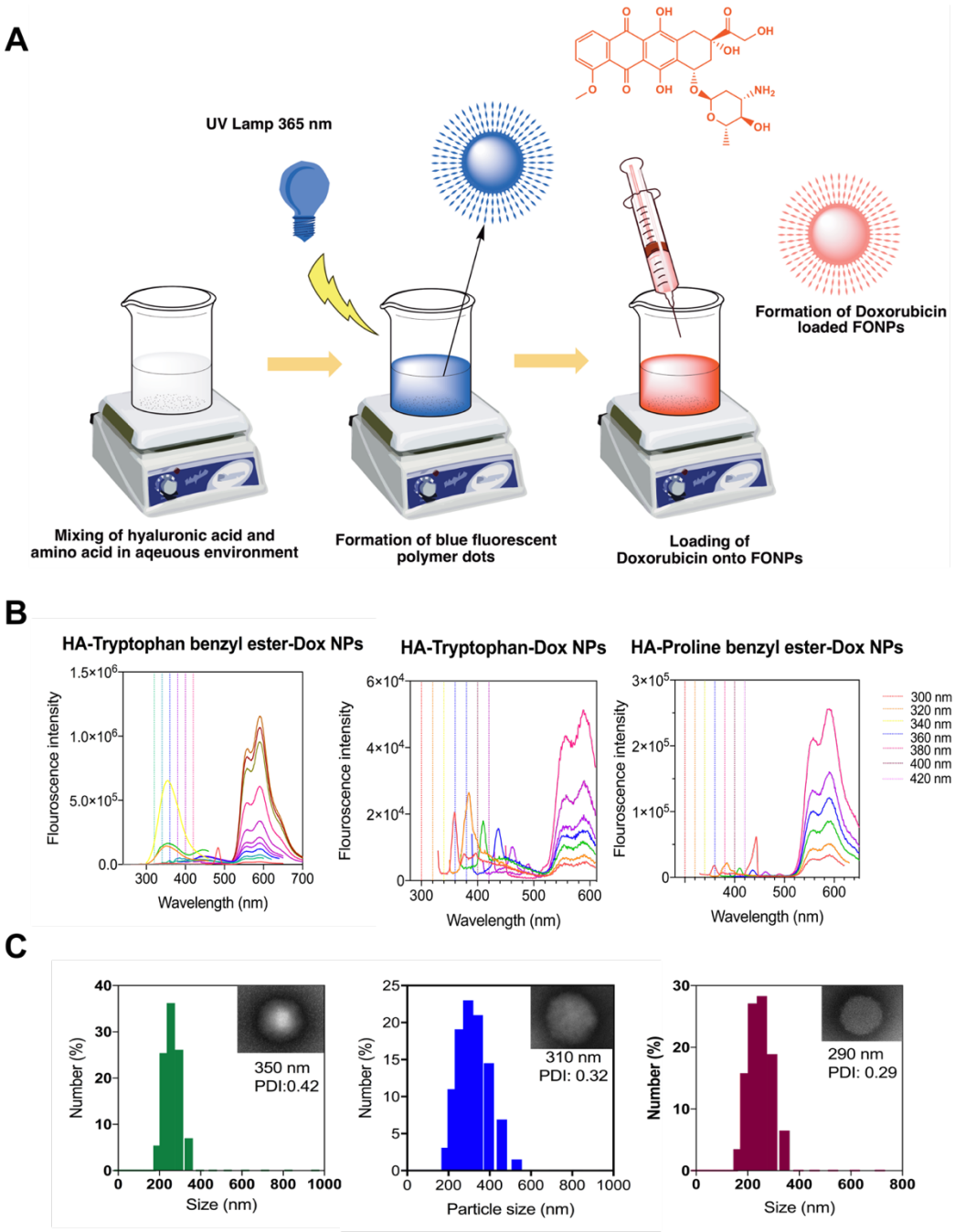

Figure 4: (A) Schematic representation of DOX loading onto HA-derived FONPs. (B) Fluorescence spectra of three DOX-loaded FONPs representing quenching of parent blue signal and appearance of DOX fluorescence (520-620 nm). (C)

Size distribution analysis by DLS and TEM inset images for each of the nanoparticles.

Furthermore, we also observed complete quenching of the blue fluorescence (400-500 nm) from FONPs and appearance of DOX fluorescence (520-640 nm) from the nanoparticles (**Fig. 4B**), indicating efficient FRET between the FONP and DOX loaded in the polymeric mesh. Similar results were obtained when indocyanine green (ICG), an FDA approved dye, which is used for image-guided surgery, was loaded onto HA-tryptophan FONP. Similar FRET-like behavior with emission in the near-infrared window was observed. Fluorescence spectra showed emergence of peak in the 700-800 nm region when FONPs were excited between 300-380 nm, indicating energy transfer between the nanoparticle and loaded ICG (**Fig. 4a**). UV-vis spectra showed both absorbances from FONP and ICG implying entrapment of ICG (**Fig. 4a**). From the UV-Vis calibration curve, ICG loading content was found to be 8.6 wt. %. ICG loaded particles also demonstrated an increase in size in similar ranges to DOX loaded FONPs. Confocal laser scanning microscopy imaging of CI66 cells incubated with ICG-loaded FONP revealed cyan-blue signal from FONPs in the cytoplasmic region when excited at 320 nm (**Fig. 4a**).

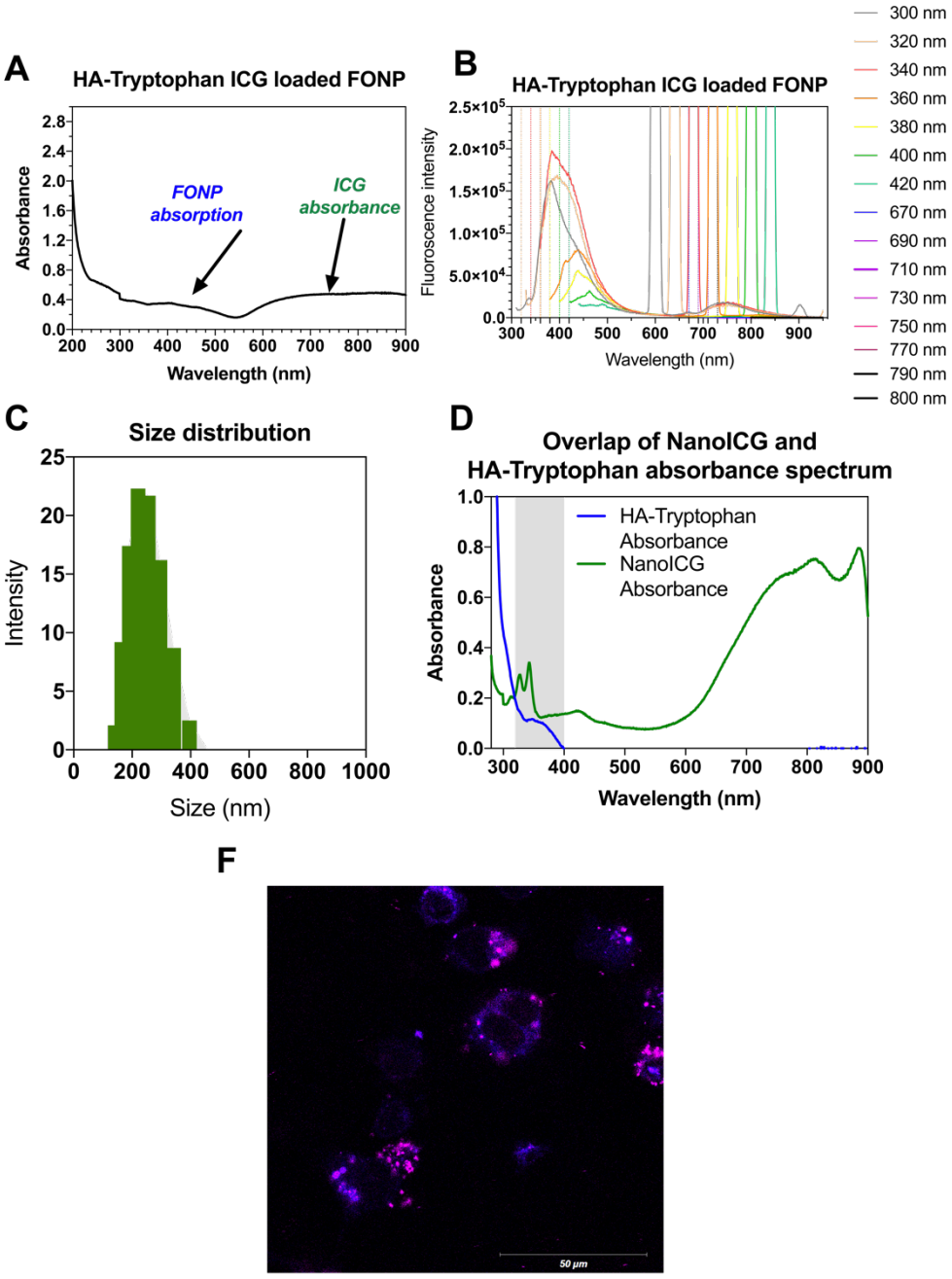

Figure 4a: (A) UV-vis absorbance spectra for ICG loaded HA-tryptophan FONP. (B) Fluorescence spectra with different excitation wavelengths (300-800 nm) (C) Size distribution by DLS. (D) Overlap region of NanoICG (ICG encapsulated in

HA-PBA) and HA-Tryptophan ICG FONP. (F) Confocal laser scanning microscopy in CI66 cells, Cyan-ICG, Blue-FONP.

Energy transfer from a non-conjugated polymeric system to dye/drug loaded is believed to mainly occur via energy diffusion within polymer host followed by energy transfer to guest molecule depending on the packing symmetry. The donor's FONP fluorescence was not completely quenched when loaded with ICG which could be attributed to the formation of twisted intramolecular charge transfer states, lower energy diffusion or transfer efficiency, and inappropriate lattice packing[42]. Although the packing of DOX and ICG might not be similar, it is difficult to accurately predict the randomness of the distribution of dye/drug within the polymeric matrix. To elucidate a piece of detailed information about energy transfer rate, decay kinetics, and excited-state lifetimes, sophisticated instrumentation such time-resolved fluorescence measurements will be required to be considered for future studies.

Future directions could include utilization of the remarkable "light-harvesting" properties of FONP[43] to obtain bright, red-shifted emission spectrums beneficial for near-infra red image-guided surgery in animals for accurate detection of positive margins[44].

Moreover, to explore cancer cell killing efficiency of DOX loaded FONP, we determined the cellular viability of CI66 and CI66-DOX resistant cells with different formulations using the CCK-8 assay. We observed in CI66 cells that HA-tryptophan DOX loaded FONP had a half-maximal inhibitory concentration (IC_{50}) of 1.82 μM and HA-tryptophan benzyl ester with an IC_{50} of 1.42 μM exhibiting higher cell killing (**Fig. 5B**) compared to free DOX of an IC_{50} of 2.2 μM. The lower

IC_{50} values for the tryptophan derivatives confirmed enhanced cytotoxicity as an effect of the nanoformulation of DOX within FONP, compared to free DOX treatment under identical conditions in CI66 cells.

Confocal microscopy showed DOX was predominantly localized in the nuclear compartment at its designated site of action, with limited fluorescence from the cytoplasm after 4 h incubation period (**Fig. 5C**). We anticipate that DOX will be released from the nanosystems under low pH conditions (4.5-5.5) in the endosomal-lysosomal compartment of the cancer cell to release DOX and target the nucleus, where its primary therapeutic impact is expected to occur by intercalating between base pairs of the nucleotides due to its planar rigid structure. We also confirmed the cell viability and confocal microscopy results above by an apoptosis analysis using flow cytometry. It is well known that DOX can cause dissipation of the mitochondrial membrane, activation of p53 protein, generation of reactive oxygen species, and DNA fragmentation[45] triggering apoptosis and potential necrosis, initiating sequential cell death[46]. Treatment with DOX loaded FONPs lead to a higher % of apoptotic/necrotic cells in the Q2 compartment (AnnexinV and PI positive) compared to free DOX alone (**Fig. 5E**), which was consistent with IC_{50} analysis from cytotoxicity assays.

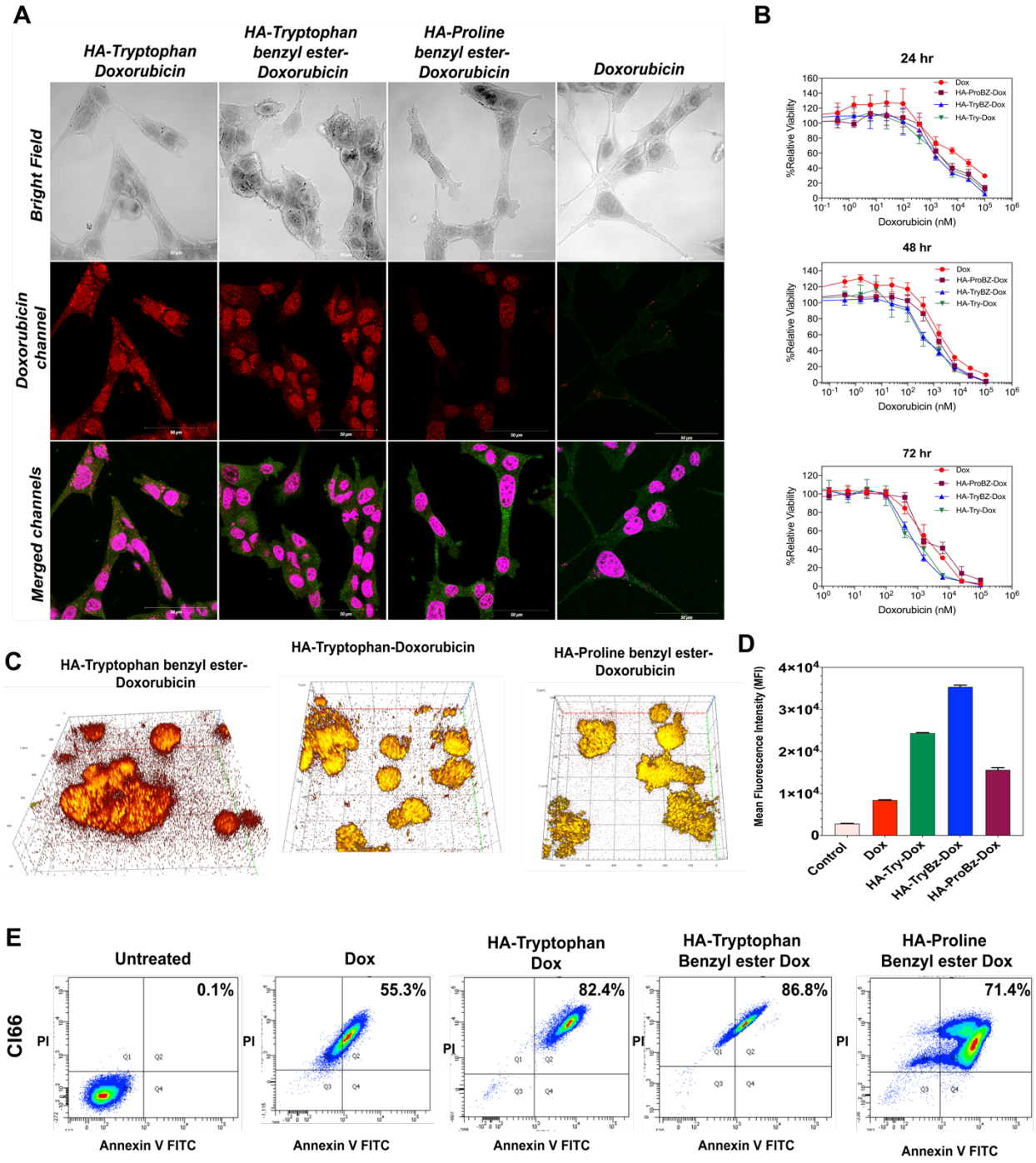

Figure 5: (A) CSLM images of CI66 cells incubated with HA-derived DOX loaded FONPs for 4h. Blue- FONPs, Green- Endosomal marker, Cyan-pink- Nuclear stain, Red- DOX. (B) IC_{50} cell killing assessments on CI66 cells at three different time points. (C) Surface plot images of CI66 tumor spheroids treated with DOX,

HA-tryptophan-Dox, HA-tryptophan benzyl-DOX, and HA-proline benzyl DOX (D) Penetration of FONPs in CI66-derived tumor spheroids, accumulation of DOX-loaded FONPs in CI66 cells from spheroids indicated as mean fluorescence intensity after flow cytometry analysis. Results are shown as mean ± SD. (E) CI66 cells were treated as indicated and stained with AnnexinV-FITC and Propidium Iodide (PI) using FITC Annexin V Apoptosis Detection Kit I and quantified with flow cytometry. The percentage of late apoptotic/necrotic (Annexin V+/PI+) are denoted in each of the panel.

To investigate where cells resistant to doxorubicin would affect the intracellular drug accumulation, uptake of the three DOX loaded FONPs were tested in CI66-DOX resistant cells. Much higher DOX fluorescence intensities from flow cytometry were observed for the tryptophan and proline conjugates with an equivalent dose of DOX for the same period of time under similar conditions (**Fig. 5a**). These results indicate that DOX loaded FONP could be retained for a longer time and not be detoxified as quickly as free DOX by multi-drug resistant efflux proteins[47]. The cellular uptake of DOX (free DOX or its equivalent in FONP) was also investigated by confocal laser scanning microscopy (**Fig. 5a**). Compared with the cells treated with free Dox, the red fluorescence intensity was higher in cells treated with the tryptophan derivatives. Furthermore, the red fluorescence intensity in the nuclei of the cells treated with Dox-FONPs was higher compared to the nuclei of cells treated with free Dox. Diffused lower signal was observed in the cytoplasm indicating that the FONP might have some affinity towards cellular organelles to facilitate sustained drug release. These results indicate that doxorubicin resistant cells internalize the Dox-FONPs, slowly release the drug for accumulation in the nuclei. This might be due to the balance of uptake and efflux of the nanocarrier and the diffusion of a small-molecule chemotherapeutic drug.

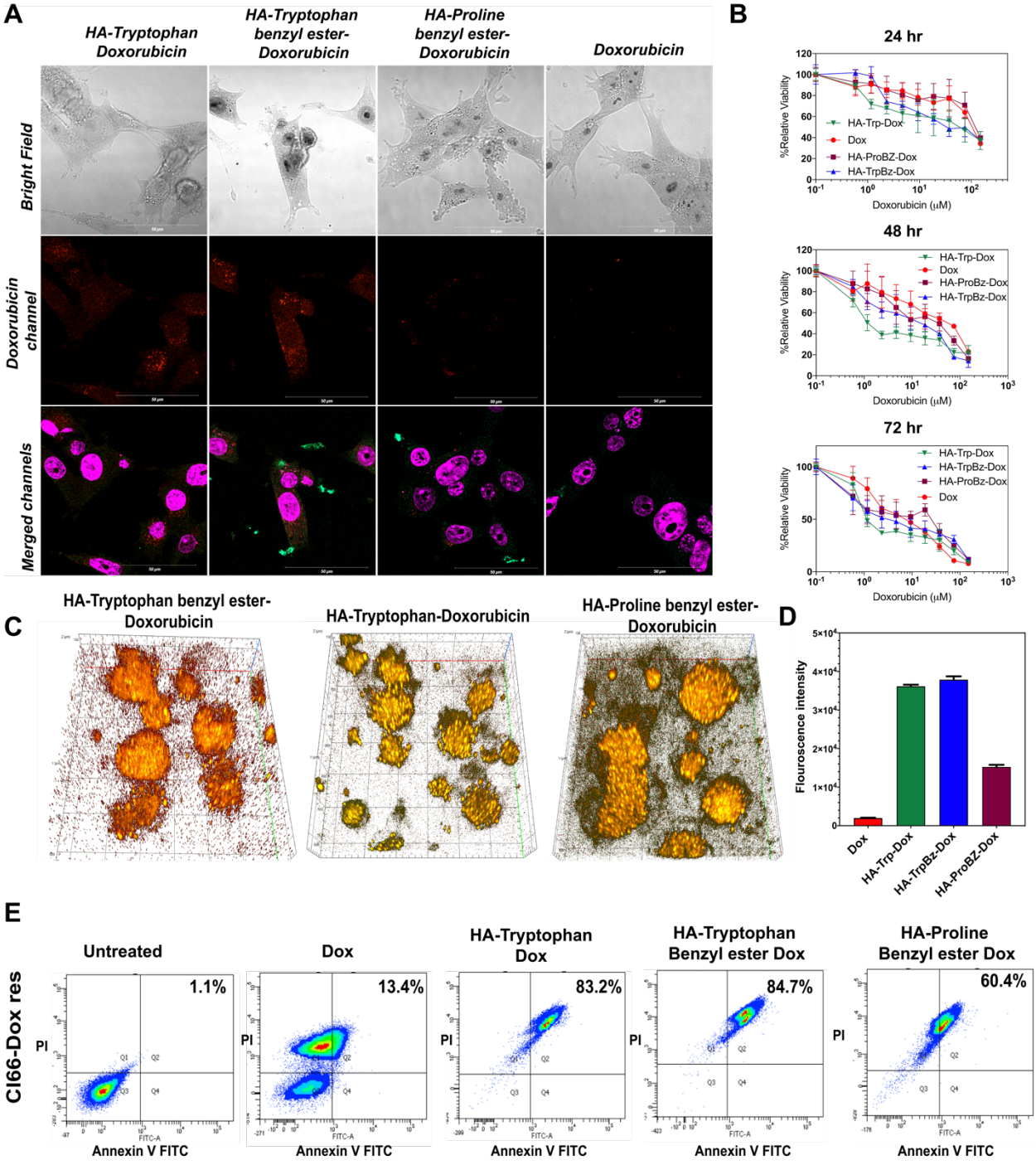

Figure 5a: (A) CSLM images of CI66-Doxorubicin resistant cells incubated with HA-derived DOX loaded FONPs for 4h. Blue- FONPs, Green- Endosomal marker, Cyan-pink- Nuclear stain, Red- DOX. (B) IC_{50} cell killing assessments on

CI66-Dox resistant cells at three different time points. (C) Penetration of FONPs in CI66-Dox resistant-derived tumor spheroids, accumulation of DOX-loaded FONPs in CI66 cells from spheroids indicated as mean fluorescence intensity after flow cytometry analysis. Results are shown as mean ± SD. (E) CI66 cells were treated as indicated and stained with AnnexinV-FITC and Propidium Iodide (PI) using FITC Annexin V Apoptosis Detection Kit I and quantified with flow cytometry. The percentage of late apoptotic/necrotic (Annexin V+/PI+) are denoted in each of the panel.

The differences in IC_{50} values and DOX content in both CI66 and CI66-Dox resistant cell lines, strongly suggest that drug loaded FONP complexes may elicit a higher antitumor efficiency and extended therapeutic effect. This can be attributed to the higher payload delivery of the drug which is conducive to slower prolonged drug release intracellularly within the cancer cell, providing a valuable platform for targeted cancer chemotherapy.

Therefore, in both non-resistant and resistant cancer cells, incubation with DOX loaded FONPs resulted in not only a higher degree of cell death but also a higher degree of apoptosis, in comparison to free DOX. Similar reports were also observed for DOX-loaded carbon dots[48] derived from carbonization of milk with increased delivery to ACC-2 adenoid cystic carcinoma cell line.

Drug delivery applications were also tested in a 3D tumoroid model using both CI66 (**Fig. 5C**) and CI66-DOX resistant cell (**Fig. 5a**) lines to investigate the penetration of particles. We observed strong DOX fluorescence from tumoroid treated with HA-tryptophan and HA-tryptophan benzyl ester derivatives compared to HA-Proline benzyl ester (**Fig. 5D and Fig. 5a**). Flow cytometry data corroborated that HA-Tryptophan and HA-Tryptophan benzyl ester both had a significant higher cellular DOX fluorescence intensity than DOX treated ones (**Fig. 5D**), which is most likely owing to DOX being delivered at a higher amount. The lower DOX delivery can be attributed to the low DOX loading in proline derivative compared to tryptophan derivatives. Similar penetration depths were

observed with confocal results obtained from unloaded FONPs of about 4-7 layers of cells.

These results, along with above data, provide initial evidence that HA-derived FONPs could be potentially used for drug delivery applications with extensive *in vivo* investigations to help translate from a pre-clinical setting to a clinical environment. Future applications could potentially include photodynamic therapy, hypoxia-activated therapy, and combination drug treatment therapy for the success of the *in vivo* tumor assessment studies.

Conclusions

We developed a new system of a novel fluorescent non-conjugated FONPs from non-fluorescent biocompatible hyaluronic acid and amino acids via Schiff base green chemistry. Merits of this system include high water dispersibility, ease of synthesis via green chemistry approaches, blue fluorescent properties, excitation dependent emission fluorescence, extraordinary stability profile, exceptional biocompatibility, and possible drug delivery carrier applications to cancer cells. Fundamental properties of fluorescence arising from the formation of Schiff bond and self-assembling properties from tuning hydrophobicity on the choice of amino acids has been discussed. Furthermore, we anticipate that this system can also be utilized for biosensing purposes for different metal ions based on the combined effect of electron transfer and inner-filter effect[49].

More importantly, future directions of this work can be extended to study and control physiochemical properties by the use of other hydrophobic amino acids such as phenylalanine or tyrosine and improve process development to control FONPs size which dictates *in vivo* biodistribution and pharmacokinetic profiles. Photoluminescent properties can also be tuned to the NIR region by use of dopants (Nitrogen, sulfur, phosphorus) for applications image-guided surgery. Targeting ligands can also be conjugated to direct FONPs to specific biomarkers on cancer cells for increased therapeutic outcomes. This work is significant in the field of non-conjugated polymer research because it provides understanding of the generation of the nanomaterials, implications in bioimaging, and improvement of available drug delivery platforms of cancer chemotherapeutics.

Competing financial interests

The authors declare no competing financial interests.

Acknowledgments

We would like to thank James Talaska and Janice Taylor at the UNMC Advanced Microscopy Core Facility which receives partial support from the National Institute for General Medical Science (NIGMS) INBRE - P20 GM103427 and COBRE - P30 GM106397 grants, as well as support from the National Cancer Institute (NCI) for The Fred & Pamela Buffett Cancer Center Support Grant- P30 CA036727, and the Nebraska Research Initiative. We would also like to thank Victoria Smith and Samantha Wall at the UNMC Flow Cytometry Research

Facility which is administrated through the Office of the Vice Chancellor for Research and supported by state funds from the Nebraska Research Initiative (NRI) and The Fred and Pamela Buffett Cancer Center's National Cancer Institute Cancer Support Grant. Major instrumentation has been provided by the Office of the Vice Chancellor for Research, The University of Nebraska Foundation, the Nebraska Banker's Fund, and by the NIH-NCRR Shared Instrument Program This work was funded by the National Institute of Biomedical Imaging and bioengineering (R01 EB019449), the Fred & Pamela Buffett Cancer Center at UNMC (P30 CA036727), and the UNMC Program of Excellence fellowship awarded to Deep S Bhattacharya. Authors are also thankful to Professor Amarnath Natarajan for providing FTIR facility to this work. We gratefully acknowledge the TEM services provided by Mr. Tom Berger at the Electron Microscopy Facility, UNMC. Authors would also like to thank Mr. Shah Valloppilly for XRD at the University of Nebraska-Lincoln and XPS by Mr. Randy Nessler and Mr. Kenny Horkley at the Central Microscopy Research Facility of the University of Iowa. We would also like to thank Madeline Olson for her technical assistance in designing manuscript figures.

References

1. Yao, J., Yang, M. & Duan, Y. Chemistry, biology, and medicine of fluorescent nanomaterials and related systems: New insights into biosensing, bioimaging, genomics, diagnostics, and therapy. *Chemical Reviews* (2014). doi:10.1021/cr200359p
2. Peng, H. S. & Chiu, D. T. Soft fluorescent nanomaterials for biological and biomedical imaging. *Chemical Society Reviews* (2015). doi:10.1039/c4cs00294f
3. Zhu, S., Song, Y., Shao, J., Zhao, X. & Yang, B. Non-conjugated polymer dots with crosslink-enhanced emission in the absence of fluorophore units. *Angew. Chemie - Int. Ed.* (2015). doi:10.1002/anie.201504951
4. Hong, Y., Lam, J. W. Y. & Tang, B. Z. Aggregation-induced emission: Phenomenon, mechanism and applications. *Chemical Communications* (2009). doi:10.1039/b904665h
5. Svechkarev, D., Kyrychenko, A., Payne, W. M. & Mohs, A. M. Development of colloidally stable carbazole-based fluorescent nanoaggregates. *J. Photochem. Photobiol. A Chem.* (2018). doi:10.1016/j.jphotochem.2017.10.042
6. Mabire, A. B. *et al.* Aminomaleimide fluorophores: a simple functional group with bright, solvent dependent emission. *Chem. Commun. (Camb).* (2015). doi:10.1039/c5cc02908b
7. Yang, Y. *et al.* One-step synthesis of amino-functionalized fluorescent carbon nanoparticles by hydrothermal carbonization of chitosan. *Chem. Commun.* (2012). doi:10.1039/c1cc15678k
8. Han, B. *et al.* Polyethyleneimine modified fluorescent carbon dots and their application in cell labeling. *Colloids Surfaces B Biointerfaces* (2012). doi:10.1016/j.colsurfb.2012.05.016
9. Ma, C. *et al.* Preparation of fluorescent organic nanoparticles from polyethylenimine and sucrose for cell imaging. *Mater. Sci. Eng. C* **68,** 37–42 (2016).
10. Zhu, S. *et al.* The crosslink enhanced emission (CEE) in non-conjugated polymer dots: From the photoluminescence mechanism to the cellular uptake mechanism and internalization. *Chem. Commun.* (2014). doi:10.1039/c4cc05806b
11. Qiao, Z. A. *et al.* A ‘ship-in-a-bottle’ approach to synthesis of polymer dots@silica or polymer dots@carbon core-shell nanospheres. *Adv. Mater.* (2012). doi:10.1002/adma.201202620
12. Liu, M. *et al.* Fluorescent nanoparticles from starch: Facile preparation, tunable luminescence and bioimaging. *Carbohydr. Polym.* **121,** 49–55 (2015).
13. Yang, X. *et al.* Novel and green synthesis of high-fluorescent carbon dots originated from honey for sensing and imaging. *Biosens. Bioelectron.* (2014). doi:10.1016/j.bios.2014.04.046
14. Li, C. L. *et al.* Carbon dots prepared from ginger exhibiting efficient inhibition

of human hepatocellular carcinoma cells. *J. Mater. Chem. B* (2014). doi:10.1039/c4tb00216d

15. Guo, S. R. *et al.* Biocompatible, luminescent Silver@Phenol formaldehyde resin core/shell nanospheres: Large-scale synthesis and application for in vivo bioimaging. *Adv. Funct. Mater.* (2008). doi:10.1002/adfm.200701440
16. Sun, B. *et al.* Fluorescent non-conjugated polymer dots for targeted cell imaging. *Nanoscale* (2016). doi:10.1039/c6nr01909a
17. Gu, G. E. *et al.* Fluorescent polydopamine nanoparticles as a probe for zebrafish sensory hair cells targeted in vivo imaging. *Sci. Rep.* (2018). doi:10.1038/s41598-018-22828-2
18. Li, W. *et al.* Simple and green synthesis of nitrogen-doped photoluminescent carbonaceous nanospheres for bioimaging. *Angew. Chemie - Int. Ed.* (2013). doi:10.1002/anie.201303927
19. Liu, S. G. *et al.* pH-Mediated Fluorescent Polymer Particles and Gel from Hyperbranched Polyethylenimine and the Mechanism of Intrinsic Fluorescence. *Langmuir* (2016). doi:10.1021/acs.langmuir.6b00201
20. Hill, T. K. *et al.* Near infrared fluorescent nanoparticles derived from hyaluronic acid improve tumor contrast for image-guided surgery. *Theranostics* **6,** 2314–2328 (2016).
21. Mondek, J., Kalina, M., Simulescu, V. & Pekař, M. Thermal degradation of high molar mass hyaluronan in solution and in powder; comparison with BSA. *Polym. Degrad. Stab.* (2015). doi:10.1016/j.polymdegradstab.2015.06.012
22. Kulandaisamy, A. J. & Rayappan, J. B. B. Significance of Nanoparticles and the Role of Amino Acids in Structuring Them—A Review. *J. Nanosci. Nanotechnol.* (2018). doi:10.1166/jnn.2018.15388
23. Shemyakin, M. M., Maimind, V. I., Ermolaev, K. M. & Bamdas, E. M. The mechanism of osazone formation. *Tetrahedron* (1965). doi:10.1016/S0040-4020(01)98362-0
24. El Khadem, H. Chemistry of Osazones. *Adv. Carbohydr. Chem.* (1965). doi:10.1016/S0096-5332(08)60298-2
25. Peelen, D. & Smith, L. M. Immobilization of amine-modified oligonucleotides on aldehyde-terminated alkanethiol monolayers on gold. *Langmuir* (2005). doi:10.1021/la048166r
26. Guo, L., Wu, S., Zeng, F. & Zhao, J. Synthesis and fluorescence property of terbium complex with novel schiff-base macromolecular ligand. *Eur. Polym. J.* (2006). doi:10.1016/j.eurpolymj.2006.01.025
27. Kaya, İ., Sandal, B. S. & Karaer, H. Synthesis, characterization and electrochemical properties of poly(phenoxy-imine)s containing peril and tert-butyl units. *J. King Saud Univ. - Sci.* (2019). doi:10.1016/j.jksus.2017.06.008
28. Kelkar, S. S., Hill, T. K., Marini, F. C. & Mohs, A. M. Near infrared fluorescent nanoparticles based on hyaluronic acid: Self-assembly, optical properties, and cell interaction. *Acta Biomater.* **36,** 112–121 (2016).
29. Ma, Y., Pan, G., Zhang, Y., Guo, X. & Zhang, H. Narrowly dispersed hydrophilic molecularly imprinted polymer nanoparticles for efficient molecular recognition in real aqueous samples including river water, milk,

and bovine serum. *Angew. Chemie - Int. Ed.* (2013). doi:10.1002/anie.201206514

30. Lavis, L. D. & Raines, R. T. Bright building blocks for chemical biology. *ACS Chem. Biol.* (2014). doi:10.1021/cb500078u
31. Liu, S. *et al.* Hydrothermal treatment of grass: A low-cost, green route to nitrogen-doped, carbon-rich, photoluminescent polymer nanodots as an effective fluorescent sensing platform for label-free detection of Cu(II) ions. *Adv. Mater.* (2012). doi:10.1002/adma.201200164
32. Vallan, L., Urriolabeitia, E. P., Benito, A. M. & Maser, W. K. A versatile room-temperature method for the preparation of customized fluorescent non-conjugated polymer dots. *Polymer (Guildf).* (2019). doi:10.1016/j.polymer.2019.05.041
33. Billman, J. H. & Diesing, A. C. Reduction of Schiff Bases with Sodium Borohydride. *J. Org. Chem.* (1957). doi:10.1021/jo01360a019
34. Gatej, I., Popa, M. & Rinaudo, M. Role of the pH on hyaluronan behavior in aqueous solution. *Biomacromolecules* (2005). doi:10.1021/bm040050m
35. Zhao, F. *et al.* Cellular uptake, intracellular trafficking, and cytotoxicity of nanomaterials. *Small* (2011). doi:10.1002/smll.201100001
36. Sun, Y. *et al.* Ultrabright and Multicolorful Fluorescence of Amphiphilic Polyethyleneimine Polymer Dots for Efficiently Combined Imaging and Therapy. *Sci. Rep.* **3,** 3036 (2013).
37. Murphy, C. B. *et al.* Probing Förster and Dexter energy-transfer mechanisms in fluorescent conjugated polymer chemosensors. *J. Phys. Chem. B* (2004).
38. Wu, C., Zheng, Y., Szymanski, C. & McNeill, J. Energy transfer in a nanoscale multichromophoric system: Fluorescent dye-doped conjugated polymer nanoparticles. *J. Phys. Chem. C* (2008). doi:10.1021/jp074149+
39. Jiang, Y. & McNeill, J. Light-harvesting and amplified energy transfer in conjugated polymer nanoparticles. *Chemical Reviews* (2017). doi:10.1021/acs.chemrev.6b00419
40. Yuan, Y. *et al.* Doxorubicin-loaded environmentally friendly carbon dots as a novel drug delivery system for nucleus targeted cancer therapy. *Colloids Surfaces B Biointerfaces* (2017). doi:10.1016/j.colsurfb.2017.07.030
41. Chen, S., Yu, Y. L. & Wang, J. H. Inner filter effect-based fluorescent sensing systems: A review. *Analytica Chimica Acta* (2018). doi:10.1016/j.aca.2017.10.026

CHAPTER V:

FUTURE DIRECTIONS

Summary of CD44 binding studies

In this work, we have shown that hyaluronic acid when modified to deacetylated HA (deHA), sulfated HA (sHA), and deacetylated sulfated HA (s-deHA) forms, have lower binding affinity to CD44 compared to natural HA. The decrease in binding is due to hindrance in recognition of key molecular fingerprints in the HA polymer backbone to essential amino acids in the active site of CD44. Future studies will evaluate different molecular weights of HA and intracellular downstream pathways.

Other chemical modifications that can be explored are selective methylation/arylation of HA. Methylation of HA has shown increased long-term stability and higher *in vivo* stability. Methylation could also lead to the recognition alteration with CD44 and could also potentially be re-targeted to other receptors, which require relatively hydrophobic groups in a polymer for binding. Longer *in vivo* stability could be attributed to resistance to hyaluronidases for degradation similar to sulfated HA. Newer imaging/drug delivery nanoparticle systems could be developed from methylated HA for assessment of *in vivo* performance in image-guided surgery.

Another approach would be engineer CD44 mutants to mutate the vital amino acids for recognition of HA and modified HA derivatives using more robust biophysical techniques such as surface plasma resonance (SPR) and bio-layer

interferometry (BLI). This will ensure that the interactions are indeed as described from computational results. However, the major drawback of chemical modifications on HA has been the non-location-specific conjugation and polydispersity, making it difficult to control the chemical reaction on a molecular level precisely. Nonetheless, HA is a highly useful biocompatible polymer, and its future applications will doubtlessly expand in biomedical research.

Summary of P-selectin binding studies

In this work, HA was synthetically modified to retarget selectin protein (P-selectin) for delivery of imaging dye Cyanine 7.5 for image-guided surgery. HA was regio-selectively sulfated to yield three polymers with different sulfate substitution ratios. Completely sulfated HA (csHA)> moderately sulfated HA > selectively sulfated HA in decreasing bound to P-selectin. Moderately sulfated HA was used to target both P-selectin with high affinity and CD44 with lower affinity as a multi-targeted system. Higher tumor accumulation was detected for sulfated HA nanoparticles was observed compared to non-sulfated HA nanoparticles in S2-013 tumors. Higher RES uptake was also observed for the sulfated HA nanoparticles as size ranged from 200-500 nm, which limit the overall dose reaching the tumor. Future directions will evaluate approaches to the optimized size of NPs and avoid macrophage recognition system to increase tumor delivery.

Size of the nanoparticle can be reduced to smaller size ranges by use of the lower molecular weight of HA (2-5 kDa) or addition of ultrasonication steps

during nanoparticle process optimization. Use of click chemistry instead of EDC/NHS conjugation chemistry might affect the overall NP product, however, iterative optimizations will be needed to design the system of interest.

One approach that can be utilized to evade the macrophage machinery is by developing a protein-carbohydrate delivery system. CD47, a protein which is known as a marker for “self” is present in all almost all cell types. Macrophages contain a receptor called SIRP-1-α which recognizes CD47 and signals the “Do not eat me” signal. This process prevents the detection and engulfing of the body’s own cells and help identify foreign objects such as nanoparticles. The design of the protein-carbohydrate system will include (i) Synthesis of HA or sHA polymer conjugates of NIR dye of interest; (ii) Conjugation of CD47 to HA or sHA-dye conjugate by lysine-mediated conjugation using EDC/NHS machinery, followed by purification. There are two potential positive outcomes of this design; first, targeting would mainly be driven by recognition by macrophages and also by macrophage-mediated penetration to tumors; or P-selectin/CD44 mediated recognition of the polymer conjugated to the protein. Drawbacks of this system could be to ascertain the exact mechanism of tumor uptake and the role of each component in the delivery system. Nonetheless, this approach might attract new channels for the design of novel-HA based delivery systems.

A better understanding of the *in vivo* performance of the sulfated system vs non-sulfated system would be to evaluate the image-guided surgery efficacy in an orthotopic pancreatic cancer model of S2-013. Subcutaneous tumor models in which tumor is grown in the back hip, providing optical protection of the NIR

signal from the tumor from visceral organs such as liver and kidneys. Future studies will also require survival surgery and direct comparison of contrast agents between target tissues. A larger animal model would be appropriate to investigate the contrast agents between tumors and other underlying tissues in a surgical setting. Large animal models that could be used are canines and porcine. However, price and availability are major limitations for routine analysis. One appropriate animal may be rats, which are substantially larger than mice while smaller than many other research species.

Non-invasive preclinical imaging methods are critical for the development of newer classes of contrast agents. Pharmacokinetics is the study of what the body does to a drug influencing biodistribution and clearance properties. Future studies will be to evaluate different pharmacokinetic parameters (half-life in the distribution phase ($t_{(1/2)\alpha}$), terminal half-life ($t_{(1/2)\beta}$), volume of distribution (V_c), the volume in steady-state(V_{ss}), the blood clearance (clearance), the estimated concentration at time 0 (C_0), Hepatic clearance, and Area under the curve (AUC) of various contrast agents (non-sulfated HA nanoparticles and sulfated HA nanoparticles) in Sprague-Dawley rats.

Summary of fluorescent organic nanoparticle studies

In this work, HA was synthetically modified with natural amino acids to yield fluorescent conjugates (FONPs) via cross-linked enhanced emission effect (CEE). Tryptophan, Tryptophan benzyl ester, and proline benzyl esters were utilized as hydrophobic ligands to help drive the self-assembly process of HA nanoparticles. The FONPs have been investigated as less toxic and more biocompatible substitutes for quantum dots. FONPs have sizes exceeding 200 nm with no smaller size ranges and lower polydispersity analogs. Carbon dots in size ranges of 10-30 nm obtain higher tumor accumulation.

Future directions to stimulate preparation of smaller sizes of FONPs would involve use of lower molecular weights of HA, ultrasonication methods, and use of cross-linking agents. This approach could also lead to improved colloidal stability and reduced degradation rates.

The fluorescence generation was associated with formation of multiple sub-fluorophoric C=N (Schiff bonds) groups in the polymeric matrix. Future studies will involve elucidating the exact underlying fluorescence mechanism by using advanced spectroscopic techniques such as time-resolved spectroscopy. A deeper understanding of the role of C=N bond in fluorescence generation can be studied using different structural analogs. Methods to control the bond rotations around C=N could include addition of bulkier groups and studying addition of different chemical substituent around C=N bond and studying the energy bad gap differences by HOMO and LUMO. Other methods to study the influence of could be the addition of dopants on fluorescence could be use of nitrogen, phosphorous

or halogens. Such chemical entities have been reported to influence the excited state dynamics in a fluorescent species.

SPRINGER NATURE

Title: Structures of the Cd44–hyaluronan complex provide insight into a fundamental carbohydrate-protein interaction
Author: Suneale Banerji et al
Publication: Nature Structural & Molecular Biology
Publisher: Springer Nature
Date: Feb 11, 2007

Order Completed

Thank you for your order.

This Agreement between Mr. Deep Bhattacharya ("You") and Springer Nature ("Springer Nature") consists of your license details and the terms and conditions provided by Springer Nature and Copyright Clearance Center.

Your confirmation email will contain your order number for future reference.

printable details

License Number	4674920976685
License date	Sep 23, 2019
Licensed Content Publisher	Springer Nature
Licensed Content Publication	Nature Structural & Molecular Biology
Licensed Content Title	Structures of the Cd44–hyaluronan complex provide insight into a fundamental carbohydrate-protein interaction
Licensed Content Author	Suneale Banerji et al
Licensed Content Date	Feb 11, 2007
Type of Use	Thesis/Dissertation
Requestor type	academic/university or research institute
Format	print
Portion	figures/tables/illustrations
Number of figures/tables/illustrations	1
High-res required	no
Will you be translating?	no
Circulation/distribution	1 - 29
Author of this Springer Nature content	no
Title	Ph.D. Candidate

Institution name	University of Nebraska Medical Center
Expected presentation date	Nov 2019
Portions	Figure 1
Requestor Location	Mr. Deep Bhattacharya 5-12384 Scott Research Tower Fred Pamella Buffett Cancer Center OMAHA, NE 68105 United States Attn: Mr. Deep Bhattacharya
Total	0.00 USD

Syntheses of defined sulfated oligohyaluronans reveal structural effects, diversity and thermodynamics of GAG–protein binding

S. Köhling, J. Blaszkiewicz, G. Ruiz-Gómez, M. I. Fernández-Bachiller, K. Lemmnitzer, N. Panitz, A. G. Beck-Sickinger, J. Schiller, M. T. Pisabarro and J. Rademann, *Chem. Sci.*, 2019, **10**, 866
DOI: 10.1039/C8SC03649G